FABRICATION AND LIGHT MANAGEMENT OF MICROSCALE SOLAR CELLS

BY

YUAN YAO

DISSERTATION

Submitted in partial fulfillment of the requirements
for the degree of Doctor of Philosophy in Chemistry
in the Graduate College of the
University of Illinois at Urbana-Champaign, 2016

Urbana, Illinois

Doctoral Committee:

Professor Ralph G. Nuzzo, Chair
Professor Andrew A. Gewirth
Professor Paul V. Braun
Assistant Professor Josh Vura-Weis

Abstract

Photovoltaic (PV) technology holds great promises to become one of the renewable alternatives that can eventually replace the depleting fossil fuel reserves. Challenges, however, remain in various disciplines to achieve a performance-to-cost ratio that can stay economically competitive against traditional energy sources. This dissertation highlights efforts that tackle such challenges from different perspectives, using lightweight microscale semiconductor membranes with unconventional form factors.

We start with the fabrication of second-generation silicon solar microcells, with enhanced processing robustness and energy conversion efficiency by utilizing a thermally grown SiO_2 material, which serves as both an etching/doping mask and a passivation/anti-reflection layer. Combined with a backside-reflector and a polymer waveguide, these ribbon-like miniature semiconductor membranes demonstrate performance merits that are comparable to commercial silicon solar cells, albeit with significantly less active material consumption. The inherent low optical absorption of these ultrathin devices can be effectively improved by either creating nanocone structures on the device surface that elongate the photon propagation path within the cell, or converting the polymer waveguide to a luminescent solar concentrator (LSC) with luminophores that actively down-converts incident sunlight and redirects it to the embedded microcells. Strategies explored in this work to improve the performance of such LSC devices include the use of core-shell quantum dots with tunable bandgaps and minimum reabsorption losses, the design of a luminescence-trapping photonic mirror with photon recycling effects and the assembly of a multilayer construct with expanded spectral coverage.

The low-cost microcell concept can be extended from Si to III-V PV materials, which have much higher efficiency due to their direct bandgap structure and the ability to form multi-junction architectures that minimize both absorption and carrier thermalization losses. Their high material cost due to the epitaxy growth process is usually compensated by use of concentrating optics, which then leads to performance constraints that include the optical losses from the geometric lenses and the inability to capture diffuse solar radiation. In the last section of this work, novel nanoporous optical materials and hybrid module architectures are created for a commercial concentration photovoltaics (CPV) module that employs triple-junction III-V microcells, with significantly reduced Fresnel losses and added capability of utilizing diffuse sunlight.

To my family, friends and everyone else that has supported me along the journey.

Acknowledgments

This work would not have been possible without the support and contributions from countless individuals. First and foremost, I would like to express my gratitude to my advisor Ralph Nuzzo, who has provided me with valuable guidance and continuous support throughout my time in graduate school, as well as Paul Alivisatos and John Rogers, with whose group that I collaborated closely for my Ph.D. work. I would also like to thank the Professors that have kindly served on my prelim and/or doctoral exam committees: Angus Rockett, Catherine Murphy, Andrew Gewirth, Paul Braun, and Josh Vura-Weis. I'm also grateful to the group of talented students and scientists that I have been fortunate to work with during my time at UIUC, who have been a constant source of inspiration for me to generate new ideas and figure out solutions, including Eric Brueckner, Lanfang Li, Noah Bronstein, Xing Sheng, Kyu-Tae Lee, Zhida Xu, Tao Shang, Jim Mabon, Lu Xu, Junwen He as well as all the Nuzzo group members. Last but not the least, I would like to thank my immediate family, especially my mother, who raised me through hardships and sacrifices.

Table of Contents

Chapter 1 Introduction to Semiconductor Membranes[1]

1.1 Semiconductor Membranes for Low-Cost Energy Applications

The production of integrated electronic circuits provides examples of the most advanced fabrication and assembly approaches that are generally characterized by large-scale integration of high-performance compact semiconductor elements that rely on rigid and essentially planar form factors. New methods of fabricating semiconductor membranes of micro- or nano-scale thickness with intrinsic mechanical flexible features are beginning to provide a set of means to lift these constraints by engendering deformable, three-dimensional device configurations that are difficult to achieve with bulk-scale materials while retaining capacities for high (or altogether new forms of) electronic and/or optoelectronic performance. Together with enabling means of deterministic assembly realized via the advancing technology of transfer-printing, these light-weight semiconductor membrane elements can be distributed over large areas on a soft, bendable, and even biocompatible secondary substrates with high throughput and yields to realize interesting new functionalities in technology. Exemplary cases include: large-area integrated electro-optical systems laminated onto curvilinear or other 3-D surfaces for use in sensing and imaging with capacities for accommodating demanding forms of mechanical flexure; and unconventional hybrid systems for lighting and photovoltaic energy conversion that provide a potentially transformational approach to supplant current technologies with high performance, low cost alternatives. Taken together, the results of recent research efforts illustrate important opportunities for exploiting advances in materials in synergy with physical means of patterning, fabrication and assembly. In the first part of the introduction, we explore several exemplary applications of semiconductor membranes, and specifically highlight scalable approaches to high performance integrated systems for low cost energy technologies.

---

[1] The content of this chapter is reproduced with modification and permission from Yuan Yao, Ralph G. Nuzzo, "Nanomembranes and soft fabrication methods for high performance, low cost energy technologies",Proc. SPIE 9608, Infrared Remote Sensing and Instrumentation XXIII, 960818,

1.2 Properties of Semiconductor Membranes

Semiconductor membranes are free-standing films of single crystalline structures with a thickness in the nanometer/micrometer range. They possess unique properties unavailable in other material formats, such as optoelectronic characteristics associated with quantum confinement effects[1-4] and flexible mechanical features[5,6] resulting from their ultra-thin geometry. For example, a Si membrane with a thickness around 100 nm has a flexural rigidity that is more than fifteen orders of magnitude lower as compared to a bulk wafer (200 μm thick)[7], allowing it bend to a small radius (less than 10 μm) without cracking[6] and thus making it compatible with common polymeric materials for device assembly and packaging. Integrated with soft substrates, these 2-D membranes have been widely studied in recent years[8,9], providing new functional capacities for accommodating demanding forms of mechanical flexure by circumventing constraints imposed by conventional electronics, where individual rigid (though high-performance) device components (usually at least a couple of hundreds micrometers thick) are fabricated to the highest density possible on a semiconductor wafer before being diced and packaged into their final form. New exemplary applications emerging from this research include bio-integrated systems[10] as well as advanced hybrid materials system for lighting[11,12], energy storage, and solar radiation conversion[13,14]. Organic membranes[15-18] have been considered a suitable candidate for these applications due to their intrinsic flexibility, although their performance is limited by the nature of charge transport within the material[9]. Inorganic membranes, on the other hand, circumvent this limitation and hold additional advantages as their fabrication processes are generally compatible with standard semiconductor processing routes. In this paper, we will focus on the energy-related applications with examples illustrating the fabrication and assembly of inorganic semiconductor membranes of varying dimensions and shapes into soft, highly flexural forms while maintaining the high electrical performance of their bulk counterparts.

1.3 Fabrication of Semiconductor Membranes

Electronic materials membranes are easily generated by means of exfoliating thin layers directly from bulk wafers bearing a heterogeneous material architecture through isotropic chemical wet etching, an example of which is illustrated in Figure 1.1(a)[14]. Alternating layers of aluminum

arsenide (AlAs) and gallium arsenide (GaAs) were first epitaxially grown onto a bulk GaAs substrate, with AlAs functioning as a sacrificial layer to be selectively removed in a hydrogen fluoride (HF) solution. Large quantities of GaAs membranes were then created during the HF etching step in a high throughput fashion, with thickness precisely controlled in the growth process and 2-D dimensions defined by standard industrial semiconductor processing procedures including photolithography and reactive ion etching (RIE). The substrate can be recovered after the etching to lower down the material cost and membranes with different chemical compositions (e.g. GaN[12,19], InP[20] and InGaP[21]) can be fabricated with appropriate sacrificial layer and substrate selection.

Similar strategies can be used to exfoliate Si membranes, where HF is used to undercut the epitaxially grown Si film by etching away the buried oxide (BOX) layer on a silicon-on-insulator (SOI) wafer[22]. High performance devices including transistors[23] and solar cells[24] have been fabricated in this manner, although the high cost of the SOI wafers hinders its widespread commercial adaption. A low-cost alternative was developed to take advantage of the different etching rates of different crystalline faces of silicon in base solutions (e.g. KOH) and to directly fabricate Si membranes from inexpensive homogeneous bulk silicon wafers[25,26], as shown in Figure 1.1(b). A trench structure with proper alignment was first defined by photolithography and then etched using RIE into a bulk Si (111) wafer. A oxide/ metal wet etching mask was then deposited using plasma enhanced chemical vapor deposition (PECVD) and angled e-beam evaporation to protect the top and sidewall surfaces of the structure. Finally, the wafer was immersed in a KOH solution at 80 °C to exfoliate the silicon ribbons as the etch rate of the low index (110) face is about two magnitudes higher than that of (111). SEM images on the right side of the Figure 1.1(b) show the state of the ribbons before and after being released from the wafer. Other masking methods that avoid metal evaporation have also been developed to avoid potential metal contamination issues[27]. These procedures, when repeated, are capable of converting the entire wafer into membranes and therefore hold significant advantages in their cost-effectiveness.

1.4 Assembly of Semiconductor Membranes Using Transfer-Printing

The exfoliated membrane inks needs to be assembled in an orderly manner before being interconnected to provide functionalities comparable to conventional electronics. One of the

most developed approaches for this purpose is the transfer-printing based assembly method[28], where a soft, elastic stamp is used to manipulate these membrane inks[29]. The procedure starts with inks still weakly attached to the donor substrates (Figure 1.2(a)), either by van der Waals forces or anchor structures that are designed to withstand the undercut etching but fracture easily during the pick-up process. These anchors may consist of the same materials with the ink or a distinct material, such as a photoresist post[30]. Compared to the system dependent solely on van der Waals adhesion, an anchored scheme provides better spatial precision prior to and during transfer and therefore is more suitable for large-area electronics where the membranes need to be integrated at specific locations with submicron accuracy. A structured stamp is then brought into contact with the inks and retracted at high speeds from the donor substrate to selective retrieve the inks from the areas of contact (Figure 1.2(b)). The transfer assembly process is complete after the inked stamp is pressed onto the receiver substrate and then delaminated at slow retraction speeds to deliver the inks (Figure 1.2(c)). The key to the last two steps is to control the adhesion dynamics occurring at the critical interfaces (donor/ink, ink/stamp, ink/receiver) by tuning the stamp peeling-off speed to achieve "pick-up" or "print" functionalities, as guided by rate dependent effects (see Figure 1.2(d)) of the viscoelastic poly(dimethylsiloxane) (PDMS) stamps, where lower separation velocity between the ink and stamp yield a lower adhesion energy[31]. More advanced stamp structures can be developed to further enhance the contrast between strong and weak adhesion modes to improve the transfer yields and broaden the ranges of applicable inks and substrates[32]. The transfer assembly method is advantageous due to the fact that it can achieve deterministic assembly of the membranes in a high-throughput manner using automated tool sets.

1.5 Exemplar Applications of Semiconductor Membranes

Arrays of devices can be assembled using the transfer-printing method to provide functionalities for a broad range of applications in technology, including lighting and photovoltaic energy conversion. Figures 1.3(a-f) demonstrate an example[12], where microscale gallium nitride (GaN) light emitting diodes (LED) were first fabricated on a bulk Si wafer bearing an epitaxially grown GaN layer (Figure 1.3(a)), and then picked-up by a PDMS stamp (Figure 1.3(b)) before being transferred to the receiving substrate (Figure 1.3(c)). With self-aligned metal features that serve

as electrical interconnects and thermal heat sinks, large sparse arrays of integrated blue LEDs embedded in a soft, polymeric substrate can be built (Figure 1.3(d)), with nearly identical device performances as compared with those measured on wafer (Figure 1.3(e)). The capacity of generating white light with tunable chromaticity in such an unconventional system was also demonstrated by coupling these arrays with phosphors and thin-film optical diffusers (Figure 1.3 (f)). The same concepts were also extended to systems using GaN grown on sapphire[33], rendering it more compatible with current commercial epitaxial growth process.

Solid state semiconductor membranes are also useful for harvesting solar radiation. For example, arrays of silicon membranes integrated with silicon dioxide passivation can be made on a bulk Si (111) wafer with anchored structures on the opposite corners that cleave during the transfer-printing step (Figure 1.3(g))[13,27]. The power-conversion-efficiency measured for a device on a non-reflective substrate is over 10%, with a fill factor ~0.75. Coupled with a diffuse backside reflector, its current output can be doubled, reaching a level that is comparable with conventional silicon solar cells. Advantages of this geometry with sparse arrays of Si membrane devices (Figure 1.3(h)) embedded in a polymer substrate include their low material consumption due to their ultrathin geometry and easy integration with secondary optics including microlens arrays[13] and luminescent waveguides[34,35] to further boost their power output and enhance their cost-effectiveness. An optical image of such as solar cell array that bends along the device long axis is shown in Figure 1.3(i), where the polymer between the Si ribbons was doped with an organic luminophore that absorbs sunlight and converts it to optical modes that are guided to the device, resulting in a 4 times higher photocurrent. With carefully designed substrates and optical coating thicknesses as well as device layouts that minimize strains on the Si membrane (Figure 1.3(j)), the solar cell modules can be bent to small radii of curvature without bringing detrimental impacts on the device performance. Other advanced concepts for solar energy conversion (e.g. spectrum splitting[36], photon recycling[37]) can also be realized using transfer-printed semiconductor membranes. Figure 1.3(k) shows an example[36], where a 3-J solar cell membrane (blue) was transfer-printed on to a bottom Ge solar cell (red) to build a mechanically stacked architecture for actively splitting the solar spectrum and minimizing carrier thermalization losses. An index matched As_2Se_3 interface layer was used to minimize the interface reflection loss and to provide both electrical insulation and heat dissipation.

A biomimetic application of impressive scope developed by Rogers is shown in Figure 1.3(l-n)[38]. A serpentine shaped interconnect structure was designed to link Si membrane photodetectors (coupled with a microlens array, Figure 1.3(l)) to minimize the strain during the deformation into hemispherical shape (Figure 1.3(m)) for integration into an apposition camera with an extremely wide angle of view (160°). The short focal length of the microlens also allows a nearly infinite depth of view, enabling the camera to image multiple objects in a field of view simultaneously, even at widely different angular positions and distances.

1.6 Figures

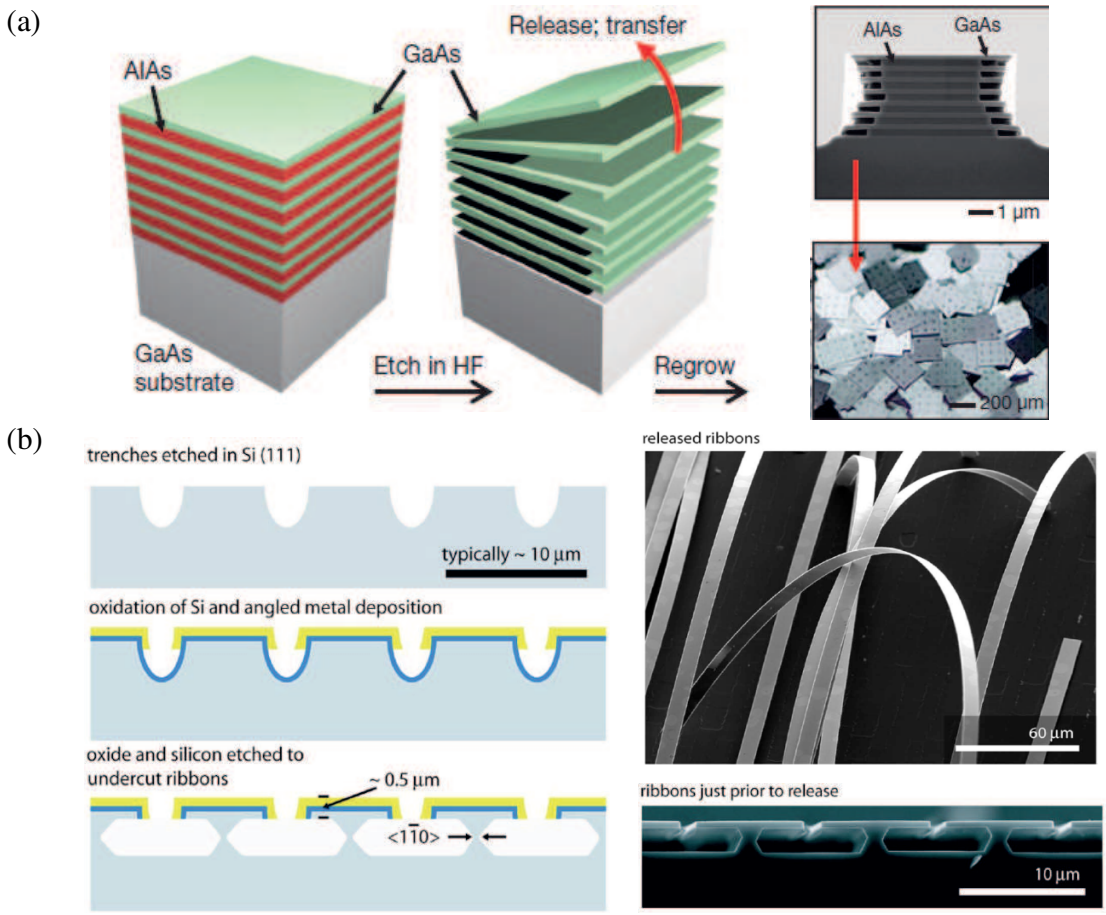

Figure 1.1 Fabrication methods of semiconductor membranes: (a) Release of GaAs membranes in a epitaxial stack with isotropic etching of the sacrificial layer AlAs[14]; (b) Undercutting silicon ribbons from bulk silicon wafers using anisotropic wet etching with KOH[25].

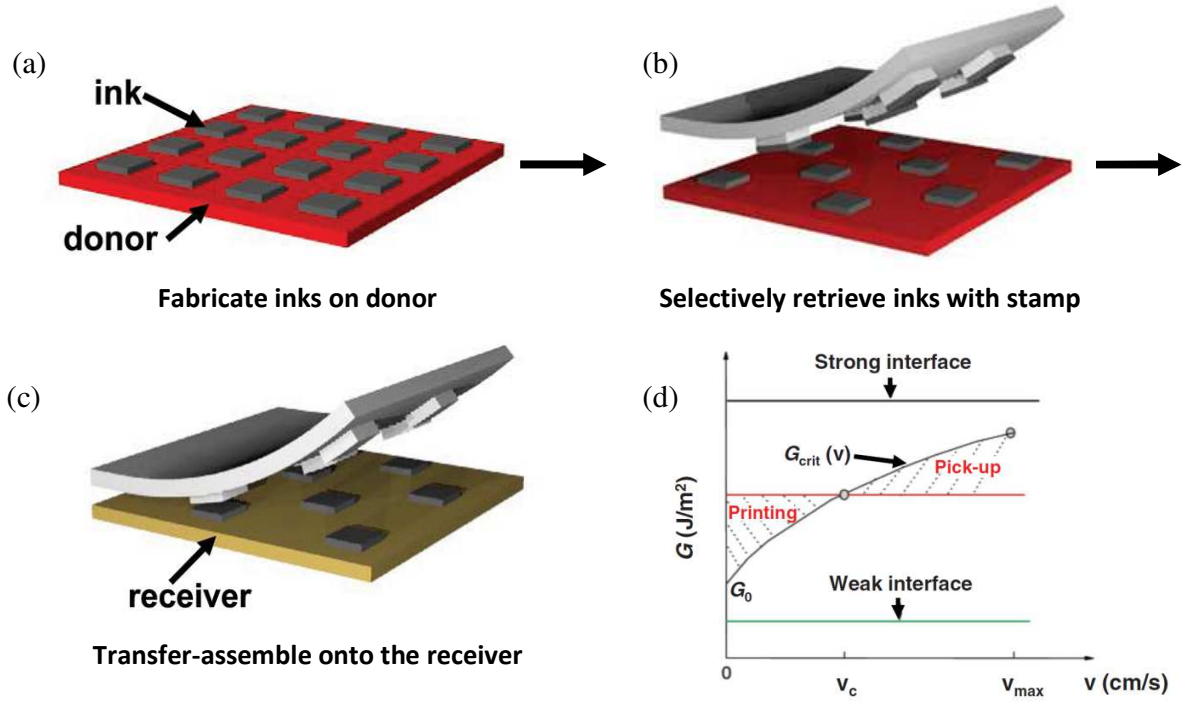

Figure 1.2 Transfer-printing of semiconductor membranes: (a-c) Schematic illustrations of the process of picking up the inks from the donor substrate and printing onto the receiver substrate[28]; (d) Critical energy release rate of the stamp/ink and ink/donor(or receiver) interface[31].

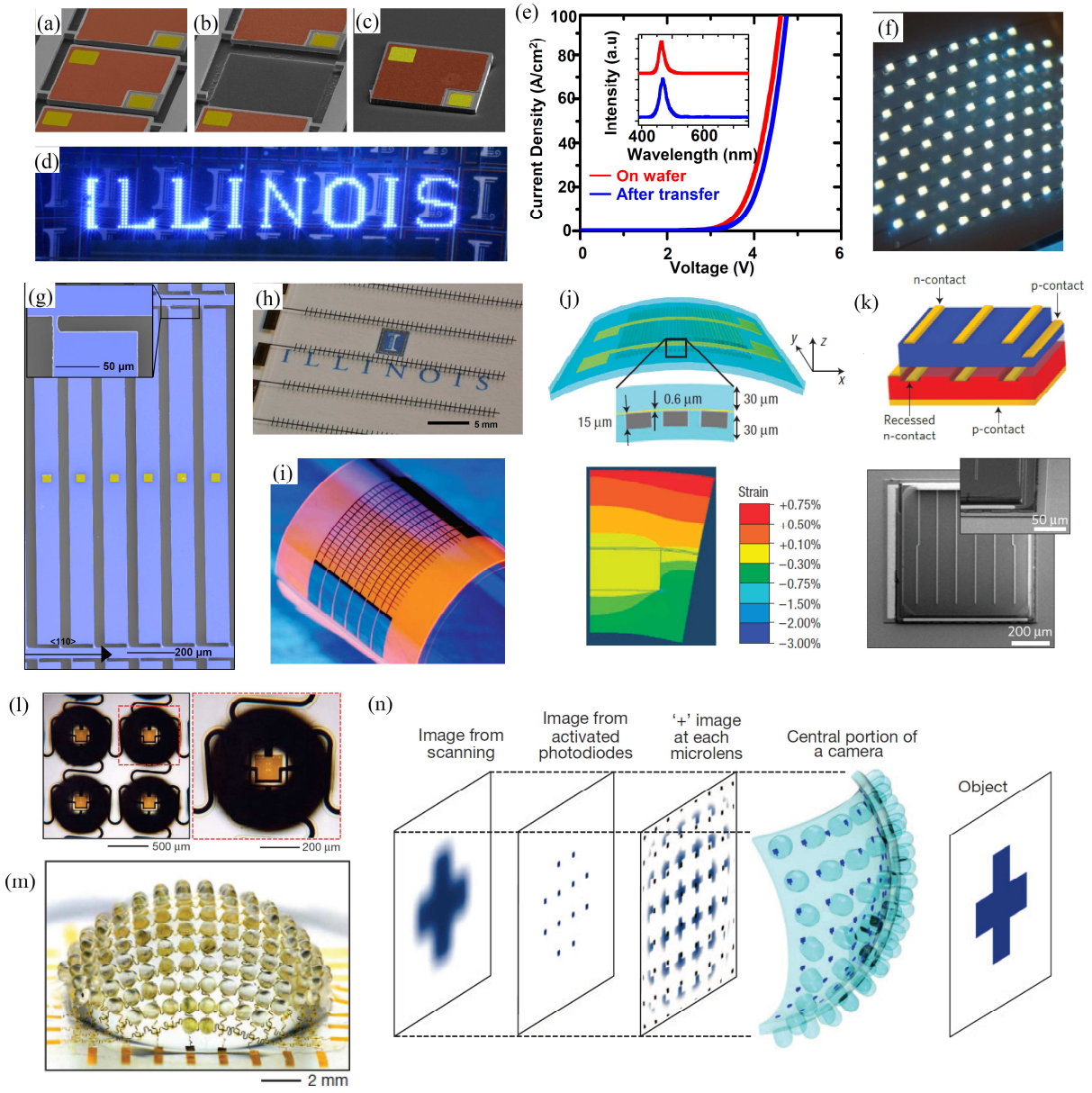

Figure 1.3 Applications of semiconductor membranes: (a-f) LEDs [12]; (g-k) solar cells [13,27,34,36]; (l-n) a biomimetic camera[38].

1.7 References

[1] Zhang, P.; Tevaarwerk, E.; Park, B.-N.; Savage, D. E.; Celler, G. K.; Knezevic, I.; Evans, P. G.; Eriksson, M. A.; Lagally, M. G. Electronic transport in nanometre-scale silicon-on-insulator membranes. *Nature* **2006**, *439*, 703-706.

[2] Yu, J.-K.; Mitrovic, S.; Tham, D.; Varghese, J.; Heath, J. R. Reduction of thermal conductivity in phononic nanomesh structures. *Nat. Nanotechnol.* **2010**, *5*, 718-721.

[3] Tang, J.; Wang, H.-T.; Lee, D. H.; Fardy, M.; Huo, Z.; Russell, T. P.; Yang, P. Holey Silicon as an Efficient Thermoelectric Material. *Nano Lett.* **2010**, *10*, 4279-4283.

[4] Fujita, M.; Takahashi, S.; Tanaka, Y.; Asano, T.; Noda, S. Simultaneous Inhibition and Redistribution of Spontaneous Light Emission in Photonic Crystals. *Science* **2005**, *308*, 1296-1298.

[5] Suo, Z.; Ma, E. Y.; Gleskova, H.; Wagner, S. Mechanics of rollable and foldable film-on-foil electronics. *Appl. Phys. Lett.* **1999**, *74*, 1177-1179.

[6] Baca, A. J.; Ahn, J.-H.; Sun, Y.; Meitl, M. A.; Menard, E.; Kim, H.-S.; Choi, W. M.; Kim, D.-H.; Huang, Y.; Rogers, J. A. Semiconductor Wires and Ribbons for High- Performance Flexible Electronics. *Angew. Chem., Int. Ed.* **2008**, *47*, 5524-5542.

[7] Symon, K. R. *Mechanics 3rd edn*; Addison-Wesley, 1971.

[8] Rogers, J. A.; Lagally, M. G.; Nuzzo, R. G. Synthesis, assembly and applications of semiconductor nanomembranes. *Nature* **2011**, *477*, 45-53.

[9] Junwen, H.; Nuzzo, R. G.; Rogers, J. A. Inorganic Materials and Assembly Techniques for Flexible and Stretchable Electronics. *Proc. IEEE* **2015**, *103*, 619-632.

[10] Rogers, J. A. In *IEEE Int. Electron Devices Meet. (IEDM)* 2012, p 1.1.1-1.1.4.

[11] Park, S.-I.; Xiong, Y.; Kim, R.-H.; Elvikis, P.; Meitl, M.; Kim, D.-H.; Wu, J.; Yoon, J.; Yu, C.-J.; Liu, Z.; Huang, Y.; Hwang, K.-c.; Ferreira, P.; Li, X.; Choquette, K.; Rogers, J. A. Printed Assemblies of Inorganic Light-Emitting Diodes for Deformable and Semitransparent Displays. *Science* **2009**, *325*, 977-981.

[12] Kim, H.-s.; Brueckner, E.; Song, J.; Li, Y.; Kim, S.; Lu, C.; Sulkin, J.; Choquette, K.; Huang, Y.; Nuzzo, R. G.; Rogers, J. A. Unusual strategies for using indium gallium nitride grown on silicon (111) for solid-state lighting. *Proc. Natl. Acad. Sci. U. S. A.* **2011**, *108*, 10072-10077.

[13] Yoon, J.; Baca, A. J.; Park, S.-I.; Elvikis, P.; Geddes, J. B.; Li, L.; Kim, R. H.; Xiao, J.; Wang, S.; Kim, T.-H.; Motala, M. J.; Ahn, B. Y.; Duoss, E. B.; Lewis, J. A.; Nuzzo, R. G.; Ferreira, P. M.; Huang, Y.; Rockett, A.; Rogers, J. A. Ultrathin silicon solar microcells for semitransparent, mechanically flexible and microconcentrator module designs. *Nat. Mater.* **2008**, *7*, 907-915.

[14] Yoon, J.; Jo, S.; Chun, I. S.; Jung, I.; Kim, H.-S.; Meitl, M.; Menard, E.; Li, X.; Coleman, J. J.; Paik, U.; Rogers, J. A. GaAs photovoltaics and optoelectronics using releasable multilayer epitaxial assemblies. *Nature* **2010**, *465*, 329-333.

[15] Burroughes, J. H.; Bradley, D. D. C.; Brown, A. R.; Marks, R. N.; Mackay, K.; Friend, R. H.; Burns, P. L.; Holmes, A. B. Light-emitting diodes based on conjugated polymers. *Nature* **1990**, *347*, 539-541.

[16] Reineke, S.; Lindner, F.; Schwartz, G.; Seidler, N.; Walzer, K.; Lussem, B.; Leo, K. White organic light-emitting diodes with fluorescent tube efficiency. *Nature* **2009**, *459*, 234-238.

[17] Hoppe, H.; Sariciftci, N. S. Organic solar cells: An overview. *J. Mater. Res.* **2004**, *19*, 1924-1945.

[18] Günes, S.; Neugebauer, H.; Sariciftci, N. S. Conjugated Polymer-Based Organic Solar Cells. *Chem. Rev.* **2007**, *107*, 1324-1338.

[19] Lee, K. J.; Meitl, M. A.; Ahn, J.-H.; Rogers, J. A.; Nuzzo, R. G.; Kumar, V.; Adesida, I. Bendable GaN high electron mobility transistors on plastic substrates. *J. Appl. Phys.* **2006**, *100*, 124507.

[20] Yang, W.; Yang, H.; Qin, G.; Ma, Z.; Berggren, J.; Hammar, M.; Soref, R.; Zhou, W. Large-area InP-based crystalline nanomembrane flexible photodetectors. *Appl. Phys. Lett.* **2010**, *96*, 121107.

[21] Sheng, X.; Corcoran, C. J.; He, J.; Shen, L.; Kim, S.; Park, J.; Nuzzo, R. G.; Rogers, J. A. Enhanced ultraviolet responses in thin-film InGaP solar cells by down-shifting. *Phys. Chem. Chem. Phys.* **2013**, *15*, 20434-20437.

[22] Khang, D.-Y.; Jiang, H.; Huang, Y.; Rogers, J. A. A Stretchable Form of Single-Crystal Silicon for High-Performance Electronics on Rubber Substrates. *Science* **2006**, *311*, 208-212.

[23] Lee, K. J.; Motala, M. J.; Meitl, M. A.; Childs, W. R.; Menard, E.; Shim, A. K.; Rogers, J. A.; Nuzzo, R. G. Large-Area, Selective Transfer of Microstructured Silicon: A Printing- Based

Approach to High-Performance Thin-Film Transistors Supported on Flexible Substrates. *Adv. Mater.* **2005**, *17*, 2332-2336.

[24] Shir, D.; Yoon, J.; Chanda, D.; Ryu, J.-H.; Rogers, J. A. Performance of Ultrathin Silicon Solar Microcells with Nanostructures of Relief Formed by Soft Imprint Lithography for Broad Band Absorption Enhancement. *Nano Lett.* **2010**, *10*, 3041-3046.

[25] Mack, S.; Meitl, M. A.; Baca, A. J.; Zhu, Z.-T.; Rogers, J. A. Mechanically flexible thin-film transistors that use ultrathin ribbons of silicon derived from bulk wafers. *Appl. Phys. Lett.* **2006**, *88*, 213101.

[26] Baca, A. J.; Meitl, M. A.; Ko, H. C.; Mack, S.; Kim, H. S.; Dong, J.; Ferreira, P. M.; Rogers, J. A. Printable Single-Crystal Silicon Micro/Nanoscale Ribbons, Platelets and Bars Generated from Bulk Wafers. *Adv. Funct. Mater.* **2007**, *17*, 3051-3062.

[27] Yao, Y.; Brueckner, E.; Li, L.; Nuzzo, R. Fabrication and assembly of ultrathin high-efficiency silicon solar microcells integrating electrical passivation and anti-reflection coatings. *Energy Environ. Sci.* **2013**, *6*, 3071-3079.

[28] Carlson, A.; Bowen, A. M.; Huang, Y.; Nuzzo, R. G.; Rogers, J. A. Transfer printing techniques for materials assembly and micro/nanodevice fabrication. *Adv. Mater.* **2012**, *24*, 5284-5318.

[29] Meitl, M. A.; Zhu, Z.-T.; Kumar, V.; Lee, K. J.; Feng, X.; Huang, Y. Y.; Adesida, I.; Nuzzo, R. G.; Rogers, J. A. Transfer printing by kinetic control of adhesion to an elastomeric stamp. *Nat. Mater.* **2006**, *5*, 33-38.

[30] Yang, Y.; Hwang, Y.; Cho, H. A.; Song, J.-H.; Park, S.-J.; Rogers, J. A.; Ko, H. C. Arrays of Silicon Micro/Nanostructures Formed in Suspended Configurations for Deterministic Assembly Using Flat and Roller-Type Stamps. *Small* **2011**, *7*, 484-491.

[31] Feng, X.; Meitl, M. A.; Bowen, A. M.; Huang, Y.; Nuzzo, R. G.; Rogers, J. A. Competing Fracture in Kinetically Controlled Transfer Printing. *Langmuir* **2007**, *23*, 12555-12560.

[32] Kim, S.; Wu, J.; Carlson, A.; Jin, S. H.; Kovalsky, A.; Glass, P.; Liu, Z.; Ahmed, N.; Elgan, S. L.; Chen, W.; Ferreira, P. M.; Sitti, M.; Huang, Y.; Rogers, J. A. Microstructured elastomeric surfaces with reversible adhesion and examples of their use in deterministic assembly by transfer printing. *Proc. Natl. Acad. Sci. U. S. A.* **2010**, *107*, 17095.

[33] Kim, T.-i.; Jung, Y. H.; Song, J.; Kim, D.; Li, Y.; Kim, H.-s.; Song, I.-S.; Wierer, J. J.; Pao, H. A.; Huang, Y.; Rogers, J. A. High-Efficiency, Microscale GaN Light-Emitting Diodes and Their Thermal Properties on Unusual Substrates. *Small* **2012**, *8*, 1643-1649.

[34] Yoon, J.; Li, L.; Semichaevsky, A. V.; Ryu, J. H.; Johnson, H. T.; Nuzzo, R. G.; Rogers, J. A. Flexible concentrator photovoltaics based on microscale silicon solar cells embedded in luminescent waveguides. *Nat. Commun.* **2011**, *2*, 343.

[35] Bronstein, N. D.; Li, L.; Xu, L.; Yao, Y.; Ferry, V. E.; Alivisatos, A. P.; Nuzzo, R. G. Luminescent Solar Concentration with Semiconductor Nanorods and Transfer-Printed Micro-Silicon Solar Cells. *ACS Nano* **2014**, *8*, 44-53.

[36] Sheng, X.; Bower, C. A.; Bonafede, S.; Wilson, J. W.; Fisher, B.; Meitl, M.; Yuen, H.; Wang, S.; Shen, L.; Banks, A. R.; Corcoran, C. J.; Nuzzo, R. G.; Burroughs, S.; Rogers, J. A. Printing-based assembly of quadruple-junction four-terminal microscale solar cells and their use in high-efficiency modules. *Nat. Mater.* **2014**, *13*, 593-598.

[37] Sheng, X.; Yun, M. H.; Zhang, C.; Al-Okaily, A. a. M.; Masouraki, M.; Shen, L.; Wang, S.; Wilson, W. L.; Kim, J. Y.; Ferreira, P.; Li, X.; Yablonovitch, E.; Rogers, J. A. Device Architectures for Enhanced Photon Recycling in Thin-Film Multijunction Solar Cells. *Adv. Energy Mater.* **2015**, *5*, 1400919.

[38] Song, Y. M.; Xie, Y.; Malyarchuk, V.; Xiao, J.; Jung, I.; Choi, K.-J.; Liu, Z.; Park, H.; Lu, C.; Kim, R.-H.; Li, R.; Crozier, K. B.; Huang, Y.; Rogers, J. A. Digital cameras with designs inspired by the arthropod eye. *Nature* **2013**, *497*, 95-99.

Chapter 2 Full Solar Spectrum Conversion via Multi-Junction Architectures and Optical Concentration[2]

2.1 Current Status of Solar Cell Efficiencies

Significant advances have been made in research to improve the performance of single-junction photovoltaic devices. Currently, the best silicon and GaAs devices have achieved efficiencies of 25.6% and 28.8%, respectively.[1] The realization of significant further enhancements in the efficiencies of photovoltaic energy conversion, however, resorts to multi-junction (MJ) architectures using semiconductor materials with subcell bandgaps tuned to target different portions of the solar spectrum, in order to minimize carrier thermalization losses and increase spectrum coverage to exceed the Shockley-Queisser limit.[2] In theory, a MJ cell can achieve an efficiency as high as 86.8% with an infinite number of junctions[3] (a value lower than the Landsberg limit[4] due to entropy losses), and a number of different cell designs have been intensively explored by the photovoltaic research community as means through which such forms of performance enhancement can be realized. These include most notably devices that embed the semiconductor elements in the form of multi-junction solar cell stacks[5], and to a lesser degree optical approaches involving various forms of spectrum splitting[6]. In the first design, the subcells are either epitaxially or mechanically stacked together in the order of decreasing bandgaps to divide the incident sunlight using the absorption of the subcells. In the second approach, separate optics (e.g. prisms, holograms, and dielectric band-pass filters) are used to split the solar spectrum and direct different portions to the relevant subcell. It has been persuasively argued that both designs would benefit from high geometric concentration of the solar irradiance as one means to both offset the high materials costs encumbered by the III-V semiconductor device elements and to enhance the system power-conversion efficiency. To date, cell stacking designs have achieved the highest benchmark performances in solar energy conversion, with world-record efficiencies of MJ cells reaching 46.0% with a 4-junction design (InGap/GaAs//GaInAsP/GaInAs) under 508 suns.[1] Exemplary recent progress includes a report

[2] The content of this chapter is reproduced with permission from Yuan Yao, Lu Xu, Xing Sheng, Noah D Bronstein, John A Rogers, A Paul Alivisatos, Ralph G Nuzzo, "Roadmap on optical energy conversion" section 11, Journal of Optics, 2016 18(7), 073004

from our group of 43.9% efficient quadruple junction, four terminal microscale solar cells that were fabricated by mechanical stacking of a top 3-J device onto a bottom Ge cell via transfer-printing-based assembly. [7]

2.2 Challenges to Further Improving PV Efficiencies

For epitaxially-grown MJ devices, the difficulty of sustaining lattice matching through multiple layers of growth limits the materials selections that are available for use in each subcell and thus directly restricts achievable limits for device performance. Mechanically-stacked devices, on the other hand, can be fabricated via high temperature wafer bonding[8] to circumvent this issue, but still carries a requirement for current matching at the electrically-conducting interfaces, which is difficult to realize as the number of subcells increase to sub-divide the solar spectrum. Alternatively, insulating adhesives can be used between mechanically stacked subcells to enable multi-terminal connections and in this way avoid the need for current matching. These interfaces need to be carefully designed to minimize reflection losses, as well as manage heat flow and thermal-mechanical stresses at high optical concentration.[7] Additional electro-optical challenges exist for the material used in each subcell. For example, a top wide-bandgap subcell (i.e. $E_g > 1.4$ eV) generally cannot be doped to a sufficiently high level to enable efficient carrier collection under high-irradiance concentration; it requires incorporation of highly doped, low bandgap materials that either degrade its optical transparency for low energy photons or complicated back contact grid configurations.[5]

It has been noted that the limitations associated with stacked MJ devices can be tackled in principle by employing external optical components to split and distribute the solar radiation to an array of spatially separated subcells.[9] By decoupling material compatibility from bandgap optimization, this approach also enables MJ designs with larger numbers of subcells and, thus, higher theoretical efficiencies. As the cell fabrication steps are reduced to providing a set of single-junction devices, simplified process flows for the semiconductor components are possible. The common proposed optical designs include holographic gratings and wavelength-selective mirrors (e.g. multilayer dielectric Bragg stacks). Their practical use, however, is hindered by the formidable requirements for high-optical quality as well as the complexity of the optical designs needed to achieve competitive system-level efficiencies.

The high cost of III-V materials, especially in MJ cell contexts, likely necessitates a high optical-concentration design to achieve commercial viability. Optical losses figure importantly in all forms of concentrator PV designs. Stacked cells, for example, are subject to significant Fresnel losses (e.g. 12% of incident photons are lost to reflection before reaching the solar cells for a system with three glass/air interfaces) that limit their optical (and thus power conversion) efficiencies. Broadband anti-reflection (AR) coatings would afford an ideal solution, but materials that can span the refractive index range needed to mitigate these effects have yet to be developed. The use of common light trapping designs on the PV cells also become more complex, as they can scatter light and otherwise limit the broad-spectrum performance of high-concentration optics. Geometric solar concentrators (GSC) also require solar tracking, and even more significantly do not utilize diffuse light—a significant component of the solar spectrum. (The diffuse component is 10% in AM1.5G illumination; most locations in the United States having 24% to 50% diffuse sunlight[10].)

2.3 Strategies to Further Enhance Efficiencies

2.3.1 Light Management Within and Between Subcells

It has been shown in single junction devices that high external radiation efficiencies (ERE), as achieved by luminescence extraction enhanced by photon recycling, are crucial for high PV performance (as demonstrated by the world record GaAs device, where the radiatively emitted photons are reflected by a metal back surface rather than absorbed by the substrate).[11,12] Likewise, MJ devices with intermediate reflectors that enhance ERE with photon recycling would improve the V_{oc} for each subcell (Figure 2.1), although these reflectors also need to transmit subbandgap photons for the next cell. Different designs have been examined theoretically that provide such effects, such as stacks spaced by an airgap coupled with AR coatings as the intermediate reflector in-between subcells.[13] The elements of this design have been demonstrated experimentally using microscale solar cells stacked onto pre-patterned airgap spacers using a soft-transfer-printing technique.[14] The opportunities for progress have also been demonstrated theoretically in the design of a high performance spectrum-splitting PV system that uses polyhedral specular reflectors coupled to spatially separated devices to enhance both photon recycling within a subcell and radiative coupling between them.[15]

2.3.2 Improving the Optical Efficiencies of GSC

There exist numerous opportunities to improve the performance of concentrator PV systems. Providing improved broadband antireflection coatings (e.g. porous films with subwavelength features to avoid scattering) forms one obvious direction in research to reduce the Fresnel losses associated with concentrating optics. The development of strategies that would allow the utilization of diffuse light within a concentrator PV design is also of significant interest. We might envision, for example, the coupling of a GSC with a luminescent solar concentrator (LSC), wherein diffuse radiation striking the backplane can be absorbed by the luminophore and down-converted into total internal reflection modes that are directed to the embedded photovoltaic device elements. A possible geometry for such a system suggested by elements of our past work is one embedding arrays of microscale solar cells directly in the LSC waveguide (Figure 2.2), such that, in addition to diffuse light conversion, the direct illumination from the sun can be concentrated at the top surface of the devices using a GSC with a higher concentration ratio and optical efficiency.[16,17] We have shown that quantum dot luminophores (QD) are particularly advantageous for use in such microcell LSC arrays as compared to traditional organic dyes, as they have high quantum yields, large (and tunable) Stokes shifts for reduced reabsorption losses, and better long-term photo-stability. Their narrow emission peak also facilitates photonic designs to better trap/ manage the luminescent photons to improve optical efficiency.[17,18] It is also of particular interest to note that high optical efficiency LSCs may engender specific capabilities for high performance CPV designs that would be transformational, specifically to obviate the need for solar tracking as well as the intriguing possibility that they might enable new approaches to spectrum splitting using discrete subcell arrays that can achieve efficiencies approaching those associated with monolithic MJ cell stacks.

2.4 Concluding Remarks

Multi-junction architectures are required to achieve full spectrum conversion and surpass the Shockley-Queisser limit. Concentration is advantageous in a MJ system in both improving their efficiency and reducing their cost. This perspective outlines new materials, optical integration strategies, and approaches to spectrum splitting that beget new opportunities through which the grand challenge of full-spectrum conversion might be realized.

2.5 Figures

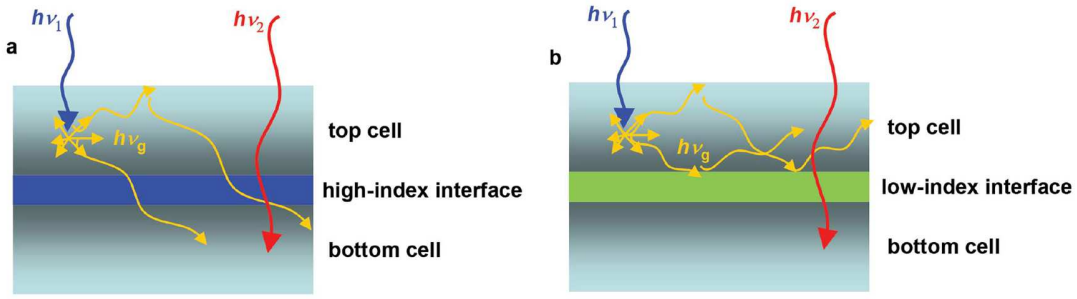

Figure 2.1 Illustrations demonstrating photon dynamics in a MJ device.[14] (a) No photon recycling: the radiative emission from the top cell is coupled to the bottom cell. (b) With photon recycling: using a low index interface as an intermediate reflector, the ERE and V_{oc} of the top cell are enhanced.

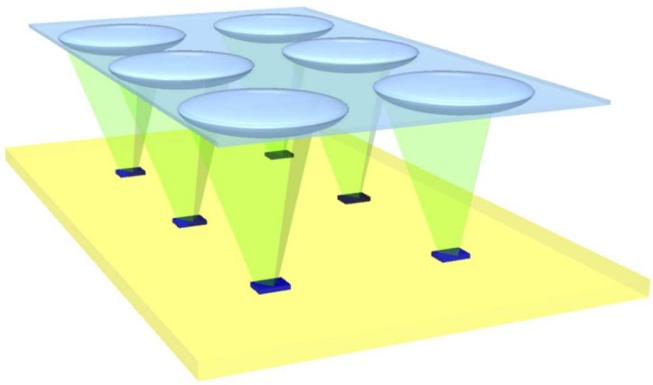

Figure 2.2 Schematic design of a hybrid concentration system with an embedded microscale solar cell module, both the device and the luminescent waveguide can be configured as a multi-junction architecture for full spectrum conversion.

2.6 References

[1] Green, M. A.; Emery, K.; Hishikawa, Y.; Warta, W.; Dunlop, E. D. Solar cell efficiency tables (Version 45). *Prog. Photovoltaics: Res. Appl.* **2015**, *23*, 1-9.

[2] Shockley, W.; Queisser, H. J. Detailed Balance Limit of Efficiency of p-n Junction Solar Cells. *J. Appl. Phys.* **1961**, *32*, 510-519.

[3] Vos, A. D. Detailed balance limit of the efficiency of tandem solar cells. *J. Phys. D: Appl. Phys.* **1980**, *13*, 839.

[4] Landsberg, P. T.; Tonge, G. Thermodynamic energy conversion efficiencies. *J. Appl. Phys.* **1980**, *51*, R1-R20.

[5] Cotal, H.; Fetzer, C.; Boisvert, J.; Kinsey, G.; King, R.; Hebert, P.; Yoon, H.; Karam, N. III-V multijunction solar cells for concentrating photovoltaics. *Energy Environ. Sci.* **2009**, *2*, 174-192.

[6] Imenes, A. G.; Mills, D. R. Spectral beam splitting technology for increased conversion efficiency in solar concentrating systems: a review. *Sol. Energy Mater. Sol. Cells* **2004**, *84*, 19-69.

[7] Sheng, X.; Bower, C. A.; Bonafede, S.; Wilson, J. W.; Fisher, B.; Meitl, M.; Yuen, H.; Wang, S.; Shen, L.; Banks, A. R.; Corcoran, C. J.; Nuzzo, R. G.; Burroughs, S.; Rogers, J. A. Printing-based assembly of quadruple-junction four-terminal microscale solar cells and their use in high-efficiency modules. *Nat. Mater.* **2014**, *13*, 593-598.

[8] Derendorf, K.; Essig, S.; Oliva, E.; Klinger, V.; Roesener, T.; Philipps, S. P.; Benick, J.; Hermle, M.; Schachtner, M.; Siefer, G.; Jager, W.; Dimroth, F. Fabrication of GaInP/GaAs//Si Solar Cells by Surface Activated Direct Wafer Bonding. *IEEE J. Photovoltaics* **2013**, *3*, 1423-1428.

[9] Polman, A.; Atwater, H. A. Photonic design principles for ultrahigh-efficiency photovoltaics. *Nat. Mater.* **2012**, *11*, 174-177.

[10] Marion, W.; Wilcox, S. *Solar radiation data manual for flat-plate and concentrating collectors*; National Renewable Energy Laboratory, 1994.

[11] Miller, O. D.; Yablonovitch, E.; Kurtz, S. R. Strong Internal and External Luminescence as Solar Cells Approach the Shockley-Queisser Limit. *IEEE J. Photovoltaics* **2012**, *2*, 303-311.

[12] Kosten, E. D.; Kayes, B. M.; Atwater, H. A. Experimental demonstration of enhanced photon recycling in angle-restricted GaAs solar cells. *Energy Environ. Sci.* **2014**, *7*, 1907-1912.
[13] Ganapati, V.; Chi-Sing, H.; Yablonovitch, E. Air Gaps as Intermediate Selective Reflectors to Reach Theoretical Efficiency Limits of Multibandgap Solar Cells. *IEEE J. Photovoltaics* **2015**, *5*, 410-417.
[14] Sheng, X.; Yun, M. H.; Zhang, C.; Al-Okaily, A. a. M.; Masouraki, M.; Shen, L.; Wang, S.; Wilson, W. L.; Kim, J. Y.; Ferreira, P.; Li, X.; Yablonovitch, E.; Rogers, J. A. Device Architectures for Enhanced Photon Recycling in Thin-Film Multijunction Solar Cells. *Adv. Energy Mater.* **2015**, *5*, 1400919.
[15] Eisler, C. N.; Abrams, Z. e. R.; Sheldon, M. T.; Zhang, X.; Atwater, H. A. Multijunction solar cell efficiencies: effect of spectral window, optical environment and radiative coupling. *Energy Environ. Sci.* **2014**, *7*, 3600-3605.
[16] Yoon, J.; Li, L.; Semichaevsky, A. V.; Ryu, J. H.; Johnson, H. T.; Nuzzo, R. G.; Rogers, J. A. Flexible concentrator photovoltaics based on microscale silicon solar cells embedded in luminescent waveguides. *Nat. Commun.* **2011**, *2*, 343.
[17] Bronstein, N. D.; Li, L.; Xu, L.; Yao, Y.; Ferry, V. E.; Alivisatos, A. P.; Nuzzo, R. G. Luminescent Solar Concentration with Semiconductor Nanorods and Transfer-Printed Micro-Silicon Solar Cells. *ACS Nano* **2014**, *8*, 44-53.
[18] Xu, L.; Yao, Y.; Bronstein, N. D.; Li, L.; Alivisatos, A. P.; Nuzzo, R. G. Enhanced Photon Collection in Luminescent Solar Concentrators with Distributed Bragg Reflectors. *ACS Photonics* **2016**.

Chapter 3 Fabrication and Assembly of Ultrathin High-Efficiency Silicon Solar Microcells Integrating Electrical Passivation and Anti-Reflection Coatings[3]

3.1 Abstract

Intensive research into ultra-thin silicon solar cell applications has generated interesting approaches to reducing both critical materials usage and their associated device and module-level costs. Here we report an extension of previous work on micro-scale Si solar cells, devices fabricated using precise methods of micromachining Si (111) wafers in conjunction with wafer-scale processing. Here we describe a simple yet robust approach to fabricate the silicon microcells by re-designing the device structure, incorporating a thermally grown oxide layer to serve as a wet-etch and diffusion mask, and illustrate modes of light management and array assembly that can provide high-efficiency PV conversion of light to electrical energy. We report a best cell efficiency of 11.7% under an AM1.5D solar spectrum for an optically thin (30 μm thick) device, which is a substantial improvement over previously reported Si solar μ-cells. We show that the improvement attends to both the optimization made in the doping profiles of the device and the presence of the thermal oxide layer, which doubles as an effective electrical passivation and anti-reflection layer. External quantum efficiency measurements specifically show a marked improvement in the blue response that results from mitigating losses due to surface recombination in the high-surface-area, micro-scale devices. We highlight new strategies for integrating these devices into functional, interconnected arrays, using front and backside electrical bus contacts, with optimized spatial distributions on transparent glass substrates. This geometry, with optimized reflector and waveguiding planarization layers, creates a simple concentrator module by redirecting light via internal reflection to illuminate the sidewalls and bottom surfaces.

---

[3] The content of this chapter is reproduced with permission from Yuan Yao, Eric Brueckner, Lanfang Li and Ralph Nuzzo, " Fabrication and assembly of ultrathin high-efficiency silicon solar microcells integrating electrical passivation and anti-reflection coatings", Energy & Environmental Science, 2013, 6, 3071-3079, Copyright © The Royal Society of Chemistry

3.2 Introduction

Green energy demands have prompted an accelerating development of photovoltaic (PV) technologies that harvest and convert abundant solar energy into electrical power.[1] To date, crystalline silicon (single- or poly-crystalline) has been the dominant PV material in commercial modules (>85% share) due to its natural abundance, established processing routes, and excellent conversion efficiencies.[2,3] Widespread implementation, however, is limited in no small measure by high costs, over 50% of which originates from wafer production.[4]

An interesting approach to reduce materials costs is utilizing ultrathin silicon (with the thickness in the range of 5-50 μm, ut-Si) as the active PV material for solar cells.[3,5] Due to the large material losses that attend conventional wafering,[4] so-called kerf-free ut-Si—materials generated variously by epitaxial growth,[6] amorphous Si deposition and recrystallization,[7-9] or exfoliating Si layers from ingots[10]—is very attractive for terrestrial PV applications. The limited thicknesses of these PV devices further permit relaxed purity requirements (because of shorter carrier diffusion lengths) within the Si, further improving their economic viability.[11] These classes of solar cells, however, retain challenges, ones both fundamental and practical, that must still be overcome. Surface recombination due to the high surface-to-volume ratio of thin devices requires careful consideration as does the design of suitable light trapping schemes to compensate for their thin geometry and poor optical absorption. Additionally, "superstrates" and/or transfer methods for manipulating these mechanically fragile films must be carefully chosen to insure net process designs that are cost-effective and tolerant to the extreme environments encountered in solar cell processing.

Recent reports from our group have shown that thin (2-50 μm), micro-scale (μ-scale) PV devices of single-crystalline Si can be fabricated using traditional semiconductor processing routes and then, following complete device fabrication, retrieved from a donor source wafer and patterned deterministically by transfer assembly as sparse arrays on light-weight, flexible substrates.[11] This approach is particularly interesting since it: (1) overcomes challenges associated with deleterious handling of thin, fragile semiconductor membranes; (2) removes restrictions on high temperature processes since full device fabrication is completed on-wafer prior to transfer assembly; (3) allows easy integration with secondary optical components for light management (e.g., micro-lens arrays,[11] nanostructured surfaces,[12,13] and luminescent waveguides[14]) to

compensate for inherently low absorption; (4) allows for application-specific distributions and orientations of devices to create, for example, semitransparent displays[11] or high voltage modules;[15] and (5) is amenable to fabricating multiple generations of devices from a single Si wafer to decrease material costs.[11] The design of our earliest generations of μ-cells, however, require crucial improvements to address fundamental criteria for optimal carrier collection efficiency. While bulk recombination is reduced due to their thin geometry, surface recombination becomes a substantial loss mechanism from unpassivated dangling bonds since a passivation layer (e.g., thermal oxide, silicon nitride) is not incorporated.[16] Additionally, based on inferences coming from electrical data, optimization of the doping profile remains an important, albeit technically challenging, need. Specifically, the earlier μ-cells likely suffered from a degradation in performance due to a low carrier lifetime in the highly doped regions (i.e., heavy doping effects).[17] Finally, previously reported fabrication methods require two costly depositions of Cr/Au during the process sequence, the metals from which can act as deep level traps[18,19] for carriers as well as impurities that can severely degrade dopant sources if the wafers are not cleaned to very demanding tolerances.

Here, by adopting a different doping profile and utilizing robust masking layers, we report a simplified and highly scalable fabrication process whereby thin, ribbon-like solar cells are fabricated from a bulk single-crystalline Si wafer. These μ-cells retain all the features needed for use as solid-phase inks suited for transfer assembly[20] onto secondary substrates. Together they provide means of integration with low-cost materials that work synergistically with the Si to harvest and efficiently convert solar radiation to electrical energy. This protocol uses a thermally grown oxide layer as a robust etching and diffusion mask to bolster fabrication reliability, while also doubling as an effective passivation and anti-reflection (AR) layer to further improve device performance. With an optimized emitter doping concentration, we demonstrate conversion efficiencies of 11.7% (fill factor (FF) = 0.762) in an optically thin (30 μm) device under a simulated AM1.5D solar spectrum. We present design criteria for assembling printed μ-cells in optimized spatial distributions and strategies for integrating them with backside reflectors as well as polymer waveguides that efficiently manage (e.g., reflect and redirect) incident solar radiation to improve performance. By increasing the optical path length within the μ-cells and orthogonalizing light to illuminate once-invisible sidewalls, we leverage the increased surface

area of the μ-scale devices, while mitigating inherent loss mechanisms from them, to dramatically improve power generation for cells with this form factor.

3.3 Silicon Solar μ-Cell Fabrication

The μ-cell design is shown in Figure 3.1A, highlighting the layout of the phosphorus- (n^+, green), and boron- (p^+, blue), and intrinsically (p, gray) doped regions. The entire top surface is phosphorus doped to form the emitter (n^+) layer, while the back surface field (BSF, p^+) is formed by boron doping the whole bottom surface following undercut etching. The entire device, except the bottom surface, is covered (i.e. passivated) by a thermal oxide (purple layer), which serves to eliminate dangling bonds and minimize surface recombination, while at the bottom, minority carrier recombination is reduced by the built-in electrical field from the BSF.[21] A vertical contact scheme is adopted here, which compliments the design of Yoon, *et al.*[11] where both emitter and base contacts are coplanar on the top surface. The principal benefit of the doping geometry is that it enables us to eliminate two photolithography steps from the process flows that defined the doping regions on top of the device, simplifying the fabrication process and reducing shading losses from frontside contacts and metal interconnections.

Figure 3.1B schematically illustrates the key processing steps for creating the devices (see Supporting Information (SI) and Figure 3.7 for a detailed fabrication protocol). A Si (111) p-type, boron-doped, single crystalline Czochralski wafer (resistivity 7.5-10 Ω·cm), which we refer to as the donor wafer, was first doped by unmasked phosphorous (n^+) diffusion from solid doping sources to form the emitter layer (the SI, Table 3.1 and Figures 3.8-3.10 show data for the optimization of the phosphorus doping condition). After growth of the top oxide mask layer (~530nm) by wet oxidation, patterning of this layer by photolithography and deep etching with inductively coupled plasma reactive ion etching (ICP-RIE) defined the lateral dimensions and thickness of the devices, respectively. For purposes of anisotropic undercut etching in tetramethylammonium hydroxide (TMAH), the short axes of the devices were aligned parallel to the <110> direction, exposing the fast etching {110} planes along their sidewalls.[22] The exposed sidewalls of the Si structures were then briefly etched in a TMAH solution to create a canopy-type structure where the Si sidewall was recessed ~2.5 μm below the edge of the top oxide layer. A second wet oxidation created ~250 nm of SiO_2 on the sidewalls and trench floor while increasing the thickness of the top oxide to ~600 nm (Figure 3.11A). An unmasked flood

reactive ion etching (flood RIE) step fully removed oxide on the trench floor while preserving the sidewall oxide, due in part to the canopy structure (Figure 3.11B). With the protection of the top and sidewall oxide, the devices were then released in an anisotropic undercut etch in TMAH, yet remained tethered to the donor wafer in their lithographically defined locations, connected by break-away anchors (Figure 3.1C inset) to structures which were not undercut (long bars whose short axis is orthogonal to the <110> direction). Utilizing the existing thermal oxide as a diffusion mask, the exposed bottom surfaces of the μ-cells were doped with a boron solid-source to form the BSF, yielding fully functional devices. SEM images show that a thermal oxide of ~170 nm and ~25 nm remains on the top and sidewalls of the devices, respectively (Figure 3.11C), serving as both passivation and AR layers, as discussed later. The completed μ-cells demonstrated here are 1.5 mm long, 100 μm wide and 30 μm thick (Figure 3.1A and 3.1C). Contact pads (50 μm×50 μm) on top of the device were formed through photolithography, oxide etching, and metal (Ti/Au) deposition. With the completion of these steps, the devices are then amenable for integration via transfer assembly into arbitrarily large and sparse arrays, an example of which is shown in Figure 3.1D.

3.4 Silicon Solar μ-Cell Characterization

Electrical measurements of individual μ-cells were carried out after transfer-printing[20] them onto a glass substrate patterned with a Au backside contact bus line running transverse to the cell long dimension as shown in Figure 3.1D. Devices were tested in the dark as well as under simulated AM1.5D illumination of 1000 $W \cdot m^{-2}$ at room temperature. Baseline analyses of the solar μ-cells were performed by mounting the glass substrate on a non-reflective anodized aluminum (AA) plate to suppress reflection (see SI and Figure 3.15 for measurement details and reflection data) from the testing table, and assuming the illumination area is only the top surface area of the device for current density (J) and efficiency (η) calculations. Measurements were also performed with additional components introduced that enhance the PV performance of the μ-cell, and serve as quantitative points of comparison to the baseline analysis (subscript "base"). These additions (which are discussed in the following sections) include a polymeric planarization layer (subscript "PL"); a diffuse backside reflector (BSR, Labsphere Spectralon® target, subscript "BSR"); or both (subscript "PL, BSR").

The inset of Figure 3.2A shows a representative dark curve measured for an individual μ-cell, with a diode ideality factor (m) of 1.82. The baseline light curve of our best cell is presented in Figure 3.2A, with J_{sc}, open circuit voltage (V_{oc}), fill factor (FF), and η of 28.7 mA·cm^{-2}, 0.534 V, 0.762, and 11.7%, respectively. These values all show substantial improvement from the previous report[11] on Si solar μ-cells and, when coupled with a backside reflector to extend the effective optical path length of the cell, provide energy conversion efficiencies that compare favorably with traditional Si solar cells.

3.5 Thermal Oxide as Masking Material, Passivation Layer and AR Coating

A fundamental requirement for efficient transfer assembly is the release of the active device from the donor wafer by the undercut etching of a thin sacrificial layer between them.[23] Previous reports[24-26] of transfer-printed μ-scale, inorganic semiconductor devices rely on differential etching rates of disparate materials in the semiconductor stack. Homogeneous systems, such as the one discussed here, have no etch rate distinction between the active device layer and the donor wafer. SiO_2/SiN_x from low pressure and plasma enhanced chemical vapor deposition (LPCVD and PECVD, respectively) and/or e-beam evaporated Au layers[27-29] have been used as masking structures on the device's sidewalls to prevent complete lateral etching across the wafer surface, but thermally grown SiO_2 is known to be a denser masking material that is less prone to etchant permeability[30] compared to PECVD films and is simpler and potentially more cost-effective for use in this form of implementation than these previous processes. As shown in Figure 3.2B, the superior wet-etch masking properties of a thermally grown oxide layer in TMAH allows the creation of dense and defect-free arrays of devices over large areas. The fabrication yield is greatly improved for these μ-cells, generally >95%, and primarily limited by imperfections in the photolithography mask and particulates on the wafer during processing. The conformal oxide layer coats the top and sidewall surfaces and also serves as a diffusion mask to protect the *p*-*n* junction during the subsequent boron doping step, which is essential to achieving consistent device performance over large areas. Figures 3.2C and 3.12 show statistical analyses of PV metrics from μ-cells evenly distributed (i.e., every sixth device) over the entire fabricated device area. The low standard deviation of all the PV metrics illustrates the robustness of the new process design. We believe the efficacies of the processing and economies of the materials

usage retain constraints that are now governed only by photolithography capabilities and requirements for achieving reliable doping profiles over large areas.

Two of the key attributes for efficient terrestrial solar cell operation are: (1) efficiently harvesting solar radiation across the entire solar spectrum; and (2) minimization of parasitic charge carrier recombination. For the solar μ-cell motif, the addition of a thermal oxide layer with processing-centric advantages due to its wet-etch and diffusion masking properties, provides important functional contributions as a direct consequence of its ability to act as both an anti-reflection (AR) coating and electrical passivation layer. The AR coating suppresses optical loss from reflection, while high level surface recombination expected for μ-scale devices (due to their increased surface area) is minimized by effective passivation. These effects are clearly evidenced in data showing the photocurrent generation achieved with and without the conformal oxide layer. The *J-V* plot shown in Figure 3.3A illustrates this, where a 32.1% decrease (9.0 $mA \cdot cm^{-2}$) in J_{sc} and a 6.6% (0.034 V) decrease in V_{oc}, results in a significant drop of η from 10.89% to 6.80% for a μ-cell after removal of the oxide layer (these devices were first etched in buffered oxide etchant 6:1, and tested both immediately and after the formation of a native oxide layer in air, see Figure 3.13A and Table 3.2 in SI for device performance data). Further measurements definitively establish that both mechanisms contribute to the decrease in performance. The results from external quantum efficiency (EQE) measurements which illustrate this point are presented in Figure 3.3B. The μ-cell with a thermal oxide layer (black curve, J_{sc} = 27.0 $mA \cdot cm^{-2}$) shows a higher EQE at all wavelengths as compared to the one without it (red curve, J_{sc} = 18.2 $mA \cdot cm^{-2}$). This enhancement is especially evident in the blue region, where photons with relatively high energy are absorbed near the surface, a region where generated charge carriers are expected to be lost by recombination when the passivation layer is absent.[31] The AR effect is markedly evidenced by the peaks in the black curve that appears around 310 and 490 nm. The relative frequency-dependent optical enhancements from the top oxide layer of this device (Figure 3.13D, where two peak positions largely match those found in the EQE data) were estimated based on its thickness (~250 nm, based on cross-sectional SEM, see Figure 3.13B) and the known refractive indices of crystalline silicon and its thermal oxide (see Figure 3.13C for calculated reflections). The results of this calculation were then used to model, using the experimental data (red curve in Figure 3.3B), the EQE of non-passivated silicon μ-cell where only benefits from the AR effects are present. The result of this simulation is presented in Figure 3.3B (blue dashed

line, see SI for calculation methods). The difference between the two EQE curves (blue and red) suggests a 1.9 $mA \cdot cm^{-2}$ increase in current output under AM 1.5D solar spectrum due to AR effects, which is about 22 % of the total enhancement seen in the full cell (8.8 $mA \cdot cm^{-2}$). It is worth noting that, although the top oxide thickness was not optimized for optical absorption, the layer thickness is tunable in principle to provide higher absorption at different wavelengths (see SI Figure 3.13E for EQE plots from other devices with different optical interference due to variations in top oxide thickness). Although better AR coatings[32-35] can be developed through multi-layer dielectric deposition, the single layer thermal oxide is advantageous in terms of the simplicity of its means of integration into the fabrication protocol and its multifunctionallity—acting as both a robust mask material and passivation layer—without requirements for additional processing.

3.6 Integrating μ-Cells on Secondary Substrates

A unique feature of these μ-cells is the ability to deterministically assemble them into organized and functional layouts via transfer printing techniques.[36] Rapid delivery of devices onto receiving substrates can be achieved via multiple stamp inking and printing cycles with automated tools in high throughput.[36] A glass slide was used in our studies as a model receiving substrate for devices. A UV-curable adhesive (Norland Optical Adhesive (NOA), see SI for experimental details) was spin-coated on the substrate, then partially cured to remain tacky, to mediate the transfer process. For the vertically-contacted devices shown here, electrical contact must be made to the backside of the μ-cell. For this purpose, bottom electrodes (300 nm thick, 150 μm wide and 30 mm long) were deposited through a shadow mask onto the adhesive layer, serving as the electrical interconnect for the p^+ layer of the printed μ-cells, as shown by the schematic and SEM images in Figure 3.4A. A viscoelastic stamp with pyramid relief features[37] was used to selectively retrieve the devices from the donor wafer and deliver them to the glass substrate in high transfer yields (100% in the case of Figure 3.1D, see SI for experimental details). The configuration shown in Figure 3.4A yields fully functional Si solar μ-cells and is the configuration for which device testing in Figures 3.2 and 3.12 was conducted (i.e., without planarization). Printed μ-cells were planarized in a simple flow-based coating process that eliminates the need for additional registered levels of photolithography. To do so, a poly(dimethylsiloxane) (PDMS) block was laminated to the printed array of μ-cells, creating an

air gap between the PDMS and substrate (Figure 3.4B, left). NOA, the photocurable liquid resin, was then flowed by capillary action into the air gap and cured under illumination with UV light through the PDMS block, resulting in planarized μ-cells embedded in a polymer matrix (Figure 3.4B, right) with low topological variations (Figure 3.14A) over the areal expanse of the array (Figure 3.1D). The intimate contact between the planarization layer and the device (i.e., no air gap) is highlighted by the inset SEM image shown in Figure 3.4B. The planarization layer electrically insulates the bottom electrode, thereby rendering the array ready for top-side (n^+) interconnection. As one means for interconnection, Ag paste (PELCO Conductive Silver 187, Ted Pella) was screen-printed through an aligned stencil mask (see SI for experimental details) to achieve a relatively narrow (~150 μm, see Figure 3.4C) and thin (20-50 μm, see Figure 3.14B) electrode. These dimensions are ones that high-resolution printing methods[38] could easily improve upon.

3.7 Optical Enhancements to μ-Cells Embedded in Polymer Waveguide

The system described here—Si solar μ-cells embedded in a transparent polymer matrix on a glass substrate of comparable refractive indices—inherently creates a simple geometric concentrator especially when coupled with a BSR, as illustrated in Figure 3.5A. Light incident on the transparent areas between μ-cells is reflected by the diffuse BSR where it is then redirected to the μ-cell through internal reflection within the planarization layer and glass substrate. Additionally, since the μ-cells fabricated here have a thickness smaller than the optical absorption length of Si for near-infrared light,[39] BSRs can reflect the transmitted photons and help to extend the effective optical path within the device for improved performance. We use a modified Monte Carlo ray tracing method that deals with reflection and scattering processes at all interfaces to model such attributes of the photon flux (Φ) incident on the various surfaces of the μ-cell.[40] As shown in Figure 3.5B, for a planarized μ-cell on a diffuse BSR, the photon flux, normalized to Φ_{top}, on the top, bottom, and sidewall surfaces are 1, 0.55, and 0.36, respectively. These data show that photons are reflected from the BSR and then redirected to the μ-cell's sidewalls and bottom, with the planarization layer serving as a simple waveguiding structure. Similar concentrating structures have been studied by us[11,14,25,41] in the past, using a variety of μ-cell types, and by others[42] using macro-scale solar cells. Although attaining maximum concentration is limited by the relative leakiness of the waveguiding structure (and scattering

losses), it does provide a simple means to exploit an effective 180º acceptance angle and utilizes the otherwise un-illuminated sidewalls and bottom of the μ-scale devices for effective photon capture. The increased illumination on devices afforded by the planarization layer and diffuse BSR results in a direct boost of their PV performance. This is shown by the data given in Figure 3.5C, where the *I-V* curves of printed individual μ-cells with different optical components (i.e., planarization layer and BSR) are compared. In all cases I_{sc} increases significantly with a slight increase in V_{oc}. The trends are consistent with an increasing incident photon flux onto the cell. As explained subsequently, a μ-cell on an AA plate without planarization receives illumination largely on the top surface only, and therefore its curve (red) (I_{sc}=37.1 μA) is used as the baseline for comparison. Adding a planarization layer or BSR to the baseline results in a 16.7% increase (blue curve, $I_{sc,PL}$=43.3 μA) and 63.6% increase (green curve, $I_{sc,BSR}$=60.7 μA) in output, respectively. Incorporating both of these optical components to a μ-cell increases photocurrent generation by 95.7% (blue curve, $I_{sc,PL,BSR}$=72.6 μA). Overall, the power generated from the three conditions increases 17.3%, 60.4%, and 102% from the baseline power (13.9 μW). Assuming the photocurrent is proportional to incident photon flux, the concentration ratio achieved here for a single cell is 1.96, a value in the range expected for a waveguide not fully satisfying total internal reflection (TIR) criteria.[42]

For a μ-cell in an array layout, the edge-to-edge spacing (*s*) between the cells controls available waveguiding area with positive implications on device performance with increasing *s*. To optimize *s* for the highest concentration ratio and maximum power generation, cells in arrays with varying *s* were tested. The values of $I_{sc}/I_{sc,0}$ provided by these measurements are shown in Figure 3.5D, where $I_{sc,0}$ represents photocurrent generated only by photons incident on the top surface of the μ-cell (i.e., *s*=0), approximated by I_{sc} of a non-planarized μ-cell on an AA plate at *s*=25 μm. On a diffuse BSR with planarization (black filled squares in Figure 3.5D), $I_{sc}/I_{sc,0}$ increases with *s* because of the expansion of the capture cross-section area for subsequently waveguided light to the printed μ-cells. $I_{sc}/I_{sc,0}$ plateaus (maximum value 1.95) at *s*≈500 μm due to leaky waveguiding and propagation losses in the NOA matrix. Using the optical simulation method described above (with modification to accommodate the array layout), the total incident photon flux (Φ_{total}) was calculated and normalized to the direct illumination on the top surface of the μ-cell (Φ_{top}) to determine the relative enhancement (Φ_{total}/Φ_{top}) at different *s*. The values of Φ_{total}/Φ_{top} (red line in Figure 3.5D) are compared directly with experimental $I_{sc}/I_{sc,0}$, assuming

that I_{sc} increases linearly with incident photon flux. The simulation without parameter fitting shows good agreement with experiment as the enhancement saturates at a similar value (1.90) at comparable *s*. The small discrepancy is likely attributable to more efficient utilization of photons for these μ-cells when under concentration, which is not accounted for in the simulation since light absorption, not photocurrent generation, is being modeled. Microcells in the control group (measured on an AA plate without planarization) show negligible enhancement ($I_{sc}/I_{sc,0}$ and $\Phi_{total}/\Phi_{top} \approx 1$, see Figure 3.5D) for all *s* in both the experimental (black circles) and simulated (red dashed line) results, a result of both the low reflectivity of the substrate and absence of the waveguide layer.

The effects of concentration on the PV parameters of the device were independently explored. We found that the silicon solar μ-cells fabricated in this work show increasing efficiency up to ~8 suns, as shown by the data presented in Figure 3.5E. While a modest value, this performance metric is sufficient to efficiently manage increased solar flux incident on the solar cells from the BSR and waveguiding layers. Efficiency vs. concentration becomes strongly dependent upon a degradation in the fill factor at higher flux due to what appears to be high series resistance R_s within the μ-cell, as shown in the data presented in Figure 3.5F. Lateral resistance within the ribbon-like μ-cell is thought to be the main contributor to the measured series resistance of approximately 0.8 $\Omega \cdot cm^2$ for the representative devices shown in Figures 3.5E and 3.5F, as calculated using the method described by Aberle, *et al.*.[43]

3.8 Silicon Solar μ-Cell Module

We used the guidance from Figure 3.5D to build an interconnected array of printed μ-cells and supporting optical components with optimized spatial distributions. In this demonstration, 10 Si μ-cells were transferred onto a glass substrate with an edge-to-edge spacing of 500 μm to maximize their power generation, then planarized and interconnected using the methods described earlier (Figure 3.6A, it should be noted that the small-scale array shown here can be, in a straightforward approach, scaled up to much larger area arrays, as shown in Figure 3.1D). The *I-V* characteristics of the 10-cell module measured on a non-reflective AA plate are plotted (blue curve) in Figure 3.6B, showing a $I_{sc,PL}$ of 0.395 mA, $V_{oc,PL}$ of 0.512 V, FF_{PL} of 0.731, and a maximum power ($P_{max,PL}$) of 0.148 mW. The $I_{sc,PL}$ for the module is 8.7 % lower than the sum of $I_{sc,PL}$ (0.432 mA) of all the individual solar cells prior to interconnection due to shading losses

from the Ag paste electrodes, which covers around 10% of the top surface of the μ-cells. With a diffuse BSR (see red curves in Figure 3.6B), the module shows an $I_{sc,PL,BSR}$ of 0.711 mA, $V_{oc,PL,BSR}$ of 0.534 V, $FF_{PL,BSR}$ of 0.709, and a $P_{max,PL,BSR}$ of 0.269 mW. Both I_{sc} and V_{oc} are increased due to enhanced illumination on the μ-cells via waveguiding and reflection from the BSR. These data implicitly illustrate an interesting attribute of the μ-cell form factor. Given that the cells in this module only weigh around 0.1 mg, the peak power-referenced Si consumption is only 0.4 g/W_p. This value is much lower than that (around 10 g/W_p)[44] of commercial Si solar cells. Although costs associated with cell fabrication and module assembly need to be taken into account, the trends illustrate that sparse array layout of μ-scale devices offers a potential route to decrease the cost of PV energy by reducing the usage of the most expensive materials components, given scalable means of manufacturing and suitable modes of optical integration.

3.9 Conclusion

In summary, fabrication and assembly (i.e. transfer-printing, planarization, and interconnection) strategies have been developed for this new generation of Si solar μ-cells. A simplified fabrication method is demonstrated, which offers improved device performance as well as higher process reliability compared to previous work. The thermal oxide on the μ-cells not only acts as an etching and diffusion mask during fabrication, but serves as a passivation and simple AR coating that enhances the overall energy conversion efficiency without additional processing for its integration. We report here a route to integrate active solar μ-cells in a simple concentrator system with low-cost polymer materials that efficiently manage incident solar radiation by waveguiding light to otherwise shadowed surfaces. Transfer-printing techniques allow these μ-cells to be assembled into arbitrary geometries to maximize incident illumination on devices and target low semiconductor material consumption per watt at the module level. In this report, a 10-cell module, interconnected by screen-printing Ag paste, demonstrates a Si consumption of only 0.4 g/W_p. The device structure presented here, however, is still relatively simple compared to the best high-efficiency research and industrial PV devices (e.g. the world-record PERL cell[45-48]). Efforts can be made to further enhance their energy conversion efficiency by incorporating advanced features[46-49] that reduce photon escape loss (e.g. in addition to the use of an optimized backside reflector, to incorporate surface texturing and double layer AR coating to minimize top surface reflection), carrier recombination loss (e.g. selective emitter and BSF diffusion, rear

surface passivation layer with embedded atomic hydrogen, and utilization of float zone substrate with lower impurities) as well as parasitic resistive loss (e.g. highly doped regions under metal contacts, metal gridlines, and higher base doping concentration to minimize series resistance) in this generation of microcells. Additionally, these devices have shown the capability to efficiently manage modest solar flux, therefore important areas of future work include coupling devices with light trapping structures (e.g. luminescent waveguide) to achieve higher concentration ratios and lower material consumption, as well as conforming printed μ-cell arrays on flexible substrates to three-dimensional structures to further improve their angular light capture properties.

3.10 Supporting Information

Figure 3.7 shows a schematic overview of the fabrication process.

3.10.1 Cleaning

The process started with a boron-doped Czochralski silicon wafer ("prime" grade, 3-inch diameter, (111) ±0.1° orientation, 7.5-10 Ω·cm, 380 μm thickness, Silicon Materials).Wafers were rinsed with acetone and isopropyl alcohol (IPA). Prior to all high temperature processes, RCA cleaning procedures were used, detailed below:

RCA1 Clean

Etch in RCA1 solution (H_2O:NH_3·H_2O:H_2O_2= 5:1:1) at 80°C for 10 min

RCA2 Clean

Etch in RCA1 solution (H_2O:HCl:H_2O_2= 5:1:1) at 80°C for 10 min

Native oxide on the wafer was removed by buffered oxide etchant (BOE 6:1, Transene) before and after each cleaning step.

3.10.2 Phosphorus Doping

The cleaned wafers were first doped by solid-state sources of phosphorus (PH-1000N, Saint Gobain). Etching the phosphosilicate glass (PSG) layer in BOE 10:1 and RCA cleaning completed the doping process.

Phosphorous doping over a variety of temperatures (900°C, 950°C, and 1000°C) and times (5 min, 15 min, and 30 min) was conducted to ultimately optimize conversion efficiency of the μ-cells. To directly compare the effect of doping time and temperature parameters, three batches of three wafers were processed simultaneously, each wafer within the batch doped for a different time (Batch 1: 1000°C, Batch 2: 950°C, Batch 3: 900°C). To eliminate possible variations in light absorption from the anti-reflective, oxide layers (the thickness of oxide on device differs from batch to batch), the μ-cells were immersed in BOE 6:1 to remove all oxide prior to testing. Figure 3.8 shows normalized efficiency vs. doping time for the three temperatures of interest. The doping conditions giving the highest conversion efficiency in each batch were 1000°C for 5 min, 950°C for 5 min, and 900°C for 15 min, giving sheet resistance values of 22 Ω/□, 80 Ω/□, and 78 Ω/□, respectively, measured by four point probe (Pro4, Signatone). These conditions were then directly compared in a fourth batch to eliminate batch-to-batch variability. Figure 3.9A shows the doping profiles measured by quantitative secondary-ion mass spectrometry (SIMS) and Figure 3.9B shows averaged *I-V* curves of cells doped at 900°C, 950°C, and 1000°C for 15 min, 5 min, and 5 min, respectively. Table 3.1 and Figure 3.10 shows the parameters of J_{sc}, V_{oc}, η, and *FF*. The data shows that doping at 900°C for 15 min gives the highest conversion efficiency, leading us to adopt this as the standard protocol for μ-cell fabrication.

3.10.3 Thermal Oxidation and Photolithography

A top oxide mask layer was then grown by wet oxidation at 1000 °C for 80-100 min under steam atmosphere (<0.2 LPM O_2 flow through boiling DI water) in a quartz tube furnace following RCA1 and RCA2 cleanings outlined above. The lateral dimensions of the μ-cells were defined by standard photolithographic processing (AZ5214-E, AZ Electronic Materials):

Spin-coat hexamethyldisilazane (HMDS) at 5000 rpm for 30 sec

Spin-coat AZ5214-E at 5000 rpm for 30 sec

Softbake at 110°C for 60 sec

Expose 310 mJ/cm^2 at 320 nm (Karl Suss MJB3 mask aligner)

Develop in metal ion free (MIF) 327 for ~100 sec

O_2 descum (20 sccm, 250 mTorr, 50 W) for 60 sec

Hardbake at 110°C for 180 sec

The oxide not covered by the photoresist was then removed by BOE 6:1 (~12 min). Inductively coupled plasma reactive ion etching (ICP-RIE, Surface Technology Systems) was utilized to define the vertical depth of the trench structures. Standard Bosch Processing conditions were used: chamber pressure of 81.5 mTorr, etching for 7 sec/cycle with 130 sccm SF_6 and 13 sccm O_2 under 600 W coil power and 12 W platen power, then passivating for 5 sec/cycle with 110 sccm C_4F_8 under 600 W coil power and 0 W platen power. Etch times were controlled such that an etch depth of 35-40 μm was achieved, typically 75 cycles. The remaining photoresist was then removed by sonicating in acetone and RCA1 cleaning.

3.10.4 Brief Undercut and Sidewall Oxidation

A short anisotropic etching step of the wafer was performed in 25 wt.% tetramethylammonium hydroxide solution (TMAH, **Sigma-Aldrich**) at 70°C for 2 min to achieve a canopy-type structure. The exposed sidewalls ({110}) of cells etched at ~1 μm/min according to cross-sectional SEM images shown in Figure 3.1B. After RCA cleanings, a second wet oxidation step (1000 °C, 20-25 min) formed an oxide layer on the side and bottom of the trenches and increased the oxide thickness on top of the cells as well, shown in Figure 3.11A.

3.10.5 Flood RIE and Undercut

The oxide on the bottom of the trenches was selectively removed by reactive-ion etching (Plasma Therm 790 series) using CHF_3 (20 sccm) and O_2 (8 sccm) under 50 mtorr and 175 W for ~9 min. This dry etch is pseudo-anisotropic such that little oxide on the sidewall was consumed (Figure 3.11B). After immersion in BOE 6:1 for ~20 sec, the wafer was immersed into 25% TMAH solution at 80°C for ~90 min to fully undercut the μ-cells and release them from the substrate except at anchor locations.

3.10.6 Boron Doping

After RCA cleaning, the back surface field was formed by solid-source boron doping (BN-975, Saint Gobain) at 1000 °C for 30 min. The borosilicate glass (BSG) layer was etched in

20:1 HF for ~2 min. Oxide remaining on the top and sidewall surfaces (Figure 3.11C) now serves as passivation and anti-reflection layers.

3.10.7 Patterning Top Contacts

Square contacts (50 μm ×50 μm) were defined through photolithography with a photoresist (AZ P4620, Clariant):

Spin-coat HMDS at 2000 rpm for 30 sec

Spin-coat AZ5214-E at 1000 rpm 10 sec, then at 2000 rpm for 30 sec

Softbake at 65°C for 5 min and then at 95°C for 20 min,

Expose 410 mJ/cm^2 at 365 nm

Develop in 3:1 AZ400K(AZ Electronic Materials) for ~1 min

Expose under UV-generated ozone for 2 min

Hardbake at 65°C for 30 min (ramp from 35°C with a ramp rate of 0.5°C/min)

The oxide not protected by the photoresist was then removed by BOE 6:1 (~5.5 min) and Ti (10 nm) /Au (300 nm) contact pads were formed by e-beam evaporation and photoresist lift-off in acetone.

3.10.8 Statistical Analysis of Fabricated Si Solar μ-Cells

To test the large-area reliability of the fabrication process, we transferred μ-cells from the entire patterned wafer area. Specifically, every sixth device in all six rows was picked-up with a PDMS stamp and transferred to a glass substrate (discussed subsequently) for *I-V* testing. The μ-cells were tested under simulated AM1.5D illumination of 1000 W·m^{-2} at room temperature prior to planarization of the μ-cells on an anodized Al plate to minimize reflection from the back plane. Using the top surface area of the μ-cells as the device area, the PV metrics of J_{sc}, V_{oc}, η, and *FF* were measured and plotted with histograms shown as insets (Figure 3.12 and Figure 3.2C).

3.10.9 Transfer Printing µ-Cells

The receiving substrate was made by spin-coating a UV-curable polymer (NOA61, Norland Products, 3000 rpm for 45 sec) on a pre-cleaned glass slide (5 cm × 5 cm × 2 mm) and partially curing under UV light (1260 mJ/cm^2 at 365 nm) with a Karl Suss MJB3 mask aligner. Bottom electrodes were then deposited by e-beam evaporation of Ti (10 nm) /Au (300 nm) through a shadow mask.

Microcells were selectively picked up by a PDMS (10:1 ratio of pre-polymer to initiator, Sylgard 184, Dow Corning) stamp with pyramidal structures and printed on the receiving substrate with an automated transfer printing machine. By applying modest pressure on the inked stamp to the receiving substrate, excellent electrical contact was achieved between the bottom electrode and device. Step and repeat printing allowed formation of arrays with arbitrary configurations. The fabrication of the pyramid PDMS stamp and the manipulation of the automated machine were described elsewhere (see Ref. 36).

After printing, the µ-cells were tested and baked at 150 °C on hotplate for 10 min. This postbake step possibly caused the partially cured NOA layer to reflow and intimately coat the bottom side of the µ-cell, preventing liquid pre-polymer to flow underneath the device and block the back contact in the following planarization step.

3.10.10 Planarization

A flat PDMS block (10:1 ratio of pre-polymer to initiator) was laminated on top of the printed devices to achieve conformal contact with the µ-cells. Silica particles (30 µm diameter, SPI) were dispersed on the substrate around the device area to support the PDMS stamp and avoid sagging. Another UV-curable polymer (NOA73, Norland Products) was dispensed in a reservoir created in the PDMS block with a 3 mm biopsy punch. The liquid pre-polymer flowed by capillary action to fill the air gap between the PDMS and substrate. The entire system was then exposed under UV light to cure the NOA, before PDMS was peeled off from the substrate, leaving the µ-cells embedded in the NOA matrix. A profilometry line scan (Figure 3.14A) of the resulting planarization layer shows minimal topological variation between cells (~5 µm).

3.10.11 Interconnection

Interconnecting the planarized μ-cells was accomplished by manually aligning a stencil mask (two pieces of Scotch® tape) to form the shape of the interconnect. A small volume (~0.5 mL) of Ag paste (Ted Pella, PELCO® Conductive Silver 187) was dispensed on one end, using a razor blade to "squeegee" the Ag paste over and into the stencil mask. The Scotch® tape stencil mask was peeled away immediately, leaving behind a well-formed interconnection line ~150 μm wide and ~50 μm tall (Figure 3.14B). The Ag paste line was cured in air at room temperature for 30 min prior to any electrical measurements.

3.10.12 Measurements under Concentration

To aid thermal and electrical conduction due to intense illumination and increased photocurrent generation, respectively, from concentrated solar flux, devices were assembled differently than the procedure described above. After device fabrication, the μ-cells were conformally contacted by a PDMS stamp and lifted off from the donor wafer. Thin-film metal ohmic contacts (~150 μm wide, Ti (5 nm)/Au (200 nm)) were e-beam evaporated on the backside of the μ-cells through a shadow mask. The μ-cells were then embedded in a thin (~200 μm) line of uncured Ag epoxy (E4110, Epoxy Technology) on a glass slide. The glass slide/Ag epoxy/μ-cell/PDMS system was baked on a 150ºC hot plate for 15 min. Following the baking step, the PDMS stamp was slowly removed, leaving the μ-cells printed on a cured Ag epoxy matrix serving as the interconnection on the backside of the devices. There was not a subsequent planarization step with NOA. During solar measurements under concentration, the glass slide was mounted on an anodized aluminum plate with a 3 inch fan used to cool the μ-cells. Concentration ratios (x) for Figures 3.5E and 3.5F were calculated by the following expression:

$$I_{\mathrm{sc,conc}} = xI_{\mathrm{sc,1sun}}$$

where $I_{\mathrm{sc,conc}}$ and $I_{\mathrm{sc,1sun}}$ is the short-circuit current for a μ-cell under concentration and 1 sun, respectively.

3.10.13 Solar μ-Cell Characterization

I-V characteristics of the μ-cells were measured with a source meter (Keithley, Model 2400) under a full-spectrum solar simulator (Model 91192, Oriel) with AM 1.5D filter calibrated

to 1000 W·cm^{-2} at room temperature using a Si reference cell (Model 91150V, Newport-Oriel). Measurements under solar concentration were obtained by placing a convex lens (Model LH-2 M4 KBX145 F62.9, Newport) in the beam path. Different concentration ratios were obtained by translating the lens vertically.

Due to the inherent transparency of printed arrays of these μ-cells, reflection from the subjacent layers will have a significant impact on PV measurements. We suppressed reflection from the solar simulator's sample stage by mounting the glass substrate on an anodized Al (AA) plate to obtain PV metrics with minimal influence of reflected light. Figure 3.15 shows reflectivity data, relative to a Spectralon® target, of the anodized Al (AA) plate used for PV measurements. To elucidate enhancements to the PV metrics of printed μ-cells from diffuse reflection, the glass substrate was also mounted on a Spectralon® target, as shown in Figure 3.5A, in some measurements. We distinguish reported PV metrics when using this diffuse backside reflector by using subscript "BSR".

For devices without oxide, *I-V* characteristics were measured right after a 5.5 min etch in BOE 6:1 as well as a few days later after the formation of the native oxide layer on an AA plate without planarization. (See Figure 3.13A and Table 3.2). The devices show a further degradation after the surface Si-H bonds formed during BOE etch were oxidized in air. The data with the native oxide layer is used in Figure 3.3A.

EQE measurements were taken using an OL750 spectroradiometer with devices embedded in NOA layer with top contact lines. The top interconnects for devices in Figure 3.3B and Figure 3.13E were formed by either sputtering a Ti (10nm)/Al (300nm) metal line or directly painting a silver paste/epoxy line through a stencil mask onto the cell. All EQE results were normalized to percentage based on device performance under AM1.5D solar spectrum measured on a non-reflective AA plate without planarization to eliminate waveguiding effects.

3.10.14 Methods for Calculating the AR Effects from the Top Oxide

The reflections on the top surface of the device were calculated based on refractive indices of thermal oxide (n_2) and silicon (n_1) at different wavelengths (λ), assuming a normal incidence of the incoming solar radiation. (Refractive indices at different wavelength for single-crystalline silicon and fused silica were taken from "*Handbook of Optical Constants of Solids,*

Edward D. Palik. Academic Press, Boston, 1985" and "*Handbook of Optics, 3rd edition, Vol. 4. McGraw-Hill 2009*", respectively.)

For devices without oxide, the top surface reflection (R_1) under air was calculated as

$$R_1 = \frac{(n_1 - 1)^2}{(n_1 + 1)^2}$$

For devices with oxide with a certain thickness (t), the top surface reflection (R_2) was calculated as

$$R_2 = \frac{{r_1}^2 + {r_2}^2 + 2r_1 r_2 \cos 2\theta}{1 + {r_1}^2 {r_2}^2 + 2r_1 r_2 \cos 2\theta}$$

where

$$r_1 = \frac{1 - n_2}{1 + n_2};\ r_2 = \frac{n_2 - n_1}{n_2 + n_1};\ \theta = \frac{2\pi n_2 t}{\lambda}$$

The relative optical enhancement (E) by adding a thermal oxide AR layer was then defined as

$$E = \frac{1 - R_2}{1 - R_1}$$

The EQE for a device with AR coating but without passivation was then estimated as

$$EQE_{\text{simulated}} = \frac{1 - R_2}{1 - R_1} \cdot EQE_{\text{without oxide}}$$

The difference between these two EQE curves were then integrated with the AM 1.5D solar spectrum to get the simulated current density enhancement from an AR layer on a device without passivation.

For the blue dashed curve in Figure 3.3B, 250 nm was used as the oxide thickness for calculation, as determined by a cross-sectional SEM image (Figure 3.13B) for another device on the same donor wafer.

3.11 Figures

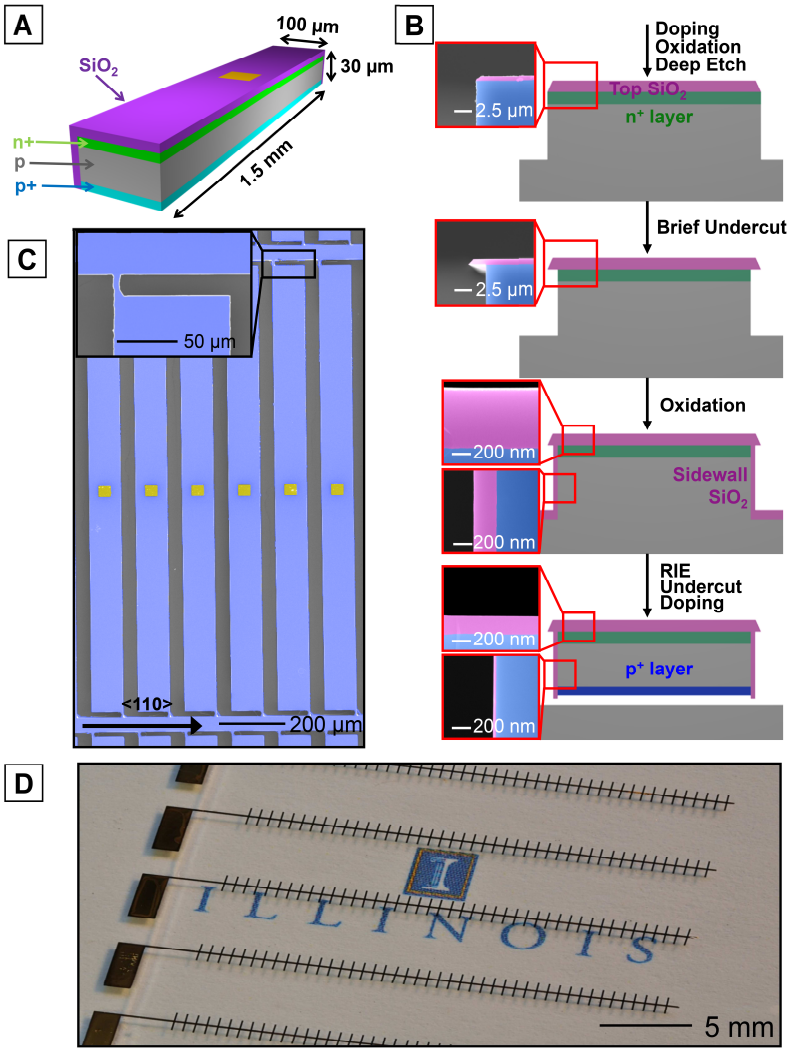

Figure 3.1 (A) Schematic illustration of the µ-cell design (oxide on the front and right side is removed to show the doping geometry); (B) Schematic illustration of key processing steps in fabricating Si solar µ-cells on a Si(111) wafer with colorized scanning electron microscopy (SEM) image insets tracking oxide (pink) thickness on the top and sidewall of the silicon (blue) ink throughout the fabrication; (C) Colorized top-view SEM image of fully fabricated Si solar µ-cells (blue) with deposited Au contacts (yellow), with the inset showing a zoomed-in image of the break-away anchors tethering the devices to the donor wafer; (D) Optical image of planarized arrays of µ-cells on a glass substrate over ~600 mm^2.

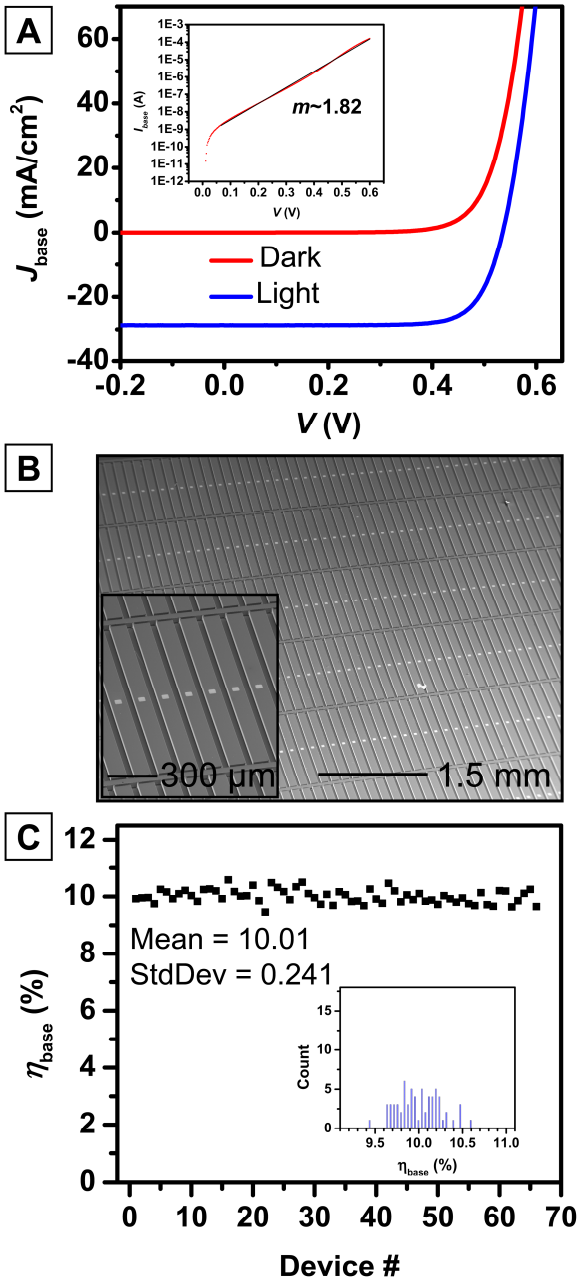

Figure 3.2 (A) Light (blue) *J-V* curve of our best performing device and a representative dark curve (red) measured on an AA plate (Inset shows the same dark *J-V* curve plotted in semi-log form with ideality factor (*m*) of 1.82); (B) SEM images of fully fabricated Si solar µ-cells on the donor wafer; (C) Statistical analysis and histogram plot (inset) of efficiencies of devices evenly distributed on a donor wafer.

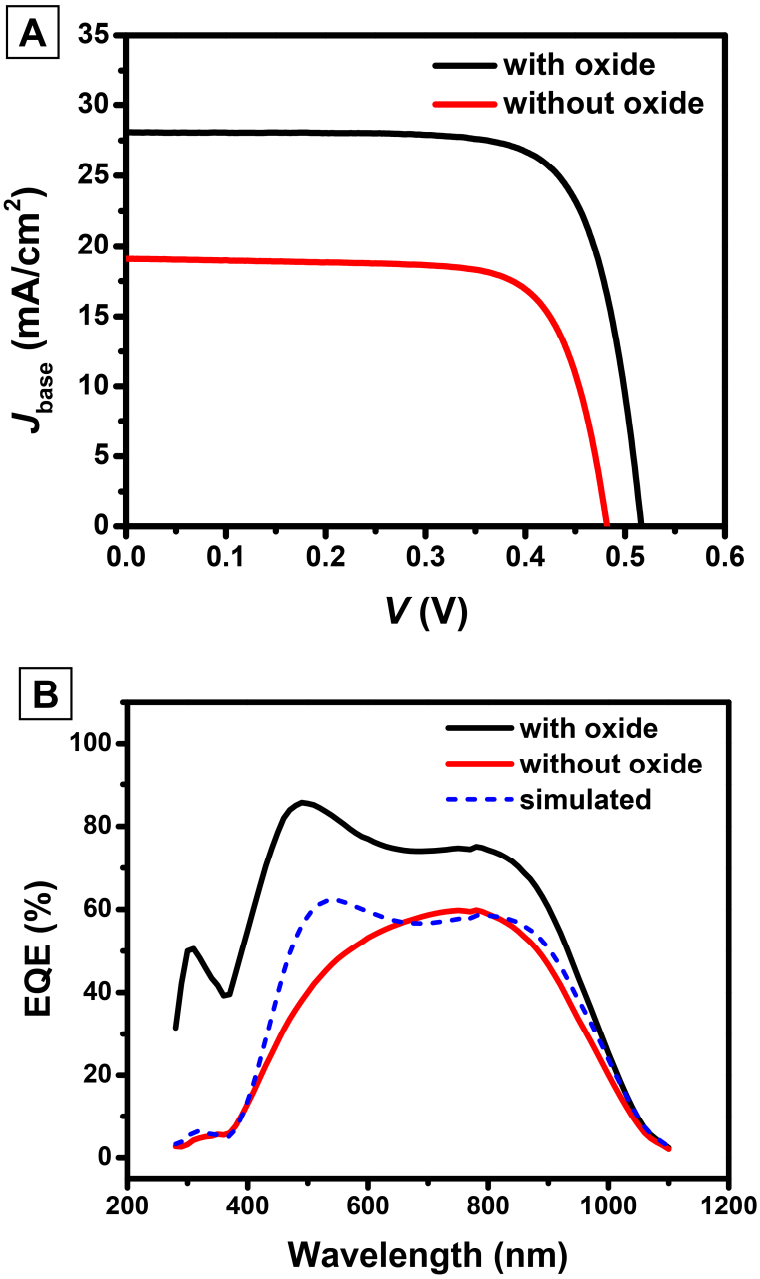

Figure 3.3 (A) a) *J-V* characteristics and (B) External quantum efficiencies (EQE) of Si solar μ-cells with (black) and without (red) the thermal oxide layer; A simulated EQE curve (blue dashed line) for a non-passivated device with enhancements only from AR coating is also plotted in (B).

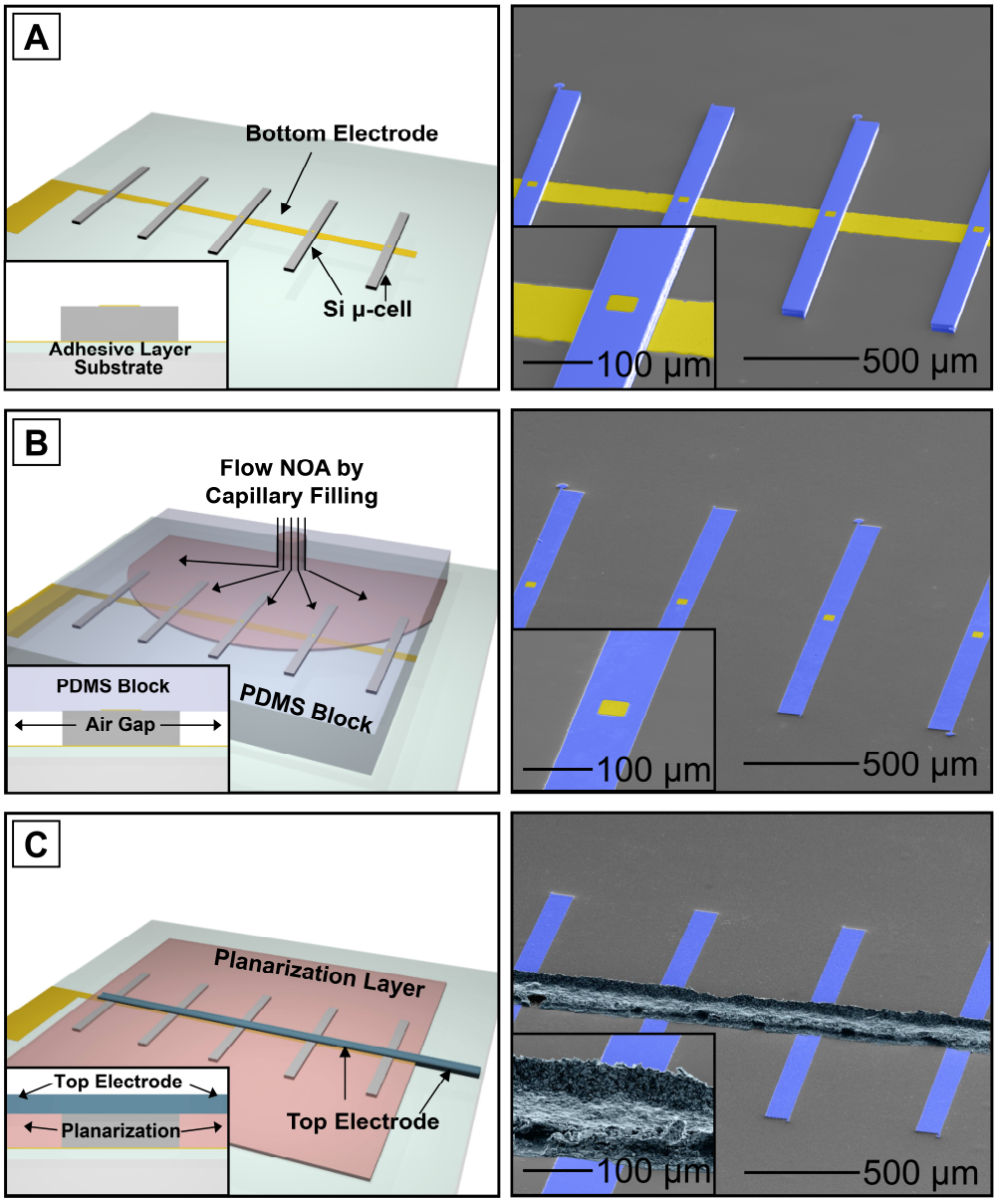

Figure 3.4 Schematic illustrations (left) and colorized (Au contacts: yellow; μ-cells: blue; Ag paste: silver) SEM images (right, with zoomed-in insets) of the key steps to build a module of silicon solar μ-cells: (A) Transfer-assembly onto a glass substrate with pre-patterned Au electrodes; (B) Planarization by flowing a photocurable resin (NOA) under a PDMS block via capillary action; (C) Interconnection by screen-printing Ag paste.

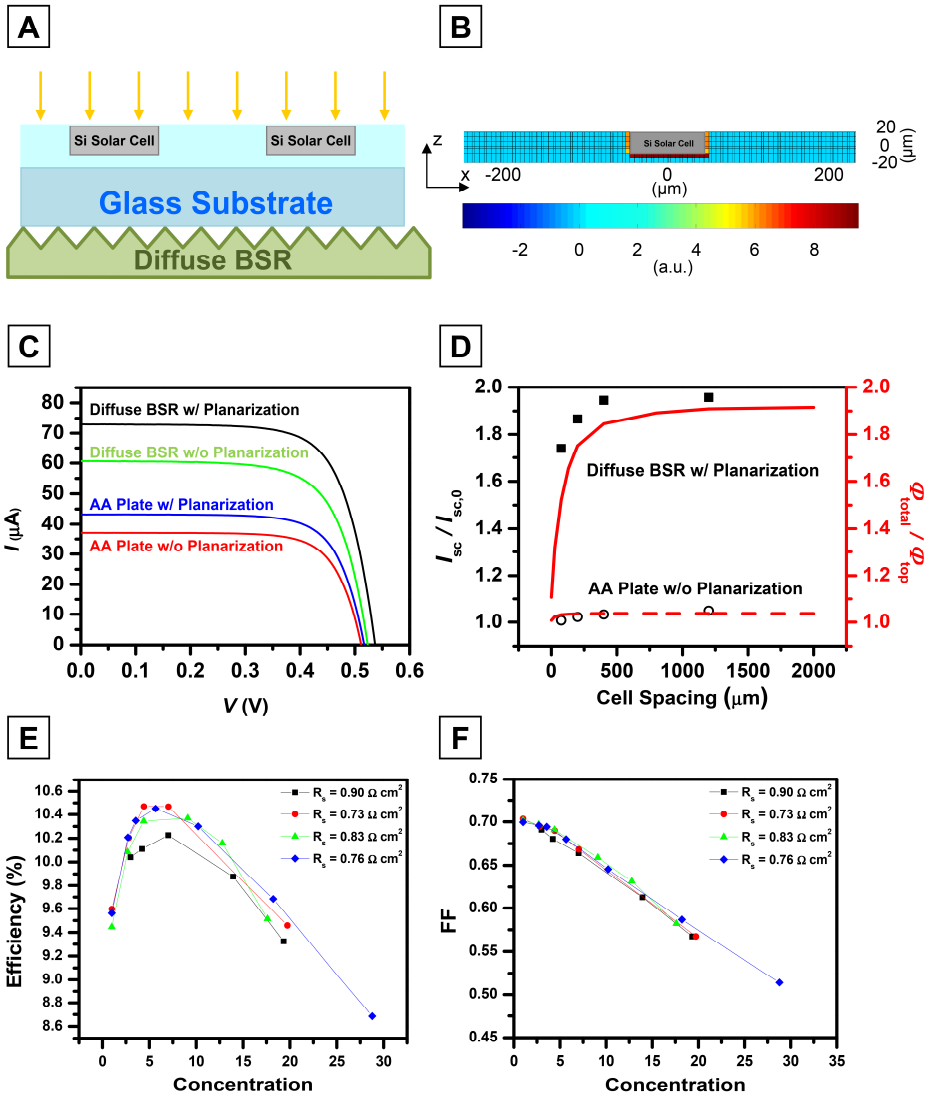

Figure 3.5 (A) Cross-sectional illustration of the concentrator geometry: Si solar μ-cells embedded in a polymer waveguide on a glass substrate with a diffuse BSR; (B) Simulated photon flux (cross-sectional view) incident on bottom and sidewall surfaces for a device in the concentrator layout shown in (A); (C) *I*-*V* curves of μ-cells with different optical components; (D) Experimental ($I_{sc}/I_{sc,0}$) and simulated (Φ_{total}/Φ_{top}) relative enhancements for devices with different intercell spacings (*s*); (E) Efficiencies and (F) Fill factors of μ-cells with different series resistance under various concentration ratios.

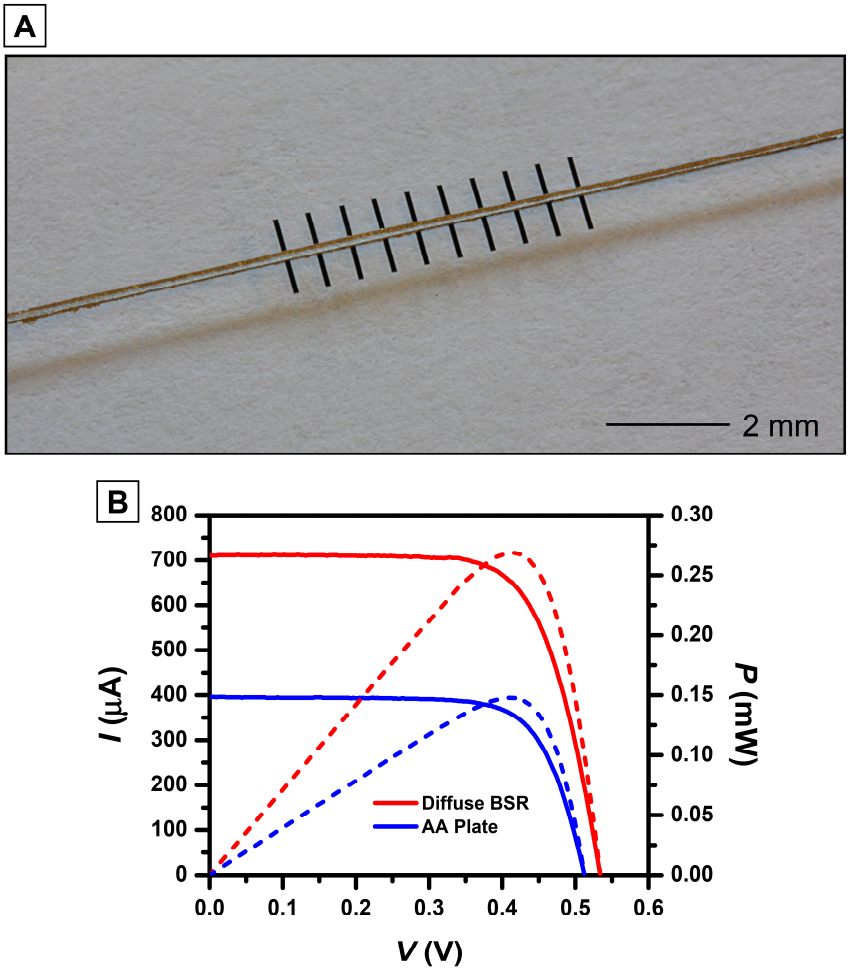

Figure 3.6 (A) Optical image of a 10-cell module with a screen-printed Ag paste top interconnect; (B) *I*-*V* (solid lines) and *P*-*V* (dashed lines) plots of the same module measured on an AA plate (blue) and on a diffuse BSR (red).

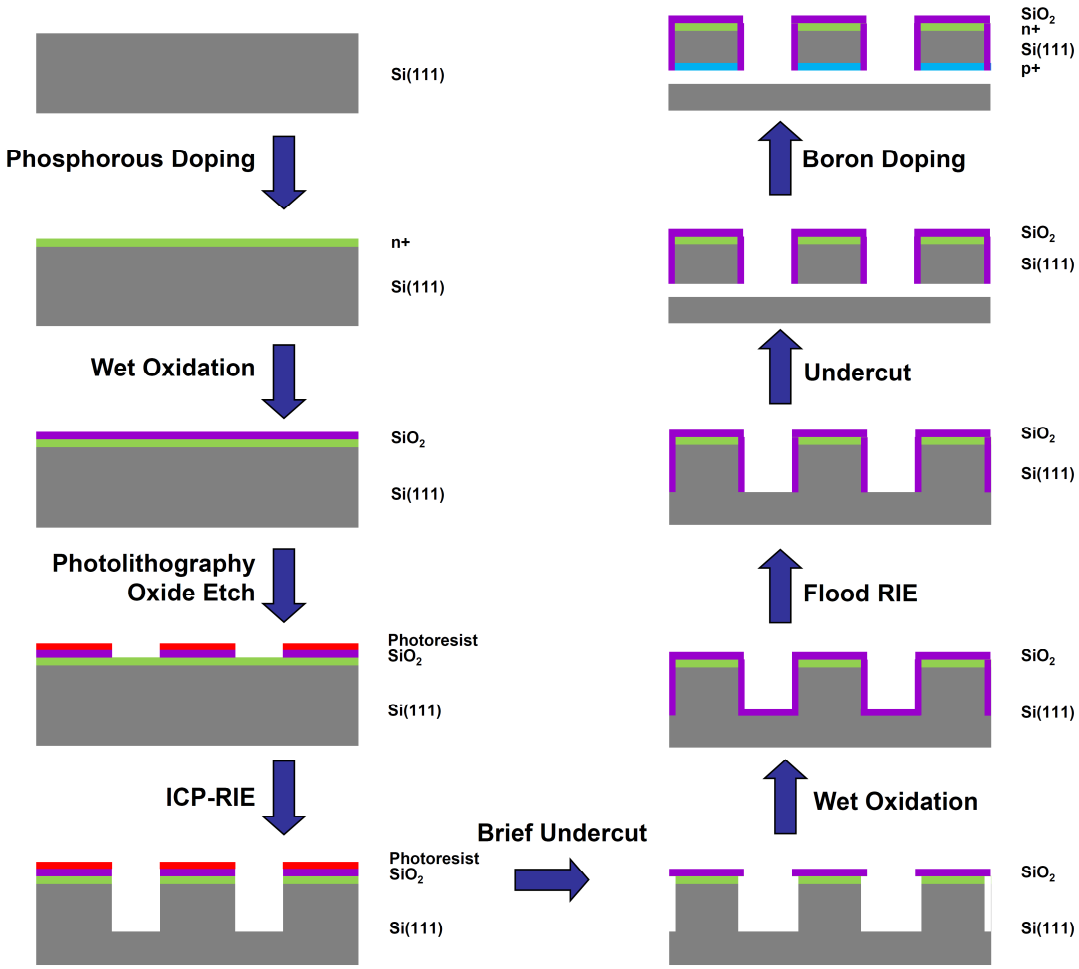

Figure 3.7 Schematic illustration of the fabrication protocol for creating Si solar μ-cells.

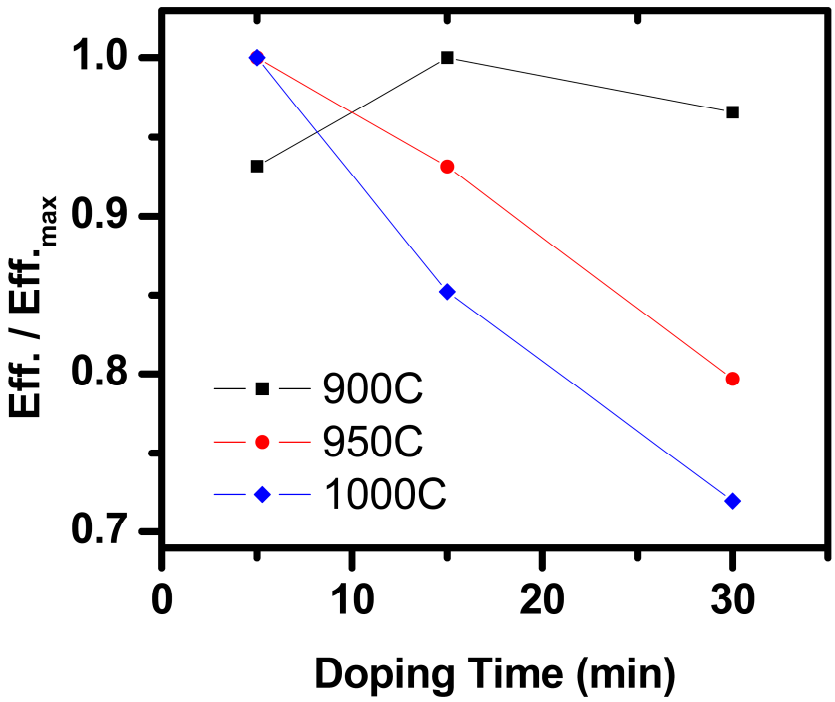

Figure 3.8 Efficiency normalized to the maximum efficiency for each data series (i.e., doping temperature) vs. phosphorous doping time. The data shows that the maximum efficiency is achieved at doping times of 15 min, 5 min, and 5 min at doping temperatures of 900°C, 950°C, and 1000°C, respectively.

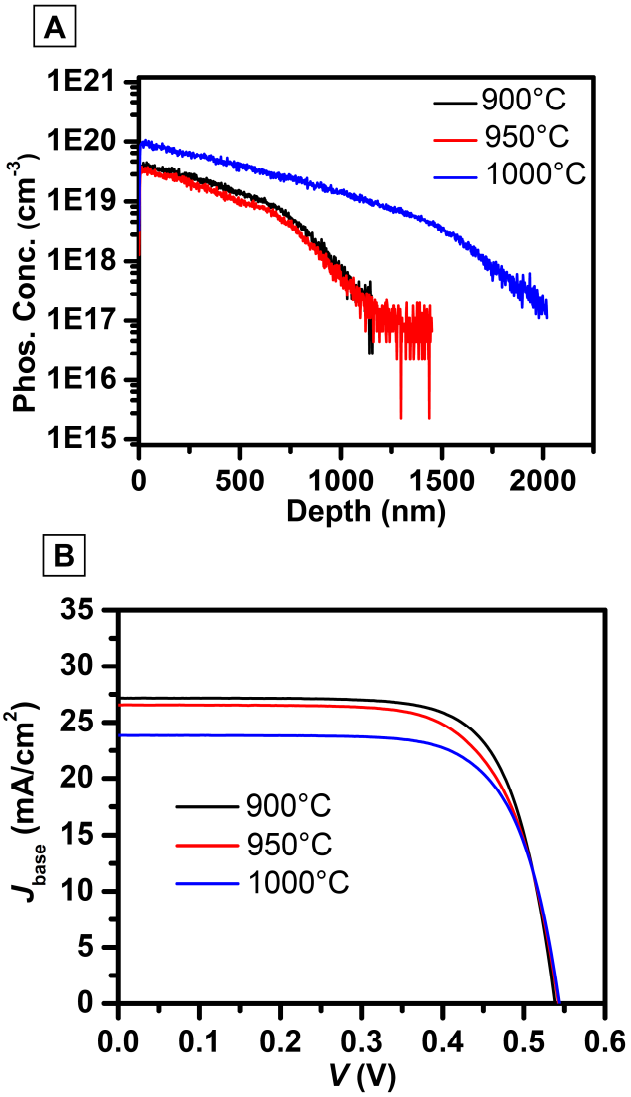

Figure 3.9 (A) SIMS depth profile of phosphorous concentration in samples doped at different conditions; (B) *J-V* curves of μ-cells doped at different conditions measured on an AA plate without planarization. (900°C, 15 min: black, 950°C, 5 min: red; 1000 °C, 5min: blue)

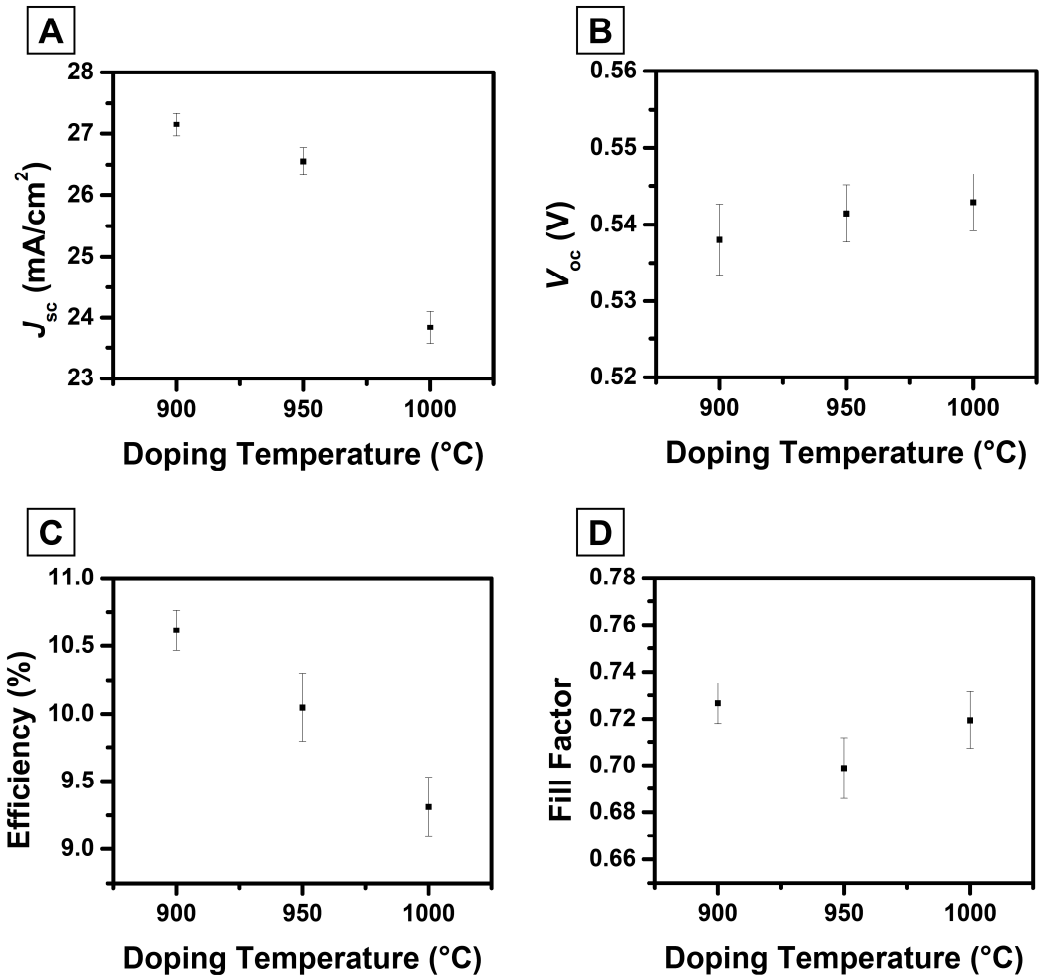

Figure 3.10 Performance metrics of devices doped at different conditions measured on an AA plate without planarization: (A) J_{sc}; (B) V_{oc}; (C) Efficiency; and (D) Fill factor.

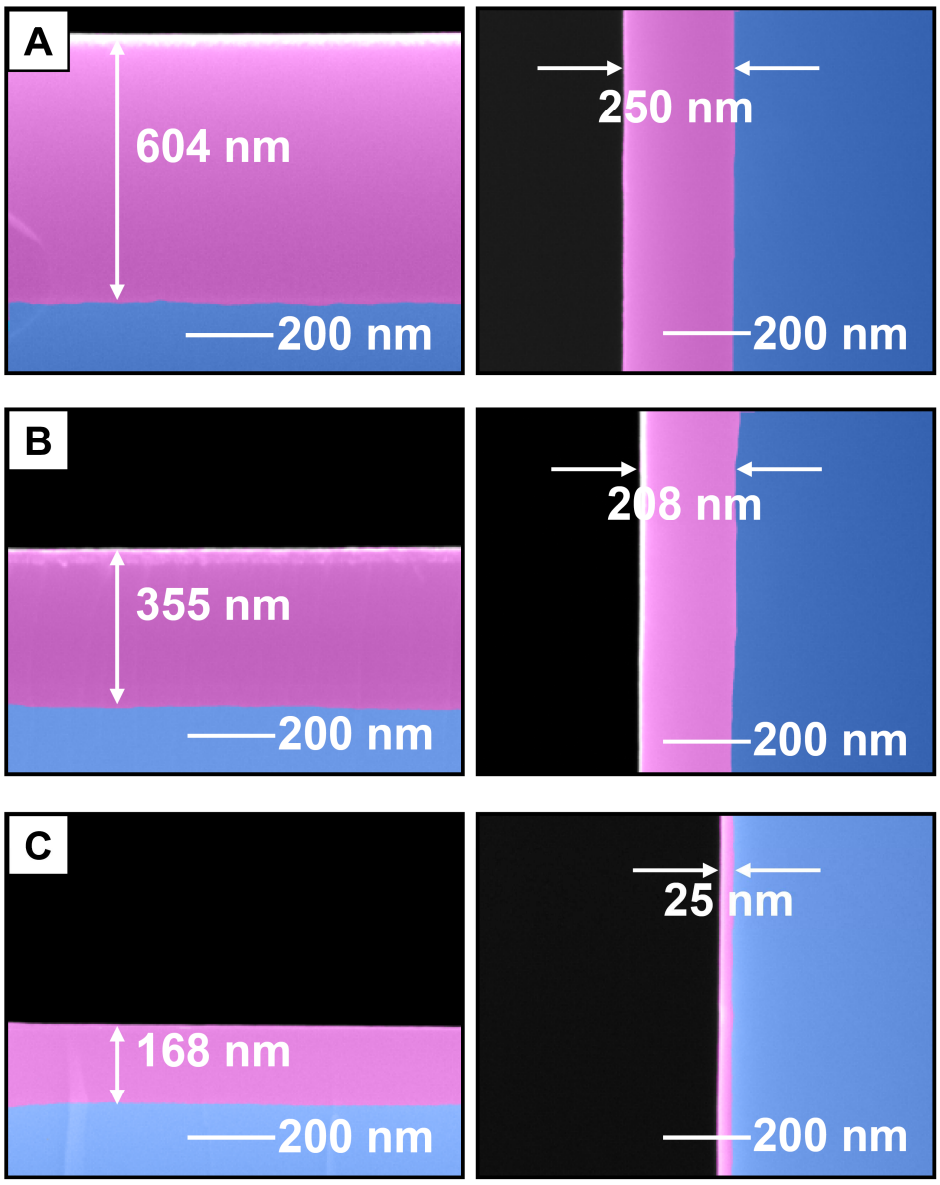

Figure 3.11 Cross-sectional SEM images of Si μ-cells (blue) with thermally grown oxide layers (pink) on the top (left frame) and sidewall (right frame) surface after different fabrication steps: (A) Sidewall oxidation; (B) Flood RIE; and (C) Full device fabrication.

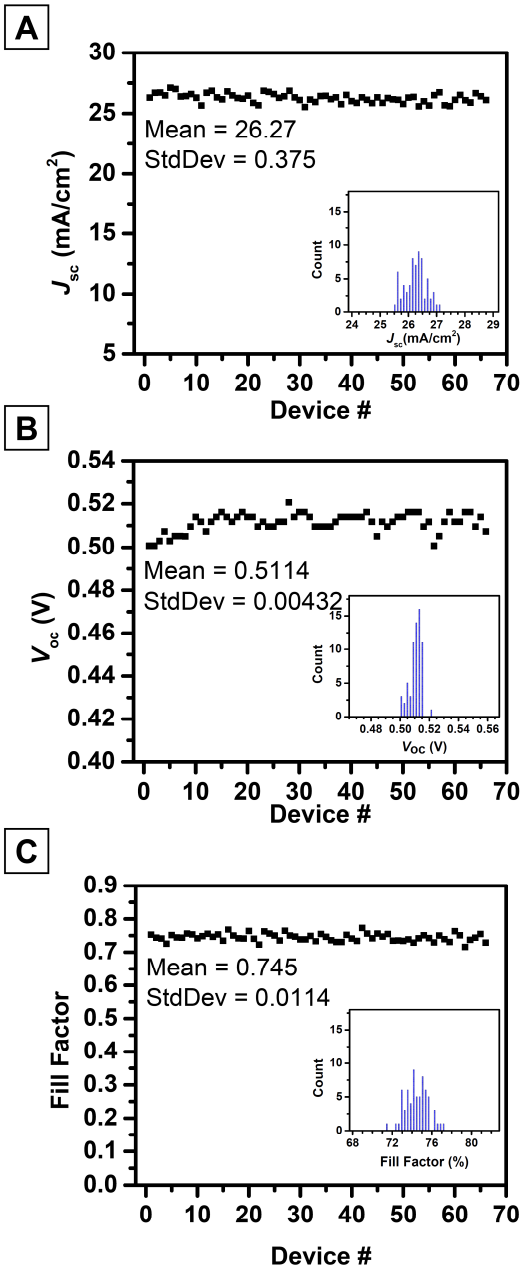

Figure 3.12 Statistical analyses and histogram plots (insets) of device performance metrics measured on an AA plate without planarization: (A) J_{sc}; (B) V_{oc}; and (C) Fill factor.

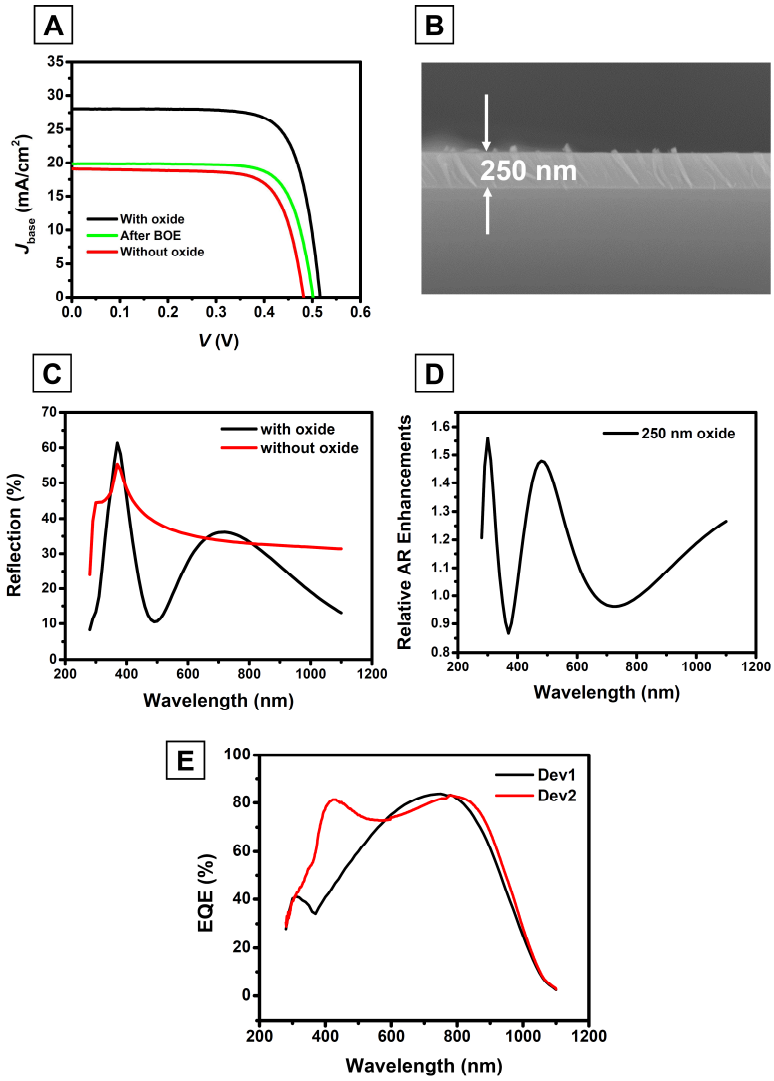

Figure 3.13 (A) *J-V* characteristics of devices with oxide (black), right after BOE etch (green) and after formation of a native oxide layer (red); (B) Cross-sectional SEM images of a Si µ-cell for EQE measurement with top oxide thickness of ~250 nm; (C) Calculated top surface reflections for devices without oxide (red) and with 250 nm thermal oxide (black); (D) Simulated relative AR enhancements for a µ-cell with 250 nm top oxide; (E) External quantum efficiencies (EQE) of passivated µ-cells with various oxide thickness.

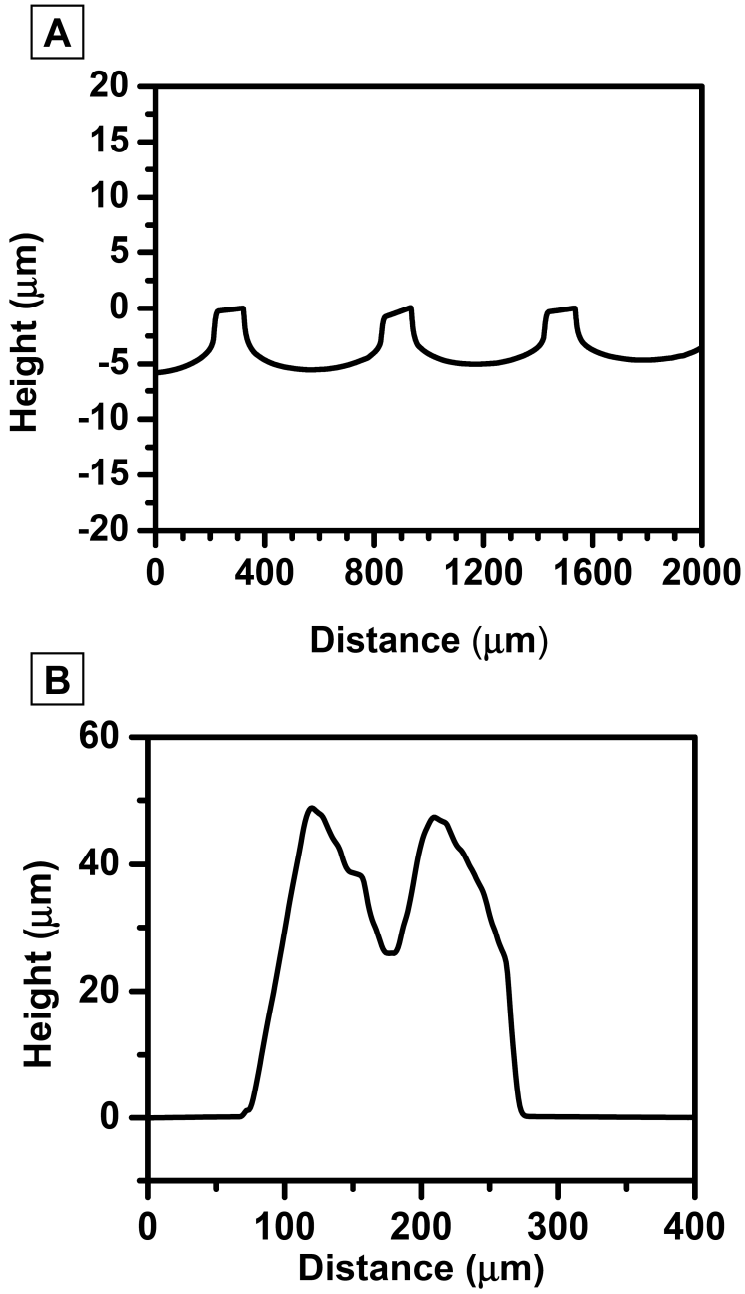

Figure 3.14 (A) Profilometry line scan across three printed Si solar μ-cells following planarization; (B) Profilometry line scan across a Ag paste interconnect.

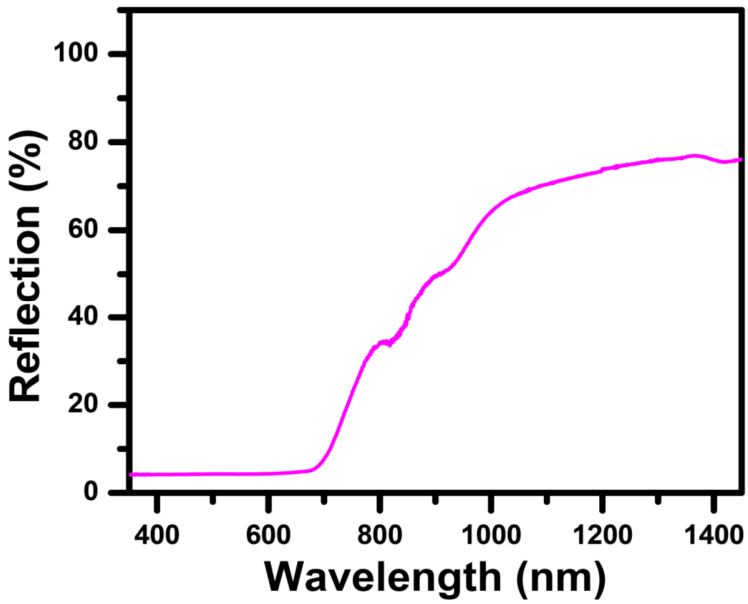

Figure 3.15 Reflectance of the non-reflective anodized aluminum (AA) plate.

3.12 Tables

Table 3.1 Device performance with different doping conditions.

Temp (°C)	J_{sc} (mA/cm^2)	V_{oc} (V)	η (%)	FF
900 (15 min)	27.15	0.538	10.6	0.727
950 (5 min)	26.55	0.541	10.0	0.699
1000 (5 min)	23.83	0.543	9.3	0.719

Table 3.2 Device performance with/without oxide.

	J_{sc} (mA/cm^2)	V_{oc} (V)	Efficiency (%)	FF
With Oxide	28.08	0.515	10.89	0.753
After BOE	19.85	0.501	7.54	0.758
Without Oxide (With Native Oxide)	19.08	0.481	6.80	0.740

3.13 References

[1] Ginley, D.; Green, M. A.; Collins, R. Solar Energy Conversion Toward 1 Terawatt. *MRS Bull.* **2008**, *33*, 355-364.

[2] Bagnall, D. M.; Boreland, M. Photovoltaic technologies. *Energy Policy* **2008**, *36*, 4390-4396.

[3] Wolden, C. A.; Kurtin, J.; Baxter, J. B.; Repins, I.; Shaheen, S. E.; Torvik, J. T.; Rockett, A. A.; Fthenakis, V. M.; Aydil, E. S. Photovoltaic manufacturing: Present status, future prospects, and research needs. *J. Vac. Sci. Technol., A* **2011**, *29*, 030801.

[4] Rodriguez, H.; Guerrero, I.; Koch, W.; Endrös, A. L.; Franke, D.; Häßler, C.; Kalejs, J. P.; Möller, H. J. In *Handbook of Photovoltaic Science and Engineering*; 2nd ed.; Luque, A., Hegedus, S., Eds.; John Wiley & Sons: 2011, p 218-264.

[5] Dross, F.; Baert, K.; Bearda, T.; Deckers, J.; Depauw, V.; El Daif, O.; Gordon, I.; Gougam, A.; Govaerts, J.; Granata, S. Crystalline thin-foil silicon solar cells: where crystalline quality meets thin‐film processing. *Prog. Photovoltaics: Res. Appl.* **2012**, *20*, 770-784.

[6] Depauw, V.; Gordon, I.; Beaucarne, G.; Poortmans, J.; Mertens, R.; Celis, J.-P. Large-area monocrystalline silicon thin films by annealing of macroporous arrays: Understanding and tackling defects in the material. *J. Appl. Phys.* **2009**, *106*, 033516.

[7] Green, M.; Basore, P.; Chang, N.; Clugston, D.; Egan, R.; Evans, R.; Hogg, D.; Jarnason, S.; Keevers, M.; Lasswell, P. Crystalline silicon on glass (CSG) thin-film solar cell modules. *Sol. Energy* **2004**, *77*, 857-863.

[8] Song, D.; Inns, D.; Straub, A.; Terry, M. L.; Campbell, P.; Aberle, A. G. Solid phase crystallized polycrystalline thin-films on glass from evaporated silicon for photovoltaic applications. *Thin Solid Films* **2006**, *513*, 356-363.

[9] Terry, M. L.; Straub, A.; Inns, D.; Song, D.; Aberle, A. G. Large open-circuit voltage improvement by rapid thermal annealing of evaporated solid-phase-crystallized thin-film silicon solar cells on glass. *Appl. Phys. Lett.* **2005**, *86*, 172108.

[10] Dross, F.; Robbelein, J.; Vandevelde, B.; Van Kerschaver, E.; Gordon, I.; Beaucarne, G.; Poortmans, J. Stress-induced large-area lift-off of crystalline Si films. *Appl. Phys. A* **2007**, *89*, 149-152.

[11] Yoon, J.; Baca, A. J.; Park, S.-I.; Elvikis, P.; Geddes, J. B.; Li, L.; Kim, R. H.; Xiao, J.; Wang, S.; Kim, T.-H.; Motala, M. J.; Ahn, B. Y.; Duoss, E. B.; Lewis, J. A.; Nuzzo, R. G.; Ferreira, P. M.; Huang, Y.; Rockett, A.; Rogers, J. A. Ultrathin silicon solar microcells for semitransparent, mechanically flexible and microconcentrator module designs. *Nat. Mater.* **2008**, *7*, 907-915.

[12] Shir, D.; Yoon, J.; Chanda, D.; Ryu, J.-H.; Rogers, J. A. Performance of Ultrathin Silicon Solar Microcells with Nanostructures of Relief Formed by Soft Imprint Lithography for Broad Band Absorption Enhancement. *Nano Lett.* **2010**, *10*, 3041-3046.

[13] Corcoran, C. J.; Kang, S.; Li, L.; Guo, X.; Chanda, D.; Nuzzo, R. G. Mechanisms of Enhanced Optical Absorption for Ultrathin Silicon Solar Microcells with an Integrated Nanostructured Backside Reflector. *ACS Appl. Mater. Interfaces* **2013**, *5*, 4239-4246.

[14] Yoon, J.; Li, L.; Semichaevsky, A. V.; Ryu, J. H.; Johnson, H. T.; Nuzzo, R. G.; Rogers, J. A. Flexible concentrator photovoltaics based on microscale silicon solar cells embedded in luminescent waveguides. *Nat. Commun.* **2011**, *2*, 343.

[15] Baca, A. J.; Yu, K. J.; Xiao, J.; Wang, S.; Yoon, J.; Ryu, J. H.; Stevenson, D.; Nuzzo, R. G.; Rockett, A. A.; Huang, Y.; Rogers, J. A. Compact monocrystalline silicon solar modules with high voltage outputs and mechanically flexible designs. *Engery Environ. Sci.* **2010**, *3*, 208-211.

[16] Green, M. A. Limiting efficiency of bulk and thin ‐ film silicon solar cells in the presence of surface recombination. *Prog. Photovoltaics: Res. Appl.* **1999**, *7*, 327-330.

[17] Shibib, M. A.; Lindholm, F. A.; Therez, F. Heavily doped transparent-emitter regions in junction solar cells, diodes, and transistors. *IEEE Trans. Electron Devices* **1979**, *26*, 959-965.

[18] Tavendale, A.; Pearton, S. Deep level, quenched-in defects in silicon doped with gold, silver, iron, copper or nickel. *J. of Phys. C: Solid State Phys.* **1983**, *16*, 1665.

[19] Sah, C.-T. In *Fundamentals of Solid-State Electronics*; World Scientific Publishing Co. Pte. Ltd.: 1991, p 282.

[20] Meitl, M. A.; Zhu, Z.-T.; Kumar, V.; Lee, K. J.; Feng, X.; Huang, Y. Y.; Adesida, I.; Nuzzo, R. G.; Rogers, J. A. Transfer printing by kinetic control of adhesion to an elastomeric stamp. *Nat. Mater.* **2006**, *5*, 33-38.

[21] Munzer, K. A.; Holdermann, K. T.; Schlosser, R. E.; Sterk, S. Thin monocrystalline silicon solar cells. *IEEE Trans. Electron Devices* **1999**, *46*, 2055-2061.

[22] Tabata, O.; Asahi, R.; Funabashi, H.; Shimaoka, K.; Sugiyama, S. Anisotropic etching of silicon in TMAH solutions. *Sens. Actuators, A* **1992**, *34*, 51-57.

[23] Baca, A. J.; Ahn, J.-H.; Sun, Y.; Meitl, M. A.; Menard, E.; Kim, H.-S.; Choi, W. M.; Kim, D.-H.; Huang, Y.; Rogers, J. A. Semiconductor Wires and Ribbons for High- Performance Flexible Electronics. *Angew. Chem., Int. Ed.* **2008**, *47*, 5524-5542.

[24] Park, S.-I.; Xiong, Y.; Kim, R.-H.; Elvikis, P.; Meitl, M.; Kim, D.-H.; Wu, J.; Yoon, J.; Yu, C.-J.; Liu, Z.; Huang, Y.; Hwang, K.-c.; Ferreira, P.; Li, X.; Choquette, K.; Rogers, J. A. Printed Assemblies of Inorganic Light-Emitting Diodes for Deformable and Semitransparent Displays. *Science* **2009**, *325*, 977-981.

[25] Yoon, J.; Jo, S.; Chun, I. S.; Jung, I.; Kim, H.-S.; Meitl, M.; Menard, E.; Li, X.; Coleman, J. J.; Paik, U.; Rogers, J. A. GaAs photovoltaics and optoelectronics using releasable multilayer epitaxial assemblies. *Nature* **2010**, *465*, 329-333.

[26] Kim, H.-s.; Brueckner, E.; Song, J.; Li, Y.; Kim, S.; Lu, C.; Sulkin, J.; Choquette, K.; Huang, Y.; Nuzzo, R. G.; Rogers, J. A. Unusual strategies for using indium gallium nitride grown on silicon (111) for solid-state lighting. *Proc. Natl. Acad. Sci. U. S. A.* **2011**, *108*, 10072-10077.

[27] Lee, S.; Park, S.; Cho, D.-I. The surface/bulk micromachining (SBM) process: a new method for fabricating released MEMS in single crystal silicon. *J. Microelectromech. Syst.* **1999**, *8*, 409-416.

[28] Baca, A. J.; Meitl, M. A.; Ko, H. C.; Mack, S.; Kim, H. S.; Dong, J.; Ferreira, P. M.; Rogers, J. A. Printable Single-Crystal Silicon Micro/Nanoscale Ribbons, Platelets and Bars Generated from Bulk Wafers. *Adv. Funct. Mater.* **2007**, *17*, 3051-3062.

[29] Lee, S.; Park, S.; Cho, D.-i. A new micromachining technique with (111) silicon. *Jpn. J. Appl. Phys.* **1999**, *38*, 2699.

[30] Yan, G.; Chan, P. C. H.; Hsing, I. M.; Sharma, R. K.; Sin, J. K. O.; Wang, Y. An improved TMAH Si-etching solution without attacking exposed aluminum. *Sens. Actuators, A* **2001**, *89*, 135-141.

[31] Spitzer, M. B.; Tobin, S. P.; Keavney, C. J. High-efficiency ion-implanted silicon solar cells. *IEEE Trans. Electron Devices* **1984**, *31*, 546-550.

[32] Nagel, H.; Aberle, A. G.; Hezel, R. Optimised antireflection coatings for planar silicon solar cells using remote PECVD silicon nitride and porous silicon dioxide. *Prog. Photovoltaics: Res. Appl.* **1999**, *7*, 245-260.

[33] Schultz, O.; Glunz, S. W.; Willeke, G. P. SHORT COMMUNICATION: ACCELERATED PUBLICATION: Multicrystalline silicon solar cells exceeding 20% efficiency. *Prog. Photovoltaics: Res. Appl.* **2004**, *12*, 553-558.

[34] Zhao, J.; Green, M. A. Optimized antireflection coatings for high-efficiency silicon solar cells. *IEEE Trans. Electron Devices* **1991**, *38*, 1925-1934.

[35] Bouhafs, D.; Moussi, A.; Chikouche, A.; Ruiz, J. M. Design and simulation of antireflection coating systems for optoelectronic devices: Application to silicon solar cells. *Sol. Energy Mater. Sol. Cells* **1998**, *52*, 79-93.

[36] Carlson, A.; Bowen, A. M.; Huang, Y.; Nuzzo, R. G.; Rogers, J. A. Transfer printing techniques for materials assembly and micro/nanodevice fabrication. *Adv. Mater.* **2012**, *24*, 5284-5318.

[37] Kim, S.; Wu, J.; Carlson, A.; Jin, S. H.; Kovalsky, A.; Glass, P.; Liu, Z.; Ahmed, N.; Elgan, S. L.; Chen, W.; Ferreira, P. M.; Sitti, M.; Huang, Y.; Rogers, J. A. Microstructured elastomeric surfaces with reversible adhesion and examples of their use in deterministic assembly by transfer printing. *Proc. Natl. Acad. Sci. U. S. A.* **2010**, *107*, 17095.

[38] Ahn, B. Y.; Duoss, E. B.; Motala, M. J.; Guo, X.; Park, S.-I.; Xiong, Y.; Yoon, J.; Nuzzo, R. G.; Rogers, J. A.; Lewis, J. A. Omnidirectional Printing of Flexible, Stretchable, and Spanning Silver Microelectrodes. *Science* **2009**, *323*, 1590-1593.

[39] Budianu, E.; Purica, M.; Rusu, E.; Manea, E.; Gavrila, R. Polysilicon thin layers for photovoltaic applications. *Semiconductor Conf., 2002. CAS 2002 Proc. Int.* **2002**, *1*, 215-218.

[40] Li, L.; Sheng, X.; Brueckner, E. P.; Yao, Y.; Rogers, J. A.; Nuzzo, R. G. Modeling and Optimization of Luminescent Solar Concentrator for Micro Cell Array Module. *Frontiers in Optics 2012, OSA* **2012**, FW6A.4.

[41] Sheng, X.; Shen, L.; Kim, T.; Li, L.; Wang, X.; Dowdy, R.; Froeter, P.; Shigeta, K.; Li, X.; Nuzzo, R. G.; Giebink, N. C.; Rogers, J. A. Doubling the Power Output of Bifacial Thin-Film GaAs Solar Cells by Embedding Them in Luminescent Waveguides. *Adv. Energy Mater.* **2013**, *3*, 991-996.

[42] Smestad, G.; Hamill, P. Concentration of solar radiation by white backed photovoltaic panels. *Appl. Opt.* **1984**, *23*, 4394-4402.

[43] Aberle, A. G.; Wenham, S. R.; Green, M. A. A new method for accurate measurements of the lumped series resistance of solar cells. *Conf. Rec. IEEE Photovoltaic Spec. Conf., 23rd* **1993**, 133-139.

[44] Aberle, A. G.; Widenborg, P. I. In *Handbook of Photovoltaic Science and Engineering*; 2nd ed.; Luque, A., Hegedus, S., Eds.; John Wiley & Sons, Ltd: 2011, p 452-486.

[45] Green, M. A.; Emery, K.; Hishikawa, Y.; Warta, W.; Dunlop, E. D. Solar cell efficiency tables (version 42). *Prog. Photovoltaics: Res. Appl.* **2013**, *21*, 827-837.

[46] Zhao, J.; Wang, A.; Altermatt, P.; Green, M. A. Twenty-four percent efficient silicon solar cells with double layer antireflection coatings and reduced resistance loss. *Appl. Phys. Lett.* **1995**, *66*, 3636-3638.

[47] Zhao, J.; Wang, A.; Green, M. A.; Ferrazza, F. 19.8% efficient ``honeycomb" textured multicrystalline and 24.4% monocrystalline silicon solar cells. *Appl. Phys. Lett.* **1998**, *73*, 1991-1993.

[48] Zhao, J.; Wang, A.; Green, M. A. 24·5% Efficiency silicon PERT cells on MCZ substrates and 24·7% efficiency PERL cells on FZ substrates. *Prog. Photovoltaics: Res. Appl.* **1999**, *7*, 471-474.

[49] Saga, T. Advances in crystalline silicon solar cell technology for industrial mass production. *NPG Asia Mater.* **2010**, *2*, 96-102.

Chapter 4 Black Silicon Solar Thin-film Microcells Integrating Top Nanocone Structures for Broadband and Omnidirectional Light-Trapping[4]

4.1 Abstract

Recently developed classes of monocrystalline silicon solar microcells (μ-cell) can be assembled into modules with characteristics (i.e., mechanically flexible forms, compact concentrator designs, and high-voltage outputs) that would be impossible to achieve using conventional, wafer-based approaches. In this paper, we describe a highly dense, uniform and non-periodic nanocone forest structure of black silicon (bSi) created on optically-thin (30 μm) μ-cells for broadband and omnidirectional light-trapping with a lithography-free and high-throughput plasma texturizing process. With optimized plasma etching conditions and a silicon nitride passivation layer, black silicon μ-cells, when embedded in a polymer waveguiding layer, display dramatic increases of as much as 65.7% in short circuit current, as compared to a bare silicon device. The conversion efficiency increases from 8.1% to 11.5% with a small drop in open circuit voltage and fill factor.

4.2 Introduction

With increasing power demands, solar radiation is serving a more important role as a clean and inexhaustible energy source. By the end of 2012, the milestone of 100 GW of installed photovoltaic capacity was achieved, with an annual growth rate of ~55% realized over the five

---

[4] The content of this chapter is reproduced with permission from Zhida Xu♦, Yuan Yao♦, Eric P Brueckner, Lanfang Li, Jing Jiang, Ralph G Nuzzo and Gang Logan Liu, " Black silicon solar thin-film microcells integrating top nanocone structures for broadband and omnidirectional light-trapping", Nanotechnology, 2014, 25, 305301, (♦Equal contribution), Copyright © IOP Publishing Ltd

year period from 2007 to 2012.[1] In the current terrestrial photovoltaic market, silicon remains the dominant semiconductor material due to its high natural abundance, excellent optical/electronic properties and well-established production and processing routes.[2] The relatively high material costs, however, still impede the broad use of solar cells, which count only 0.41% of global energy consumption, ranked behind two other renewable energy sources—hydropower (3.4%) and wind power (1.39%).[3] Solar cells based on thin films of amorphous or crystalline silicon require substantially less material compared to bulk wafer-based systems, while offering additional benefits including mechanical flexibility and ease of integration with advanced concentrating designs. One exemplary case is found in the fabrication and assembly of arrays of silicon solar thin-film microcells (μ-cell) with diverse and arbitrary spatial layouts on light-weight, flexible substrates via the transfer printing technique.[4-6] This unique design engenders advantages in allowing application-enabling distributions of devices to be made on a foreign substrate to create, as notable examples, semitransparent displays[4] or high voltage modules[7]. To compensate for the inherent low absorption of thin-film silicon, different concentrating optical components are integrated with μ-cells, including micro-lens arrays[4], nanostructured backside reflectors[8] as well as luminescent waveguides[9]. The more common strategies used to provide enhanced light absorption in commercial cells, surface texturation (e.g. alkaline etching[10] and micromachining[11]), cannot be easily accommodated in the fabrication of μ-cells. Efforts have been made to reduce the top surface reflection on μ-cells by adding a single-layer anti-reflection coating (ARC)[12] or creating nano-pillar arrays patterned by soft imprint lithography[13]. Both methods have their limitations. The ARC layer can only suppress the reflection for a limited range of wavelengths and angles. The nano-pillar array achieves broader wavelength coverage, however, its pillar-like geometry is not optimized to minimize reflections according to effective medium theory (EMT)[14], as the effective refractive index (RI) change within the structure is rather abrupt.

The black silicon (bSi) process, which is capable of creating nanocone structures with a gradual RI change at the silicon/air interface, is an alternative solution which can potentially further improve the broadband and omnidirectional absorption of a μ-cell device format and enable the full use of solar energy over the whole spectrum. Black silicon is a semiconductor material whose surface is modified with micro- or nanostructures in ways that make it highly absorptive and thus appear black. It was discovered in the 1980s as an unexpected side effect of the use of reactive ion etching (RIE) in the semiconductor industry.[15] Over the years, its potential has been recognized in various research areas including superhydrophobicity, ARCs for photovoltaics, highly sensitive photodetectors in optoelectronics, and biomedical sensing, for this reason, motivating intensive efforts to provide new and/or optimized approaches to the production of bSi materials.[16-18] In addition to RIE, effective processing methods to produce bSi include metal-assisted chemical etching[19-21] and pulsed-laser irradiation.[22] Among them, though, RIE retains the advantages of high throughput, low cost and short manufacturing cycle. We have developed a 3-step lithography-free RIE process (15~20 minutes per cycle) that is capable of producing wafer-scale bSi with dense nanocone forests on silicon surfaces of various doping type, crystallographic planes and morphologies[23]—structures that in past work have been applied to both optical sensors[24] and solar cells[25]. The adaptability of this RIE process enables the creation of bSi on photovoltaic devices after doping, circumventing the deleterious consequences of uneven doping that tend to degrade the performance of nanostructured silicon materials.[20] It was demonstrated by us previously that the efficiency of a bulk silicon solar cell could be increased by 14.7% using this RIE-based bSi process.[25] The mask-free nature of this approach also enables a simple means through which textures can be added to μ-cells to mitigate losses from top surface reflections and further increase their power output. In this work, subwavelength bSi nanocone structures are produced on μ-cell devices (black μ-cell) for broadband and omnidirectional light trapping. Combined with a silicon nitride passivation layer[26], the energy

conversion efficiency (η) of the black μ-cell embedded in a polymer matrix increases by 42.8%, and short circuit current (I_{sc}) increases by 65.7%.

4.3 Production of bSi on μ-Cell

The bSi was produced with a 3-step lithography-free plasma RIE process in a PlasmaTherm SLR-770 inductively coupled plasma reactive ion etcher (ICP-RIE), reported in details by us previously.[23] Figure 4.1 shows the cross-sectional schematics of the bSi fabrication process. First, a thin layer of oxide was formed on the silicon surface under an oxygen plasma for 5 min (Figure 4.1(a)). The oxide was etched using a high-power CHF_3 plasma to form randomly dispersed oxide islands (Figure 4.1(b)). Finally, a HBr plasma was used for the silicon etching step. The random oxide mask protects the silicon underneath it from being etched by HBr plasma and the nanocone forest is in this way created (Figure 4.1(c)). The oxide mask was removed using a buffered oxide etchant (BOE), leaving uniform and large-area bSi with dense nanocone structures on the silicon surface, as shown by both the optical and SEM images in Figure 4.1(d) and 4.1(e). The tapered shape of sub-wavelength structures created by this approach makes the effective refractive index gradually increase from the top (air) to the bottom (silicon) of the nanocone forest without abrupt change. As predicted by the effective medium theory[14,27] (inset on the right of Figure 4.1(e)), the reflection is greatly suppressed and the omnidirectional absorption enhanced over both the optical[28,29] and radio frequency ranges[30]. Compared to metal-assisted wet etching methods[19-21], our RIE process offers several benefits: (1) both mask creation (step 2) and etching (step 3) are completed in the same plasma chamber in a continuous fashion in about 15~20 min; (2) the process eliminates the need of using metal, a material usually disfavored in a semiconductor processing route due to potential contamination issues; and (3) the anisotropic nature of the RIE dry etching makes it better suited than the isotropic wet chemical etching as a means for creating high aspect-ratio silicon nanocones.

The advantage of this 3-step RIE process lies in its high controllability compared with other RIE bSi methods. By altering the conditions in each step, different properties of the nanocone forest can be tuned effectively: First, the tapered nanocone shape is mainly determined by the ratio between the RIE DC bias (which controls directional physical ion bombardment) and the inductively coupled plasma (ICP) power (which controls the plasma density and isotropic radical reaction) in step 3. A higher DC bias will lead to nanocones with straighter sidewalls, while a higher ICP power would result in a more tapered morphology. Second, the density of the nanocones can be controlled by the power and etching time used in step 2, which uses a CHF_3 plasma to randomly etch the oxide layer to form the required oxide nanomask. We can reliably attain the highest density structures with a 300 W power setting for the RIE and 500 W for the ICP with an etching time of 2 min (step 2). Third, the depth of the nanocones can be changed by varying the HBr etching time (step 3). In the supplementary materials, we included the SEM images (Figure 4.6) and absorption spectra (Figure 4.7) of bSi attained with different set values of etching time (from 1 min to 10 min). It is shown in these SEM images (Figure 4.6) that the length and width of the nanocones initially increase with a longer etching duration (up to 6 min), corresponding to an associated higher level of optical absorption (Figure 4.7). For the case of longer etching-time values of 10 min or more, the nanocone structures attained are finer in scale, with defects and even broken nanostructures evidenced that are further correlated with degraded optical properties. The bSi samples attained using an intermediate value of the etching time, here of 6 min and 8 min, display both similar morphologies and optical absorption. We chose 6 min as the optimal processing condition for bSi devices for the reason that longer etching induces more defects on the surface.

The μ-cells (30 μm thick, 100 μm wide and 1.5 mm long) utilized in this work were fabricated on a p-type Czochralski silicon wafer (i.e. donor wafer) by a previously reported process of photolithography, deep ICP-RIE etching and undercut in basic anisotropic etchant solutions (the oxide mask was removed by BOE for the bSi etching).[12] Figure 4.2(a) illustrates the structure of

the device with a vertical contact scheme, highlighting the phosphorus- (n+, green), and boron- (p+, blue), and intrinsically (gray) doped regions. Following the completion of the device fabrication, the μ-cells with top contact pads (gold) are amenable for transfer-assembly onto secondary substrates bearing pre-patterned bottom contact bus lines in programmable layouts, as shown by the SEM image presented in Figure 4.2(b). The devices were then planarized with a photocurable liquid resin (NOA61, Norland Products, Inc), leaving μ-cells embedded in a polymer matrix before bSi etching (Figure 4.2(c), orange region is the reflective silicon surface, the gold square and line are the top and bottom contacts for the device). The RIE process described earlier was utilized to create dense and sharp nanocone features on top of the devices, rendering them black (Figure 4.2(d), the polymer matrix was also textured by the RIE, making the background darker than that seen in Figure 4.2(c)). The depth of the nanocone surface texture was controlled to fall in the range of ~200 nm (Figure 4.1(e)) by tuning the etching time (6 min). Although the absorption enhancements from bSi generally increase with the feature size, the nanocone depth needs to be tailored to avoid excessive surface defects and the penetration of the p-n junction (less than 1 μm deep[12]) of the photovoltaic device. (It is shown by Figure 4.8 in the Supplementary Materials that after 6 min etching, the current output of the device begins to reach an asymptotic limit; the dark saturation current of the device increases as well with the use of longer etching time.) To passivate the dangling bonds of the black silicon surface and thus reduce the surface recombination rate, we deposited 20 nm of SiN_x onto the black μ-cells by plasma enhanced chemical vapor deposition (PECVD, PlasmaLab) at 220 ^oC, which comformally covers the nanocone features (see the SEM images before and after deposition in Figure 4.2(e) and 2(f)).

4.4 Angular Absorption Spectra of bSi

The broadband and omnidirectional light trapping properties of bSi on devices were examined by measuring the angular absorption spectra of a bulk bSi wafer, processed using RIE conditions

identical to those applied to the μ-cells. This measurement was made with a Cary 5000 UV-Vis-NIR spectrophotometer equipped with an integration sphere, as illustrated in Figure 4.3(a). The sample, mounted in the center of the sphere, was rotated along its z axis to vary the incidence angle (θ, relative to the norm of the wafer) of the incoming monochromatic light beam along the x axis. The reflected and scattered light not absorbed by the silicon surface is collected by the photo-detector at the bottom, the signal from which is subtracted from that measured for 100% reflection (calibrated using a diffuse reflector) to determine the angle-dependent light absorption of the sample. The values of effective absorption (A_{eff}) measured between 300 and 1100 nm at each angle, as calculated from these data are tabulated in Table 4.1 in the supplementary materials and plotted in Figure 4.4. The A_{eff} values were calculated by using the R_{eff} method, taking into account the solar flux distribution found under AM-1.5G standard solar irradiation[31]. The absorption spectra of polished p-type silicon samples (identical to the wafer used for cell fabrication) measured before and after the RIE bSi processing are presented in Figure 4.3(b) and 3(c), respectively. The bSi nanostructures dramatically enhance the absorption by more than 30% over the whole measured spectral range, here from 300 nm to 1100 nm (in the UV region, the enhancement is even greater—between 50% and 70%). The bSi sample effects a significantly higher absorption of the light than does a polished one even at high incident angles ($\theta > 60^o$), where the absorption of the latter declines rapidly with increasing θ. At $\theta = 70^o$, for example, bSi still achieves an absorption of over 90% between 300 nm and 800 nm, while that of the original silicon drops below 50%. Depositing a 20 nm of SiN_x passivation layer onto the bSi wafer (compare Figure 4.3(d) with Figure 4.3(c)), reduces its ability to absorb incident light for $\theta > 60^o$, but as seen in the data still outperforms the polished sample over a broad wavelength range.

4.5 *I-V* Characteristics of Black μ-Cell

The effects of the subwavelength nanocone features on the photovoltaic performance of the μ-cells were investigated by measuring their *I-V* characteristics under a simulated AM1.5G solar

spectrum of 1000 W/m^2 at room temperature. Figure 4.5 shows *I-V* curves of the same μ-cell after different processing steps, including: transfer-printing (original cell, bare silicon); embedding in a polymer matrix (after planarization); RIE treatment; and SiN_x deposition. A non-reflective anodized aluminum plate was placed under the device array in all cases to suppress backside reflections. The waveguiding effects[12] from the polymer matrix lead to a 23.3% increase (from 31.37 to 38.68 μA) in current output from a representative cell (as seen comparing the black and red curves in Figure 4.5). RIE treatment adds another 6.76 μA enhancement to the short circuit current (green curve in Figure 4.5) due to the light trapping properties of the top nanocone structures, bringing the total relative enhancement to 44.9%. As compared with the original device, however, both the open circuit voltage (V_{oc}, decreases from 0.515 V to 0.485 V) and fill factor (FF, decreases from 0.712 to 0.622) deteriorate, as the RIE also generates surface defects during the etching process. A 20 nm thick PECVD SiN_x, deposited as a passivation layer, partially repairs the dangling bonds on the surface, resulting a significant enhancement in I_{sc} (from 45.44 to 51.95 μA, as seen comparing the green and blue curves in Figure 4.5) and a slight recovery of the FF (from 0.622 to 0.645) and V_{oc} (from 0.485 to 0.490 V). After all the processing steps, the short circuit current of the device increases dramatically by 65.7% (compare black and blue curves in Figure 4.5), a result obtained as a consequence of enhanced photon capturing properties introduced by the bSi nanostructures. Relative to the original device, the efficiency (η, calculated based on the top surface area of the device without accounting for contributions from light incident on the side of the cells) improves by 42.8% (from 8.07% to 11.52%) after SiN_x deposition, a value principally limited by the increased surface recombination rate induced by the RIE process.

4.6 Discussion

The continuously tapered morphology of the bSi nanostructures demonstrated in this work bears a close resemblance to the pyramidal subwavelength pillar arrays found on moth eyes.[32] These

natural structures provide a superior graded index profile at the air/device interface that greatly suppresses top surface reflections. As compared to cylindrical pillars, a more common fabricated structure that mainly diffracts light into μ-cells[13,33], the non-periodical nanocone forests created by the lithography-free RIE step elicits a different photon capturing mechanism, one characterized by photon randomization or scattering that is largely insensitive to its wavelength or incidence angle. These broadband and omnidirectional absorption enhancements translate directly into boosts in power output of as much as 42.8%, leading to a more efficient utilization of the active photovoltaic material (silicon). The power-referenced material consumption here could be significantly lowered to further improve the system's cost-effectiveness when coupling devices with compact concentrator designs, including microlens array[4] or luminescent waveguides[9] as demonstrated in our earlier studies of concentrator designs using flat μ-cells. The concentrated photon flux would be more effectively converted to electrical power by the black μ-cell than a device without texturing due to the increased optical interaction length within the nanocone structures.

As evidenced from an inspection of the experimental results presented above, however, the relative enhancement for the energy conversion efficiency (~40%) of the black silicon μ-cell is not as significant as that for the absorption or short circuit current values (~60%), as the carrier recombination losses introduced by the RIE etching is only partially mitigated by the SiN_x passivation layer. Modifications might be made to the RIE process to reduce the processing-generated surface defects. One possible source of defects is the severe ion bombardment that accompanies the HBr etching in the third step, a result of the high atomic weight of bromine ion (atomic weight = 80 Da). The ion related energy transfer can be reduced by using Cl_2 as the etching gas. Since the chlorine ion has a much lower atomic weight (35.5 Da), the etching process would be dominated by chemical reactions with chlorine radicals rather than physical bombardment, leading to less surface defects albeit also engendering a slower etching rate. The

etching protocols, however, can be adjusted in principle to generate the same nanocone structures as are obtained with the HBr process.

PECVD deposited dielectrics (including SiN_x and hydrogenated amorphous silicon (a-Si:H)) have been shown to effectively passivate the surface of macro-scale solar cells due to the embedded the hydrogen atoms at the Si/dielectric interface.[26,34] For a black μ-cell with a highly textured surface, however, processes with improved step coverage and film quality, such as atomic layer deposition (ALD)[35] and thermal oxidation[12,20], could potentially generate a passivation layer with better uniformity and lower surface recombination velocity. Hydrogen passivation is an alternative approach that in principle is capable of repairing deeper dangling bonds due to the longer diffusion length of the hydrogen atom.[36] The high temperature requirements (>500 ^oC) of these above-mentioned processes, however, are not compatible with transfer-printed μ-cells, as both supporting elements (i.e. polymer matrix, glass substrate) and metal contacts would be damaged. Significant modifications would need to be made to the μ-cell fabrication sequence to incorporate the b-Si etching and high-temperature passivation steps before metal contact patterning, which is both a challenging and interesting direction to pursue in the future.

4.7 Conclusion

We produced black silicon (bSi) nanocone structures on fully functional silicon solar thin-film microcells (μ-cells) with a simple 3-step RIE process along with a silicon nitride passivation layer for broadband and omnidirectional light absorption enhancements. The photon capturing properties of the black μ-cell increased significantly, as shown by the marked short circuit current enhancements of as much as 65.7%. The RIE process, however, also creates surface defects in the device, which limits the enhancements in power output (~40%). The increased surface recombination could be potentially mitigated by both advanced passivation methods (e.g. ALD Al_2O_3, thermal oxidation, hydrogen passivation) and adjustments to the etching process. In

addition, optical concentration elements (e.g. backside reflectors, microlens array and luminescent waveguides) and module assembly strategies developed for microscale devices in our previous work[4,9,12] could also be utilized for the black μ-cells to create large-scale functional arrays of high power output with low material consumption.

4.8 Figures

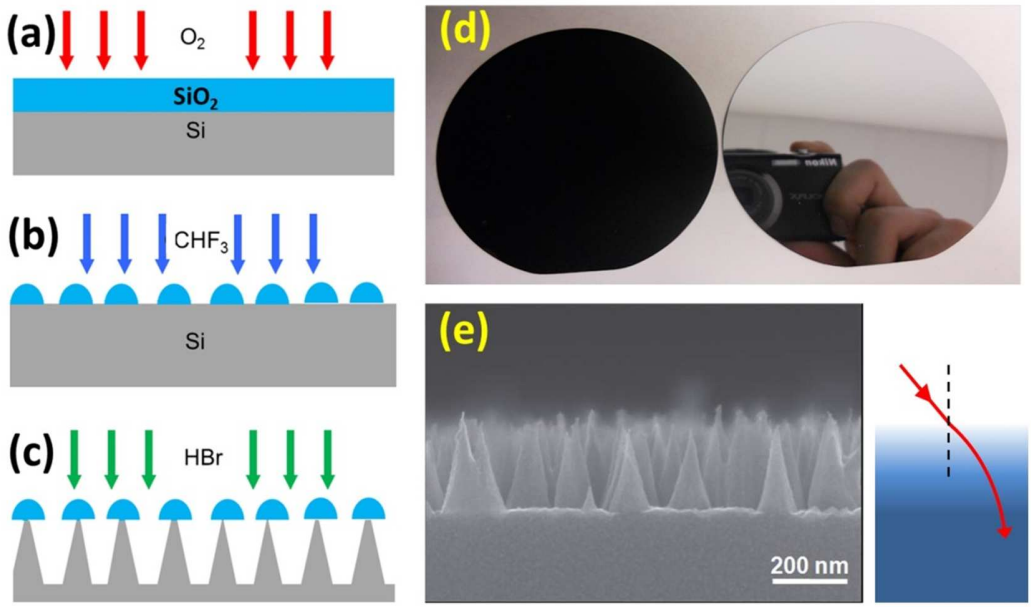

Figure 4.1 (a-c) Fabrication process of bSi. (a) Thin oxide layer on silicon surface formed by oxygen plasma. (b) Randomly dispersed oxide mask formed by CHF_3 plasma etching of thin oxide layer. (c)Silicon nanocones formed by HBr plasma etching. (d) Comparison of a 3" polished silicon wafer (right) and a 3" bSi wafer. (e) Cross-sectional SEM image of nanocone forest on bSi. The inset on the right shows how the gradient effective refractive index of nanocone forest enhances the absorption.

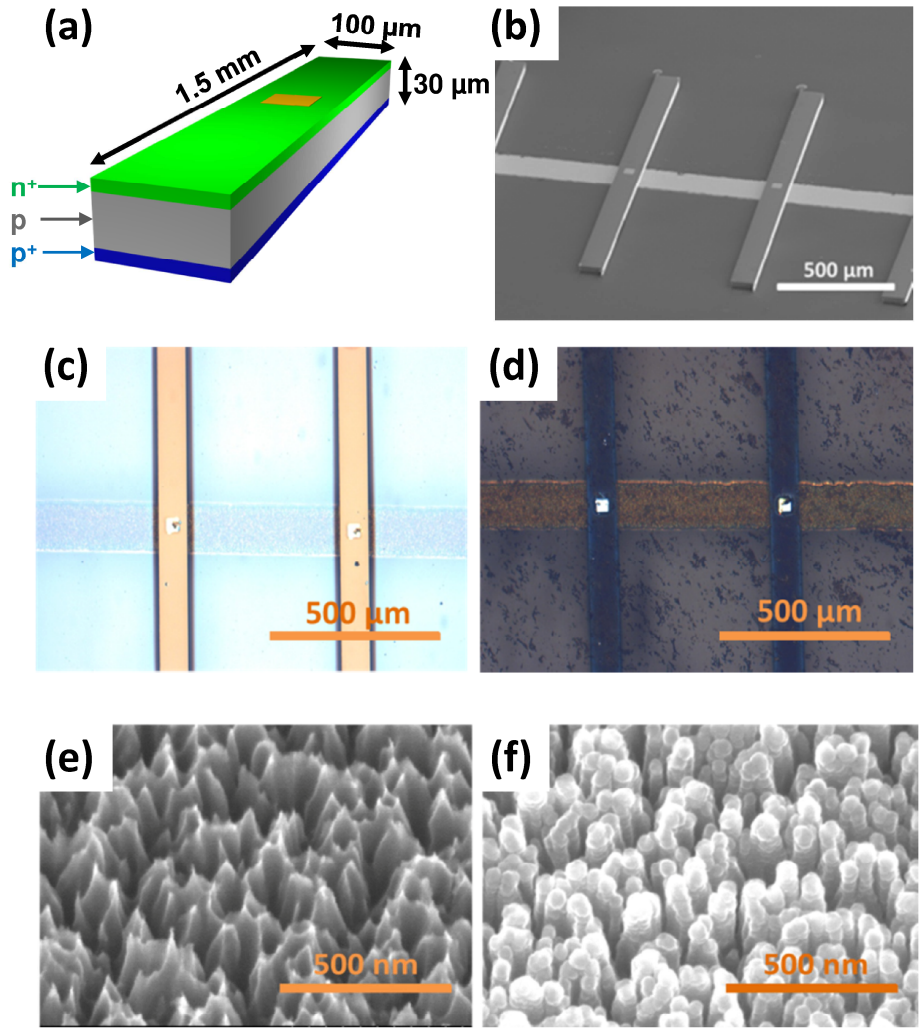

Figure 4.2 (a) Schematic illustration of the structure of a silicon solar microcell. (b) A SEM image of an array of µ-cells after being transfer-printed onto glass substrate finished with top contact pad and backside contact bus line. (c) Optical image of original µ-cells embedded in a polymer matrix. (d) Optical image of black µ-cells treated by the 3-step RIE process. (e) SEM image of the surface of a black µ-cell. (f) SEM image of the surface of a black µ-cell after deposition of 20 nm SiN_x.

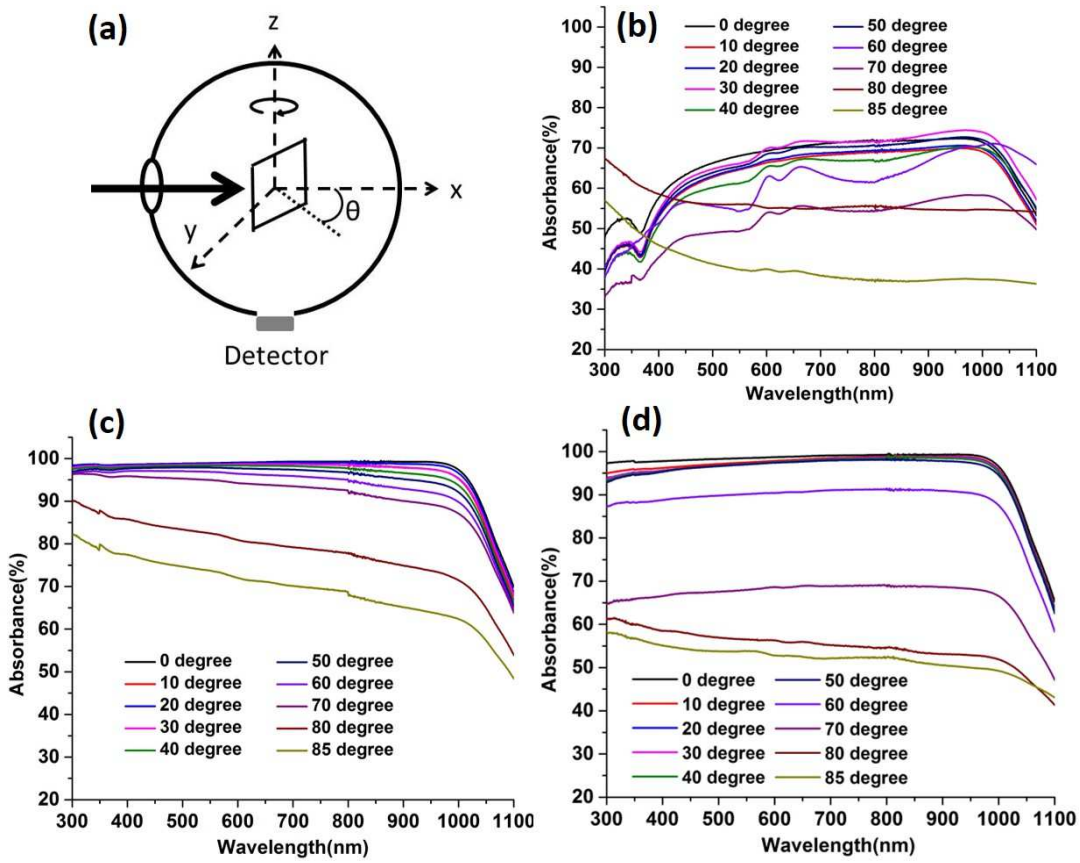

Figure 4.3 (a) Illustration of the experimental setup of integration sphere measurement for absorption spectra of bSi. θ is the angle between the incident light beam and the norm of sample. (b) Absorption spectra of the polished p-type silicon wafer at θ from 0° to 85°. (c) Absorption spectra of p-type bSi wafer at θ from 0° to 85°.(d) Absorption spectra of p-type bSi wafer deposited with 20 nm of SiN_x at θ from 0° to 85°.

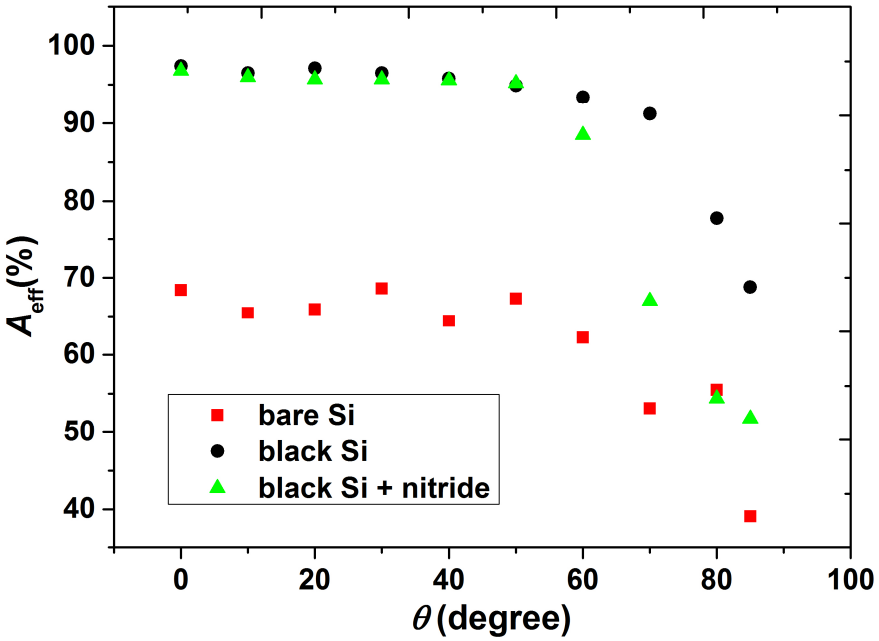

Figure 4.4 Effective Absorption (A_{eff}/%) of bare Si, bSi and bSi+nitride at different incident angle θ.

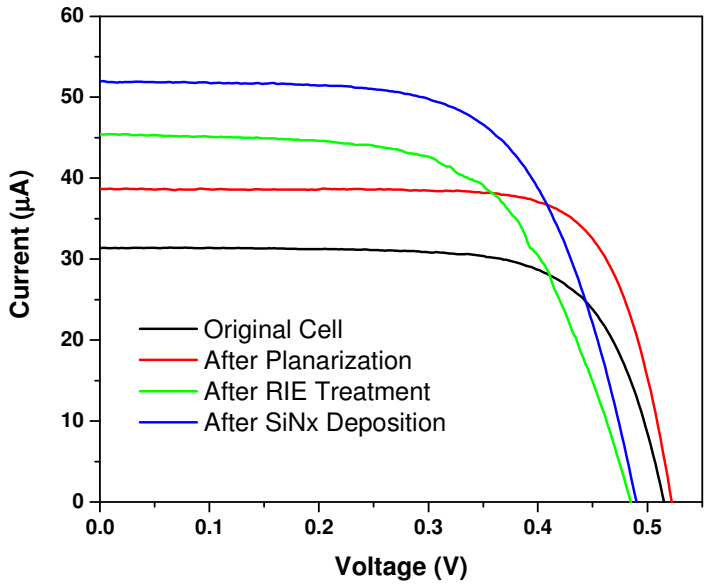

Figure 4.5 *I-V* characteristics of the μ-cell under AM 1.5G solar spectrum after different fabrication steps

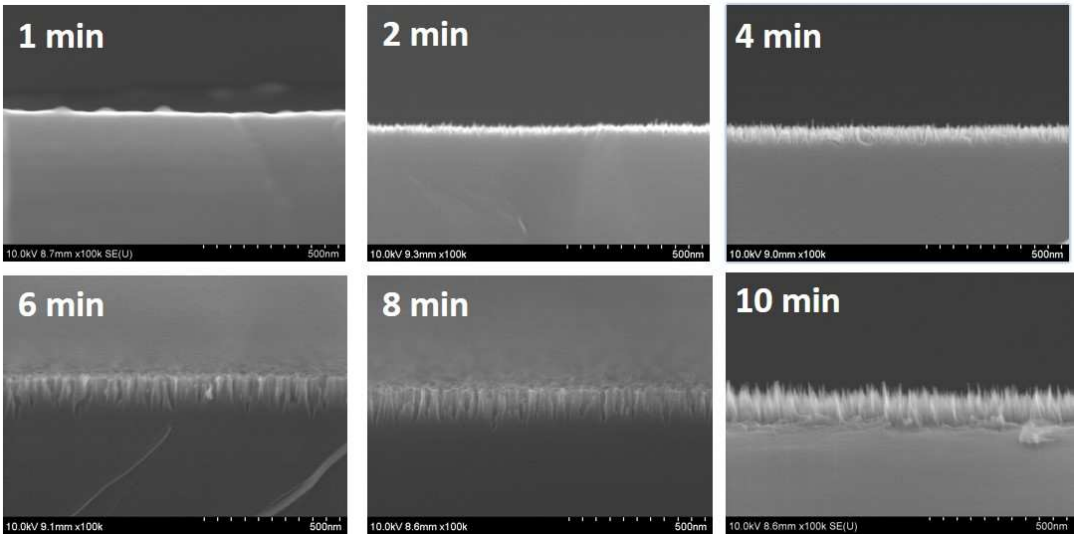

Figure 4.6 Cross-sectional SEM images of black silicon with different etching time.

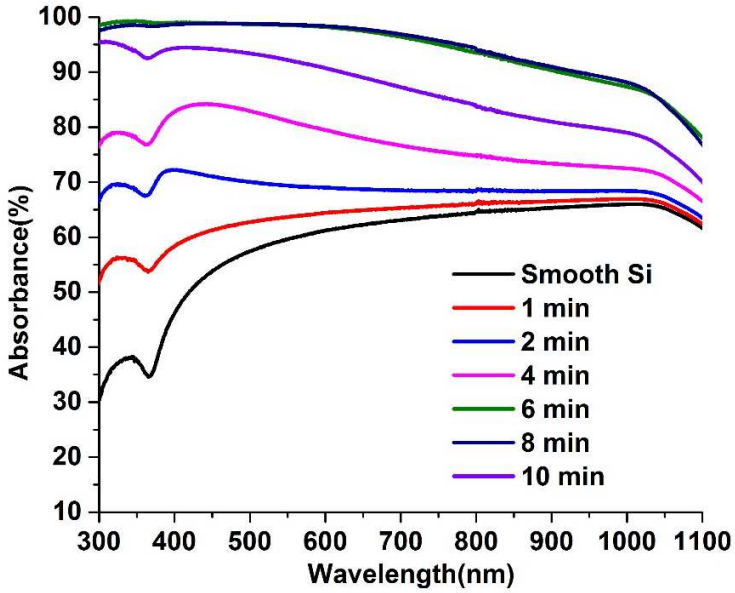

Figure 4.7 Absorption spectra of black silicon with different etching time.

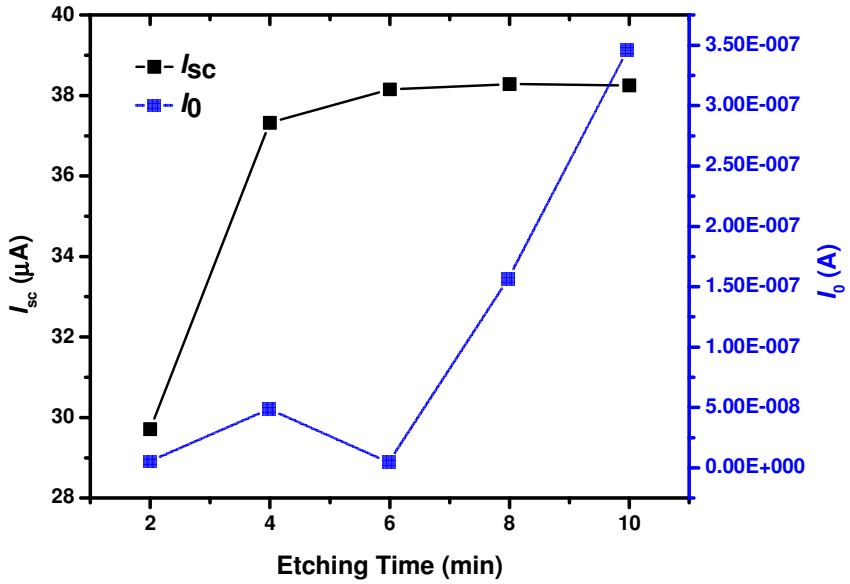

Figure 4.8 I_{sc} and I_0 (dark saturation current measured at a reverse bias of -0.5V) of a device (without planarization) after various etching time in step 3.

4.9 Table

Table 4.1 Effective Absorption (A_{eff}/%) of bare Si, bSi and bSi+nitride.

θ (degree)	0	10	20	30	40	50	60	70	80	85
bare Si	68.4	65.4	65.9	68.6	64.4	67.3	62.2	53.1	55.5	39.1
bSi	97.4	96.5	97.1	96.5	95.8	94.9	93.4	91.2	77.7	68.8
bSi + nitride	96.8	96.0	95.7	95.7	95.6	95.2	88.5	67.0	54.4	51.8

4.10 References

[1] Masson, G.; Latour, M.; Rekinger, M.; Theologitis, I.-T.; Papoutsi, M. Global market outlook for photovoltaics 2013-2017. *European Photovoltaic Industry Association* **2013**, 12-32.

[2] Bagnall, D. M.; Boreland, M. Photovoltaic technologies. *Energy Policy* **2008**, *36*, 4390-4396.

[3] REN, R. global status report, 2012. *Renewable energy policy network for the 21st century: Paris: REN21 Secretariat* **2012**.

[4] Yoon, J.; Baca, A. J.; Park, S.-I.; Elvikis, P.; Geddes, J. B.; Li, L.; Kim, R. H.; Xiao, J.; Wang, S.; Kim, T.-H.; Motala, M. J.; Ahn, B. Y.; Duoss, E. B.; Lewis, J. A.; Nuzzo, R. G.; Ferreira, P. M.; Huang, Y.; Rockett, A.; Rogers, J. A. Ultrathin silicon solar microcells for semitransparent, mechanically flexible and microconcentrator module designs. *Nat. Mater.* **2008**, *7*, 907-915.

[5] Meitl, M. A.; Zhu, Z.-T.; Kumar, V.; Lee, K. J.; Feng, X.; Huang, Y. Y.; Adesida, I.; Nuzzo, R. G.; Rogers, J. A. Transfer printing by kinetic control of adhesion to an elastomeric stamp. *Nat. Mater.* **2006**, *5*, 33-38.

[6] Carlson, A.; Bowen, A. M.; Huang, Y.; Nuzzo, R. G.; Rogers, J. A. Transfer printing techniques for materials assembly and micro/nanodevice fabrication. *Adv. Mater.* **2012**, *24*, 5284-5318.

[7] Baca, A. J.; Yu, K. J.; Xiao, J.; Wang, S.; Yoon, J.; Ryu, J. H.; Stevenson, D.; Nuzzo, R. G.; Rockett, A. A.; Huang, Y.; Rogers, J. A. Compact monocrystalline silicon solar modules with high voltage outputs and mechanically flexible designs. *Engery Environ. Sci.* **2010**, *3*, 208-211.

[8] Corcoran, C. J.; Kang, S.; Li, L.; Guo, X.; Chanda, D.; Nuzzo, R. G. Mechanisms of Enhanced Optical Absorption for Ultrathin Silicon Solar Microcells with an Integrated Nanostructured Backside Reflector. *ACS Appl. Mater. Interfaces* **2013**, *5*, 4239-4246.

[9] Yoon, J.; Li, L.; Semichaevsky, A. V.; Ryu, J. H.; Johnson, H. T.; Nuzzo, R. G.; Rogers, J. A. Flexible concentrator photovoltaics based on microscale silicon solar cells embedded in luminescent waveguides. *Nat. Commun.* **2011**, *2*, 343.

[10] Gangopadhyay, U.; Kim, K.; Kandol, A.; Yi, J.; Saha, H. Role of hydrazine monohydrate during texturization of large-area crystalline silicon solar cell fabrication. *Sol. Energy Mater. and Sol. Cells* **2006**, *90*, 3094-3101.

[11] Terheiden, B.; Fath, P. In *Proc. 3rd World Conf. Photovoltaic Energy Convers.* 2003; Vol. 2, p 1443-1446.

[12] Yao, Y.; Brueckner, E.; Li, L.; Nuzzo, R. Fabrication and assembly of ultrathin high-efficiency silicon solar microcells integrating electrical passivation and anti-reflection coatings. *Energy Environ. Sci.* **2013**, *6*, 3071-3079.

[13] Shir, D.; Yoon, J.; Chanda, D.; Ryu, J.-H.; Rogers, J. A. Performance of Ultrathin Silicon Solar Microcells with Nanostructures of Relief Formed by Soft Imprint Lithography for Broad Band Absorption Enhancement. *Nano Lett.* **2010**, *10*, 3041-3046.

[14] Chen, S.-H.; Wang, H.-W.; Chang, T.-W. Absorption coefficient modeling of microcrystalline silicon thin film using Maxwell-Garnett effective medium theory. *Opt. Express* **2012**, *20*, A197-A204.

[15] Jansen, H.; Boer, M. d.; Legtenberg, R.; Elwenspoek, M. The black silicon method: a universal method for determining the parameter setting of a fluorine-based reactive ion etcher in deep silicon trench etching with profile control. *J. Micromech. Microeng.* **1995**, *5*, 115.

[16] Huang, Y.-F.; Chattopadhyay, S.; Jen, Y.-J.; Peng, C.-Y.; Liu, T.-A.; Hsu, Y.-K.; Pan, C.-L.; Lo, H.-C.; Hsu, C.-H.; Chang, Y.-H.; Lee, C.-S.; Chen, K.-H.; Chen, L.-C. Improved broadband and quasi-omnidirectional anti-reflection properties with biomimetic silicon nanostructures. *Nat. Nanotechnol.* **2007**, *2*, 770-774.

[17] Barberoglou, M.; Zorba, V.; Pagozidis, A.; Fotakis, C.; Stratakis, E. Electrowetting Properties of Micro/Nanostructured Black Silicon. *Langmuir* **2010**, *26*, 13007-13014.

[18] Huang, Z.; Carey, J. E.; Liu, M.; Guo, X.; Mazur, E.; Campbell, J. C. Microstructured silicon photodetector. *Appl. Phys. Lett.* **2006**, *89*, 033506.

[19] Koynov, S.; Brandt, M. S.; Stutzmann, M. Black nonreflecting silicon surfaces for solar cells. *Appl. Phys. Lett.* **2006**, *88*, 203107.

[20] Oh, J.; Yuan, H.-C.; Branz, H. M. An 18.2%-efficient black-silicon solar cell achieved through control of carrier recombination in nanostructures. *Nat. Nanotechnol.* **2012**, *7*, 743-748.

[21] Yuan, H.-C.; Yost, V. E.; Page, M. R.; Stradins, P.; Meier, D. L.; Branz, H. M. Efficient black silicon solar cell with a density-graded nanoporous surface: Optical properties, performance limitations, and design rules. *Appl. Phys. Lett.* **2009**, *95*, 123501.

[22] Carey, J. E.; Crouch, C. H.; Shen, M.; Mazur, E. Visible and near-infrared responsivity of femtosecond-laser microstructured silicon photodiodes. *Opt. Lett.* **2005**, *30*, 1773-1775.

[23] Xu, Z.; Jiang, J.; Gartia, M. R.; Liu, G. L. Monolithic Integrations of Slanted Silicon Nanostructures on 3D Microstructures and Their Application to Surface-Enhanced Raman Spectroscopy. *J. Phys. Chem. C* **2012**, *116*, 24161-24170.

[24] Xu, Z.; Chen, Y.; Gartia, M. R.; Jiang, J.; Liu, G. L. Surface plasmon enhanced broadband spectrophotometry on black silver substrates. *Appl. Phys. Lett.* **2011**, *98*, 241904.

[25] Xu, Z.; Jiang, J.; Liu, G. L. Lithography-free sub-100 nm nanocone array antireflection layer for low-cost silicon solar cell. *Appl. Opt.* **2012**, *51*, 4430-4435.

[26] Kerr, M. J.; Cuevas, A. Recombination at the interface between silicon and stoichiometric plasma silicon nitride *Semicond. Sci. Technol.* **2002**, *17*, 166-172.

[27] Stephens, R. B.; Cody, G. D. Optical reflectance and transmission of a textured surface. *Thin Solid Films* **1977**, *45*, 19-29.

[28] Yu-Hsiang, T.; Mao-Jung, H.; Jien-Yin, S.; Ming-Hua, S. Fabrication of Nanocone Subwavelength Antireflection Structures on Quartz Substrates. *Japan J. Appl. Phys.* **2012**, *51*, 06FF06.

[29] Zhu, J.; Yu, Z.; Burkhard, G. F.; Hsu, C.-M.; Connor, S. T.; Xu, Y.; Wang, Q.; McGehee, M.; Fan, S.; Cui, Y. Optical Absorption Enhancement in Amorphous Silicon Nanowire and Nanocone Arrays. *Nano Lett.* **2009**, *9*, 279-282.

[30] Ding, F.; Cui, Y.; Ge, X.; Jin, Y.; He, S. Ultra-broadband microwave metamaterial absorber. *Appl. Phys. Lett.* **2012**, *100*, 103506.

[31] Overstraeten, R. J. V.; Mertens, R. P. *Physics, technology and use of photovoltaics*; Bristol: Boston, 1986.

[32] Bernhard, C. G. Structural and functional adaptation in a visual system. *Endeavour* **1967**, *26*, 79-84.

[33] Yu, K. J.; Gao, L.; Park, J. S.; Lee, Y. R.; Corcoran, C. J.; Nuzzo, R. G.; Chanda, D.; Rogers, J. A. Light Trapping in Ultrathin Monocrystalline Silicon Solar Cells. *Adv. Energy Mater.* **2013**, *3*, 1401-1406.

[34] Dauwe, S.; Schmidt, J.; Hezel, R. Very low surface recombination velocities on p- and n-type silicon wafers passivated with hydrogenated amorphous silicon films. *Conf. Rec. IEEE Photovoltaic Spec. Conf., 29th* **2002**, 1246-1249.

[35] Wang, W.-C.; Lin, C.-W.; Chen, H.-J.; Chang, C.-W.; Huang, J.-J.; Yang, M.-J.; Tjahjono, B.; Huang, J.-J.; Hsu, W.-C.; Chen, M.-J. Surface Passivation of Efficient Nanotextured Black Silicon Solar Cells Using Thermal Atomic Layer Deposition. *ACS Appl. Mater. Interfaces* **2013**, *5*, 9752-9759.

[36] Teplin, C. W.; Lee, B. G.; Fanning, T. R.; Wang, J.; Grover, S.; Hasoon, F.; Bauer, R.; Bornstein, J.; Schroeter, P.; Branz, H. M. Pyramidal light trapping and hydrogen passivation for high-efficiency heteroepitaxial (100) crystal silicon solar cells. *Energy Environ. Sci.* **2012**, *5*, 8193-8198.

Chapter 5 Quantum Dot Luminescent Concentrator Cavity Exhibiting 30-Fold Concentration[5]

5.1 Abstract

Luminescent solar concentrators doped with CdSe/CdS quantum dots provide a potentially low-cost and high-performance alternative to costly high band-gap III-V semiconductor materials to serve as a top junction in multi-junction photovoltaic devices for efficient utilization of blue photons. In this study, a photonic mirror was coupled with such a luminescent waveguide to form an optical cavity where emitted luminescence was trapped omnidirectionally. By mitigating escape cone and scattering losses, 82% of luminesced photons travel the length of the waveguide, creating a concentration ratio of 30.3 for blue photons in a waveguide with a geometric gain of 61. Further, we study the photon transport inside the luminescent waveguide, showing unimpeded photon collection across the entire length of the waveguide.

5.2 Introduction

Luminescent solar concentrators[1-4] (LSCs) have been studied extensively for the last three decades as low-cost alternatives to single- and multi-junction photovoltaic devices. As silicon prices have fallen, it has become increasingly clear that future solar panels will need to have both low cost and high efficiency. One promising strategy for achieving a higher efficiency is to use different parts of the solar spectrum in photovoltaic materials with varying bandgaps to minimize losses associated with carrier thermalization and incomplete photon absorption. For these multi-junction (MJ) PV devices, there is a strong need for developing low-cost, high-bandgap solar cells for efficient utilization of the high energy part of the solar spectrum. A luminescent solar concentrator could provide exactly this function, serving as the top junction in a multi-junction architecture by converting blue photons into guided luminescence. Due to the concentration effect, only small amounts of high-performing but expensive III-V photovoltaic materials are

---

[5] The content of this chapter is reproduced with permission from, Noah D. Bronstein♦, Yuan Yao♦, Lu Xu♦, Erin O' Brien, Alexander S. Powers, Vivian E. Ferry, A. Paul Alivisatos, and Ralph G. Nuzzo, "Quantum Dot Luminescent Concentrator Cavity Exhibiting 30-fold Concentration", ACS Photonics, 2015, 2 (11), pp 1576–1583 (♦Equal contribution), Copyright © American Chemical Society

needed to collect the light from an inexpensive luminescent waveguide. Such a device requires high concentration factors to reduce the cost of the III-V photovoltaic material. High concentration also allows the Stokes Shift of the lumophore to be recovered in the operating voltage of the photovoltaic cell.

The concentration factor and collection efficiency achieved by LSCs to date has been limited due to parasitic losses such as non-unity quantum yields of the lumophores, imperfect light trapping within the waveguide, and reabsorption and scattering of propagating photons.[5] Previous studies have sought to solve each of these parasitic losses individually, resulting in modest performance improvements.[6-15] Here we achieve a luminescent concentration ratio greater than 30 with an optical efficiency of 82% for blue photons by simultaneously addressing the materials and optical challenges of the LSC system. These concentration ratios are achieved through the combination of designer quantum dot lumophores and photonic mirrors, and microscale silicon photovoltaic cells are used to detect the concentration of light in the waveguide. To the best of our knowledge, this is the highest luminescent concentration factor in literature to date. Previously, a concentration factor of 22 was reported in 1984 by Roncali and Garnier[12,16] using a dye with high luminescence quantum yield in a highly polished waveguide with mirrored edges. Such a strategy resulted in a low waveguide efficiency due to unmitigated escape cone losses. In contrast, our use of photonic mirrors that are carefully matched to narrow bandwidth emitting quantum dots lumophores allowed us to achieve waveguide efficiency exceeding the limit imposed by total internal reflection. Lessons learned from our design offer guidance towards the development of devices with both high concentration factors and high collection efficiencies.

The general principle behind LSCs is illustrated in Figure 5.1: broadband photons from the sun are absorbed by lumophores in a waveguide, and the emitted photons are guided via total internal reflection (TIR) to an adjacent solar cell where they are converted to electricity. The thermodynamic limit of the concentration ratio (C), the ratio of the photon fluxes at the absorption energy (E_1) and emission energy (E_2), is approximated[17-19] by

$$C \leq \frac{E_2^3}{E_1^3} \exp\left(\frac{E_1 - E_2}{k_B T}\right) \tag{5.1}$$

Equation 5.1 indicates that *C* should increase exponentially with the difference in photon energies (often called the Stokes Shift). According to equation 5.1, for a Stokes Shift greater than 300 meV, *C* could exceed the geometric optical limit[20] of 46,200 for direct solar radiation.

Recent renewed interest in LSCs has been driven by materials research to overcome the reabsorption losses due to insufficient Stokes shifts, with particular emphasis on nanocrystal lumophores.[7] One such class of nanocrystals is the quantum dot heterostructure shown in Figure 5.1, where the effectives Stokes shift can be controlled by tuning either the core size or the thickness of the larger bandgap shell.[21-23] As the shell-to-core volume ratio increases, the overlap between absorption and emission decreases, thereby reducing reabsorption losses for luminesced photons traveling through the waveguide.[21]

It has previously been shown that a wavelength-selective dielectric filter is thermodynamically required to achieve high efficiency.[24] Under idealized circumstances where the lumophore species has unity quantum yield, the polymer-lumophore matrix exhibits no scattering over the length-scale of the concentrator, and the Stokes shift is large enough to allow for a high thermodynamic limit for *C*, the performance of the LSC will still be limited by inefficient light guiding to the solar cell. In the traditional LSC design (Figure 5.1), the waveguide acts as a rudimentary wavelength-selective filter for photons: high energy solar photons are refracted to subtend only a fraction of the solid angle inside the waveguide, whereas low energy luminesced photons exist at all angles and accumulate inside the totally internally reflected modes.[19] The wavelength-selectivity of this filter is inherently poor due to escape cone losses, and can be improved with the addition of a wavelength-selective photonic mirror between the waveguide and the sun.[6,10,25]

Our strategy is to embed the lumophore in an optical cavity integrated with a carefully tuned wavelength-selective photonic mirror that transmits blue light and reflects red luminesced photons at all angles (Figure 5.1). Designer quantum dot materials offer an advantage over dye molecules in this regard. The emission spectra of nanocrystals are intrinsically narrower and more symmetric, enabling the design of a one-dimensional photonic mirror that operates omnidirectionally across the entire emission band. The design presented here targets high quantum yield, large Stokes shift, narrow emission band CdSe/CdS core-shell nanocrystals with

low scattering cross sections at the emission wavelength, combined with photonic structures that trap luminescence inside the waveguide.

5.3 CdSe/CdS Nanocrystal and Photonic Mirror Design

Although the Stokes shift of CdSe/CdS nanocrystals increases with increasing shell thickness thereby reducing LSC losses, scattering between the nanoparticle and polymer matrix also increases with the volume and increases LSC losses. To find the optimal nanocrystal geometry, we synthesized CdSe/CdS nanoparticles with constant 2.5 nm core diameter and varying shell thicknesses, and compared the ratio of absorption at 450 nm to the extinction at the peak luminescence wavelength as shown in Figure 5.2(a). For small shell thicknesses, the extinction is dominated by absorption in the CdSe core, whereas for large shell thicknesses the extinction is dominated by scattering between the nanoparticle and the waveguide polymer. The experimental results match well with theoretical calculations based on the electrostatic dipole model[26] using bulk refractive index data for CdSe and CdS.[27-30] For CdSe core sizes between 2 and 5 nm, there exists a maximum in the extinction ratio corresponding to a total particle diameter between 15 and 20 nm, or total volume between 2000 and 4000 nm^3. The particles chosen to make devices in this study have a 2.5 nm core and a 15.4 ± 1 nm total diameter, yielding an experimental extinction ratio of 230 to 1. A characteristic transmission electron micrograph is shown in Figure 5.1. The solution-phase luminescence quantum yield of the nanocrystals is 68%, and the luminescence is centered at 600 nm with a FWHM of 40 nm.

Based on the properties of these nanocrystals, we designed a wavelength-selective photonic mirror that accepts incident blue sunlight and traps luminescence. From 350 to 520 nm the photonic mirror exhibits 90% average transmission at normal incidence. Over the emission band of the lumophore, the hemispherically averaged reflectance of the mirror is 98%, with a maximum reflectivity >99.999% at 650 nm at normal incidence. The dependence of reflectivity against angle of incidence is characterized in Figure 5.2(b); luminesced photons are reflected efficiently up to 60 degrees from normal, with diminished reflectivity at higher angles. The photographs in Figure 5.2(c) show the effect of the photonic mirror on luminescence from the quantum dot solution under 440 nm excitation. In the first photograph, two mirrors are arranged in a tent over the cuvette and all luminescence is directed to the opening since it cannot pass

through the mirror. In the second, the scattered blue laser light transmits through the mirror while the luminescence from the lumophore solution is blocked.

The quantum dots are integrated into a poly(lauryl-methacrylate) (PLMA) matrix to form an optically clear LSC waveguide. The photoluminescence quantum yields (PLQY) of the nanocrystals decrease upon integration with the polymer, decreasing from 68% to 60% (Figure 5.2(d)). The effect of the photonic mirror was quantified by measuring the optical trapping efficiency (η_{trap})—the fraction of photons that propagate to the edges of the waveguide (i.e. no embedded solar microcell). Without the photonic mirror, $\eta_{trap}$is limited by the fraction (η_{TIR}) of photons initially trapped by total internal reflection (TIR) in a polymer with refractive index n

$$\eta_{trap} \leq \eta_{TIR} = (1 - n^{-2})^{\frac{1}{2}} \tag{5.2}$$

For the PLMA/QD composite (n =1.44), $\eta_{TIR} = 0.72$. For a 30 μm thick luminescent film placed between two thin glass coverslips, η_{trap} averages around 66% (Figure 5.2(d)), slightly lower than η_{TIR} due to scattering and reabsorption losses. Replacing both glass coverslips with photonic mirrors, luminesced photons cannot escape out of the front and back surface of the waveguide, increasing η_{trap} to 82% (Figure 5.2(d)), exceeding the value Snell's law would allow without the dielectric mirrors.

5.4 Concentrator Cavity Design and Characterization

Figure 5.3(a) shows the concentrator cavity, consisting of the wavelength-selective photonic mirror on top, a PLMA/QD waveguide with an embedded Si solar microcell[31,32], and a trench-shaped diffuse reflector that both enhances absorption of incident photons and recycles photons that escape through the bottom and edges of the waveguide. It is important to note that in this iteration, the single Si microcell acts as a detector of the optical concentration. The overall EQE and collection efficiency of the device are low due to the small area covered by the single microcell. In the future, arrays of microcells could be integrated so as to capture more of the

waveguided light with minimal shadowing. The champion device performance under AM1.5G illumination is summarized in Table 5.1, with current density (J)-voltage (V) curves shown in Figure 5.3(b). Both the J_{sc} and the V_{oc} of the microcell increase significantly upon integration with the LSC including the trench reflector, and increase further with the addition of the photonic mirror. The total J_{sc} of the Si microcell is 7.7 times higher after integration with the complete device. The spectral dependence of C is plotted in Figure 5.3(c), and shows that the current enhancement originates from concentration of blue photons, the spectral region where the nanocrystals absorb. From 550 to 800 nm C is greatly suppressed, as this spectral region is reflected by the photonic mirror and prevented from entering the LSC. This loss is outweighed by the improvement in the concentration of blue photons as demonstrated by the total current enhancement.

The optical density (OD) at 450 nm of the nanocrystal-polymer films was then varied from 0.1 to 1.2, and the LSCs were characterized under blue-filtered illumination. The highest concentration factor occurs when OD=0.65 (Figure 5.4(a)). At lower OD, absorption of incident sunlight in the blue portion of the spectrum is diminished, while at higher OD reabsorption and scattering of luminesced photons decrease the optical efficiency. All samples demonstrate more than 60% enhancement in C after applying the photonic mirror except the control device (no QDs added in the polymer). The optimum C under the blue-filter illumination with the photonic mirror reaches 30.3, a value unprecedented in the LSC literature.

To study the propagation of photons inside the LSC, we compared a sample with high internal scattering (Figure 5.4(b), due to the absence of thorough QD cleaning before polymerization) to one with low scattering (Figure 5.4(c)) (See Supporting Method S4 for details). Both samples had an optimal OD of 0.65 at 450 nm, and were measured under blue-filtered illumination with variable illumination spot diameter resulting in variable geometric gain G (the ratio of illuminated area to illuminated edge area; see Supporting equation S5.6 and Supporting discussion S5). Without the photonic mirror acting as a photon-recycling element, the sample with high scattering (Figure 5.4(b)) shows a limited growth of C that quickly plateaus with increasing G, as luminesced photons are scattered out of the waveguide and lost. In comparison,

the sample with low scattering exhibits a quasi-linear increase of *C* with *G* (Figure 5.4(c)), as contributed by the uninterrupted TIR modes inside the waveguide.[21]

Adding the photonic mirror on top allows both non-TIR and scattered photons to be recycled and then to propagate inside the concentrator cavity before finally reaching the solar cell. As a result, the losses associated with scattering are strongly reduced, and photons are concentrated over distances much longer than the scattering length of the waveguide. In the high scattering case (Figure 5.4(b)) *C* becomes quasi-linear with increasing *G*, and reaches 16 at *G*=37, nearly five times higher than without the mirror. This value is still smaller than that in the low scattering case (*C*=20), indicating that scattering loss is not completely mitigated as the mirror reflectivity diminishes at oblique angles. Measurement of the luminescent concentration factor of the high scattering sample with the dielectric mirror at *G*=61 resulted in *C*=26, only slightly reduced from the champion value of 30.3 for the non-scattering device. In the device with low scattering (Figure 5.4(c)), *C* increases super-linearly with the illumination diameter, increasing faster than the TIR limit imposed by Equation 5.2. This super-linearity marks the onset of a transition from ballistic, single-pass photon transport to diffusion-based transport afforded by photon-recycling. Our results suggest that efficient trapping of luminescence with a dielectric mirror can keep the luminescence inside the cavity regardless of the optical clarity and smoothness of the waveguide. If the optical quality of the waveguide could truly be made irrelevant by the dielectric mirror, the fabrication of the devices could be simplified.

To further investigate the connection between photon scattering, the photonic mirror, and *C,* we used a Monte-Carlo ray tracing model. These simulations assume that scattering derives from the refractive index contrast between the nanocrystals and the PLMA waveguide. For each device, a range of scattering lengths are simulated and fit to the experimental data (Figure 5.4(a)). All other model inputs are measured experimentally. For the high and low scattering devices (Figures 5.4(b-c)), the best fit is achieved with 0.18 mm and 3 mm scattering lengths (Supporting method S7). A scattering length of 3 mm corresponds to roughly one scattering event for a photon propagating the 19 mm from the edge of the waveguide to the solar cell. Figure 5.4(d) shows the results of simulations systematically modeling the effect of scattering on device performance. Without the photonic mirror, *C* is negligible until the scattering length approaches

the waveguide length, and asymptotes when the scattering length is longer than the waveguide length. With the photonic mirror on top, the performance is less sensitive to the detrimental effects of scattering. However, the best results are still achieved when the scattering length is greater the waveguide length.

5.5 Conclusion

In conclusion, the design presented here achieves luminescent solar concentration ratios over 30 while maintaining a high waveguide efficiency of 82%. This is due to the combination of designer nanocrystal lumophores with a photonic cavity that traps luminescence. The narrow emission linewidth of the nanocrystal lumophores enables the use of a highly reflective, wavelength-selective photonic mirror as the top surface of the cavity. In addition to improving the photon concentration ratio, the luminescence-trapping effect of the mirror also dramatically mitigates the detrimental effect of scattering.

The device fabricated here is tuned to utilize the blue portion of the spectrum due to the engineered absorption spectrum of the CdSe/CdS QDs. The system efficiency remains limited, as only one silicon microcell is utilized to detect rather than fully convert the luminescence in the waveguide. Using transfer-printing based assembly, however, arrays of these microscale devices could be embedded in the waveguide to dramatically enhance the PV conversion efficiency.[33] Coupling with III-V (e.g. InGaP) microcell arrays with bandgaps tailored to match QD emission, a luminescent concentrator cavity module could be constructed with efficiencies comparable to conventional PV panels but with reduced materials consumption. Additionally, this LSC module can be potentially used as the top layer (e.g. over Si) in a mechanically-stacked multi-junction architecture for full spectrum conversion, utilizing both the high energy photons in the LSC and the low energy photons in the bottom photovoltaic. We expect that future devices will achieve even higher concentration ratios while maintaining high waveguide efficiency through improvements to the luminescence quantum yield, waveguide geometry, and photonic mirror design.

5.6 Methods

5.6.1 Quantum Dot Synthesis

CdSe quantum dots were synthesized following literature procedures. Details can be found in Supporting method S1.

5.6.2 Quantum Dot Characterization

Optical absorption spectra were taken on a Shimadzu UV-3600 absorption spectrometer. Fluorescence spectra were collected with a Jobin-Yvon FluoroLog 2, calibrated with an Ocean Optics HL3-plus radiometric calibration lamp and a Spectralon™ diffuse reflector from Lab Sphere.

Fluorescence quantum yields were measured on a custom integrating sphere fluorometer, as described in Supplementary method S2. To ensure proper quantitative measurement technique, the fluorescence quantum yield of Rhodamine 590 in ethanol was measured, and found to be 93.5%, reproducible to within 1%.

Transmission electron micrographs were obtained on a 200 kV Tecnai G220 S-TWIN with a Gatan SC200 CCD camera. Sizing was accomplished by analyzing the particles with an automated sizing algorithm (Supporting method S2).

5.6.3 Dielectric Mirror Design, Fabrication, and Analysis

The wavelength-selective dielectric mirror was designed and fabricated by Optical Filter Source, LLC (Austin, Texas). The reflectivity spectrum was measured by mounting a mirror on an optics post and measuring the transmittance as a function of angle. The average reflectivity is calculated by multiplying a normalized quantum dot luminescence spectrum $PL_{norm}(\lambda)$ by the reflectivity spectrum $R(\lambda,\theta)$ and integrating over a hemispherical emission, following equation 5.3. Details can be found in Supporting method S3.

$$R_{avg} = \int_0^{\pi} \int_{\lambda} R(\lambda, \theta) * PL_{norm}(\lambda) * d\lambda * \cos(\theta) \sin(\theta)\, d\theta \qquad (5.3)$$

5.6.4 Luminescent Waveguide Fabrication and Characterization

The monomer lauryl methacrylate (LMA, Sigma Aldrich) and the crosslinker ethylene glycol dimethacrylate (EGDMA, Sigma Aldrich) was first purified to remove the inhibitor and then mixed at a 10:1 volume ratio. The CdS/CdSe quantum dots were then dispersed in this solution and polymerized under UV illumination (365 nm) and inert atmosphere with Darocur® 1173 (Sigma Aldrich) added as the initiator (1% by volume).

The film absorption was measured using Varian Cary 5G spectrophotometer. The photo-luminescence quantum yields (PLMA) and optical trapping efficiency (η_{trap}) of the waveguide was measured in a custom setup, as detailed in Supporting method S4.

5.6.5 Device Fabrication and Characterization

Monocrystalline silicon microcells (30 µm thick, 100 µm wide and 1500 µm long) with a thermal oxide passivation layer were fabricated using photolithography, reactive ion etching and wet chemical etching from p-type (111) Czochralski Si wafers (10 Ω·cm, Silicon Materials Inc.), as reported previously. The resulting devices were transfer-printed individually onto a glass substrate (170 µm thick) with a thin (~30 µm), partially cured adhesive (NOA61, Norland Products) layer. A 1.5-inch square quartz plate, treated with repel silane (GE healthcare), was placed on top of the device. The microcell was then embedded in the luminescent waveguide (30 µm thick) through capillary filling of the LMA/QD solution and subsequent polymerization. The film thickness (30 µm) was controlled by using soda lime glass spacers (SPI product #2714) at the corners of the substrate. After removing the quartz plate, the interconnects of the device were formed by screen-printing silver epoxy (E4110, Epo-Tek) lines and curing at room temperature.

The photovoltaic characteristics of the microcells in the concentrator cavity were measured using a source meter (model 2400, Keithley) and a 1,000 W full spectrum solar simulator (Oriel, 91192) with a AM1.5 G filter. The concentration ratio (a.u.) as a function of excitation wavelength was measured using an OL-750 automated spectroradiometric system (Gooch & Housego). The LSC device was placed inside a trench diffuse reflector (Spectralon, Labsphere) at all these measurements, while the PV performance of the microcell before integrating with the concentrator cavity was measured on a non-reflective substrate.

The propagation curve was obtained by placing a circular iris diaphragm (Newport) on top of the waveguide with the solar cell located in the center. The photocurrent was measured with a blue filter (Hoya 390) under the solar simulator while changing the illumination area with the diaphragm aperture size. The concentration factor C is calculated from the short circuit current density J_{LSC} in mA*cm^{-2} by

$$C = \frac{J_{LSC}}{\int T(\lambda) AM1.5G(\lambda) d\lambda * EQE_{device}(600\,nm)} \quad (4)$$

where $T(\lambda)$ is the transmission spectrum of the Hoya 390 filter, $AM1.5G(\lambda)$ is the solar spectrum flux in mA*cm^{-2}nm^{-1} and $EQE_{device}(600\,nm)$ is the EQE of the silicon photovoltaic device measured on a non-reflective substrate at the emission wavelength (600 nm). Further details can be found in Supporting method S6.

5.7 Supporting Information

5.7.1 Method S1: Synthesis of Quantum Dots

CdSe Quantum Dot Synthesis

CdO (99.99%, Sigma Aldrich), octadeclylphosphonic acid (99%, PCI), tri-n-octylphosphine oxide (99%, STREM), tri-n-octlyphosphine (97%, STREM), selenium powder (99.999%, Alfa Aesar), octanethiol (99%, Sigma Aldrich), 1-octadecene (tech grade, Acros Organics), and oleic acid (tech grade, Sigma Aldrich) were all used without purification.

CdSe quantum dots were synthesized following literature procedures.[34,35] 60 mg CdO is added to 280 mg n-octadecylphosphonic acid (ODPA) and 3 g TOPO in a 25 mL 3-neck roundbottom flask with a glass thermocouple adapter and a silicone septum. The reaction is connected to a Schlenk line with a glass condenser column and rubber hosing. H-grease is used for all ground-glass joints (size 14/20). The mixture is stirred vigorously and degassed at 150 ºC at 150 mTorr for 1 hour, followed by complexation at 320 ºC under argon for 2 hours. During complexation, red CdO-containing solid condenses at the top of the flask, requiring the flask to be unclamped and shaken vigorously to dislodge and melt it. After the mixture turns clear and light yellow, it is cooled to 150 ºC and placed under dynamic vacuum (150 mTorr) and degassed for an hour. At

380 °C, 60 mg Se in 360 mg tri-n-octylphosphine is injected and the reaction mixture is then cooled rapidly to room temperature using forced air. The rapid cooling is used to yield small (2.5 nm diameter) particles.

The reaction mixture is brought into an argon-filled glovebox and cleaned by precipitation and centrifugation. The first precipitation was performed with acetone, followed by centrifugation at 8000 RPM for 10 minutes. The clear supernatant is discarded and the colorful pellet is dissolved in hexanes. Precipitation with acetone and centrifugation at 8000 RPM are repeated. The particles are then dissolved in hexanes and left overnight in the freezer in the glovebox, at -30 °C. The next day, the centrifuge swing-bucket is cooled to -20 °C by storing in a freezer for two hours and the particles are centrifuged at 4000 RPM for 3 minutes. The colorful solid is discarded and the colorful solution is kept.

CdS Shelling of CdSe Quantum Dots

CdS shelling of the CdSe quantum dots was performed following Chou *et al*.[36]

$Cd(Oleate)_2$ was synthesized by mixing CdO with oleic acid at a molar ratio of 10 oleic acid per CdO and diluted to 0.2 molar in Cd with 1-octadecene. The mixture is degassed on the Schlenck line at 110 °C at 150 mTorr and complexed at 240 °C under argon. The mixture is then brought into an air-free glovebox where it can be melted and measured out by volume. The mixture is made 100 mL at a time, and typically used within a few weeks of synthesis.

Quantum dot concentration was measured with the optical absorption curve provided in Jasieniak et al.[28] 1e-7 moles of CdSe quantum dots are brought to 320 °C in 3 mL oleylamine and 3 mL 1-octadecene (ODE). As the mixture is being heated, injection at 3 mL per hour of 0.2 molar $Cd(oleate)_2$ in 2:1 oleic acid:ODE along with a separate solution of 0.2 molar 1-octanethiol in ODE is initiated at 250 °C with a heating rate of 20-30 °C per minute. Total injection volume sets the total shell size. After injection is complete, the solution is maintained at 320 °C for 1 hour.

The solution is then cooled to room temperature and cleaned in an air-free glovebox.by 8 successive centrifugations at 8000 RPM. The centrifugation proceeds as follows:

1) Centrifuge the reaction solution.

2) Dissolve in hexanes, precipitate with acetone, centrifuge.
3) Dissolve in hexanes, precipitate with acetone, centrifuge.
4) Dissolve in chloroform, precipitate with acetonitrile, centrifuge.
5) Dissolve in hexanes, precipitate with acetone, centrifuge.
6) Dissolve in chloroform, precipitate with acetonitrile, centrifuge.
7) Dissolve in hexanes, precipitate with acetone, centrifuge.
8) Dissolve in hexanes, store in freezer overnight, centrifuge at -20 ^{o}C. Keep colorful supernatant.

5.7.2 Method S2: Characterization of Quantum Dots

Sizing of Core/Shell particles

Sizing was accomplished with by analyzing transmission electron micrographs with a custom-written MatLab script to be published elsewhere in detail. Transmission electron micrographs were obtained on a 200 kV Tecnai G220 S-TWIN with a Gatan SC200 CCD camera. The automated method utilizes FFT filters, thresholding, watershed segmentation, and roundness and circularity filtering. This method allows the analysis of thousands of particles per sample. The areas and Feret diameters of thousands of particles are measured, and the distribution of particle sizes is fit to a Gaussian. The average area is used to calculate the average volume of the particles by assuming a spherical shape:

Equation S5.1 $$V = \frac{4}{3\sqrt{\pi}} A^{\frac{3}{2}}$$

A representative TEM image of the particles used to make devices in this study is shown in Figure 5.5 with automatically detected particle outlines. Detected particles are outlined in red if they pass the roundness and circularity filter, or outlined in blue if they fail. A histogram of particles that pass are shown in Figure 5.6, along with the roundness and circularity for all particles according to

Equation S5.2 $$Roundness = 4\frac{Area}{\pi(Major\ Axis)^2}$$

Equation S5.3 $$Circularity = 4\pi\frac{Area}{Perimeter^2}$$

where Major Axis is that of fitted ellipse that encloses the shape, and the Perimeter is the distance around the particle.

Extinction ratio measurement

The ratio of extinction at 450 nm to the luminescent wavelength is measured by transmission of light through a cuvette in a Shimadzu UV-3600 double-beam spectrometer using the slowest integration time and 2 nm slit widths. The particles are dissolved in hexanes, and the instrument is referenced against a cuvette of hexanes immediately before measurement. Then the sample is added to the same cuvette, and the measurement is taken again. Then, more particle solution is added to the cuvette and the measurement is repeated. The two spectra are stitched together to provide a dynamic range exceeding 10^4.

The fluorescence spectrum is measured on a Horiba Jobin-Yvon FluoroLog 2 spectrofluorometer, with wavelength calibrated to a Raman signal from water (350 nm excitation, 397 nm Raman peak) to within 1 nm accuracy. The instrument sensitivity was calibrated using a NIST traceable HL3-plus radiometric calibration lamp (serial number 089440003) from Ocean Optics pointed at a Spectralon™ diffuse reflector from Lab Sphere placed at the sample location. The peak wavelength was measured by this method.

The extinction ratio, then, is the ratio of extinction at 450 nm to the extinction at the emission peak wavelength (Figure 5.7).

Extinction Ratio Simulation

The absorption and scattering spectra of CdSe/CdS core/shell particles were simulated using the electrostatic dipole approximation for core-shell particles and the bulk dielectric constants of CdSe and CdS. The results are plotted in Figure 5.8. If scattering is not taken into account, the particles demonstrate increasing ratios of absorption at 450 to absorption at the emission peak wavelength with increasing shell diameter at all sizes (represented by Abs_{450}/Abs_{600}). However, when scattering is taken into account at either the emission wavelength alone (Abs_{450}/Ext_{600}) or at both the absorption and emission wavelengths (Ext_{450}/Ext_{600}), the model predicts a maximum for shells of 7 – 10 nm thickness at all core sizes.

Luminescence Quantum Yield Measurement

Luminescence quantum yield of nanoparticles was measured in a home-built integrating sphere spectrofluorometer. A schematic of the instrument is depicted in Figure 5.9. All lenses used in the instrument are 1" diameter CaF_2 in order to reduce chromatic aberration. A Fianium SC450 supercontinuum pulsed laser is used as a white light source, which provides 4 W average illumination from 470 nm to 2500 nm. The laser light is focused onto a Princeton Instruments SP150 monochromator with a 150 g/mm grating blazed to 750 nm. The output of the monochromator is focused onto the entrance of a Princeton Instruments SP275 monochromator with a 1200 g/mm grating, blazed at 500 nm. The output of the SP275 is focused into the 1" entrance port of a 5.3" Spectralon integrating sphere from LabSphere. A piece of a quartz wafer reflects part of the beam on to a ThorLabs S120VC calibrated silicon photodiode, which continuously measures the laser power. The sample is held in the integrating sphere by a cylindrical quartz cuvette in a custom holder made of Spectralon. The cylindrical cuvettes have PTFE plugs. The laser spot is the same size as the sample cuvette, about 7 mm by 20 mm, and the laser is aligned to hit the sample cuvette. There is a baffle inside the integrating sphere between the sample and the exit port to prevent any direct reflections from being detected. The exit port is reduced with a custom Spectralon port reducer to ¼" diameter. The light leaving the exit port is focused onto the entrance slit of a Princeton Instruments SP2300 monochromator with a 300 g/m grating blazed at 500 nm. The spectrum is detected with a Princeton Instruments PIXIS 400B thermoeletrically cooled silicon CCD. The instrument sensitivity as a function of

wavelength is calibrated with a NIST-traceable radiometric calibration lamp, model HL3-plus from Ocean Optics, serial number 089440003.

5.7.3 Method S3: Photonic Mirror Reflectance Spectrum

The photonic mirror reflectance spectrum was measured in transmittance mode in a Shimadzu UV-3600 double-beam absorption spectrometer. The mirror was glued to a post and rotated to different angles. The angles were measured with a protractor. The spectra are plotted in Figure 5.10.

Photonic Mirror Average Reflectance Calculation

The average reflectance of the photonic mirror (Figure 5.11) is calculated by considering both wavelength- and angle-weighting. The wavelength-weighting is a normalized quantum dot luminescence spectrum with an integrated value of unity. The angle-weighting is the hemispherical emission solid angle, $2\cos(\theta)\sin(\theta)\,d\theta$. Accordingly, the angle-average reflectance is calculated by equation S5.4. Finally, the angle- and wavelength-average reflectance is calculated by equation S5.5.

Equation S5.4 $$R_{avg}(\lambda) = 2\int_0^{\frac{\pi}{2}} R(\lambda,\theta)\cos(\theta)\sin(\theta)\,d\theta$$

Equation S5.5 $$R_{avg} = \int_\lambda PL_{norm}(\lambda)R_{avg}(\lambda)d\lambda$$

5.7.4 Method S4: Optical Characterization of QD-PLMA Films

The absorption of the QD/PLMA films (30 μm thick) were measured at different optical densities and shown in Figure 5.12. The high optical qualities of these films are highlighted by the lack of measurable scattering in the transparent window of the spectra. The absorption spectra of the high and low scattering sample are compared in Figure 5.13. The QD loading fraction in the two films is identical. The high scattering sample shows a significantly higher

signal in the absorption spectrum at all wavelengths due to the absence of thorough QD cleaning before polymerization.

The photo-luminescence quantum yield (PLQY) of the QD/PLMA film was measured using a custom setup (Figure 5.14) that includes a light source (Acton Research Corp 75W xenon lamp with an Opti-Quip 1200 power supply), a monochromator (Jarrel-Ash M-20, slit size 0.5 mm) and an integration sphere (Labsphere RTC-060-SF, with a center sample mount) that collects all transmitted, scattered and emitted light from the sample. The output from the integration sphere is coupled into a 200 μm FT400EMT optical fiber (Thorlabs) before being measured by Acton Research SpectroPro3001 spectrometer equipped with a calibrated Acton Pixis 100 CCD camera. The detection system's spectral response was calibrated with a Labsphere halogen standard light source IRF G3 (NIST traceable). The dark current background was collected over a 1 s integration time. Both the sample and reference (a thin glass substrate) spectra were taken by changing the excitation wavelength between 380 nm and 520 nm. The peak area of the transmitted and emitted signal was compared with the reference to obtain the film absorption and emission. The ratio between the emitted and absorbed photons was then calculated as the PLQY.

The same setup is also used to measure the optical trapping efficiency of the QD/PLMA film. The samples were prepared in the same way as fabricating the LSC device. Specifically, two coverslips or photonic mirrors were secured with 30 μm spacers in between, and QD monomer solution was capillary filled into the cavity and cured under UV illumination. The samples were measured in the integrating sphere and the total emitted luminescence photons (I_{total}) were obtained. The photons escaped from the top surface (I_{top}, i.e. escape cone loss) were then measured after painting the edges of the samples with a black matte paint to block the edge emissions. Trapping Efficiency (η_{trap}), the fraction of the photons coupled to the film edge, is then calculated as 1- I_{top}/I_{total}.

5.7.5 Discussion S5: Definition of Geometric Gain

The cross-section of the luminescent concentrator cavity is illustrated in Figure 5.15. The inner dimensions of the trench reflector (see Figure 5.17 for its reflectance) are 50 mm wide, 67 mm long and 2 mm deep. The PLMA/QD film is a 30 μm thick square with a side length of 38.1 mm.

The substrate (48 mm X 65 mm) is composed of a thin glass coverslip (170 μm thick) and a NOA adhesive layer (30 μm thick) used when transfer-printing the solar cell device. The total thickness (t) of the LSC device is 230 μm. For a certain illumination diameter (D), the geometrical gain (G) of the LSC device can be calculated by the equation below:

Equation S5.6 $$G = \frac{A_{LSC}}{A_{edge}} = \frac{\pi D^2/4}{\pi D t} = \frac{D}{4t}$$

The TIR limit calculated in Figure 5.4(c) assumes at short distances, the white diffuse reflector contributes directly scattered photons to the solar cell and complicates the shape of the curve for C vs G. After some short distance (around G=4), the concentration factor increases linearly with G as photons travel perfectly through the waveguide, resulting in a concentration factor of

Equation S5.7 $$C(G) = \eta_{TIR} * PLQY * (G - 4) + C(G = 4)$$

Equation S5.8 $$C(G) = 0.432\ G + 0.77$$

Our definition of geometric gain (i.e. waveguide top area/edge area) is slightly different from previous literature reports, where the geometric gain is considered as a device property, and calculated as the ratio of illuminated area to solar cell area. And in the classic case where solar cells cover the sides and the whole LSC waveguide is illuminated from the top, these two definitions are practically identical. However, if we imagine a luminescent waveguide with no photovoltaic material at all, immediate confusion arises. It should be apparent that such a device does exhibit luminescent concentration, but that the concentration is not harvested and as such does no useful work. If one wanted to measure that concentration, one could place a very small optical detector inside the waveguide so as not to perturb the photon field too much. This is what

we have done in this study. Such an embedded detector must have a well-understood wavelength-dependent response, geometry, and illumination pattern in order to use it to measure the concentration of photons. These conditions are all met for our detector. Although luminescence is being directed to multiple surfaces (4 sides and the bottom surface, Figure 5.16) of the solar cell, the resulted concentration is not over-estimated as the side area is smaller than the top surface and the luminescence intensity incident on the bottom is lower. Our Monte-Carlo simulation (See Table 5.2 and Figure 5.16) shows that if we were able to measure the photon concentration ratios on each face of the micro PV cell, the vertical edges would experience a photon concentration ratio nearly identical to value determined from the photocurrent. This convenient coincidence allows us to use the photocurrent as a good proxy for the photon concentration ratio.

Here, we use a variable illumination spot within the same device to generate a series of geometric gains. In this case, using a definition of geometric gain that considers only the illumination spot and not the size of the whole waveguide is a useful definition. If, as is usually the case, photons traveling away from that very small optical detector and toward the edge of the waveguide have little chance of reaching the detector, then the non-illuminated part of the waveguide plays very little role. When this condition is broken, and photons traveling toward the edge can indeed be reflected back by the cavity and edge reflectors, then this behavior is clearly visible as a super-linear increase in concentration factor versus geometric gain.

Some might worry that this definition allows the concentration to grow faster than the geometric gain, and to actually exceed the geometric gain, and that this is an artifact of the definition and the very small detector. However, an ideal photovoltaic material would recycle photons just as efficiently as a reflective edge through efficient band-edge luminescence. Therefore, our choice to use a very small optical detector and highly reflective edges approximates what would happen if we had access to highly luminescent photovoltaic materials (e.g. GaAs) instead of the weakly luminescent silicon micro-cell that we used as a detector.

5.7.6 Method S6: PV Characterization of the Concentrator Cavity

PV performance was measured both under full solar spectrum and blue-filtered illumination (see Figure 5.18 for the filter transmission spectrum). Modulating the film optical densities (OD) between 0.11 and 1.2, the current density of the LSC device peaks at 219 mA/cm^2 with an OD of 0.65 (Figure 5.19). A similar trend was observed in both spectrally-resolved concentration data (Figure 5.20) and propagation curves under blue-filtered illumination (Figure 5.21) collected for these samples, matching well with the results shown in Figure 5.4(a).

5.7.7 Method S7: Extraction of Scattering Length from Monte-Carlo Simulation

Monte Carlo simulations were performed to reproduce device performance by varying the characteristic scattering length of the lumophores. The scattering spectrum was estimated by the electrostatic dipole approximation. The scattering spectrum is then multiplied by a scalar to provide a parameterized scattering length at 600 nm wavelength. An example is plotted Figure 5.22.

The optical density of each device is measured, and used to fix the optical density of the quantum dots in the simulation. After performing the simulations with a variety of scattering lengths, both with and without the photonic mirror, results at OD=0.652 are plotted against the experimental data in Figure 5.23 as an example.

5.8 Figures

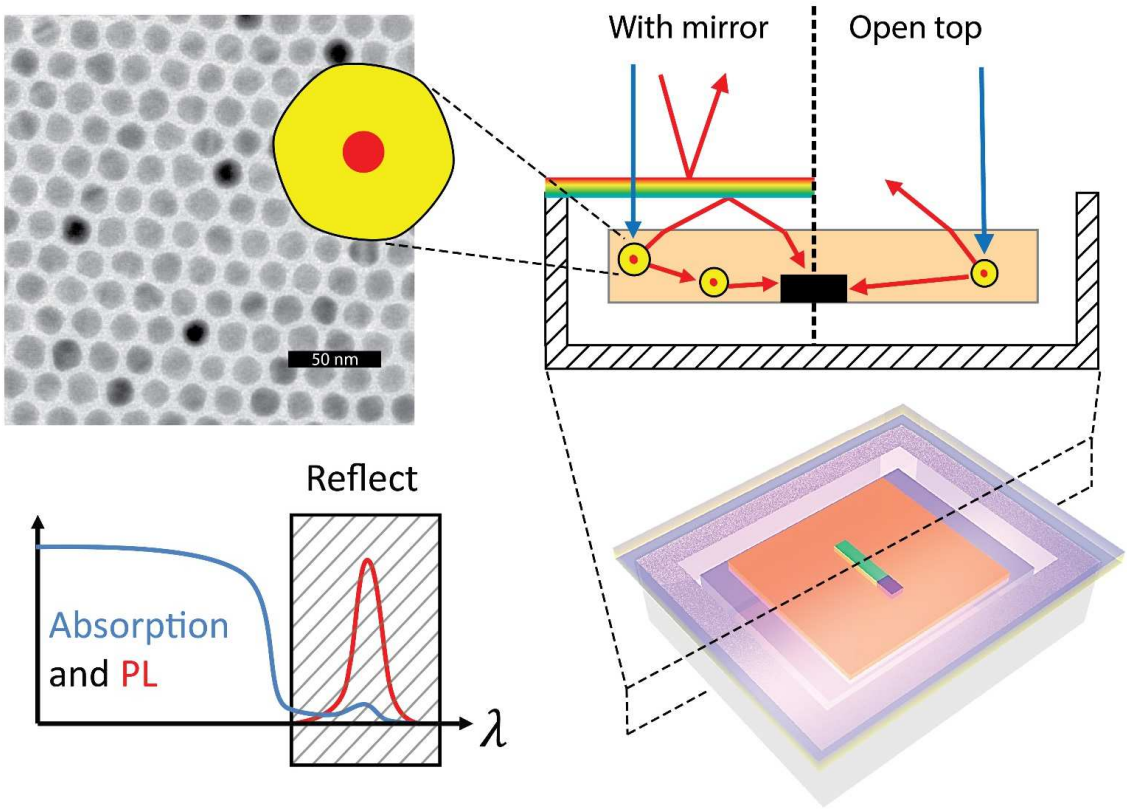

Figure 5.1 Graphic showing a typical transmission electron micrograph and schematic of giant CdSe/CdS quantum dots, incorporated into a traditional luminescent solar concentrators (open top) and the luminescent concentrator cavity (with Mirror). The black rectangle is a photovoltaic cell. The blue arrows represent solar photons which are then converted to red light by the quantum dots and either collected by the solar cell or lost to the escape cone. In the new design, a wavelength-selective mirror traps the luminescence inside the cavity, increasing the intensity of red light inside the cavity. The desired absorption, photoluminescence (PL) and reflectance spectra are sketched. The result is improved collection efficiency of red photons, which cannot escape, and improved power output from the solar cell.

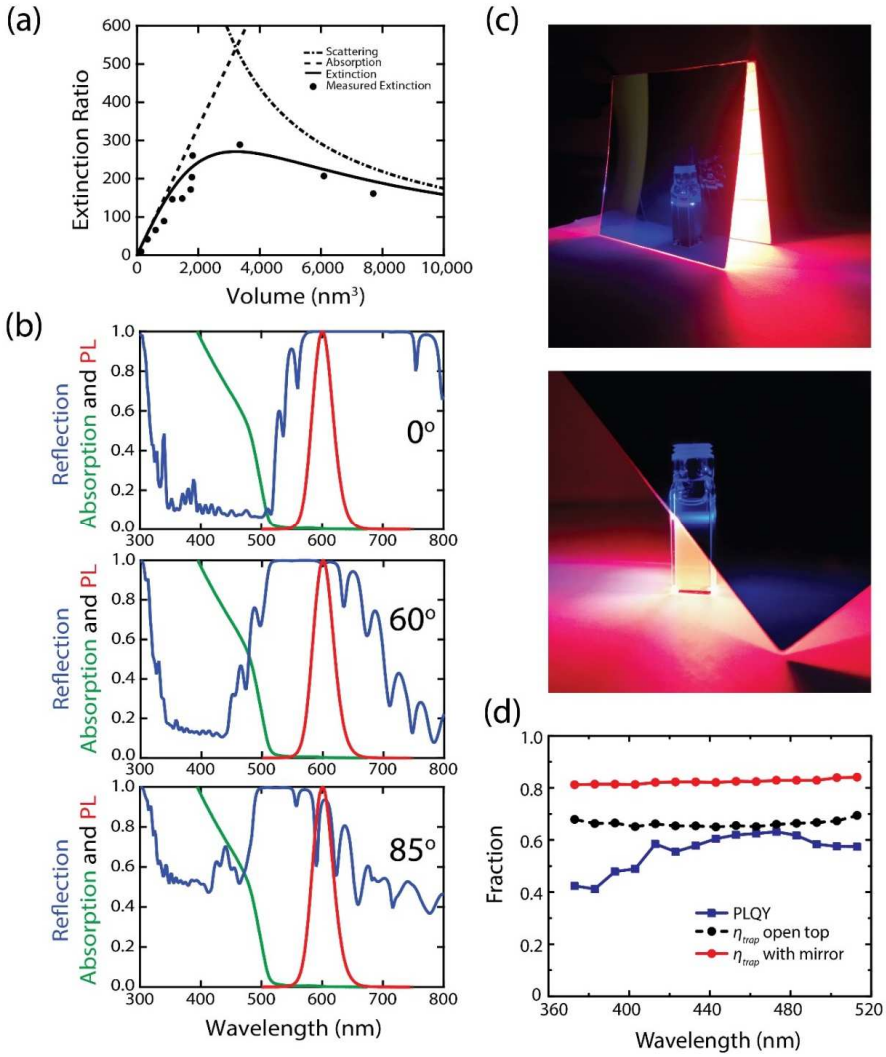

Figure 5.2 (a) Data and simulation of the relationship between shell volume and the ratio of extinction at 450 nm to extinction at 600 nm for CdSe/CdS core/shell nanoparticles with a 2.5 nm core diameter. The dashed lines represent the ratio of extinction at 450 nm to the absorption at 600 nm and scattering at 600 nm, as calculated by the electrostatic dipole approximation. The solid line is the ratio of the extinction at 450 nm to the sum of absorption and scattering at 600 nm. (b) Absorption and emission spectra of the QDs as compared to the reflectivity of the photonic mirror at different incidence angles; (c) Photographs of the QD solution under blue laser illumination with photonic mirrors reflecting the luminesced red light; (d) PLQY of the QD/PLMA film and the trapping efficiency before and after integration with the photonic mirror.

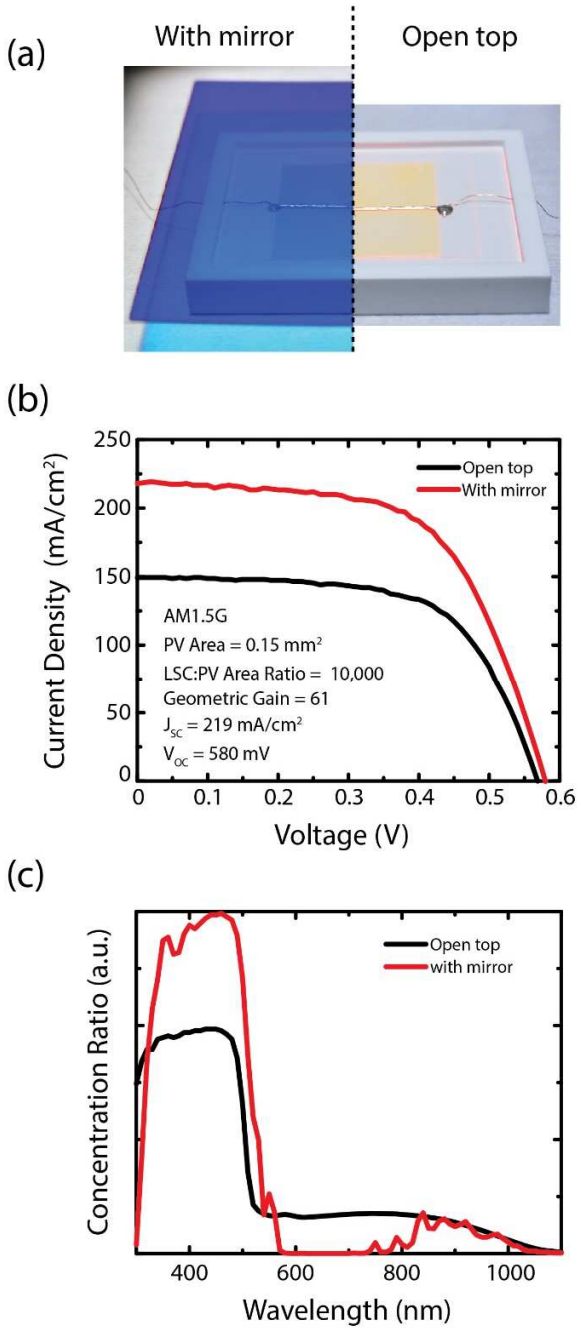

Figure 5.3 (a) Photograph of a microcell-LSC integrated with a photonic mirror and a trench-shaped diffuse trench reflector; (b) J-V characteristics of the LSC device with and without the photonic mirror; (c) Concentration ratio as a function of excitation wavelength of the LSC-PV device with and without the photonic mirror.

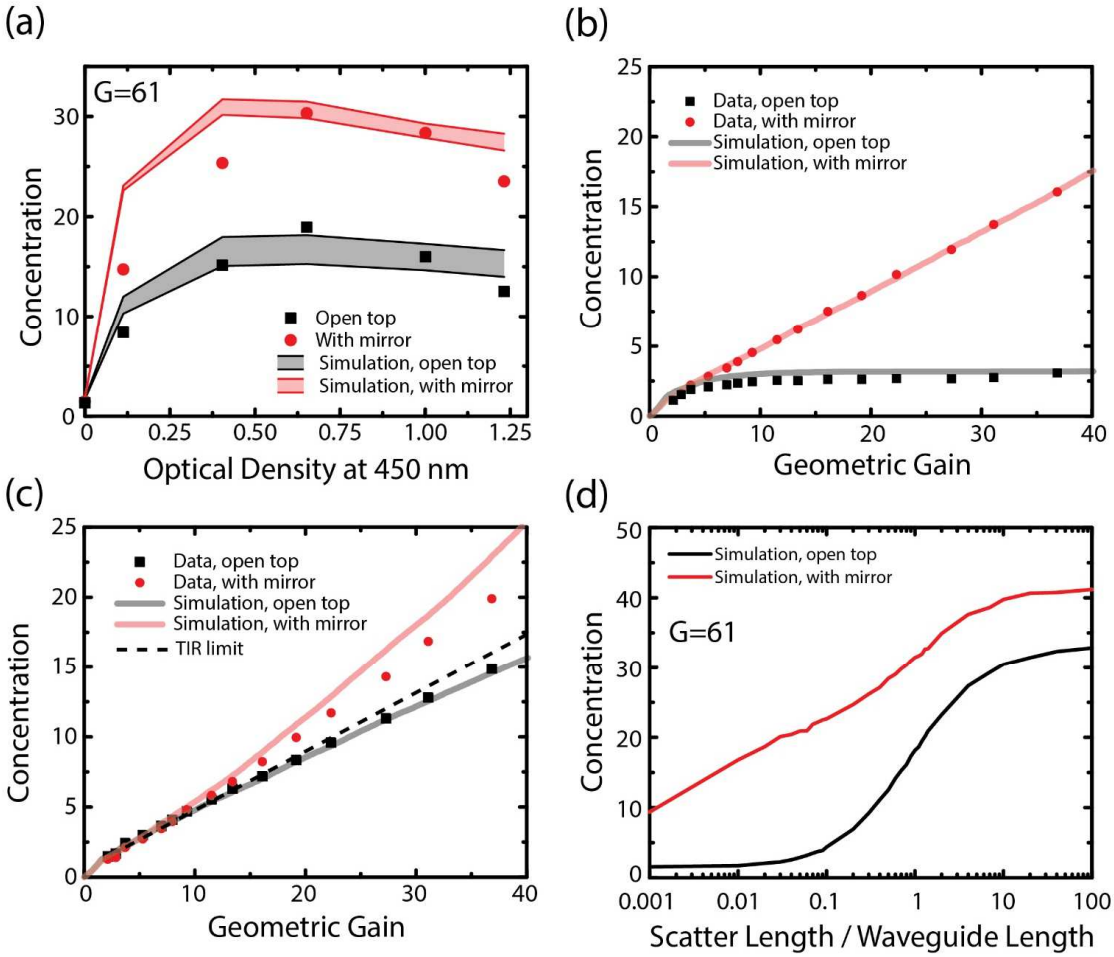

Figure 5.4 (a) Experimental and simulated photon concentration ratios at different optical densities of QD, with Geometric Gain (G) of 61. The range of simulation results represent the best-fit range of scattering lengths, from 2.1 mm to 3.0 mm. Luminescence propagation data and simulation for (b) the highly scattering sample (with a scattering length of 0.18 mm) and (c) the record device (with a scattering length of 3 mm) compared to the limit imposed by total internal reflection (TIR); (d) Simulated effects of scattering length on concentration with and without a luminescence-trapping mirror, with G=61.

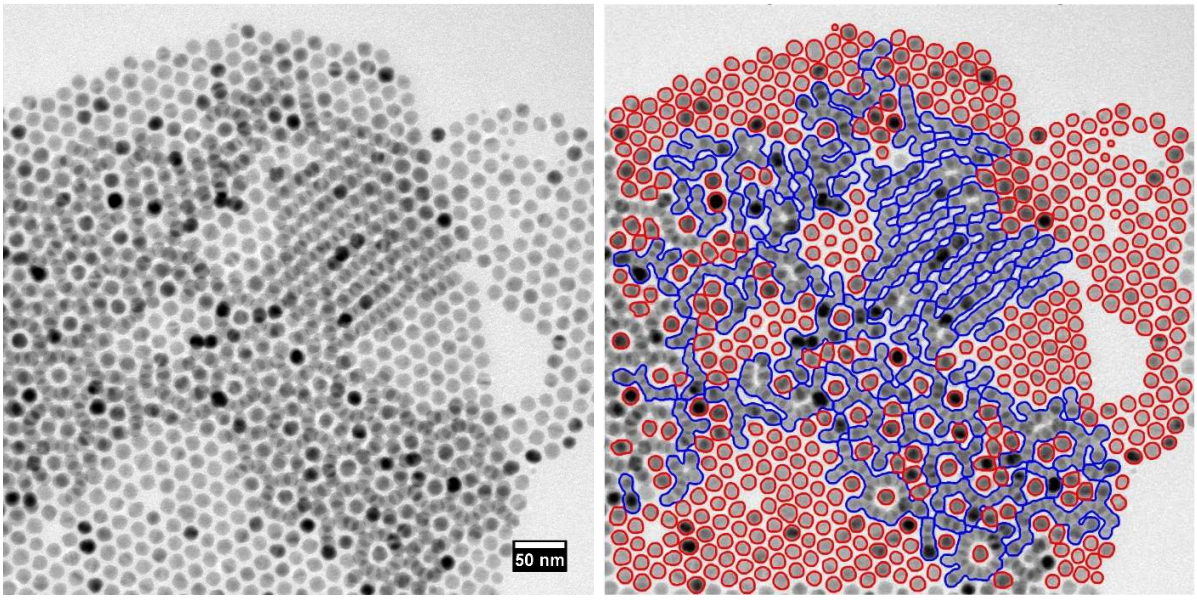

Figure 5.5 Representative TEM micrograph of quantum dots with automatically detected particle outlines. Red outlines pass the circularity and roundness criteria, and blue outlines fail, allowing the algorithm to distinguish between isolated particles and multiple overlapping particles.

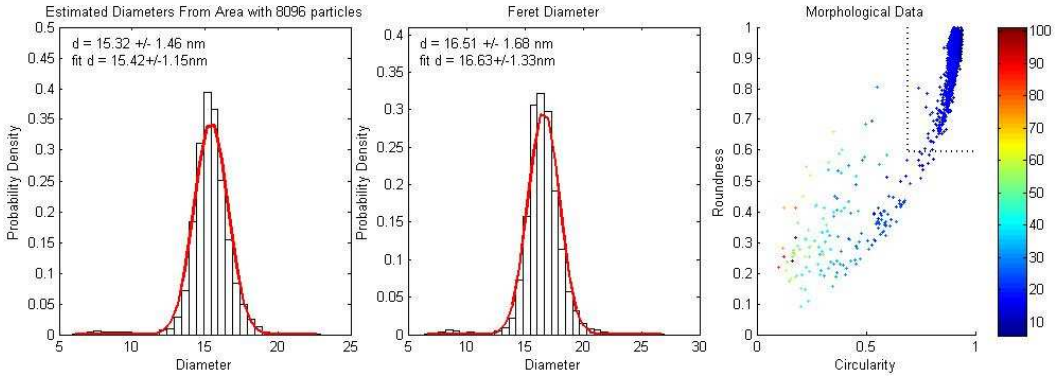

Figure 5.6 Automatically detected histograms of diameter estimated from area and Feret diameter for the sample shown in Figure 5.5. In the third plot, the roundness and circularity of each particle is plotted as a dot with the color of the dot indicating the diameter. The dashed black line indicates the circularity and roundness cutoffs.

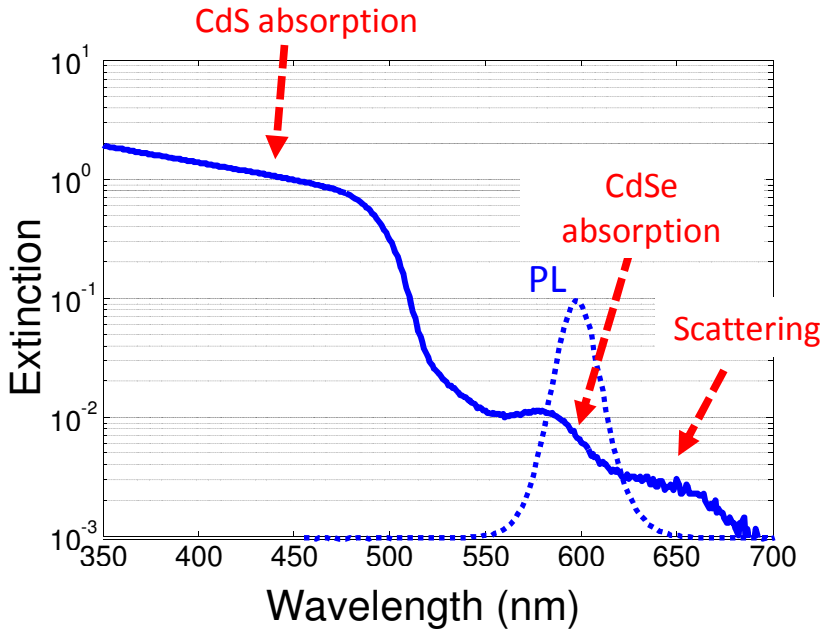

Figure 5.7 Measurement of the extinction spectrum for a CdSe/CdS core/shell quantum dots with a large CdS shell thickness. Three different parts of the spectrum are visible: the absorption in the CdS shell, the absorption in the CdSe core, and the scattering below the CdSe bandgap.

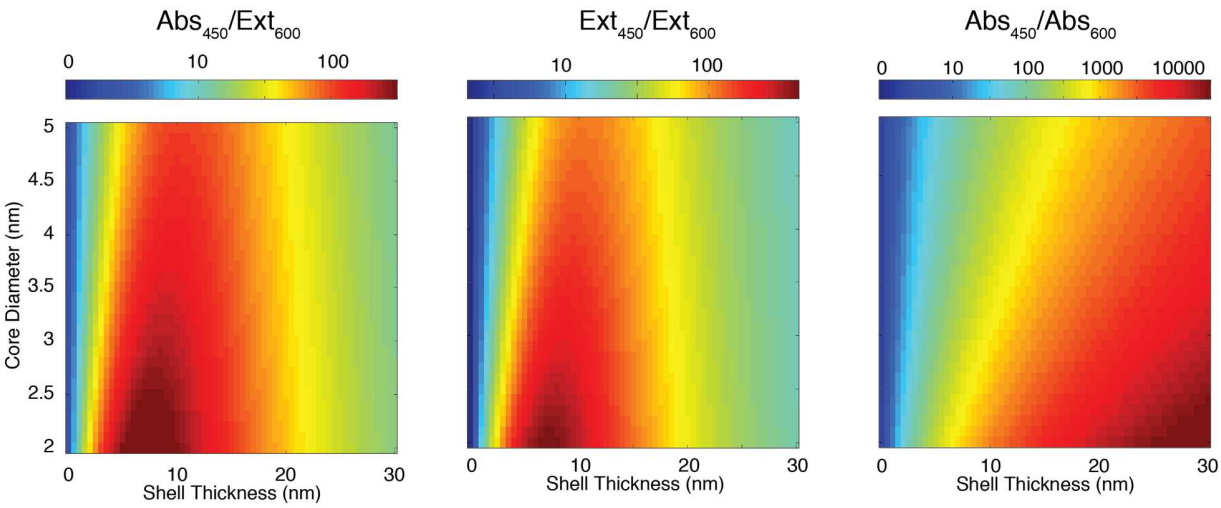

Figure 5.8 Simulated ratio of extinction or absorption at 450 nm and 600 nm wavelengths for CdSe/CdS core/shell particles. The shell thickness is the component of the radius corresponding to CdS material.

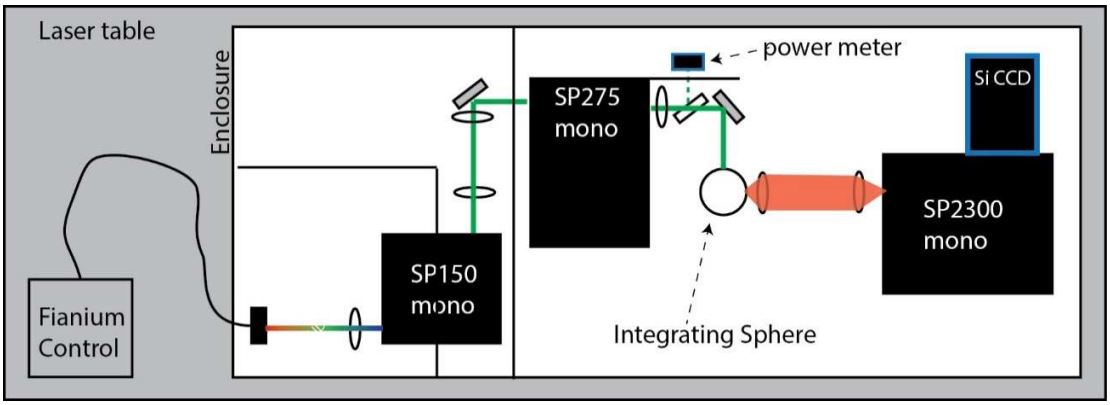

Figure 5.9 Schematic of the integrating-sphere luminescent spectrometer.

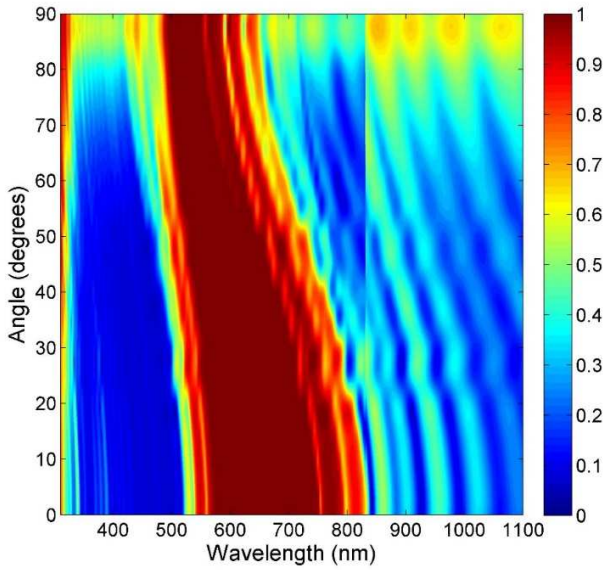

Figure 5.10 Measured reflectivity as a function of angle and wavelength for the photonic mirrors used in this study.

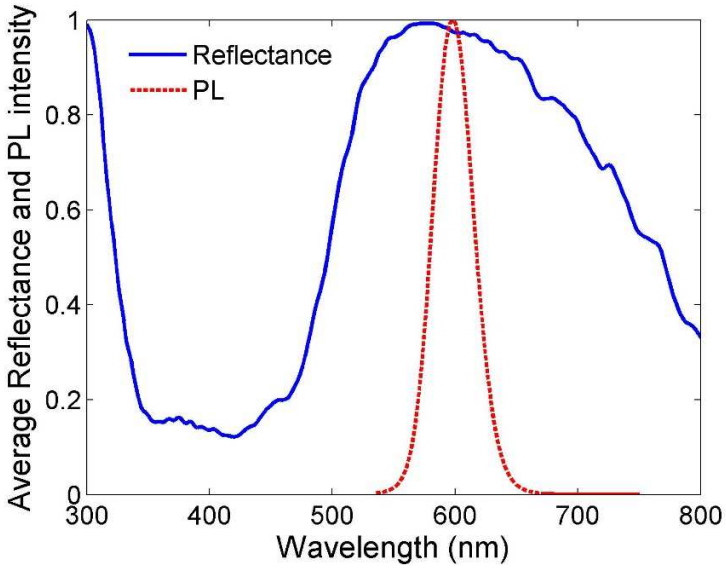

Figure 5.11 Angle-averaged reflectance and a representative luminescence spectrum. The integral of the product of these two spectra yields the total average reflectivity.

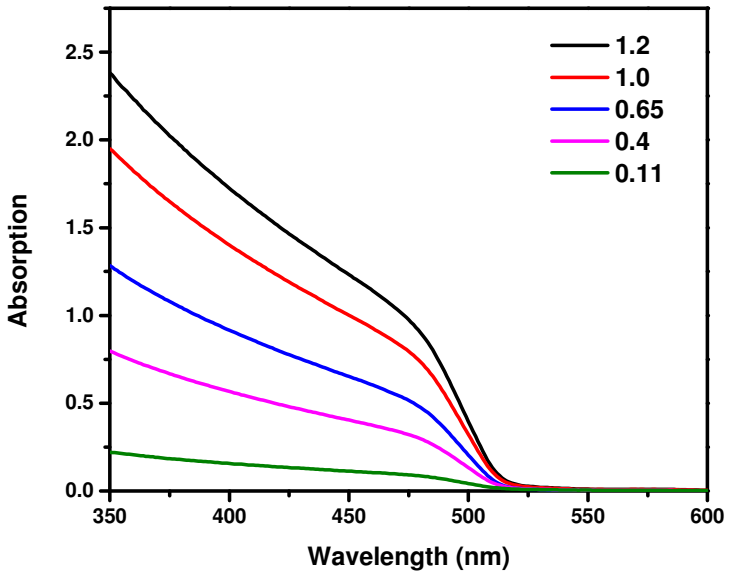

Figure 5.12 Absorption spectra of QD-PLMA film sample with different optical density.

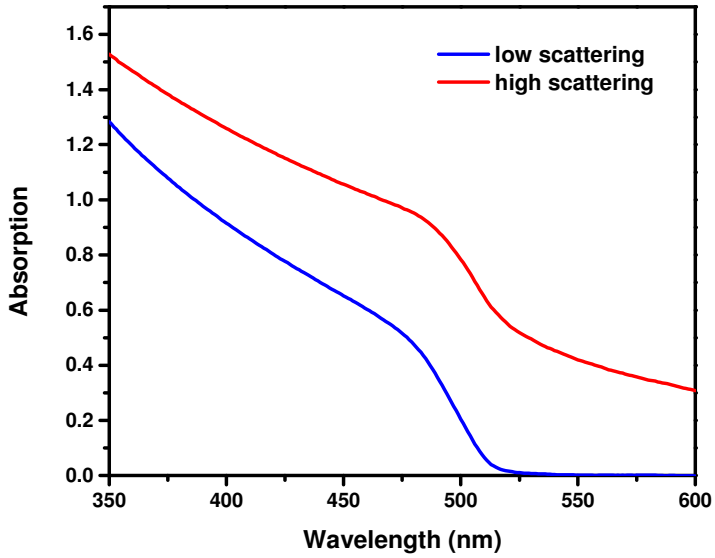

Figure 5.13 Absorption spectra of the high scattering and low scattering sample.

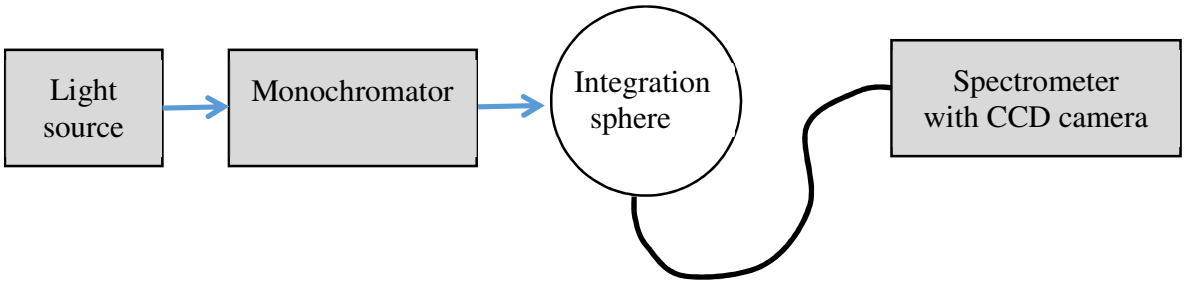

Figure 5.14 Schematic of the custom setup for measuring film QY and trapping efficiency.

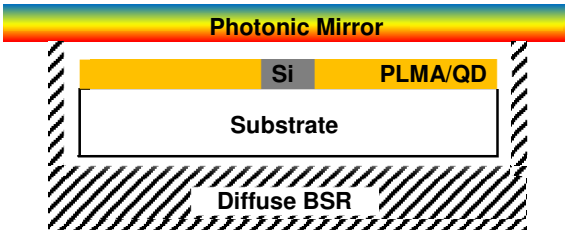

Figure 5.15 Cross-sectional illustration of the luminescent concentrator cavity.

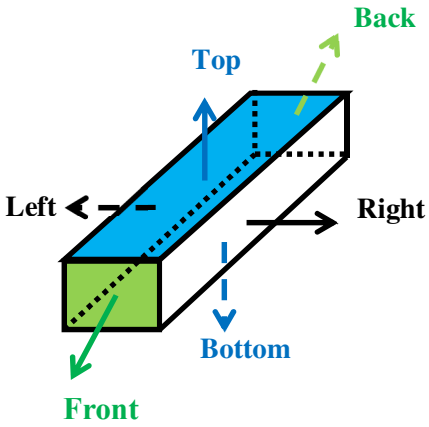

Figure 5.16 Illustration showing different surfaces of the microcell detector

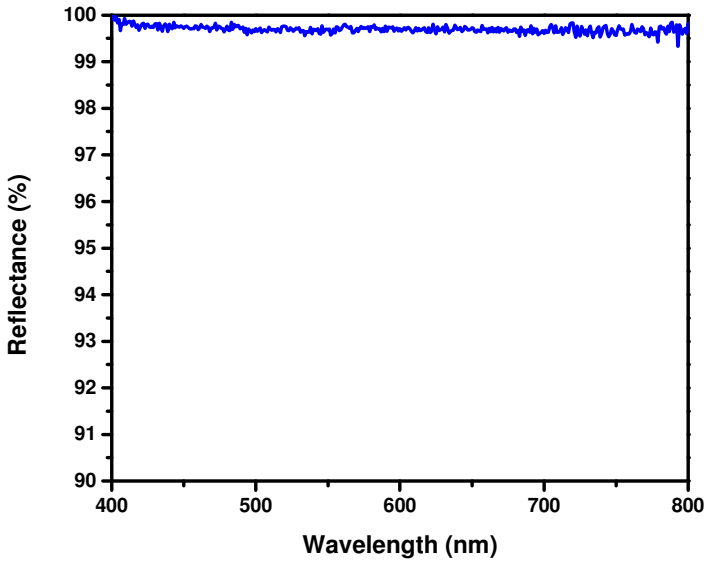

Figure 5.17 Reflectance of the trench diffuse reflector.

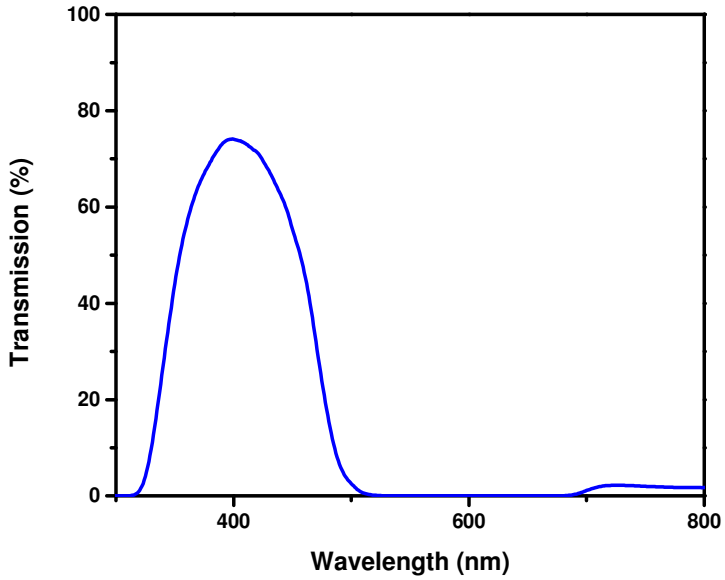

Figure 5.18 Transmission spectrum of blue band-pass filter.

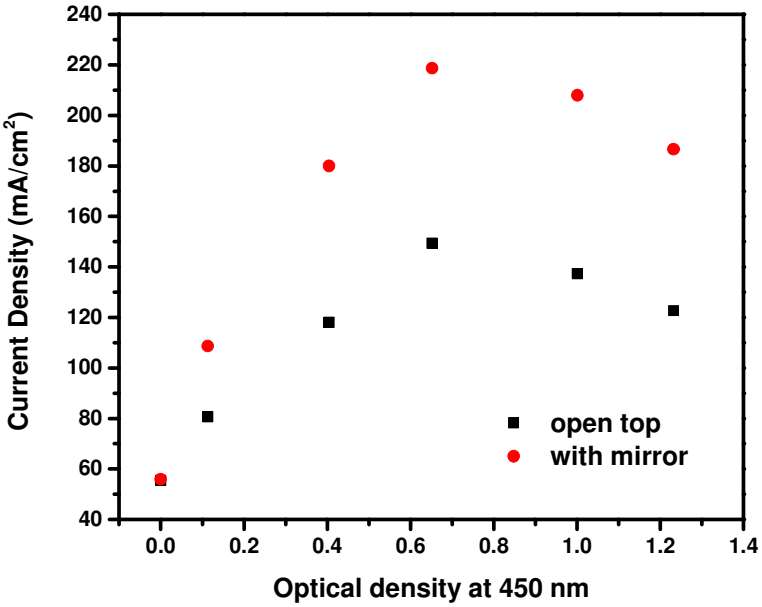

Figure 5.19 Photocurrent density of the LSC devices under full AM1.5 G solar spectrum.

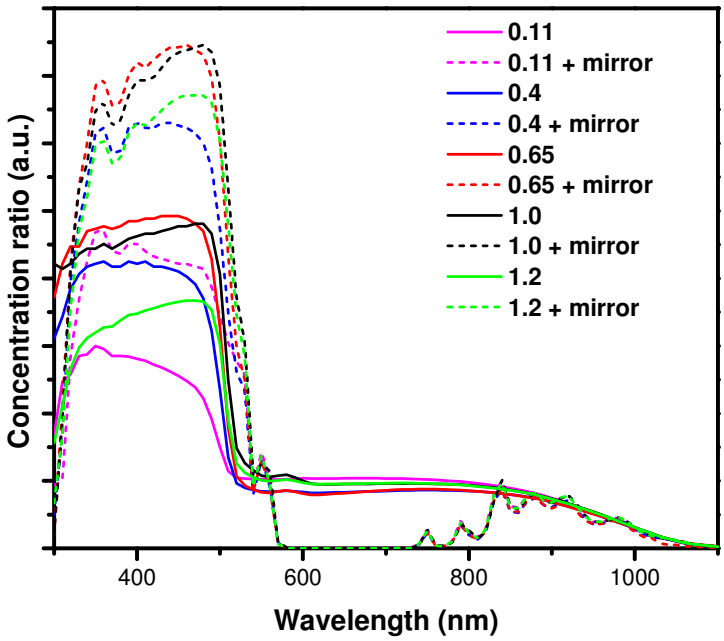

Figure 5.20 Concentration ratio of the LSC device as a function of incident wavelength.

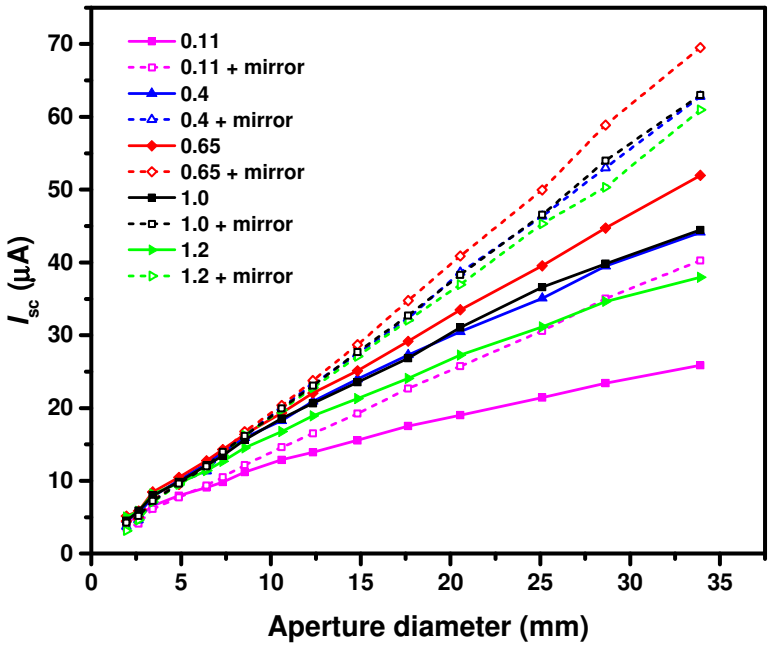

Figure 5.21 Photocurrent of the LSC device under the blue filtered illumination at various aperture size.

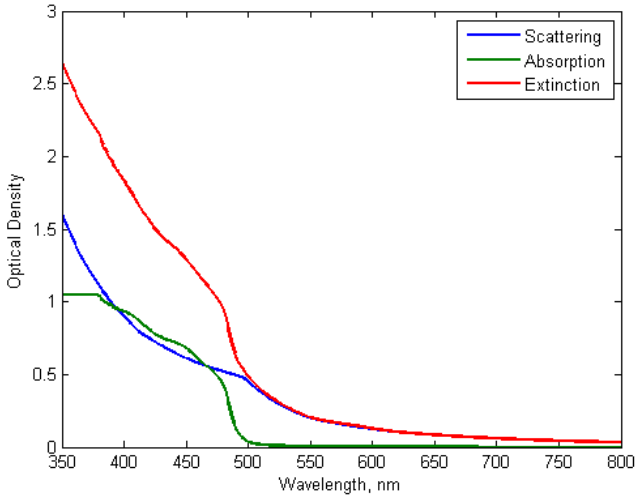

Figure 5.22 Scattering spectrum plotted with absorption spectrum for an example quantum dot sample. The two spectra are summed to make the extinction spectrum.

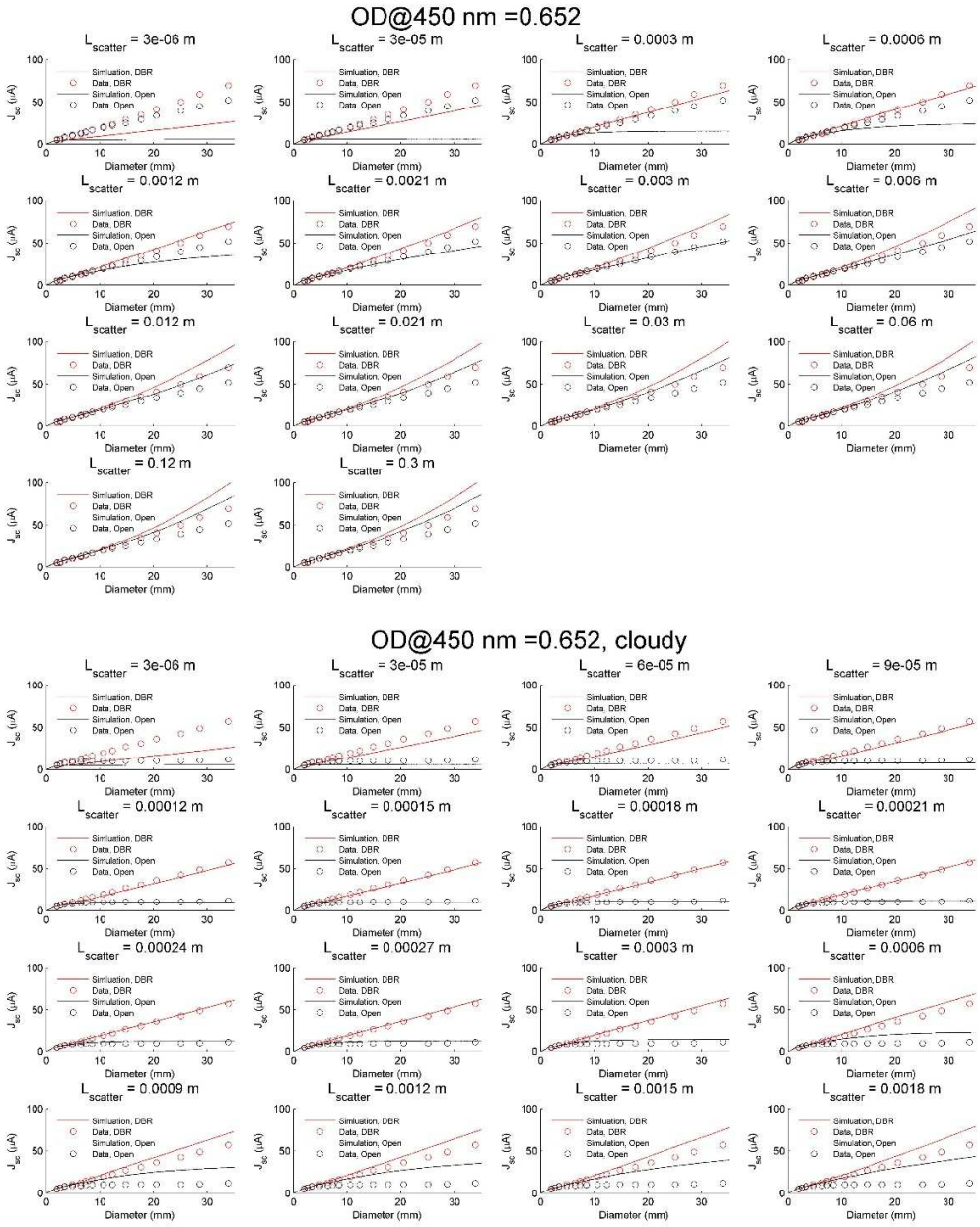

Figure 5.23 Light propagation curves, showing short circuit current (J_{sc}) against aperture diameter for a variable illumination aperture. The two devices simulated above have optical densities of 0.652, but differ in scatter length. The data are shown as open circles, and the lines are the simulated values. Red circles and lines have used the photonic mirror, and the black symbols and lines have an open top.

5.9 Tables

Table 5.1 Summary of PV device performance before and after the integration with the LSC, trench reflector and photonic luminescence-trapping mirror under AM1.5G illumination.

Testing Condition	**J_{SC} (mA/cm^2)**	**Concentration λ = 300-500 nm**	**V_{OC} (V)**	**Fill Factor**	**Power (mW/cm^2)**
μ-Si device	28.51	1	0.504	0.72	10.35
μ-Si device with LSC with trench reflector	149.3	18.9	0.569	0.64	54.37
μ-Si device with LSC with trench reflector with photonic mirror	218.7	30.3	0.580	0.61	77.38

Table 5.2 Comparison of simulated concentration factor on different faces of the solar cell with measured photocurrent ratio.

Device Configuration	Side of micro-cell	Area of the side	Simulated Concentration on each side	Simulated Concentration by photocurrent	Measured Concentration by photocurrent
No DBR	Top	0.15 mm^2	1.00	18.0	18.9
	Bottom	0.15 mm^2	12.8		
	Left, Right	0.045 mm^2 each	21.3		
	Front, Back	0.003 mm^2 each	21.9		
With DBR	Top	0.15 mm^2	7.7	31.7	30.3
	Bottom	0.15 mm^2	21.4		
	Left, Right	0.045 mm^2 each	28.5		
	Front, Back	0.003 mm^2 each	28.5		

5.10 References

[1] Batchelder, J. S.; Zewail, A. H.; Cole, T. Luminescent Solar Concentrators. 1: Theory of Operation and Techniques for Performance Evaluation. *Appl. Opt.* **1979**, *18*, 3090.

[2] Batchelder, J. S.; Zewail, A. H.; Cole, T. Luminescent Solar Concentrators. 2: Experimental and Theoretical Analysis of Their Possible Efficiencies. *Appl. Opt.* **1981**, *20*, 3733.

[3] Goetzberger, A.; Greube, W. Applied Physics Solar Energy Conversion with Fluorescent Collectors. *Appl. Phys.* **1977**, *14*, 123.

[4] Weber, W. H.; Lambe, J. Luminescent Greenhouse Collector for Solar Radiation. *Appl. Opt.* **1976**, *15*, 3.

[5] Debije, M. G.; Verbunt, P. P. C. Thirty Years of Luminescent Solar Concentrator Research: Solar Energy for the Built Environment. *Adv. Energy Mater.* **2012**, *2*, 12-35.

[6] Goldschmidt, J. C.; Peters, M.; Gutmann, J.; Steidl, L.; Zentel, R.; Bläsi, B.; Hermle, M.; Chemie, O.; Mainz, U. Increasing Fluorescent Concentrator Light Collection Efficiency by Restricting the Angular Emission Characteristic of the Incorporated Luminescent Material - the "Nano-Fluko" Concept. *Proc. SPIE* **2010**, *7725*, 77250.

[7] Bradshaw, L. R.; Knowles, K. E.; McDowall, S.; Gamelin, D. R. Nanocrystals for Luminescent Solar Concentrators. *Nano Lett.* **2015**, *15*, 1315.

[8] Chatten, A. J.; Barnham, K. W. J.; Buxton, B. F.; Ekins-Daukes, N. J.; Malik, M. A. Quantum Dot Solar Concentrators. *Semiconductors* **2004**, *38*, 909.

[9] Debije, M. G.; Teunissen, J. P.; Kastelijn, M. J.; Verbunt, P. P. C.; Bastiaansen, C. W. M. The Effect of a Scattering Layer on the Edge Output of a Luminescent Solar Concentrator. *Sol. Energy Mater. Sol. Cells* **2009**, *93*, 1345.

[10] Debije, M. G.; Van, M.-P.; Verbunt, P. P. C.; Kastelijn, M. J.; van der Blom, R. H. L.; Broer, D. J.; Bastiaansen, C. W. M. Effect on the output of a luminescent solar concentrator on application of organic wavelength-selective mirrors. *Appl. Opt.* **2010**, *49*, 745-751.

[11] Krumer, Z.; Pera, S. J.; van Dijk-Moes, R. J. A.; Zhao, Y.; de Brouwer, A. F. P.; Groeneveld, E.; Van Sark, W. G. J. H. M.; Schropp, R. E. I.; de Mello Donegá, C. Tackling Self-Absorption in Luminescent Solar Concentrators with Type-II Colloidal Quantum Dots. *Sol. Energy Mater. Sol. Cells* **2013**, *111*, 57.

[12] Roncali, J.; Garnier, F. Photon-Transport Properties of Luminescent Solar Concentrators: Analysis and Optimization. *Appl. Opt.* **1984**, *23*, 2809.
[13] Bomm, J.; Büchtemann, A.; Chatten, A. J.; Bose, R.; Farrell, D. J.; Chan, N. L. A.; Xiao, Y.; Slooff, L. H.; Meyer, T.; Meyer, A. Fabrication and Full Characterization of State-of-the-Art Quantum Dot Luminescent Solar Concentrators. *Sol. Energy Mater. Sol. Cells* **2011**, *95*, 2087.
[14] Van Sark, W. G. J. H. M.; Barnham, K. W. J.; Slooff, L. H.; Chatten, A. J.; Büchtemann, A.; Meyer, A.; McCormack, S. J.; Koole, R.; Farrell, D. J.; Bose, R. Luminescent Solar Concentrators--a Review of Recent Results. *Opt. Express* **2008**, *16*, 21773.
[15] Giebink, N. C.; Wiederrecht, G. P.; Wasielewski, M. R. Resonance-Shifting to Circumvent Reabsorption Loss in Luminescent Solar Concentrators. *Nat. Photonics* **2011**, *5*, 694.
[16] Roncali, J.; Garnier, F. New Luminescent Back Reflectors for the Improvement of the Spectral Response and Efficiency of Luminescent Solar Concentrators. *Sol. Cells* **1984**, *13*, 133.
[17] Yablonovitch, E. Thermodynamics of the fluorescent planar concentrator. *J. Opt. Soc. Am.* **1980**, *70*, 1362-1363.
[18] Smestad, G.; Ries, H.; Winston, R.; Yablonovitch, E. The Thermodynamic Limits of Light Concentrators. *Sol. Energy Mater.* **1990**, *21*, 99.
[19] Ries, H.; Smestad, G. P.; Winston, R. Thermodynamics of Light Concentrators. *Proc. SPIE* **1991**, *1528*, 7.
[20] Wurfel, P. *Physics of Solar Cells*, 2009.
[21] Bronstein, N. D.; Li, L.; Xu, L.; Yao, Y.; Ferry, V. E.; Alivisatos, A. P.; Nuzzo, R. G. Luminescent Solar Concentration with Semiconductor Nanorods and Transfer-Printed Micro-Silicon Solar Cells. *ACS Nano* **2014**, *8*, 44-53.
[22] Meinardi, F.; Colombo, A.; Velizhanin, K. A.; Simonutti, R.; Lorenzon, M.; Beverina, L.; Viswanatha, R.; Klimov, V. I.; Brovelli, S. Large-Area Luminescent Solar Concentrators Based on "Stokes-Shift-Engineered" Nanocrystals in a Mass-Polymerized PMMA Matrix. *Nat. Photonics* **2014**, *8*, 392.
[23] Coropceanu, I.; Bawendi, M. G. Core/shell Quantum Dot Based Luminescent Solar Concentrators with Reduced Reabsorption and Enhanced Efficiency. *Nano Lett.* **2014**, *14*, 4097.
[24] Rau, U.; Einsele, F.; Glaeser, G. C. Efficiency Limits of Photovoltaic Fluorescent Collectors. *Appl. Phys. Lett.* **2005**, *87*, 1.

[25] Slooff, L. H.; Burgers, A. R.; Debije, M. G. Reduction of Escape Cone Losses in Luminescent Solar Concentrators with Cholesteric Mirrors. *Proc. SPIE* **2008**, *7043*, 704306.
[26] Bohren, C. F.; Huffman, D. R. *Absorption and Scattering of Light by Small Particles*, 1983.
[27] Palik, E. D. *Handbook of Optical Constants of Solids*, 1997.
[28] Jasieniak, J.; Smith, L.; van Embden, J.; Mulvaney, P. Re-Examination of the Size-Dependent Absorption Properties of CdSe Quantum Dots. *J. Phys. Chem. C* **2009**, *113*, 19468.
[29] Ninomiya, S.; Adachi, S. Optical Properties of Wurtzite. *J. Appl. Phys.* **1995**, *78*, 1183.
[30] Moreels, I.; Allan, G.; De Geyter, B.; Wirtz, L.; Delerue, C.; Hens, Z. Dielectric Function of Colloidal Lead Chalcogenide Quantum Dots Obtained by a Kramers-Krönig Analysis of the Absorbance Spectrum. *Phys. Rev. B: Condens. Matter Mater. Phys.* **2010**, *81*, 235319.
[31] Yao, Y.; Brueckner, E.; Li, L.; Nuzzo, R. Fabrication and assembly of ultrathin high-efficiency silicon solar microcells integrating electrical passivation and anti-reflection coatings. *Energy Environ. Sci.* **2013**, *6*, 3071-3079.
[32] Yoon, J.; Baca, A. J.; Park, S.-I.; Elvikis, P.; Geddes, J. B.; Li, L.; Kim, R. H.; Xiao, J.; Wang, S.; Kim, T.-H.; Motala, M. J.; Ahn, B. Y.; Duoss, E. B.; Lewis, J. A.; Nuzzo, R. G.; Ferreira, P. M.; Huang, Y.; Rockett, A.; Rogers, J. A. Ultrathin silicon solar microcells for semitransparent, mechanically flexible and microconcentrator module designs. *Nat. Mater.* **2008**, *7*, 907-915.
[33] Yoon, J.; Li, L.; Semichaevsky, A. V.; Ryu, J. H.; Johnson, H. T.; Nuzzo, R. G.; Rogers, J. A. Flexible concentrator photovoltaics based on microscale silicon solar cells embedded in luminescent waveguides. *Nat. Commun.* **2011**, *2*, 343.
[34] Carbone, L.; Nobile, C.; De Giorgi, M.; Sala, F. D.; Morello, G.; Pompa, P.; Hytch, M.; Snoeck, E.; Fiore, A.; Franchini, I. R.; Nadasan, M.; Silvestre, A. F.; Chiodo, L.; Kudera, S.; Cingolani, R.; Krahne, R.; Manna, L. Synthesis and Micrometer-Scale Assembly of Colloidal CdSe/CdS Nanorods Prepared by a Seeded Growth Approach. *Nano Lett.* **2007**, *7*, 2942-2950.
[35] Talapin, D. V.; Nelson, J. H.; Shevchenko, E. V.; Aloni, S.; Sadtler, B.; Alivisatos, A. P. Seeded Growth of Highly Luminescent CdSe/CdS Nanoheterostructures with Rod and Tetrapod Morphologies. *Nano Lett.* **2007**, *7*, 2951-2959.
[36] Chen, O.; Zhao, J.; Chauhan, V. P.; Cui, J.; Wong, C.; Harris, D. K.; Wei, H.; Han, H.-S.; Fukumura, D.; Jain, R. K.; Bawendi, M. G. Compact high-quality CdSe–CdS core–shell

nanocrystals with narrow emission linewidths and suppressed blinking. *Nat. Mater.* **2013**, *12*, 445-451.

Chapter 6 Triple-Layer Tandem Luminescent Solar Concentrator for Microscale Solar Cells with Enhanced Spectrum Coverage and Material Consumption

6.1 Introduction

Luminescent solar concentrators (LSCs) are gaining renewed attention in recent years as a means for harvesting solar radiation by utilizing a fluorescent material (i.e. luminophores) which absorbs sunlight and then emits into lower-energy photons of confined total internal reflection (TIR) modes that are subsequently concentrated onto the attached photovoltaic device.[1-4] LSC could potentially cut down the cost of a photovoltaic system by replacing the active PV materials with large-area, inexpensive polymer/luminophore composites. Compared to geometrical concentrators (GSCs), LSCs operates independent of incidence angles, absorb both direct and diffuse sunlight and eliminate the need of a precise mechanical tracking system.

Single-junction photovoltaic (PV) devices are subjected to performance constrains defined by the Shockey-Quisser limit[5], which is largely associated with limited spectral losses, including the thermalization of the photons above the bandgap and the transmission of those below the bandgap. The same principle applies to LSC devices, where the embedded luminophore typically has an even more limited absorption range compared to semiconductor PV materials, as a fraction of photons above the bandgap also gets transmitted due to the discontinuous band structure in an isolated dye molecule.

This constraint for single-junction devices could be surpassed by splitting the solar spectrum into small energy bands and converting each of these bands separately with a cell of appropriate bandgap.[6] For a conventional PV system, this concept can be realized by using a III-V epitaxy-grown multi-junction device[7] or employing optics that separate portions of the incident solar spectrum and direct them to different spatial locations[6,8]. In the latter case, individual III-V PV cells with matched bandgaps are utilized to circumvent lattice match issues in the epitaxy growth process and the current matching requirement across the epitaxy multi-junction stack. A variety

of optical designs have been proposed, mostly employing either dispersion in optics (e.g. prisms) or wavelength selective reflective surfaces[9] (e.g. dichroic mirrors). Both the epitaxial and optical approaches, however, need to integrate with geometric concentration to boost the device power output and offset the high cost initiated by the expensive III-V PV materials, which inherently restricts their ability to convert the diffuse component of the solar spectrum. For systems using wavelength selective mirrors, there are additional drawbacks as they only perform optimally for illumination within very small dispersion angles.

A multilayer LSC architecture, on the other land, serves as an alternative to effectively split and convert both direct and diffuse solar radiation. As shown by the design illustrated in Figure 6.1, several dyes with suitable bandgaps are combined to expand the spectral coverage of the LSC: the luminophore in each layer acts as a wavelength-selective filter with broad accepting angles, converting both direct and diffuse sunlight within its absorption ranges into TIR modes while transmitting the rest which can then be utilized by the beneath layers. As a result, different portions of the solar spectrum are separated in the same fashion as multi-junction devices while achieving effective optical concentration at the same time. Compared to III-V epitaxy stacks, a tandem LSC achieves both spectral division and concentration within one single element, circumvents the issues related to epitaxy growth and current matching, and holds additional advantages in easy expansion to large areas and replacement of the costly PV active materials with inexpensive polymer/dye composites. A various groups tried to realize this concept through simulations and experiments, however, the experimentally achieved values are pretty limited so far.[10,11]

Recent advent in microscale solar cell fabrication and assembly[12,13] offers new opportunities in developing efficient tandem LSCs. These devices are fabricated from bulk silicon wafers using standard industrial semiconductor processing routes and can be transfer-printed onto secondary substrates with application-specific layouts. The space between these miniature devices can be filled by polymer/dye materials, and the emitted luminescence can be utilized by all the cell surfaces in a 3-D fashion. Their thin geometry offers potential reduction of the photon travelling path and reabsorption losses, and large geometrical gains to achieve high concentration ratio and low material consumption. Here, in this study, we designed and fabricated a microcell based

tandem LSC composed of three dye layers, as illustrated in Figure 6.1. The top layer, doped with a higher bandgap dye, acts as filter for the layer underneath to actively split the incident solar radiation. The originally trapped total internal reflection (TIR) modes remain undisrupted by maintaining an airgap between layers, while the photons lost through the escape cone can be recycled by the adjacent layers via radiative coupling. Experimental results shows that the power output from the system nearly tripled using the same illumination area after stacking three layers to achieve expanded spectrum coverage, as demonstrated by external quantum efficiency measurements. Design strategies to further improve the current design are also discussed.

6.2 Tandem LSC Design

We chose three luminophores for the current design, CdSe/ZnS quantum dots (QDs), two organic dyes, namely 4-dicyanomethylene-2-methyl-6-p-dimethylaminostyryl-4H-pyran (DCM) and 3,3'-Diethyloxadicarbocyanine iodide (DODCI), all of which are incorporated into a polymer matrix (PLMA for QDs and NOA for DCM and DODCI) according to previously reported procedures. The absorption and emission spectra of these polymer/luminophore films are plotted in Figure 6.2(a), while Figure 6.2(b) shows their photoluminescence quantum yields measured in an integration sphere at various excitation wavelengths. The combined absorption of these three luminophores covers a broad spectrum range from 350 to 650 nm: the green QDs absorb the higher energy photons (below 450 nm) and exhibit the highest PLQY (averaged around 60%); the DCM dye with a QY averaged round 50% utilize the photons between 450 and 550 nm; while the DODCI (QY~40%) converts photons between 550 nm and 650 nm.

It is worthy to note that the emission of the QD falls in the absorption range of DCM (same for the emission of DCM and absorption of DODCI), enabling a radiative coupling mechanism between adjacent luminescent films to further boost system efficiency. For a single layer LSC (e.g. doped with DCM, Figure 6.2(c)), it utilizes the incident solar radiation by converting it into TIR modes that eventually reaches the embedded solar cell, with an optical efficiency limited by the fraction of TIR modes in the total dye emission, as determined by the refractive index contrast between the waveguide and air:

$$\eta_{opt} \leq \eta_{TIR} = \sqrt{1 - n^{-2}}$$

For a waveguide with n=1.44 (PLMA/QD), η_{TIR}=0.72. Therefore at least 28% of the absorbed solar energy escaped (i.e. 14% photons or 16.9 μA photocurrent lost from each side of the waveguide). In a tandem LSC stack with multiple dye species, however, these escaped photons from the layer with a higher band gap (e.g. QD) can be coupled into the one with a lower band gap (e.g. DCM), provided that their emission and absorption bands matches, as illustrated by Figure 6.2(d). Experimentally, this effect is quantified by measuring the current output from a DCM LSC device before and after putting a green QD LSC beneath. (In order to isolate the radiative coupling effects, DCM layer is kept above the QD layer to keep the DCM absorption of sunlight identical in both cases; for similar reasons, a non-reflective black backside plate is utilized to allow only single pass of incident illumination.) As shown by results plotted in Figure 6.2(e), with an adjacent QD layer, the current output from the DCM layer increases by 6.3 μA, as it recollects the emission escaped from the topside of the bottom QD layer (The recycling efficiency is 37%, which can be improved on a diffuse reflector where the photons can have a second pass). A similar effect exists between DODCI and DCM, as detailed in Figure 6.5.

Figure 6.2(f) illustrates the triple-layer tandem LSC design, consisting of three separate layers, each includes a waveguide doped with one afore-mentioned luminophore, an embedded silicon solar microcell and a thin glass substrate. (Fabrication details can be found in the Experimental section, see Figure 6.6 for *I-V* curves of each layer measured separately on a non-reflective substrate). The order of the layers is determined by the PLQY and the absorption band of the material in order to place the luminophore that absorbs the higher energy photons and possesses a higher quantum efficiency in the upper layer. The incident solar radiation is then split into different energy bands due to the varied absorption range of each luminophore. An air gap exists between adjacent layers so that the TIR modes remain trapped separately in each waveguide, avoiding parasitic reabsorption among different dye species. The bottom and side of the microcell is utilized to absorb the trapped luminescence, while its top surface can accept the transmitted direct illumination. The emissions from all three layers can be seen in the optical image (Figure 6.2(g)) taken at the edge of the waveguide stack.

6.3 Tandem LSC Performance

These LSC devices are then characterized in both single-layer and tandem layout on a diffuse backside reflector, which enhances the film absorption of incident light. The short-circuit current (I_{sc}) extracted from these measurements are shown in Figure 6.3(a). When measured separately, the current outputs from the silicon solar cells in the QD, DCM and DODCI layer are 107 μA, 139 μA and 138 μA respectively (384 μA in total). These values are 2-3 times higher than the current output from the bare silicon solar cell (40 μA) due to the concentration of luminescent photons onto the device, as evidenced by the results provided by the Monte Carlo Ray tracing model where the spectral distribution of incident photon flux matches well with the dye emission spectra in each layer (Figure 6.3(b)). After stacking the three layers together, the current in each layer decreases slightly due to absorption overlap among dye species and other optical losses including interface reflections. The total current output of the tandem layout (348 μA), retains a 90% of the original current output, while effectively cutting the occupational area of the device by 2/3, which improves both the power-conversion and land-use efficiency of this concentration system. The results from the external quantum efficiency (EQE) measurements (Figure 6.3(c)) offer more insights into this enhancement: the EQE of each layer decreased slightly in a tandem structure (dashed lines) as compared to the one measured in a single layer layout (solid lines), consistent with the I_{sc} results. Among the three dyes, the DCM layer was impacted more severely as a result of the reduction of EQE in the absorption overlap range (300-500 nm) with the top QD layer. The QD, with no shading losses as the top layer and DODCI, whose absorption was well separated from the other two dyes, on the other land, maintain a similar EQE level before and after the stacking process. As shown in Figure 6.3(c), the combined EQE (black solid curve) of the three layers in the tandem layout demonstrates significantly expanded spectrum coverage as compared to the single dye devices.

The photon propagation behavior in each LSC layer was investigated separately by measuring the photo-current under a round aperture that controls the illumination area (Figure 6.3(d)). All three layers demonstrate a similar trend. At smaller aperture diameters (D), the photo-current is contributed by the direct incident illumination on the cell, the scattered photons reflected by the backside diffuse reflector as well as both TIR and non-TIR emissions near the device, leading a

rapid increase of I_{sc} with D. After a certain aperture diameter (~5 mm), the slope of the curve goes down as the contributions from the short-range waveguiding effects (i.e. scattering and non-TIR modes) diminishes. When D>10mm, where only TIR photons can be directed to the cell, the curve becomes quasi-linear, indicating a larger current output can be achieved with a much larger aperture diameter.

A tandem LSC module, composed of fifteen silicon microcells and three dye layers, was constructed and demonstrated by optical images in Figure 6.4(a). Each LSC layer has a five-cell array interconnected in parallel. Their PV characteristics were measured in the tandem layout and plotted in Figure 6.4(b). The total power output of the tandem LSC module reaches 0.491 mW. Considering the silicon devices weighs only 0.157 mg, the power-referenced Si consumption is only 0.32 g/W_p, a value that is significantly lower than that (~10 g/W_p) of commercial Si solar cells. Although costs associated with cell fabrication and module assembly need to be taken into account, the trends illustrate that these lightweight μ-scale devices embedded in a luminescent waveguide offers a potential route to decrease the cost of PV energy by reducing the usage of the most expensive PV active materials components via effective concentration.

6.4 Conclusion

We have demonstrated here a triple-layer luminescent concentrator stack with expanded spectrum coverage and low material consumption, where spectrum splitting and optical concentration is achieved at the same time. In addition, the radiative coupling among adjacent layers provide additional boost to the system efficiency. Several strategies can be utilized to further boost the system performance: (a) Use different III-V solar cells in each layer that matches its emission band to lower the carrier thermalization loss; (b) Develop functional dye species to cover the wavelength above 700 nm; (c) Minimize the spectral overlap between dye species; (d) Optimize the device distribution inside each waveguide to maximize device power output and efficiency;(e) Expand to large areas.

6.5 Experimental

CdSe/CdSe quantum dots were purchased from Sigma-Aldrich. Lauryl methacrylate (LMA) and ethylene glycol dimethacrylate (EGDMA) were purchased from Sigma Aldrich and purified over an inhibitor removing column (Sigma Aldrich product #306312) three times to remove the monomethyl ether of hydroquinone (MEHQ) polymerization inhibitor. LMA and EGDMA were mixed at a 10:1 volume ratio. QD in hexane solution, together with 4% (by volume) trioctylphosphine was added to the mixture and then the solvent was evaporated with a rotovap at room temperature. Photoinitiator Darocur® 1173 (Sigma Aldrich) was added (1% by volume) followed by 1 min sonication before polymerization. 4-dicyanomethylene-2-methyl-6-p-dimethylaminostyryl-4H-pyran (DCM) and DODCI were purchased from Exciton. The dye powders were first dissolved in methyl ethyl ketone and then mixed with polyurethane (NOA 61,Norland Optical Adhesive) followed by vacuum removal of the solvent.

Fabrication and transfer-printing of micro solar cells has been described previously. A coverslip is prepared by spin-coating a 10 μm layer of partially-cured UV-curable adhesive (NOA61 from Norland). The substrate and device were ozone activated for 2 min in a UVOCS T10X19 OES and immediately brought into 3-(Trimethoxysilyl) propyl methacrylate (Sigma Aldrich) vapor under vacuum condition for 1 hour to enhance adhesion between the PLMA and the substrate. Then 30 μm spacer soda lime glass beads (SPI product #2714) were sprinkled onto the edges of the substrate. A 1.5-inch square quartz plate was immersed in repel silane (GE healthcare) solution for 30 min, and then cleaned with IPA and DI water followed by air blow-drying. The treated quartz plate was then secured on top of the printed cell module and spacers by aligning the cell to the center of the quartz plate. For QD-LSC, the QD in monomer solution was capillary-filled into the cavity with the flow parallel to the long axis of the micro-cell under inert atmosphere. The assembly was cured for 40 minutes under UV illumination. For organic dye-LSC, the dye-PU solution was capillary-filled and cured under UV in air. The quartz top-plate was then relieved, leaving the top surface of the micro cell and polymer exposed. The top contact of the device is achieved by screen-printing silver epoxy (E4110, Epoxy Technology) lines and curing at room temperature for over 48 hours.

The film absorption was measured using Varian Cary5G UV-VIS-NIR. The photo-luminescence quantum yield (PLQY) was measured using a custom setup. The light source is an Acton Research Corp 75W xenon lamp with an Opti-Quip 1200 power supply. The monochromater is a Jarrel-Ash M-20, with a slit size set to 0.5 mm. A Labsphere RTC-060-SF integration sphere with a center sample mount is used to collect all transmitted, scattered and emitted light from the sample. The output from the integration sphere is coupled into a 200 μm FT400EMT optical fiber (Thorlabs), then into an Acton Research SpectroPro3001 spectrometer with an Acton Pixis 100 CCD camera. The detection system's spectral response was calibrated with a Labsphere halogen standard light source IRF G3 (NIST traceable). The dark current background collected over a 1 s integration time was recorded. The reference was taken with only the glass substrate in the integration sphere. The sample spectrum was taken by changing the excitation wavelength from 380 nm to 520 nm. The peak area of the transmitted signal was compared with the reference to obtain the amount absorbed and the peak area of the emission signal was compared with the reference to obtain the amount emitted. The ratio between the emitted and absorbed photons was calculated as the apparent PLQY.

Photovoltaic characterization was performed with a Keithley 2400 sourcemeter. The illumination source is an Oriel 91192-1000W solar simulator with AM1.5G filter. External Quantum Efficiency is measured using a Gooch & Housego OL-750 Automated Spectroradiometric System.

6.6 Figures

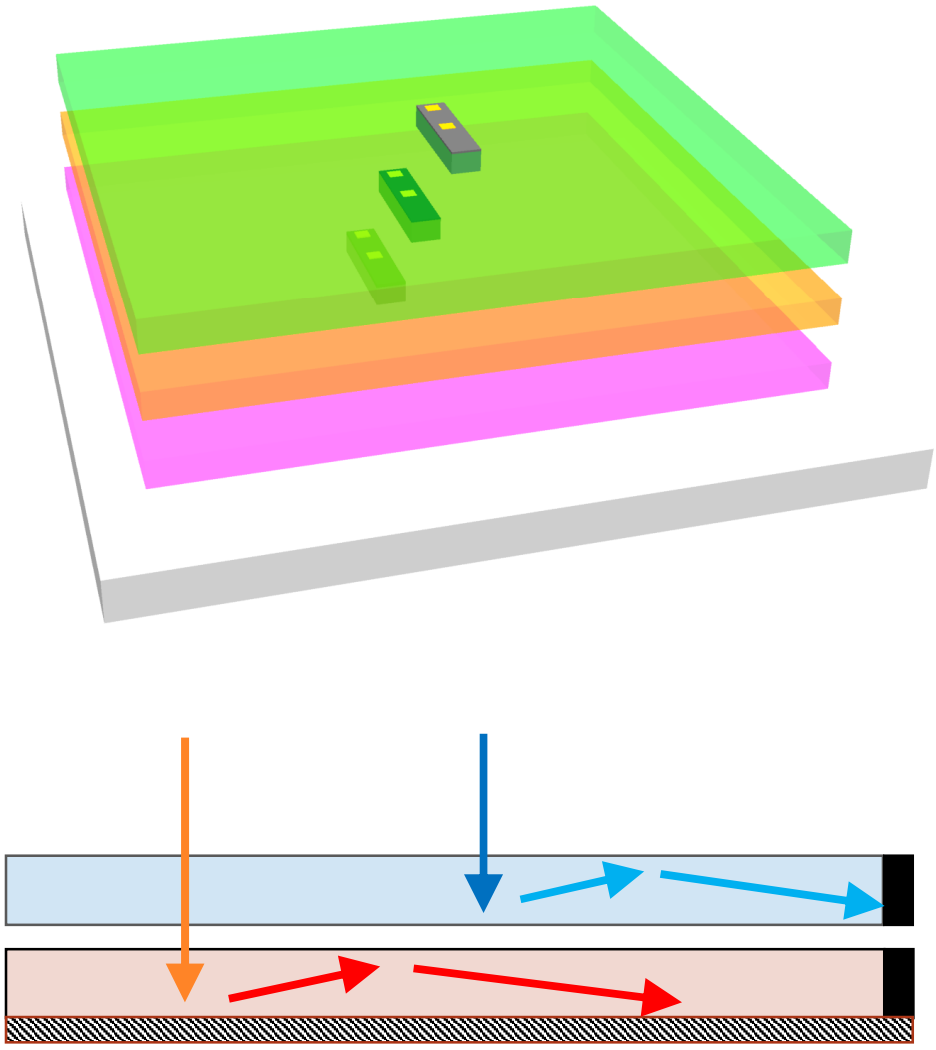

Figure 6.1 3D and cross-sectional illustration of the tandem LSC concept

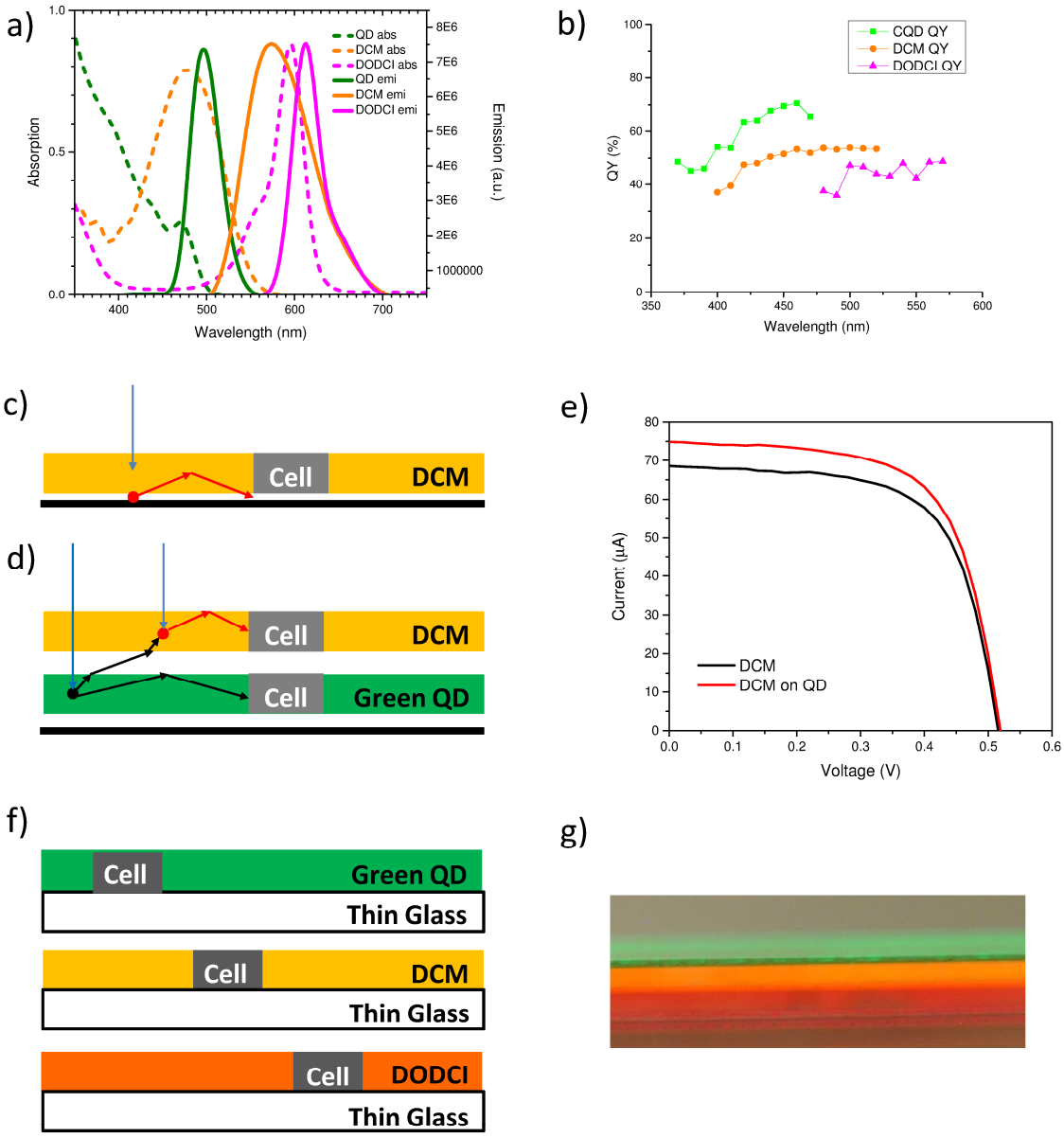

Figure 6.2 (a) Absorption and emission spectra and (b) quantum yield of the luminescent films; (c-e) Illustration and PV measurement results of radiative coupling between adjacent LSC layers; (f) Cross-sectional illustration of the tandem LSC with embedded microcells; (g) Optical images of the edges of the tandem LSC device under illumination with three distinctive emission bands.

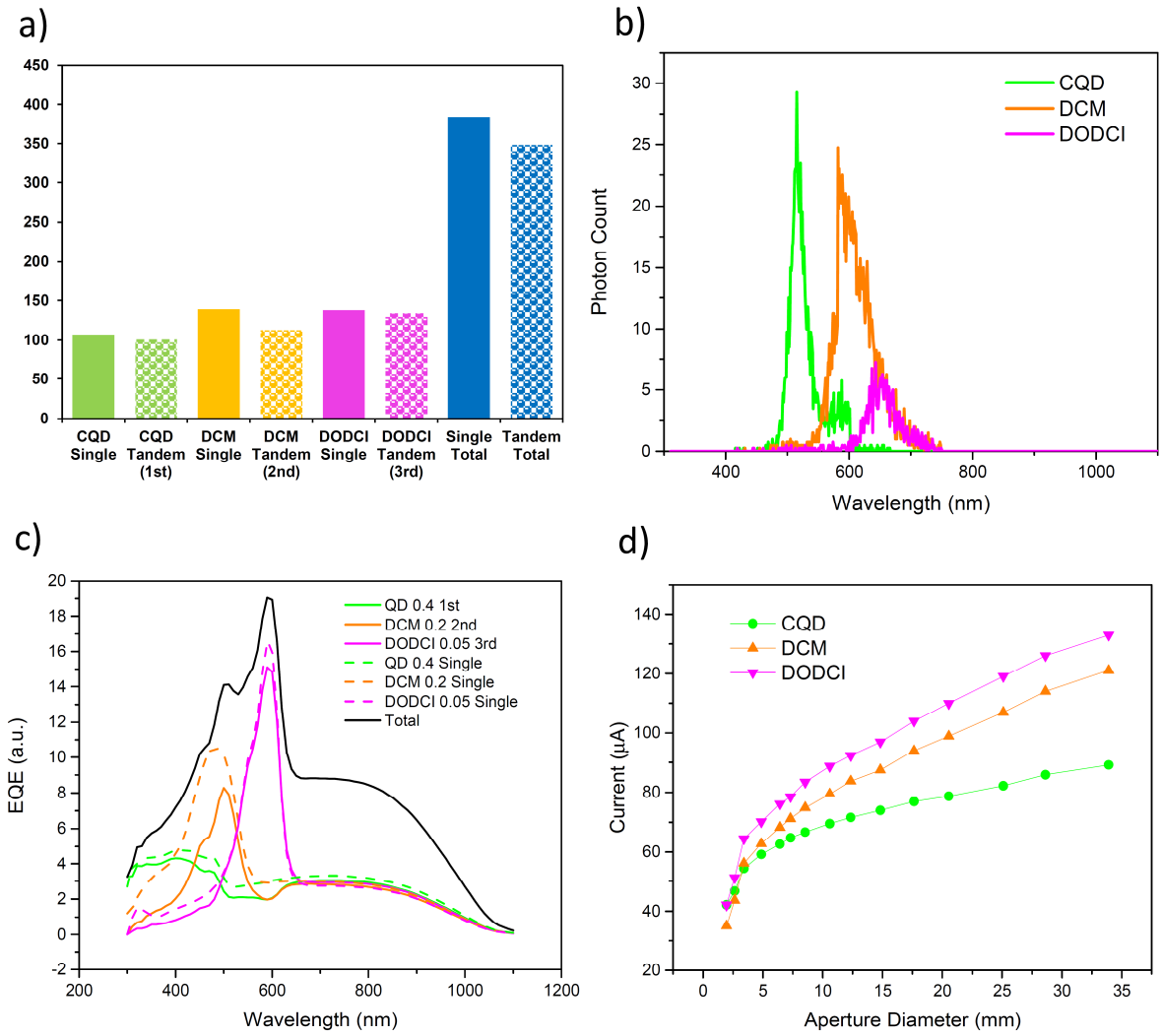

Figure 6.3 (a) Comparison of the current output from a LSC layer that are measured separately and measured in a tandem construct; (b) Simulated photons collected by Si solar microcells in a tandem LSC device; (b) Measured external quantum efficiency of a tandem LSC device; (d) Photo-current output as a function of illumination aperture diameter in each LSC layer.

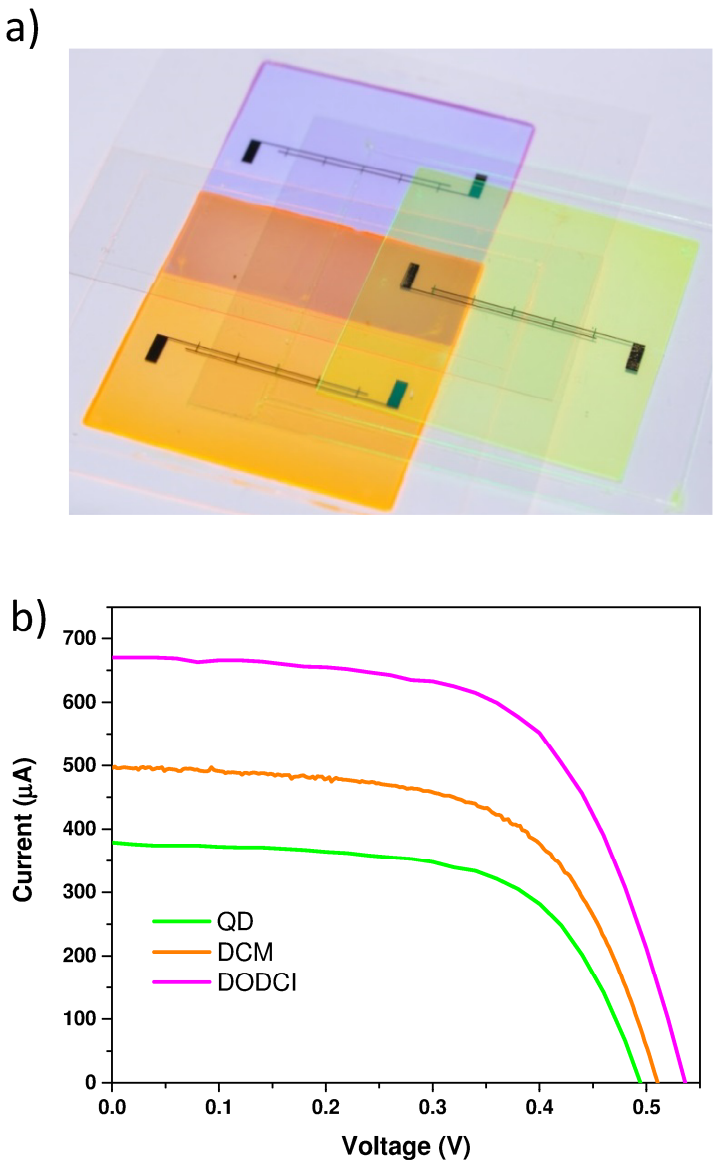

Figure 6.4 (a) Optical image and (b)PV characteristics of a 15-cell tandem LSC module.

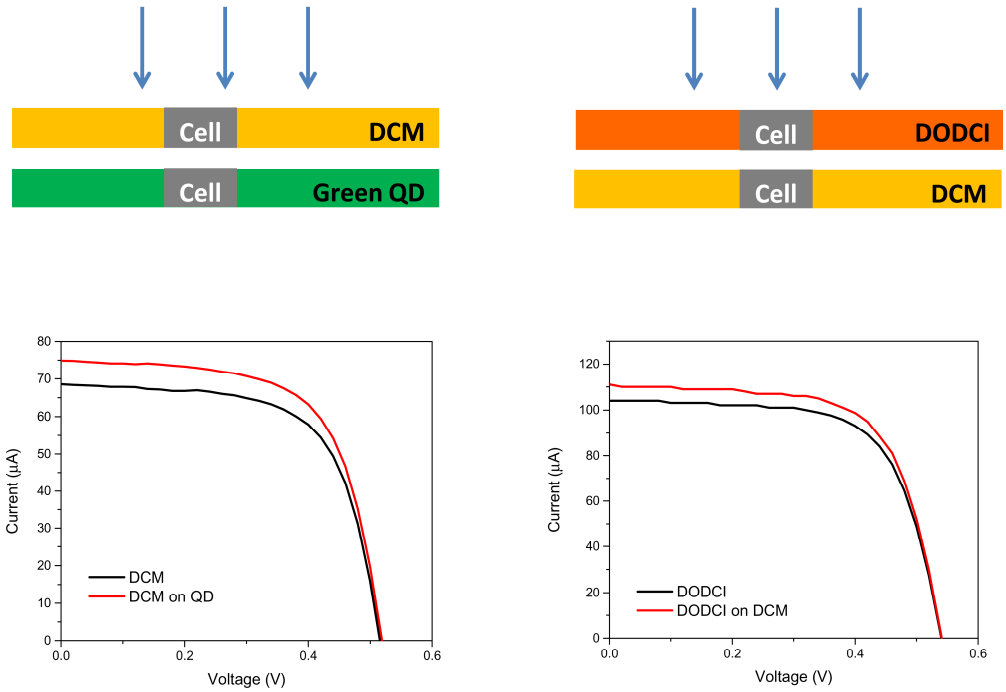

Figure 6.5 Radiative coupling between adjacent LSC layers

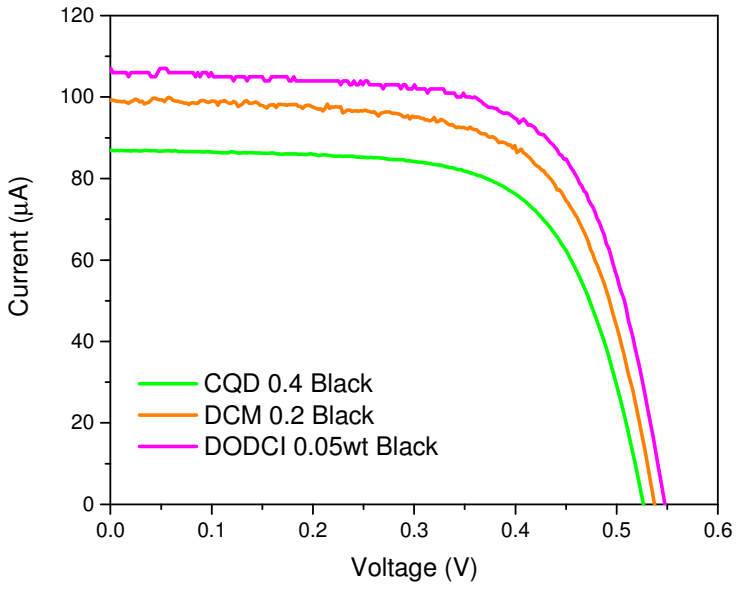

Figure 6.6 *I-V* curves of each LSC layer as measured separately on a non-reflective substrate before being integrated into the tandem LSC design

6.7 References

[1] Weber, W. H.; Lambe, J. Luminescent Greenhouse Collector for Solar Radiation. *Appl. Opt.* **1976**, *15*, 3.

[2] Batchelder, J. S.; Zewail, A. H.; Cole, T. Luminescent Solar Concentrators. 1: Theory of Operation and Techniques for Performance Evaluation. *Appl. Opt.* **1979**, *18*, 3090.

[3] Batchelder, J. S.; Zewail, A. H.; Cole, T. Luminescent Solar Concentrators. 2: Experimental and Theoretical Analysis of Their Possible Efficiencies. *Appl. Opt.* **1981**, *20*, 3733.

[4] Debije, M. G.; Verbunt, P. P. C. Thirty Years of Luminescent Solar Concentrator Research: Solar Energy for the Built Environment. *Adv. Energy Mater.* **2012**, *2*, 12-35.

[5] Shockley, W.; Queisser, H. J. Detailed Balance Limit of Efficiency of p-n Junction Solar Cells. *J. Appl. Phys.* **1961**, *32*, 510-519.

[6] Polman, A.; Atwater, H. A. Photonic design principles for ultrahigh-efficiency photovoltaics. *Nat. Mater.* **2012**, *11*, 174-177.

[7] Cotal, H.; Fetzer, C.; Boisvert, J.; Kinsey, G.; King, R.; Hebert, P.; Yoon, H.; Karam, N. III-V multijunction solar cells for concentrating photovoltaics. *Energy Environ. Sci.* **2009**, *2*, 174-192.

[8] Eisler, C. N.; Abrams, Z. e. R.; Sheldon, M. T.; Zhang, X.; Atwater, H. A. Multijunction solar cell efficiencies: effect of spectral window, optical environment and radiative coupling. *Energy Environ. Sci.* **2014**, *7*, 3600-3605.

[9] Debije, M. G.; Van, M.-P.; Verbunt, P. P. C.; Kastelijn, M. J.; van der Blom, R. H. L.; Broer, D. J.; Bastiaansen, C. W. M. Effect on the output of a luminescent solar concentrator on application of organic wavelength-selective mirrors. *Appl. Opt.* **2010**, *49*, 745-751.

[10] Currie, M. J.; Mapel, J. K.; Heidel, T. D.; Goffri, S.; Baldo, M. A. High-Efficiency Organic Solar Concentrators for Photovoltaics. *Science* **2008**, *321*, 226-228.

[11] Desmet, L.; Ras, A. J. M.; de Boer, D. K. G.; Debije, M. G. Monocrystalline silicon photovoltaic luminescent solar concentrator with 4.2% power conversion efficiency. *Opt. Lett.* **2012**, *37*, 3087-3089.

[12] Yoon, J.; Baca, A. J.; Park, S.-I.; Elvikis, P.; Geddes, J. B.; Li, L.; Kim, R. H.; Xiao, J.; Wang, S.; Kim, T.-H.; Motala, M. J.; Ahn, B. Y.; Duoss, E. B.; Lewis, J. A.; Nuzzo, R. G.; Ferreira, P. M.; Huang, Y.; Rockett, A.; Rogers, J. A. Ultrathin silicon solar microcells for

semitransparent, mechanically flexible and microconcentrator module designs. *Nat. Mater.* **2008**, *7*, 907-915.
[13] Yao, Y.; Brueckner, E.; Li, L.; Nuzzo, R. Fabrication and assembly of ultrathin high-efficiency silicon solar microcells integrating electrical passivation and anti-reflection coatings. *Energy Environ. Sci.* **2013**, *6*, 3071-3079.

Chapter 7 Porous Nanomaterials for Ultrabroadband Omnidirectional Anti-reflection Surfaces with Applications in High Concentration Photovoltaics

7.1 Abstract

Materials for nanoporous coatings have been developed that exploit optimized chemistries and self-assembly processes, with capabilities to reach ~98% transmission efficiency and negligible scattering losses over a broad wavelength range of the solar spectrum from 350 nm to 1.5 μm, on both flat and curved glass substrates. These nanomaterial anti-reflection (nAR) coatings also offer wide acceptance angles, up to ±40°, for both s- and p-polarization states of incident light. Carefully controlled bilayer films have allowed for the fabrication of dual-sided, gradient index profiles on plano-convex lens elements. In concentration photovoltaics (CPV) platforms, the resultant enhancements in the PV efficiencies were ~8%, as defined by experimental measurements on systems that used microscale triple-junction solar cells. These materials and their applications in technologies that require control over interface reflections have the potential for broad utility in imaging systems, photolithography, light-emitting diodes (LEDs) and display technologies.

7.2 Introduction

Recent advances have made concentration photovoltaics (CPV) technology increasingly attractive for utility scale power generation. Such systems incorporate multi-junction (MJ) solar cells that operate on separate spectral bands of the solar radiation to reduce carrier thermalization losses, in which the addition of junctions provides a scalable pathway for increasing the photovoltaic (PV) conversion efficiencies.[1] Geometric optical elements that concentrate rays of direct sunlight onto these MJ cells enhance the materials utilization such that in geographic regions with high direct normal irradiance, the cost of electricity generated by the latest CPV modules can compete with conventional flat-plate PV technologies. Many advances in CPV

technologies follow from the development of epitaxial growth techniques and/or from novel stacking, bonding and mechanical assembly strategies[2-15] to increase the numbers of junctions in the MJ cells. Over the last decade, cell efficiencies have improved at a rate of ~1% per year, to values that are presently ~46.0%, with corresponding module efficiencies of 38.9%.[16] Alternative approaches that use spectrum-splitting techniques and arrays of separate, single-junction cells are also possible.[17,18] Hybrid optical designs at the module level allow utilization of both direct and diffuse solar radiation, thereby further improving the module level efficiencies.[19-22]

In all of these embodiments, Fresnel reflections associated with the concentrating and/or spectrum splitting optics result in optical losses and, by consequence, reductions in performance. For the most advanced commercial CPV modules (Semprius Inc.) in a two-stage optics system (*i.e.*, a primary lens array along with ball lenses, the latter of which enhance the angular acceptance and illumination uniformity), such losses are ~12% due to the presence of three optic/air interfaces.[23] Although reflections at the surfaces of MJ cells can be minimized using standard multilayer coating approaches, reflections at the air/glass interfaces are much more difficult to address technically. The simplest approach relies on a single-layer coating having an index of refraction intermediate between the air and the substrate (*i.e.*, $n_{opt} = \sqrt{n_i \cdot n_s}$ where n_i and n_s are the refractive indices of the incident medium and the substrate, respectively) optimized for operation at a given wavelength by selecting a thickness equal to a quarter of the wavelength evaluated in the coating (*i.e.*, $t = \lambda / 4n_{opt}$). Multilayer coatings increase the wavelength bandwidth for effective operation, as demonstrated on a variety of photovoltaic devices.[24-26] Application of this type of anti-reflection (AR) strategy for optical materials such as glass, with index values ~1.5, is, however, limited by the absence of materials with appropriate indices of refraction (ideal value for a single layer AR coating is $n \approx 1.2$). One solution involves materials with homogeneously distributed nanopores as air voids, to reduce the index of refraction of the medium in an averaged sense. Approaches to realize such porous structures include phase separation and etching processes[27,28], oblique angle deposition[26,29-33], sol-gel techniques[34] and sacrificial organic pore generators (*e.g.*, dendrimers and amphiphilic block copolymers).[35-42] In all cases, the pores must have dimensions significantly smaller than the wavelengths of sunlight

to avoid the detrimental effects of scattering, which can be particularly problematic for CPV applications.[43] An alternative approach relies on conical features of relief with sub-wavelength lateral dimensions, to create an effective spatial gradient in index and an associated smooth optical transition from the air to the substrate. Such textured surfaces can be created on silicon (Si) solar cells using standard etching techniques, with reflection losses typically below 1% across a broad range of the solar spectrum.[44-50] The formation of similar structures on the curved surfaces of glass or polymer optics in CPV technologies is, by comparison, highly challenging.

We describe herein materials approaches to broadband AR coatings that rely on single or dual layers of low index nanoporous spin-on-glasses formed using block copolymers and self-assembly, a process that has been widely studied to create low-k materials for applications in microelectronics.[51] The ability to adjust the index over a wide range, the excellent optical properties and the ease of formation of these coatings on flat and curved surfaces, in single or multilayer geometries, represent key attractive features. Specifically, the material consists of a dielectric matrix with a templating agent—an amphiphilic block copolymer (ABC) that self-assembles into nanospheres— that can be removed in a thermal process that simultaneously transforms the matrix into a silica-like form with dispersed pores that have diameters (~ 12 nm) far below values that could lead to light scattering or other disruptions in the optical path needed for effective concentration.[35,36,38,40,41,52] The molecular weight of the copolymer, and its relative concentration, define the sizes and densities of the pores, thereby providing deterministic control over the index of refraction. Single- and dual-layer coatings of this nanoporous anti-reflection (nAR) silica material have yielded optical performance in quantitative agreement with the modeling. The resulting transmission values exceeded ~98% for wavelengths between 350 nm to 1.5 μm over angular ranges of up to ±40°, which are relevant to the most aggressive concentrating optics used in commercial CPV systems. As a functional demonstration, the application of optimized coatings onto the front and back side surfaces of plano-convex lenses for concentrating light onto microscale triple junction (3J) solar cells has improved the short-circuit current values by 8.2%. The results suggest opportunities not only in PV but also in other photonic and optoelectronic devices, such as light-emitting diodes (LEDs), imaging devices, display components and optical sensors.

7.3 Fabrication of nAR Coatings

The chemistry and processing approaches (Figure 7.1A) followed procedures described previously[38]. Poly(methyl silsesquioxane) (PMSSQ, yellow) served as a matrix dielectric material and poly(styrene-b-2-vinylpyridine) (PS-*b*-P2VP, Mn: PS(7800)-P2VP(10000), red and blue represent PS and P2VP blocks, respectively) acted as a sacrificial templating agent. Upon spin casting and curing a mixture of these two components at elevated temperatures (120 for 3 hrs and 350 °C for 1 hr), the Si-OH groups in the PMSSQ crosslinked to form Si-O-Si bonds, thereby transforming the matrix from hydrophilic to hydrophobic. This process also induced a phase separation of the PS-*b*-P2VP into core-shell nanospheres that exposed the hydrophobic PS block to the PMSSQ matrix, minimizing unfavorable interactions between P2VP and PMSSQ (Figure 7.1A). A pyrolysis step at 400 °C under an inert atmosphere removed the PS-*b*-P2VP (see Figure 7.6 for thermogravimetric analysis data), resulting in an organically modified silica dielectric matrix with spherical pores that had diameters of 12.2±3.0 nm, as shown in the top-view scanning-electron microscopy (SEM) image (Figure 7.1B). The molecular weight of the PS-*b*-P2VP defined the sizes of these pores to values that are much smaller than the wavelengths of terrestrial solar radiation (280~2500 nm). Hence, the nanoporous structure can be effectively regarded as a homogeneous medium with an effective refractive index (n) described by the Maxwell-Garnett model:[38]

$$\frac{n^2-1}{n^2+2} = (1-\Delta p)\frac{n_{\mathrm{MSSQ}}^2 - n_{\mathrm{air}}^2}{n_{\mathrm{MSSQ}}^2 + 2n_{\mathrm{air}}^2} \tag{7.1}$$

where Δp is the porosity of the structure, and n_{MSSQ} and n_{air} represent the refractive indices of the PMSSQ matrix and air, respectively.

The small dimensions of the pores minimized scattering losses, thereby maximizing the amount of direct sunlight that could be effectively focused onto the MJ cells. Simulations (COMSOL, Inc.) can capture the dependence of scattering on dimensions for operation across the solar spectrum, as shown in Figure 7.1C. The scattered field decreased rapidly to negligible levels for pore sizes below 50 nm, in a manner consistent with a reduction proportional to the sixth power

of the size, as expected in the Rayleigh regime (*i.e.*, $x\ (=\frac{\pi d}{\lambda})$ <<1 where d is the diameter of the pore and λ is the wavelength). For sizes comparable to the wavelength of incident light (*i.e.*, d >100 nm), a transition from Rayleigh to Mie scattering occurred with characteristic oscillating behaviors, as solutions to Maxwell's equations in the Mie regime take the form of an infinite series of spherical waves represented by Bessel functions. The total amount of scattering (weighted against the AM 1.5G spectrum) also increased dramatically in this regime, from 0.034% for d = 10 nm to 44.2% for d = 300 nm. For all cases reported here, appropriate choices of the molecular weight of PS-b-P2VP yielded d ~ 12 nm in a very simple, but well-controlled process. Such dimensions in lithographically defined structures, such as those required for sub-wavelength surfaces, would be difficult to achieve.

7.4 Optical Properties of nAR Coatings

The properties of these nanoporous films were examined as coatings on flat substrates, with their refractive indices and thicknesses controlled by PS-*b*-P2VP loading and solution concentration (and spin speed), respectively (Figure 7.7). Figure 7.2A presents a cross-sectional SEM image of a single-layer film (PS-*b*-P2VP loading ~40%, index ~1.2) on a Si wafer. The flatness, uniformity and pore-size distributions of the film have been described elsewhere.[38] Calculations based on the transfer matrix method defined optimal values of the thickness (t) and refractive index (n) for AR performance on a glass substrate across a broad solar spectral range from 350 nm to 1.5μm, corresponding to the operation of a typical 3J solar cell. Figure 7.2B provides a calculated contour plot of the average transmission (T_{avg}) from 350 nm to 1.5μm as a function of n and t. A value of T_{avg} > 98% can be produced when n = 1.15~1.31 and t = 85~200 nm. By selecting the appropriate PS-*b*-P2VP loading, a film with features within this optimum range (n = 1.24, t = 122 nm), as measured by spectroscopic ellipsometry (VASE, J. A. Woollam Co.) was spin-casted (2000 rpm for 30 seconds) onto a glass substrate in both single-side and double-side configurations. Figure 7.2C shows the transmission spectra measured by a spectrometer (Varian Cary 5G) for a bare, flat glass plate (black) and for glass with an nAR coating on one side (red) and on both sides (blue). The results quantitatively correspond to simulation results conducted by the transfer matrix method (Figure 7.2D). The measurements indicate that the double-sided case

has a transmission (T) of 98.5% at a target wavelength (600 nm, where irradiance peaks in the standard solar spectrum), significantly higher than that of bare glass (T = 91.3%) or of glass with a single-side coating (T = 95.0%). The coated film showed a uniform thickness and index distribution, both of which are within the optimal ranges shown in Figure 7.2B, as mapped by the ellipsometer measurement (Figure 7.8). The spectral range of such single layer nAR coatings is, however, still narrower than that desired for operation of advanced MJ cells. The double-layer nAR coatings described in the following section address this issue.

For the bilayer coatings, transfer matrix calculations were used to determine the optimal values for both the refractive index (n_1 and n_2, denoting the top and bottom layer, respectively) and the thickness (t_1 and t_2) of each layer. Figure 7.3A presents a calculated contour plot of T_{avg} between 350 nm to 1.5 µm as a function of n_1 and n_2, when $t_1 = t_2 =$120 nm. The results indicate that T_{avg} > 99% is possible when n_1 = 1.08~1.22 and n_2 = 1.23~1.39. The thicknesses of the two layers can be optimized for fixed refractive indices (n_1 = 1.15 and n_2 = 1.31), as presented in Figure 7.3B. The optimal ranges were calculated to be t_1 = 100~180 nm and t_2 = 90~160 nm. The formation of a double-layer film (n_1 = 1.12, n_2 = 1.34, t_1 = 108 nm, t_2 = 103 nm) began with the formation of a base layer (with a higher index) using the procedures described above. Exposure to ultraviolet (UV) induced ozone then produced –OH groups that improved the wettability of the film for spin-casting a MSSQ/PS-*b*-P2VP precursor solution to define the top layer. Figure 7.3C provides the measured transmission spectra of such double-layer nAR coated glass samples at normal incidence, with the data exhibiting excellent agreement with simulated transmission data shown in Figure 7.3D. The data obtained from the single-layer nAR coated samples have also been displayed in the same plot as dashed lines. As evidenced by both the simulated and experimental results, a remarkably improved spectral coverage was achieved with the double-layer configuration (measured T_{avg} = 98.2%) as compared to the single-layer one (measured T_{avg} = 96.1%). Such highly efficient transmission over a wide range of wavelengths spanning the solar spectrum is suitable for use with MJ solar cells, as validated in the last section of this paper.

The performance of these nAR coatings across a range of angles of incidence is important to their use on lens surfaces in CPV modules. For instance, for the microlens arrays (f# ≈ 2) used in certain commercial CPV modules (Semprius), sunlight with normal incidence strikes the edges

of the optics at an angle of nearly 40° (see Figure 7.9). For advanced hybrid CPV modules that enable the capture of diffuse light[21], the effective angles of incidence could even exceed this value. Figure 7.4 presents measured and simulated angle-resolved transmission spectra under unpolarized illumination for a flat glass substrate with a double-sided nAR coating in both single-layer (Figure 7.4A and B) and double-layer (Figure 7.4C and D) configurations. The experimental data were taken using an ellipsometer, while the simulations were performed using the finite-element based method (COMSOL Multiphysics software). Figure 7.10 shows the measured angle-dependent transmission of the control sample without nAR coatings. Compared to the single-layer coatings, the double-layer case offered increased angular bandwidth and improved transmission, as expected due to the gradient refractive index profile of the nAR bilayer. For incident angles up to 40º, T_{avg} was ~98% between 350 nm and 1.5 μm for the sample with the double-layer coating. The measured and simulated angle-dependent spectral results for p- and s-polarizations are presented in Figure 7.11 (single layer) and Figure 7.12 (double layer), showing an insensitivity to polarization up to 40º. Such angle- and polarization-insensitive properties of these nAR films arose primarily from very weak optical interference effects due to a small index contrast between the nAR layer and the air/substrate, thereby leading to a broad resonance with a poor quality factor (Q-factor). Although the resonant wavelength shifted slightly towards shorter wavelengths with increasing angle of incidence, a typical observation in many cavity systems, the ample breadth of the resonance minimized these effects. In multilayer AR coatings (e.g. Bragg mirrors), strong optical interference effects can occur at certain wavelengths, resulting in significant variations in performance with angle. In addition to the broad resonance, the randomly distributed pores also promote angle-invariant characteristics as compared to traditional AR schemes that use periodic structures, in which photonic resonances and/or diffraction effects result from the periodic nature of these systems.[45,53]

7.5 nAR Coated Lens and PV Enhancements

Applying nAR coatings to both sides of the primary plano-convex lens surfaces in a CPV measurement set up (see Figure 7.5A) demonstrated their utility in this type of application. The processing used the spin-coating and pyrolysis steps described earlier here, yielding sufficient uniformity in film thickness to maintain the high-transmission performance observed on flat

substrates (see Figure 7.13). Figure 7.5B presents optical images of the samples with (top) and without (bottom) the nAR coating on both sides, clearly showing that the coated lens exhibited notably reduced reflections as compared to the bare lens. The PV performance characteristics measured with a solar microcell 3J (InGaP/GaAs/InGaAsNSb, 1.9eV/1.4eV/1.0eV) under simulated AM 1.5G solar irradiance (the experimental configuration is provided in Figure 7.5A, concentration ratio 50x) shows a relative photo-current enhancement of 6.0% and 8.2% with the single- and double-layer nAR coatings, respectively (Figure 7.5C). Based on the efficiency (35.5%) of the CPV module (1000x) that employs the same type of 3J cells[54], the absolute module efficiency gain is estimated to be 2.9% when applying the double-layer coating on the large-area lens array.

7.6 Conclusion

A low-dielectric-constant AR coating material featuring a nanoporous structure composed of subwavelength pores enabled tunable index of refraction, in single or multilayer coatings, with excellent optical transmission properties and minimal light scattering. The index of refraction can be tuned in the range between 1.1 and 1.4 by control over the sacrificial polymer loading. An AR coating with a double-layer configuration and a gradient refractive index profile (n_1 = 1.12, n_2 = 1.34) on a glass substrate (n = 1.5) led to transmission efficiency higher than 98% over a broad spectral range from 350 nm to 1.5 μm, with high angular performance up to ±40º. Exploiting the double layer AR scheme onto the curved surfaces of the concentrating optics in the CPV technologies led to an 8.2% improvement in the current from the 3J microcells, translating to a nearly 3% enhancement in the absolute CPV module efficiency. This approach has the potential to produce substantial performance enhancements in a wide variety of applications, including light-emitting diodes, solar cells, geometric optics and display components. Future work focuses on the development of low temperature processing procedures as well as fabrication methods (*e.g.*, aerosol spray) that would enable applications onto large area or highly curved surfaces (*e.g.*, ball lens) with high throughput and uniformity.

7.7 Experimental Section

7.7.1 Nanoporous Anti-Reflection Coating Fabrication

The single layer nAR films were prepared by dissolving PS-*b*-P2VP and PMMSQ mixtures in tetrahydrofuran (THF) and spinning onto pre-cleaned substrates (Si wafer, coverslip glass or lens) at 2000 rpm for 30 s, where the film refractive index was controlled by PS-*b*-P2VP loading and the film thickness by solution concentration. The coated substrate was then baked in a tube furnace with flowing N_2 first at 120 ºC for 3 hr, then ramped to 350 ºC for 1 hr, followed by 400 ºC for 3 hrs before slowly cooling down to room temperature. The ramp rate was set to be 1 ºC/min. For double layer coatings, after the fabrication of the bottom layer, the surface was treated with ozone using UVOCS for 2 min before spinning the top layer to ensure proper adhesion. SEM images of the nAR films were obtained on Helios 600i and JEOL 7000F Scanning Electron Microscopes.

7.7.2 Optical Simulations and Characterizations

Optical simulations to explore scattering properties and angular dependence of the nanoporous structure were carried out using finite-element method (FEM) with the commercial COMSOL Multiphysics software. Optimal ranges of the refractive index and the film thickness for single- and double-layer nAR coatings were calculated by using the transfer matrix method.

Spectral transmittance curves at normal incidence were measured by using a spectrometer (Varian Cary 5G). The angle-resolved transmission spectra were obtained by a Focused RC2 spectroscopic ellipsometer (J. A. Woollam Co.). Refractive index and thickness of the nAR layers were determined by using ellipsometers (VASE and Focused RC2, J. A. Woollam Co.).

PV performance of the microscale 3J cell was characterized with a Keithley 2400 sourcemeter. The illumination source was an Oriel 91192-1000W Solar Simulator with an AM1.5G filter

(calibrated to one sun, 100 mW cm^{-2}). The concentrating optic used was an N-BK7 plano-convex lens (LA1102, Thorlabs, D = 30.0 mm, f = 50.0 mm), with or without dual-side nAR coatings. The position of the lens was accurately adjusted by a x-y-z manipulator to ensure proper optical alignment.

7.8 Figures

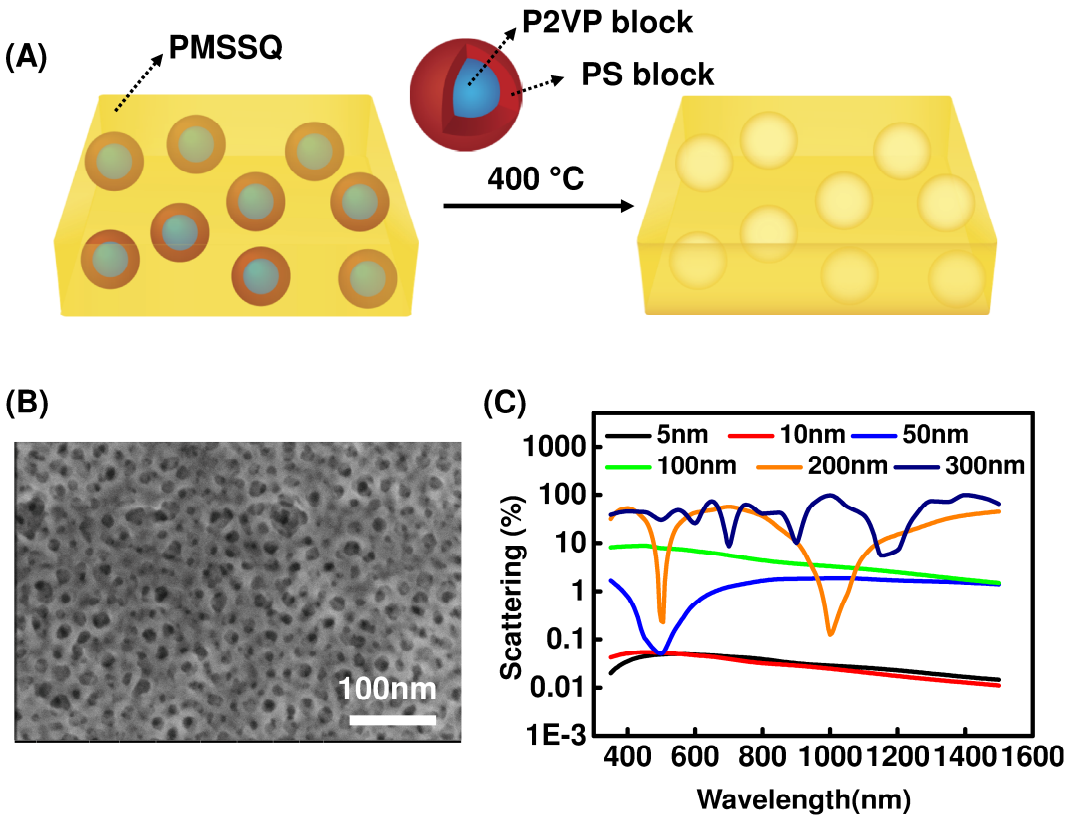

Figure 7.1 (A) Schematic illustration of the formation of nanoporous, organically modified silica films: core (P2VP, blue)-shell (PS, red) polymer spheres were formed in the PMSSQ matrix (yellow) before being removed during a pyrolysis step to create the nanoporous structure. (B) A top-view SEM image of a single-layer nanoporous film. (C) Simulated scattering for light transmission through such films as a function of characteristic pore diameter.

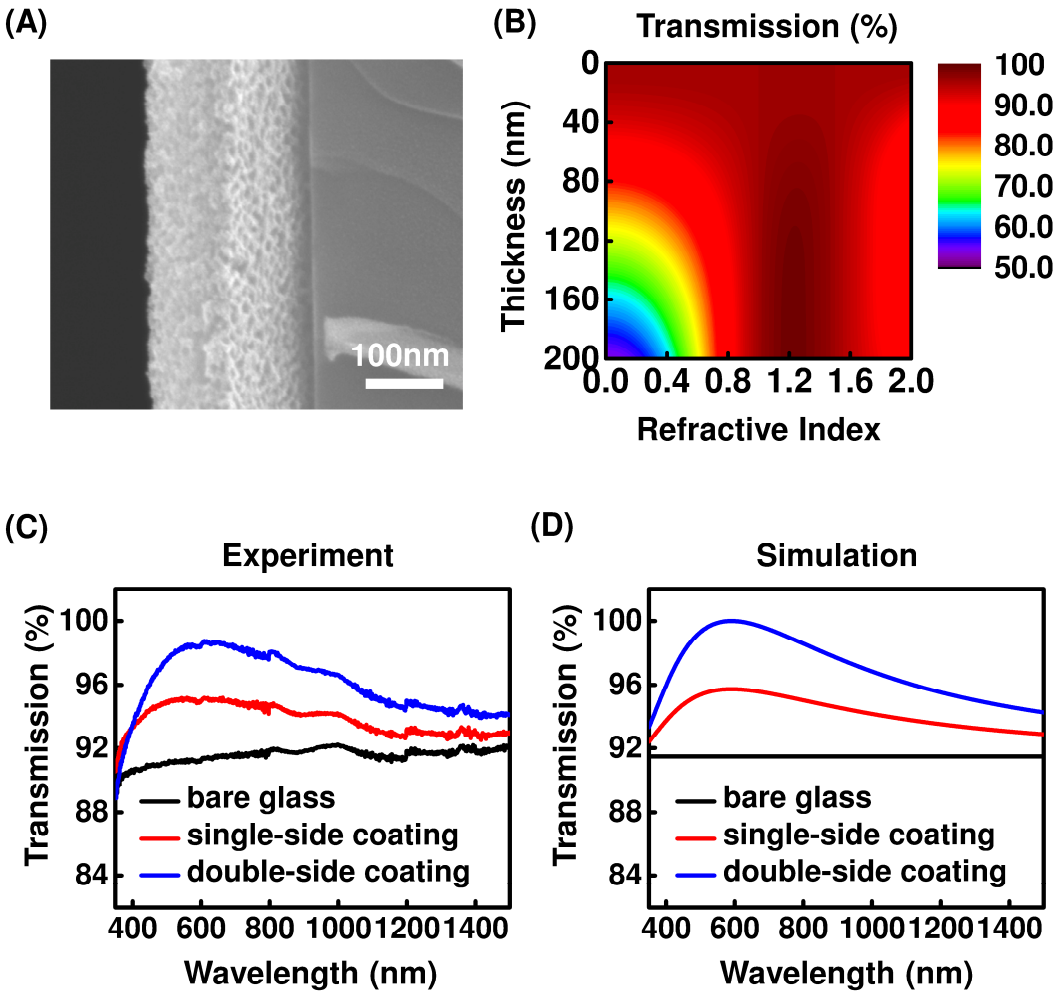

Figure 7.2 (A) Cross-sectional SEM image of the fabricated single-layer nanoporous film. (B) Calculated contour plot of the transmission averaged from 350 nm to 1.5 μm for a single-layer nAR film as a function of the refractive index and the thickness. (C) Measured and (D) simulated transmission spectra of a single-layer nanoporous coating at normal incidence for bare (black), single-side (red) and double-side (blue) cases.

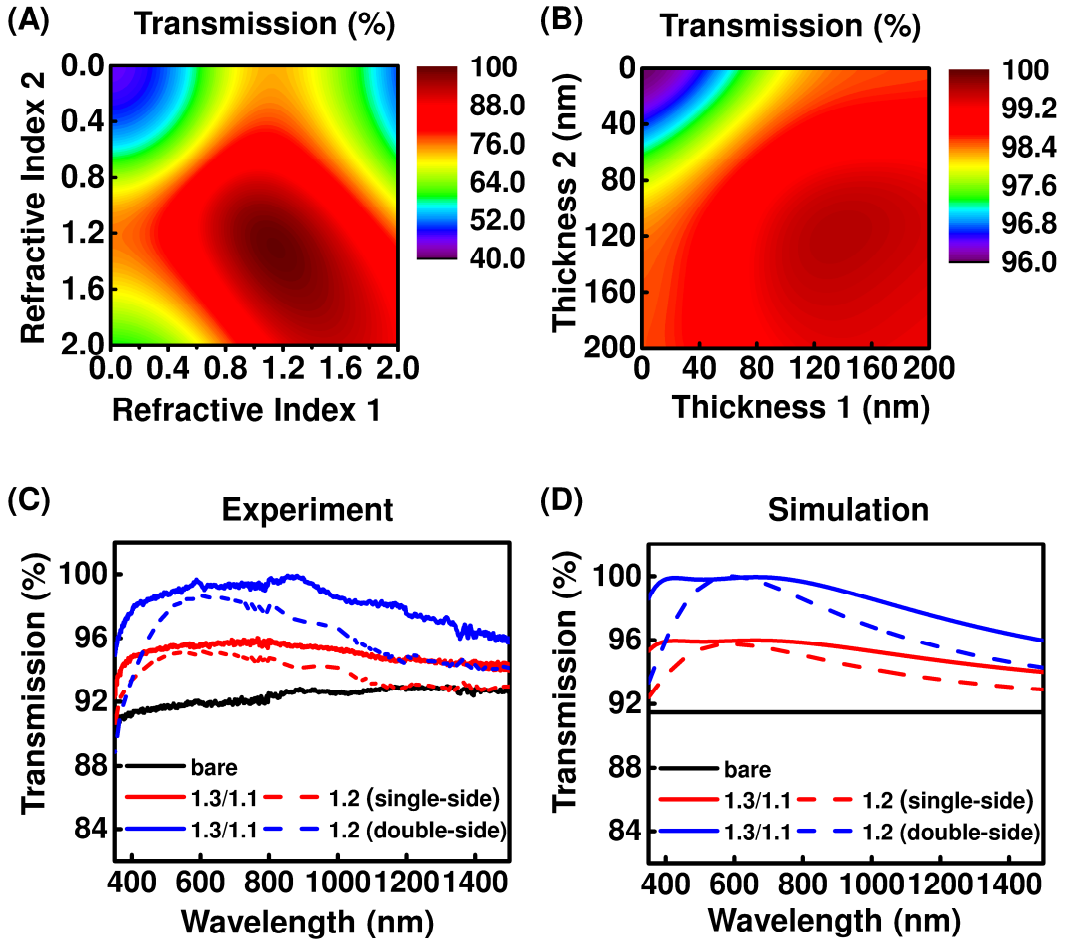

Figure 7.3 Calculated contour plots of the average transmission as a function of (A) refractive indices of bilayers at fixed thicknesses of $t_1 = t_2 = 120$ nm and (B) thicknesses at fixed refractive indices of $n_1 = 1.15$ and $n_2 = 1.31$. (C) Measured and (D) simulated transmission spectra of double-layer nanoporous coatings at normal incidence for bare (black), single-side (red) and double-side (blue) cases. For ease of comparison, this plot also includes results for the single-layer coating.

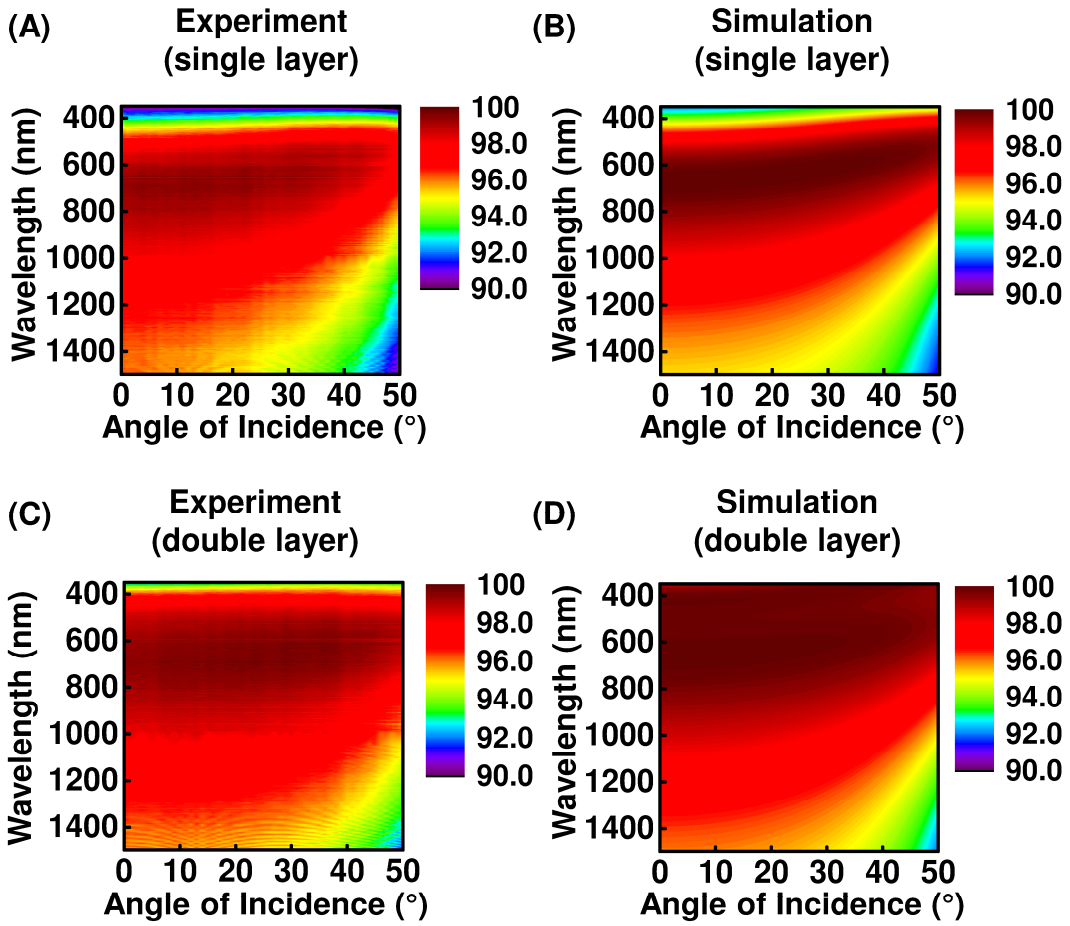

Figure 7.4 Measured and simulated angle-resolved transmission spectra of single-layer (A, B) and double-layer (C, D) nanoporous coatings under unpolarized light illumination. Optical properties of the nanoporous film were only weakly sensitive to angle of incidence up to 40º. The spectral range of operation increased with the introduction of an additional layer (*i.e.*, bilayer configuration) with optimal refractive indices.

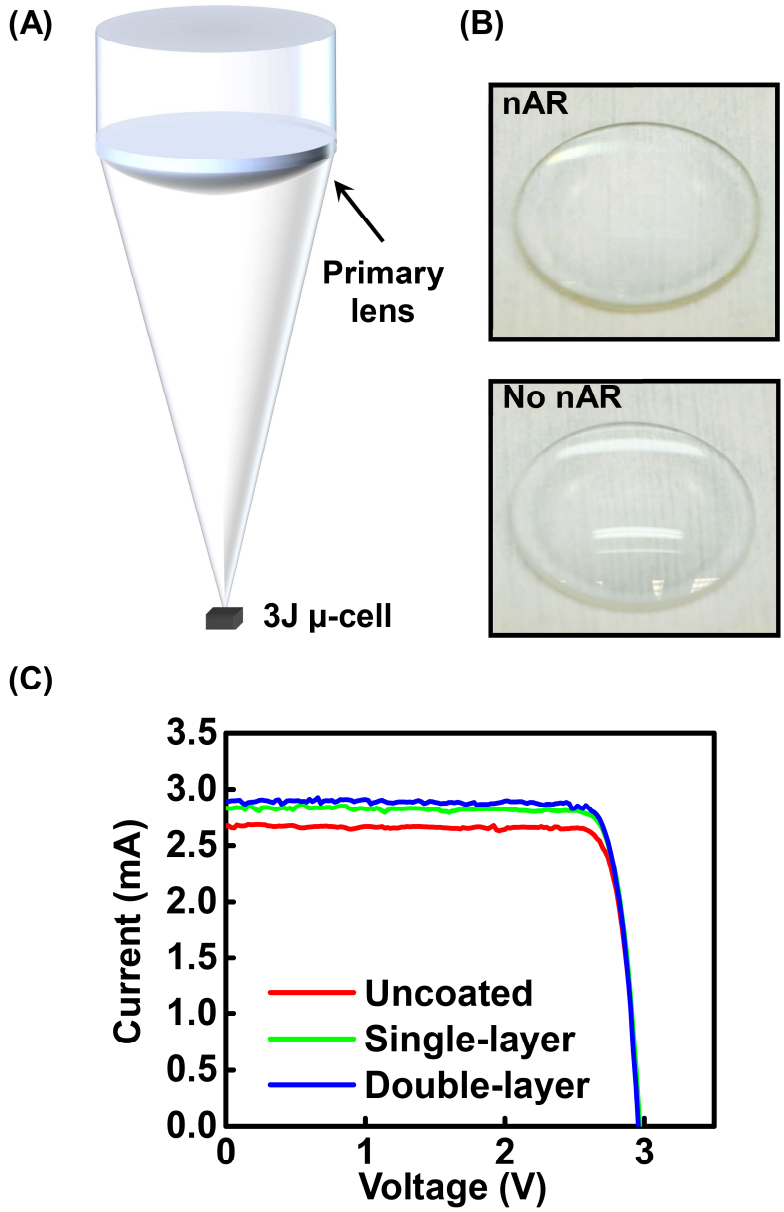

Figure 7.5 (A) Schematic illustration of incident light focusing onto a 3J solar cell through a primary plano-convex lens. (B) Optical images of a plano-convex lens with (top) and without (bottom) nAR coatings on both sides, revealing the suppression of reflections in the former case. (C) PV performance of the 3J solar cells (InGaP/GaAs/InGaAsNSb, 1.9eV/1.4eV/1.0eV) without (red) and with single-layer (green) and double-layer (blue) nAR coatings. The relative enhancement in short-circuit current was 8.2% for the latter case.

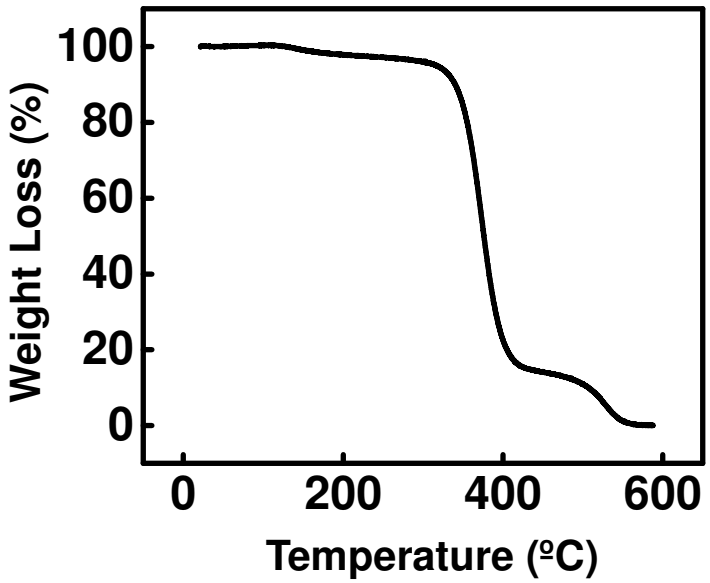

Figure 7.6 Thermogravimetric analysis data of PMMSQ/PS-*b*-P2VP mixture (65% PS-*b*-P2VP loading) measured by Q50-TGA at a temperature ramp of 5 ºC per minute.

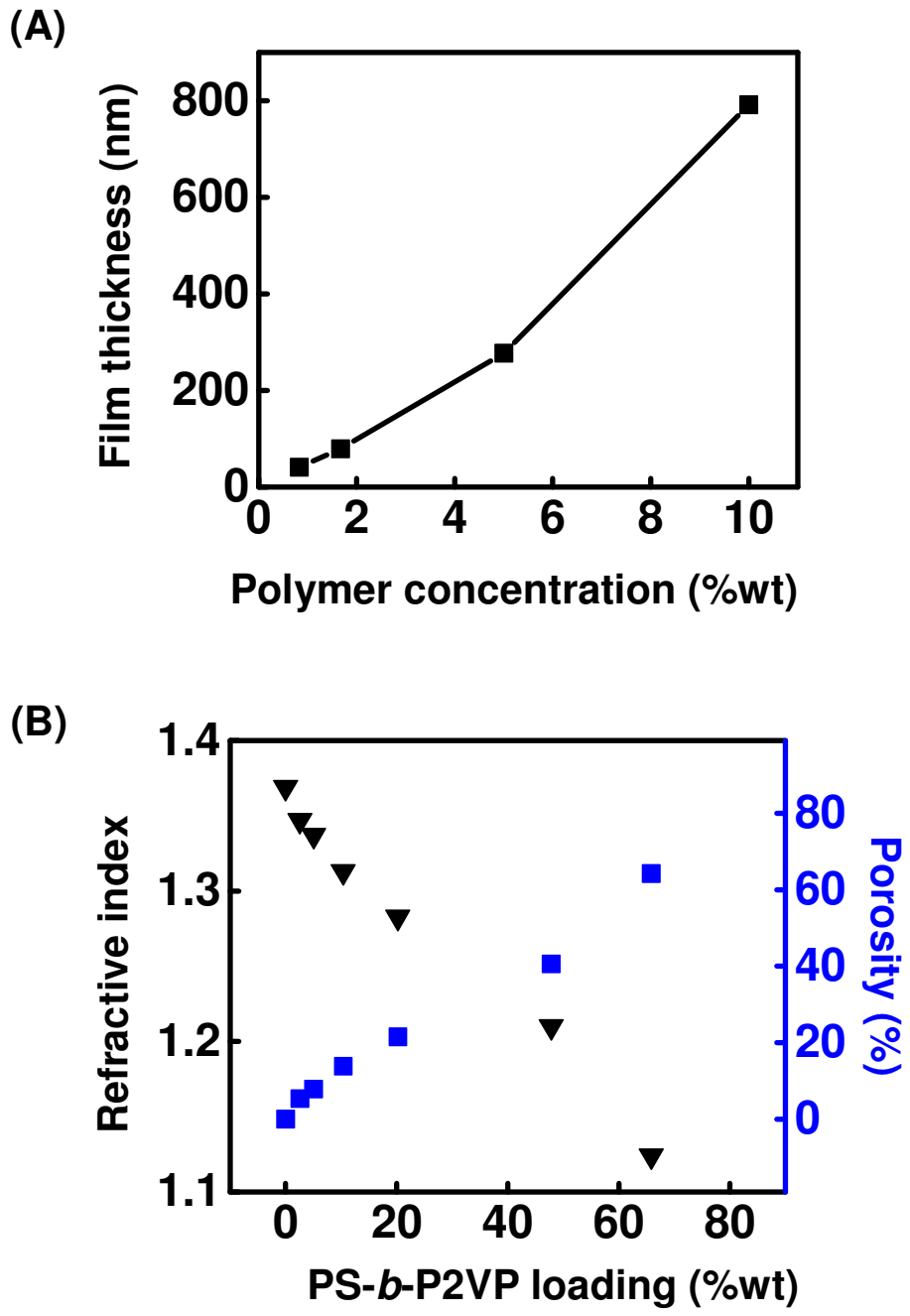

Figure 7.7 (A) Film thickness as a function of polymer mixture solution concentration (~48% P2VP loading, 2000 rpm); (B) Refractive index as a function of PS-P2VP loading.

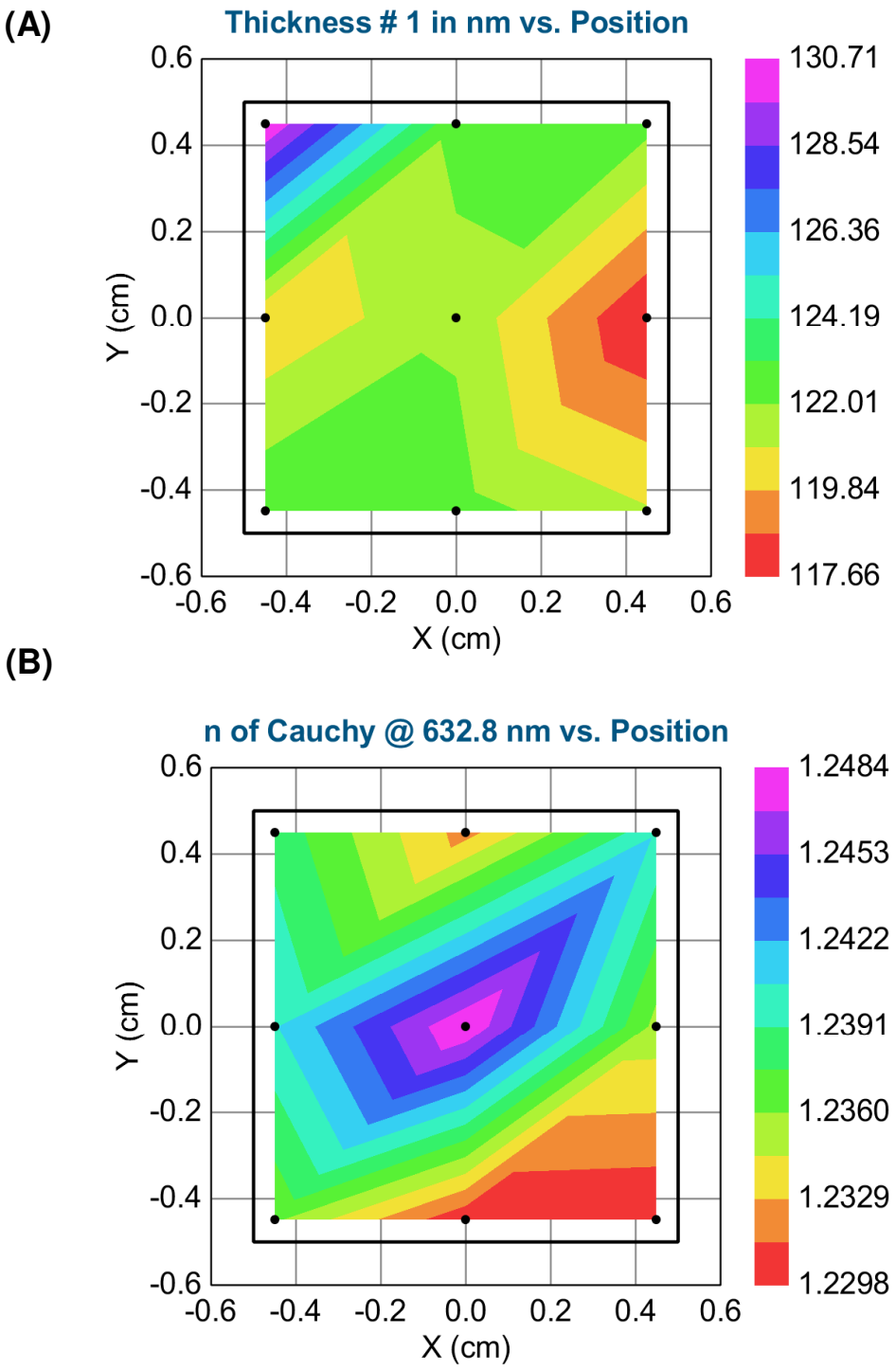

Figure 7.8 (A) Film thickness and (B) refractive index distribution on a single layer film coated on a glass substrate as mapped by a Focused RC2 spectroscopic ellipsometer.

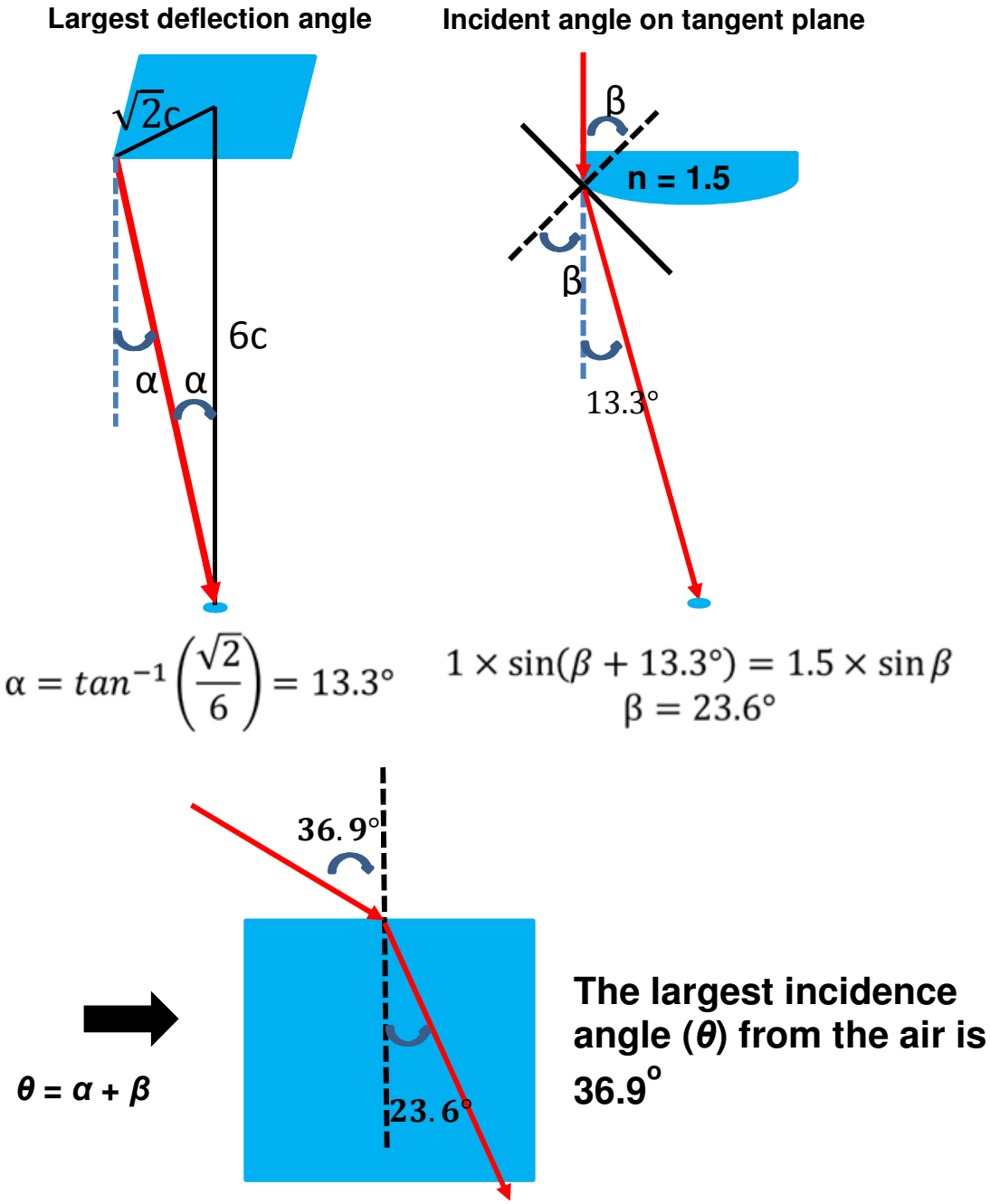

Figure 7.9 Calculations for the largest angle of incidence to consider for the lens unit in the commercial Semprius CPV module employing 3J cells.

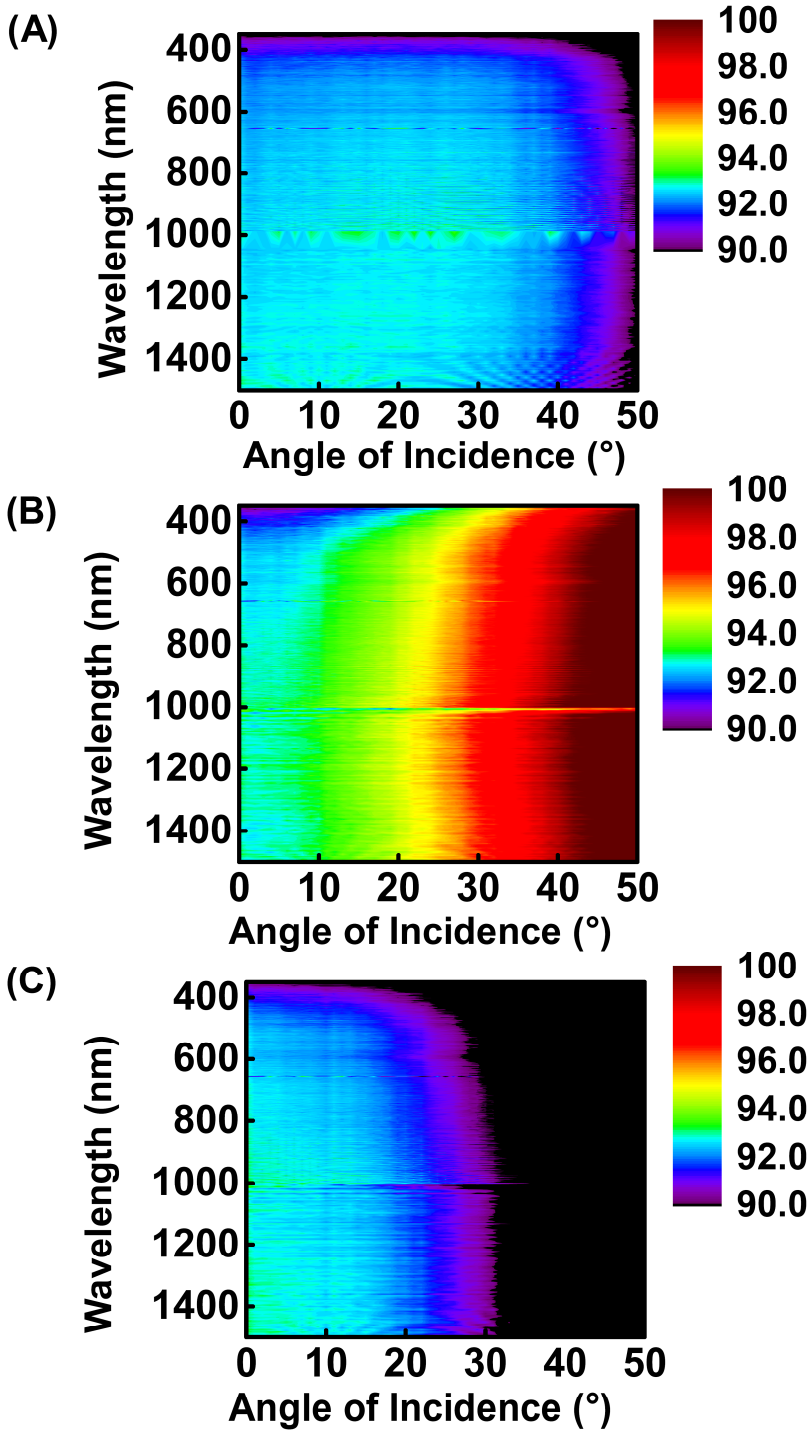

Figure 7.10 Measured angle-resolved transmission spectra for (A) unpolarized, (B) p- and (C) s-polarized light through a glass substrate (170 µm thick coverslip).

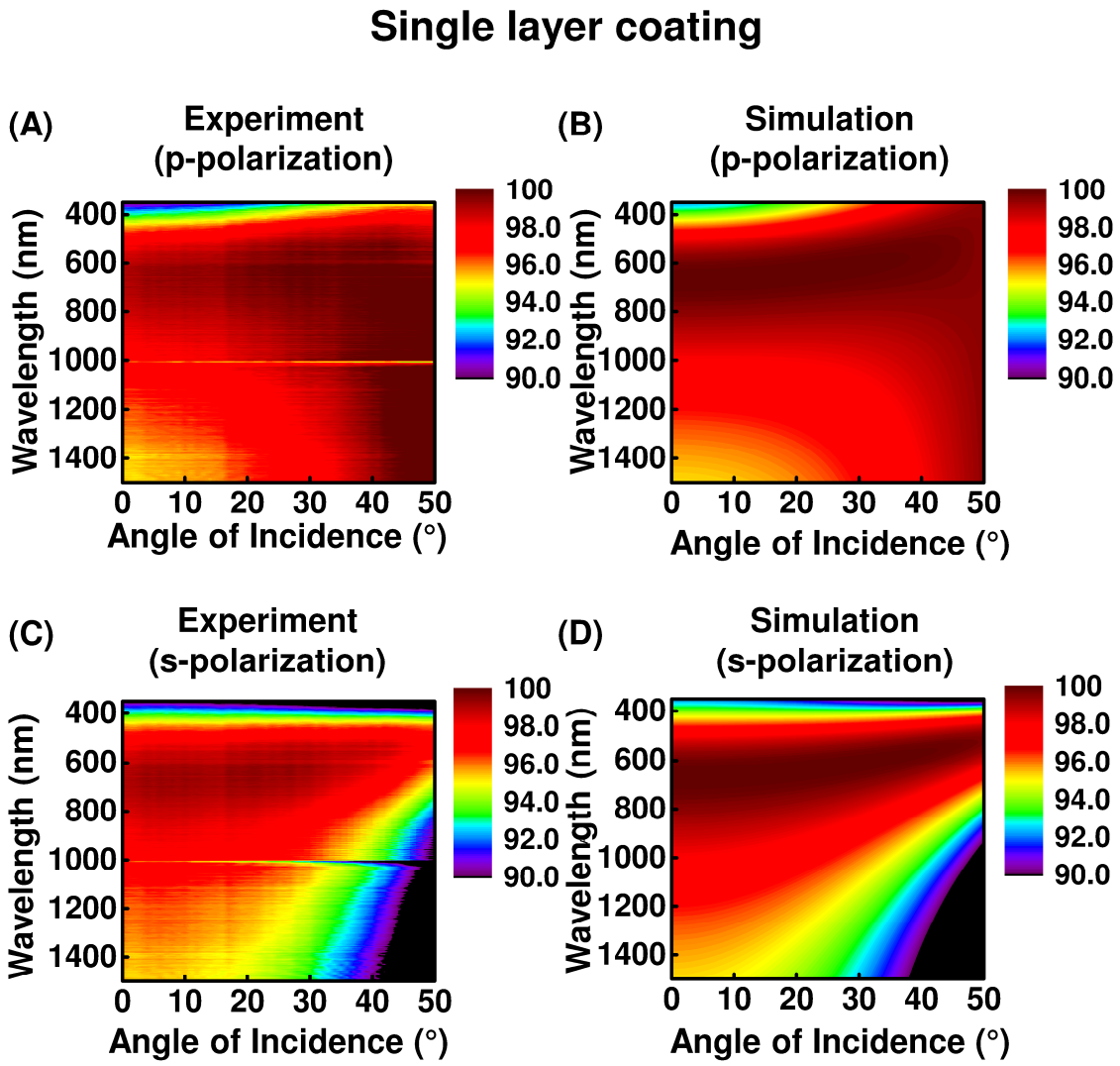

Figure 7.11 Measured and simulated angle-resolved transmission spectra of a glass substrate coated with a dual-side single-layer AR coating for (A, B) p- and (C, D) s-polarization.

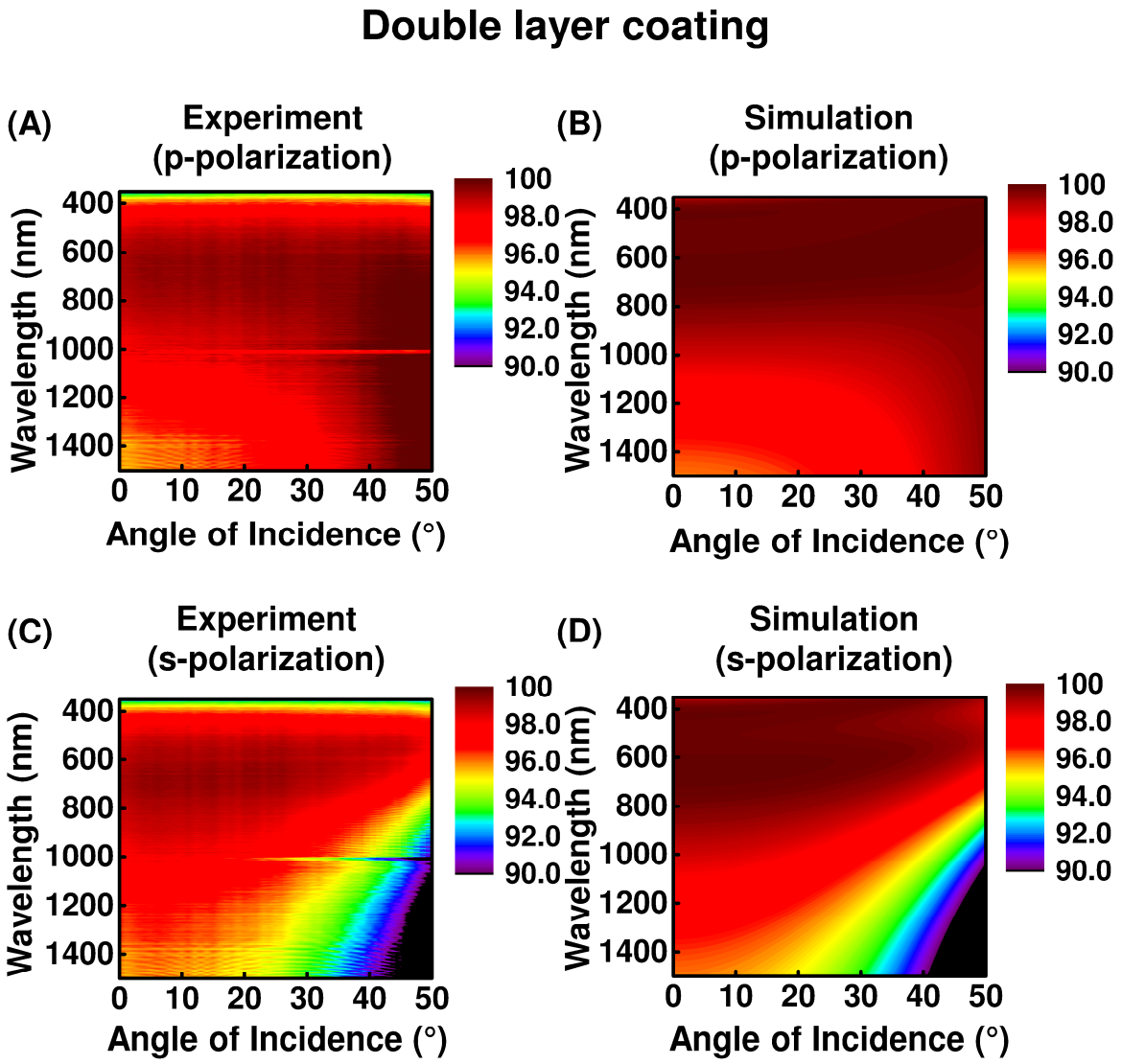

Figure 7.12 Measured and simulated angle-resolved transmission spectra of a glass substrate coated with a dual-side double-layer AR coating for (A, B) p- and (C, D) s-polarization.

Film Uniformity on Curved Lens Surface

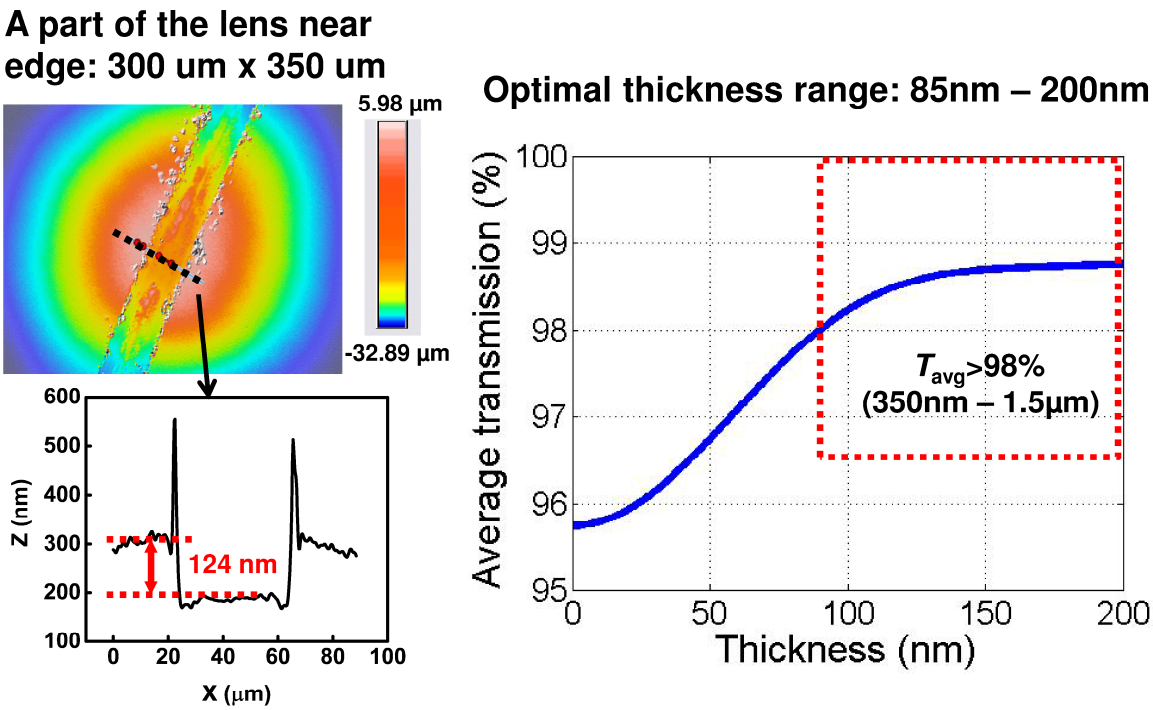

Measured film thickness on different locations (Sensofar S-Neox 3D Optical Profiler) on a curved lens surface with a single-layer nAR coating

- **Center: 94 nm**
- **Halfway: 108 nm**
- **Edge: 124 nm**

Figure 7.13 Single-layer nAR film thickness at three locations coated on a curved lens surface, with a variation within the optimal thickness range.

7.9 References

[1] Cotal, H.; Fetzer, C.; Boisvert, J.; Kinsey, G.; King, R.; Hebert, P.; Yoon, H.; Karam, N. III-V multijunction solar cells for concentrating photovoltaics. *Energy Environ. Sci.* **2009**, *2*, 174-192.

[2] Gee, J. M.; Virshup, G. F. A 31% efficient GaAs/silicon mechanically stacked, multijunction concentrator solar cell. *Proc. 20th IEEE Photovolt. Spec. Conf.* **1988**, *1*, 754-758.

[3] Fraas, L. M.; Avery, J. E.; Sundaram, V. S.; Dinh, V. T.; Davenport, T. M.; Yerkes, J. W.; Gee, J. M.; Emery, K. A. Over 35% efficient GaAs/GaSb stacked concentrator cell assemblies for terrestrial applications. *Proc. 21st IEEE Photovolt. Spec. Conf.* **1990**, *1*, 190-195.

[4] Takamoto, T.; Ikeda, E.; Agui, T.; Kurita, H.; Tanabe, T.; Tanaka, S.; Matsubara, H.; Mine, Y.; Takagishi, S.; Yamaguchi, M. InGaP/GaAs and InGaAs mechanically-stacked triple-junction solar cells. *Proc. 26th IEEE Photovolt. Spec. Conf.* **1997**, 1031-1034.

[5] King, R. R.; Law, D. C.; Edmondson, K. M.; Fetzer, C. M.; Kinsey, G. S.; Yoon, H.; Sherif, R. A.; Karam, N. H. 40% efficient metamorphic GaInP/GaInAs/Ge multijunction solar cells. *Appl. Phys. Lett.* **2007**, *90*, 183516.

[6] Geisz, J. F.; Kurtz, S.; Wanlass, M. W.; Ward, J. S.; Duda, A.; Friedman, D. J.; Olson, J. M.; McMahon, W. E.; Moriarty, T. E.; Kiehl, J. T. High-efficiency GaInP/GaAs/InGaAs triple-junction solar cells grown inverted with a metamorphic bottom junction. *Appl. Phys. Lett.* **2007**, *91*, 023502.

[7] King, R. R.; Boca, A.; Hong, W.; Liu, X.; Bhusari, D.; Larrabee, D.; Edmondson, K.; Law, D.; Fetzer, C.; Mesropian, S. Band-gap-engineered architectures for high-efficiency multijunction concentrator solar cells. *Proc. 24th Euro. Photovolt. Solar Energy Conf.* **2009**, 55-61.

[8] Zhao, L.; Flamand, G.; Poortmans, J. Recent progress and spectral robustness study for mechanically stacked multi-junction solar cells. *AIP Conf. Proc.* **2010**, *1277*, 284-289.

[9] Wojtczuk, S.; Chiu, P.; Zhang, X.; Pulver, D.; Harris, C.; Siskavich, B. 42% 500X bi-facial growth concentrator cells. *AIP Conf. Proc.* **2011**, *1407*, 9-12.

[10] Derkacs, D.; Jones-Albertus, R.; Suarez, F.; Fidaner, O. Lattice-matched multijunction solar cells employing a 1 eV GaInNAsSb bottom cell. *J. Photon. Energy* **2012**, *2*, 021805.

[11] Tanabe, K.; Watanabe, K.; Arakawa, Y. III-V/Si hybrid photonic devices by direct fusion bonding. *Sci. Rep.* **2012**, *2*, 349.

[12] Sasaki, K.; Agui, T.; Nakaido, K.; Takahashi, N.; Onitsuka, R.; Takamoto, T. Development of InGaP/GaAs/InGaAs inverted triple junction concentrator solar cells. *AIP Conf. Proc.* **2013**, *1556*, 22-25.

[13] Sheng, X.; Bower, C. A.; Bonafede, S.; Wilson, J. W.; Fisher, B.; Meitl, M.; Yuen, H.; Wang, S.; Shen, L.; Banks, A. R.; Corcoran, C. J.; Nuzzo, R. G.; Burroughs, S.; Rogers, J. A. Printing-based assembly of quadruple-junction four-terminal microscale solar cells and their use in high-efficiency modules. *Nat. Mater.* **2014**, *13*, 593-598.

[14] Dimroth, F.; Grave, M.; Beutel, P.; Fiedeler, U.; Karcher, C.; Tibbits, T. N. D.; Oliva, E.; Siefer, G.; Schachtner, M.; Wekkeli, A.; Bett, A. W.; Krause, R.; Piccin, M.; Blanc, N.; Drazek, C.; Guiot, E.; Ghyselen, B.; Salvetat, T.; Tauzin, A.; Signamarcheix, T.; Dobrich, A.; Hannappel, T.; Schwarzburg, K. Wafer bonded four-junction GaInP/GaAs/GaInAsP/GaInAs concentrator solar cells with 44.7% efficiency. *Prog. Photovoltaics: Res. Appl.* **2014**, *22*, 277-282.

[15] Derendorf, K.; Essig, S.; Oliva, E.; Klinger, V.; Roesener, T.; Philipps, S. P.; Benick, J.; Hermle, M.; Schachtner, M.; Siefer, G.; Jager, W.; Dimroth, F. Fabrication of GaInP/GaAs//Si Solar Cells by Surface Activated Direct Wafer Bonding. *IEEE J. Photovoltaics* **2013**, *3*, 1423-1428.

[16] Green, M. A.; Emery, K.; Hishikawa, Y.; Warta, W.; Dunlop, E. D. Solar cell efficiency tables (version 48). *Prog. Photovoltaics: Res. Appl.* **2016**, *24*, 905-913.

[17] Polman, A.; Atwater, H. A. Photonic design principles for ultrahigh-efficiency photovoltaics. *Nat. Mater.* **2012**, *11*, 174-177.

[18] Eisler, C. N.; Abrams, Z. e. R.; Sheldon, M. T.; Zhang, X.; Atwater, H. A. Multijunction solar cell efficiencies: effect of spectral window, optical environment and radiative coupling. *Energy Environ. Sci.* **2014**, *7*, 3600-3605.

[19] Yamada, N.; Okamoto, K. Experimental measurements of a prototype high concentration Fresnel lens CPV module for the harvesting of diffuse solar radiation. *Opt. Express* **2014**, *22*, A28-A34.

[20] Yamada, N.; Hirai, D. Maximization of conversion efficiency based on global normal irradiance using hybrid concentrator photovoltaic architecture. *Prog. Photovoltaics: Res. Appl.* **2016**, *24*, 846-854.

[21] Lee, K.-T.; Yao, Y.; He, J.; Fisher, B.; Sheng, X.; Xu, L.; Anderson, M. A.; Kang, Y.; Gumus, A.; Bahabry, R. R.; Lee, J. W.; Paik, U.; Bronstein, N. D.; Alivisatos, A. P.; Meitl, M.; Lumb, M.; Burroughs, S.; Hussain, M. M.; Lee, J. C.; Nuzzo, R. G.; Rogers, J. A. Concentrator Photovoltaic Module Architectures With Capabilities for Capture and Conversion of Full Global Solar Radiation. *submitted to PNAS* **2016**.

[22] Boriskina, S. V.; Green, M. A.; Catchpole, K.; Yablonovitch, E.; Beard, M. C.; Okada, Y.; Lany, S.; Gershon, T.; Zakutayev, A.; Tahersima, M. H.; Sorger, V. J.; Naughton, M. J.; Kempa, K.; Dagenais, M.; Yao, Y.; Xu, L.; Sheng, X.; Bronstein, N. D.; Rogers, J. A.; Alivisatos, A. P.; Nuzzo, R. G.; Gordon, J. M.; Wu, D. M.; Wisser, M. D.; Salleo, A.; Dionne, J.; Bermel, P.; Greffet, J.-J.; Celanovic, I.; Soljacic, M.; Manor, A.; Rotschild, C.; Raman, A.; Zhu, L.; Fan, S.; Chen, G. Roadmap on optical energy conversion. *J. Opt.* **2016**, *18*, 073004.

[23] Hecht, E. *Optics*; 4 ed.; Addison Wesley: San Francisco, 2002.

[24] Zhao, J.; Wang, A.; Altermatt, P.; Green, M. A. Twenty-four percent efficient silicon solar cells with double layer antireflection coatings and reduced resistance loss. *Appl. Phys. Lett.* **1995**, *66*, 3636-3638.

[25] Bouhafs, D.; Moussi, A.; Chikouche, A.; Ruiz, J. M. Design and simulation of antireflection coating systems for optoelectronic devices: Application to silicon solar cells. *Sol. Energy Mater. Sol. Cells* **1998**, *52*, 79-93.

[26] Chhajed, S.; Schubert, M. F.; Kim, J. K.; Schubert, E. F. Nanostructured multilayer graded-index antireflection coating for Si solar cells with broadband and omnidirectional characteristics. *Appl. Phys. Lett.* **2008**, *93*, 251108.

[27] Liu, L.-Q.; Wang, X.-L.; Jing, M.; Zhang, S.-G.; Zhang, G.-Y.; Dou, S.-X.; Wang, G. Broadband and Omnidirectional, Nearly zero reflective Photovoltaic Glass. *Adv. Mater.* **2012**, *24*, 6318-6322.

[28] Du, Y.; He, H.; Jin, Y.; Kong, F.; Guan, H.; Fan, Z. Graded porous glasses for antireflective applications formed by chemical treatment. *Appl. Surf. Sci.* **2012**, *258*, 6431-6435.

[29] Kennedy, S. R.; Brett, M. J. Porous broadband antireflection coating by glancing angle deposition. *Appl. Opt.* **2003**, *42*, 4573-4579.

[30] Xi, J. Q.; Schubert, M. F.; Kim, J. K.; Schubert, E. F.; Chen, M.; Lin, S.-Y.; LiuW; Smart, J. A. Optical thin-film materials with low refractive index for broadband elimination of Fresnel reflection. *Nat. Photonics* **2007**, *1*, 176-179.

[31] Kim, J. K.; Chhajed, S.; Schubert, M. F.; Schubert, E. F.; Fischer, A. J.; Crawford, M. H.; Cho, J.; Kim, H.; Sone, C. Light-Extraction Enhancement of GaInN Light-Emitting Diodes by Graded-Refractive-Index Indium Tin Oxide Anti-Reflection Contact. *Adv. Mater.* **2008**, *20*, 801-804.

[32] Yan, X.; Poxson, D. J.; Cho, J.; Welser, R. E.; Sood, A. K.; Kim, J. K.; Schubert, E. F. Enhanced Omnidirectional Photovoltaic Performance of Solar Cells Using Multiple-Discrete-Layer Tailored- and Low-Refractive Index Anti-Reflection Coatings. *Adv. Funct. Mater.* **2013**, *23*, 583-590.

[33] Yeo, C. I.; Choi, H. J.; Song, Y. M.; Kang, S. J.; Lee, Y. T. A single-material graded refractive index layer for improving the efficiency of III-V triple-junction solar cells. *J. Mater. Chem. A* **2015**, *3*, 7235-7240.

[34] Prado, R.; Beobide, G.; Marcaide, A.; Goikoetxea, J.; Aranzabe, A. Development of multifunctional sol–gel coatings: Anti-reflection coatings with enhanced self-cleaning capacity. *Sol. Energy Mater. Sol. Cells* **2010**, *94*, 1081-1088.

[35] Nguyen, C. V.; Carter, K. R.; Hawker, C. J.; Hedrick, J. L.; Jaffe, R. L.; Miller, R. D.; Remenar, J. F.; Rhee, H.-W.; Rice, P. M.; Toney, M. F.; Trollsås, M.; Yoon, D. Y. Low-Dielectric, Nanoporous Organosilicate Films Prepared via Inorganic/Organic Polymer Hybrid Templates. *Chem. Mater.* **1999**, *11*, 3080-3085.

[36] Kim, H. C.; Wilds, J. B.; Kreller, C. R.; Volksen, W.; Brock, P. J.; Lee, V. Y.; Magbitang, T.; Hedrick, J. L.; Hawker, C. J.; Miller, R. D. Fabrication of Multilayered Nanoporous Poly(methyl silsesquioxane). *Adv. Mater.* **2002**, *14*, 1637-1639.

[37] Yang, S.; Mirau, P. A.; Pai, C.-S.; Nalamasu, O.; Reichmanis, E.; Pai, J. C.; Obeng, Y. S.; Seputro, J.; Lin, E. K.; Lee, H.-J.; Sun, J.; Gidley, D. W. Nanoporous Ultralow Dielectric Constant Organosilicates Templated by Triblock Copolymers. *Chem. Mater.* **2002**, *14*, 369-374.

[38] Yang, C.-C.; Wu, P.-T.; Chen, W.-C.; Chen, H.-L. Low dielectric constant nanoporous poly(methyl silsesquioxane) using poly(styrene-block-2-vinylpyridine) as a template. *Polymer* **2004**, *45*, 5691-5702.

[39] Lee, B.; Park, Y.-H.; Hwang, Y.-T.; Oh, W.; Yoon, J.; Ree, M. Ultralow-k nanoporous organosilicate dielectric films imprinted with dendritic spheres. *Nat. Mater.* **2005**, *4*, 147-150.

[40] Biswas, K.; Gangopadhyay, S.; Kim, H.-C.; Miller, R. D. Nanoporous organosilicate films as antireflection coatings. *Thin Solid Films* **2006**, *514*, 350-354.

[41] Kim, S.; Cho, J.; Char, K. Thermally Stable Antireflective Coatings Based on Nanoporous Organosilicate Thin Films. *Langmuir* **2007**, *23*, 6737-6743.

[42] Su, H.-W.; Chen, W.-C. Preparation of nanoporous poly(methyl silsesquioxane) films using core-shell silsesquioxane as porogen. *Mater. Chem. Phys.* **2009**, *114*, 736-741.

[43] Hiller, J. A.; Mendelsohn, J. D.; Rubner, M. F. Reversibly erasable nanoporous anti-reflection coatings from polyelectrolyte multilayers. *Nat. Mater.* **2002**, *1*, 59-63.

[44] Philippe, L.; Morris, G. M. Antireflection behavior of silicon subwavelength periodic structures for visible light. *Nanotechnology* **1997**, *8*, 53.

[45] Huang, Y.-F.; Chattopadhyay, S.; Jen, Y.-J.; Peng, C.-Y.; Liu, T.-A.; Hsu, Y.-K.; Pan, C.-L.; Lo, H.-C.; Hsu, C.-H.; Chang, Y.-H.; Lee, C.-S.; Chen, K.-H.; Chen, L.-C. Improved broadband and quasi-omnidirectional anti-reflection properties with biomimetic silicon nanostructures. *Nat. Nanotechnol.* **2007**, *2*, 770-774.

[46] Sun, C.-H.; Jiang, P.; Jiang, B. Broadband moth-eye antireflection coatings on silicon. *Appl. Phys. Lett.* **2008**, *92*, 061112.

[47] Chen, Q.; Hubbard, G.; Shields, P. A.; Liu, C.; Allsopp, D. W. E.; Wang, W. N.; Abbott, S. Broadband moth-eye antireflection coatings fabricated by low-cost nanoimprinting. *Appl. Phys. Lett.* **2009**, *94*, 263118.

[48] Boden, S. A.; Bagnall, D. M. Optimization of moth-eye antireflection schemes for silicon solar cells. *Prog. Photovoltaics: Res. Appl.* **2010**, *18*, 195-203.

[49] Yamada, N.; Kim, O. N.; Tokimitsu, T.; Nakai, Y.; Masuda, H. Optimization of anti-reflection moth-eye structures for use in crystalline silicon solar cells. *Prog. Photovoltaics: Res. Appl.* **2011**, *19*, 134-140.

[50] Rahman, A.; Ashraf, A.; Xin, H.; Tong, X.; Sutter, P.; Eisaman, M. D.; Black, C. T. Sub-50-nm self-assembled nanotextures for enhanced broadband antireflection in silicon solar cells. *Nat. Commun.* **2015**, *6*.

[51] Maex, K.; Baklanov, M. R.; Shamiryan, D.; lacopi, F.; Brongersma, S. H.; Yanovitskaya, Z. S. Low dielectric constant materials for microelectronics. *J. Appl. Phys.* **2003**, *93*, 8793-8841.

[52] Huang, E.; Toney, M. F.; Volksen, W.; Mecerreyes, D.; Brock, P.; Kim, H.-C.; Hawker, C. J.; Hedrick, J. L.; Lee, V. Y.; Magbitang, T.; Miller, R. D.; Lurio, L. B. Pore size distributions in nanoporous methyl silsesquioxane films as determined by small angle x-ray scattering. *Appl. Phys. Lett.* **2002**, *81*, 2232-2234.

[53] Siddique, R. H.; Gomard, G.; Holscher, H. The role of random nanostructures for the omnidirectional anti-reflection properties of the glasswing butterfly. *Nat. Commun.* **2015**, *6*.

[54] *Semprius' 35.5 Percent Efficiency Sets New Record for Commercially Available Solar Modules*, 2013.

Chapter 8 Concentrator Photovoltaic Module Architectures With Capabilities for Capture and Conversion of Full Global Solar Radiation

8.1 Abstract

Emerging classes of concentrator photovoltaic (CPV) modules reach efficiencies that are far greater than those of even the highest performance flat plate PV technologies, with architectures that have the potential to provide the lowest cost of energy in locations with high direct normal irradiance (DNI). A disadvantage is their inability to effectively utilize diffuse sunlight, thereby constraining widespread geographic deployment and limiting performance even under the most favorable DNI conditions. This study introduces a module design that integrates capabilities in flat plate PV directly with the most sophisticated CPV technologies, for capture of both direct and diffuse sunlight, thereby achieving unmatched efficiency in PV conversion of the global solar radiation. Specific examples of this scheme exploit commodity silicon (Si) cells integrated with two different CPV module designs, where they capture light that is not efficiently directed by the concentrator optics onto large-scale arrays of miniature multi-junction (MJ) solar cells that use advanced III-V semiconductor technologies. In this CPV^{+} scheme ("+" denotes the addition of diffuse light capture and conversion), the Si and MJ cells operate independently on indirect and direct solar radiation, respectively. On-sun experimental studies of CPV^{+} modules at latitudes of 35.9886° N (Durham, NC), 40.1125° N (Bondville, IL) and 38.9072° N (Washington DC) show improvements in absolute module efficiencies of between 1.02 to 8.45% over values obtained using otherwise similar CPV modules, depending on weather conditions. These concepts have the potential to expand the geographic reach and improve the cost effectiveness of the highest efficiency forms of PV power generation.

8.2 Introduction

The levelized cost of electricity (LCOE) is a primary metric that defines the economic competitiveness of photovoltaic (PV) approaches to electrical power generation [1]. As the performance of the highest efficiency single-junction flat plate PV modules begins to reach

theoretical limits, research toward cost reductions in such technologies shifts from performance to topics related to materials utilization and manufacturing [2-5]. By contrast, the efficiencies of multi-junction (MJ) solar cells based on III-V compound semiconductors continue to improve steadily, at a rate of ~1% per year over the last fifteen years, due largely to progress in epitaxial growth processes, mechanical stacking techniques and microassembly methods for adding junctions that further maximize light absorption and minimize carrier thermalization losses [6-20]. Record MJ cell efficiencies now approach ~46.0%, with realistic pathways to the 50% milestone [5]. For economic deployment, however, the sophistication and associated costs of these cells demand the use of lenses, curved mirrors or other forms of optics to geometrically concentrate incident sunlight in a manner that maximizes cell utilization [21,22]. One commercial technology of interest uses a two-stage optical concentrating system that consists of an array of aspheric primary lenses and ball lenses interfaced to arrays of ultrathin, triple junction (3J) III-V cells with sub-millimeter lateral dimensions formed by lithographic processes and epitaxial liftoff [23-25]. Here, transfer printing enables high volume manufacturing and assembly of cells with these small dimensions [26-32]. The ball lenses, as secondary optics, improve manufacturing tolerances, produce uniform irradiation profiles on the cells by correcting for chromatic aberration, and expand the acceptance angle to nearly ±1° even at concentration ratios of >1000 [22]. The compact sizes and weights of the resulting high concentrator PV (HCPV) modules facilitate transport and installation and enable use of mechanical trackers with cost effective designs. Production systems exhibit efficiencies of 35.5% at concentration ratios >1000x under Concentrator Standard Test Conditions (CSTC).

Terrestrial use of these, and other, types of HCPV technologies is most economically attractive in geographic locations with high levels of direct normal irradiance (DNI) (e.g., >6 kWh/m^2/day). Typical sites in the United States include California, Arizona and New Mexico [33]. Limitations follow from the inability to utilize non-direct (i.e., diffuse) sunlight due to their narrow acceptance angles, as dictated by the étendue conservation law (e.g., with a passive concentrator operating at a concentration ratio of 1,000, the acceptance angle is theoretically limited to 1.8°) [34]. Even in locations such as Tucson (17% diffuse) and Daggett (20% diffuse) that have exceptionally high DNI, the enhancements associated with capture and conversion of diffuse illumination can be significant. In other locations such as San Francisco (29.6% diffuse) and Portland (39.2% diffuse), operation under diffuse light becomes even more essential to the

economics. Engineering solutions to this challenge have the potential to expand the application of concentrator systems to areas where they have previously been uncompetitive [35,36]. Figure 8.7 presents estimates for the absolute increases in efficiency that can be expected in these locations [35]. As a perspective on the significance, calculations using detailed balance predict that the efficiency enhancements enabled by adding a diffuse collector with an optimized bandgap can exceed those provided by a replacement of 4J cells with 5J alternatives under standard AM 1.5G spectrum (10% diffuse) (see Figure 8.8). The ability to utilize diffuse sunlight also makes CPV less susceptible to soiling issues, as the scattered (by soiling) direct beam rays, which are not concentrated onto the high efficiency MJ cells (ranges from 2-10% depending on locations and weather conditions), can be captured by the diffuse collectors. As a first attempt to capture diffuse light, a recent report described a conventional CPV platform with single-stage concentrator optics (<500x) modified through the addition of silicon (Si) cells with arrays of circular holes to allow passage of focused light onto underlying MJ cells [36].

The work reported here examines advanced modes of implementation and detailed analysis in the context of the most advanced commercially available HCPV module, designed for utility scale power generation in solar farms, as described above, and of a previously unpublished, ultrathin design, configured for use on rooftops and in space applications. Specifically, the following results experimentally and theoretically examine schemes that incorporate capabilities in diffuse light capture into these two types of module architectures. The version that uses the HCPV technology outlined above exploits laser-cut strips of conventional Si cells, without machined holes, mounted in a form-fitting manner onto the module backplanes. These systems offer economically viable concentration ratios, (>1000x) with advanced micro-scale cells for improved thermal management, and dual-stage optics for efficient/accurate tracking and manufacturing tolerances. (In the following, we refer to this module architecture as HCPV^{+}-DS, where the '+' refers to capabilities in diffuse light capture and DS to the dual-stage optics). The other architecture employs a compact design optimized for diffuse light capture, where MJ cells on a transparent substrate stack directly onto an unmodified commodity Si cell. These components couple to an overlying thin plano-convex (PCX) lens array, enabling an exceptionally low-profile module (<5 mm in total thickness) suitable for deployment in space-restricted areas (e.g., rooftops) or in applications where weight is a primary concern (e.g., portable systems, or space applications). (In the following, we refer to this module architecture

as CPV$^+$-LP, where the LP refers to low-profile optics and the absence of H refers to the modest concentration ratios.) As compared to conventional designs, the CPV+-LP architecture offers additional cost advantages because its ultra-compact size and light-weight design significantly reduce both installation/transportation expenses and the steel required for the mechanical tracker.

The economic rationale for both of these designs rests on the fact that ~80% of the cost of energy from flat plate PV technology comes from non-cell related balance-of-module and balance-of-system (BOS) cost associated with land, transport, installation and maintenance (i.e., the turnkey cost in Q4-2015 of a utility scale plant with tracking is \$1.54/W_{dc} and the cost of the Si cells is \$0.33/W) [2,37]. As a result, the addition of the Si cells to an otherwise well-designed CPV platform can represent an incremental cost, justified by the improved performance and consistency of output. Specifically, at current market prices, the cost of the Si cells (i.e., without enclosure, package, inverter, BOS cost, etc.) in a conventional flat plate PV system corresponds to ~15% of the LCOE for that system [1,37]. Assuming that the CPV technology used in this work is economically competitive with Si flat plate in regions of moderate to high DNI [38], the cost for adding Si cells to CPV is approximately only 7.5% of the LCOE, since the output per unit area of a Si module is roughly one half that for a corresponding CPV module. The economic case for the CPV$^+$ concept follows from comparison of the marginal cost of adding the Si (7.5%) to the benefit in terms of additional energy generated. Experimental results reported here suggest that the addition of Si cells to CPV modules increases the overall energy production by roughly 10% even in regions of the United States with the most abundant direct solar radiation resources (diffuse component ≈ 20%, assuming the Si cell efficiency is ~50% of the CPV module), thereby supporting the potential for an overall reduction in the LCOE. Current trends in reductions in the costs of Si cells and increases in the efficiencies of III-V cells could make such CPV$^+$ architectures even more attractive in the future.

The CPV$^+$ concept also yields significant increases in power per unit area, relevant for all applications: from deployment in regions of high DNI where ~20% of the solar resource is in the form of diffuse light, to markets with constrained rooftop space, and to geographic domains with modest DNI. Outdoor field testing of HCPV$^+$-DS and CPV$^+$-LP modules, as described in detail subsequently, shows absolute increases in efficiencies of between 1.02 to 8.45% at a latitude of 35.9886° N (Durham, North Carolina), 1.97 to 6.06% at a latitude of 40.1125° N (Bondville,

Illinois) and 5.20% at a latitude of 38.9072° N (Washington DC) in typical weather conditions in the Spring, Summer and Fall months. An additional advantage of these systems is that the large numbers of cells in the platforms provide flexibility in matching their electrical outputs to yield standardized two terminal module interfaces [39].

8.3 HCPV$^+$ Design: Dual-Stage and Low-Profile

Figure 8.1*A* shows a schematic illustration of the working principles of the HCPV$^+$-DS design. Two-stage optics (i.e., a primary high concentration, (HC), inward-facing array of PCX lenses on a front panel and a collection of secondary ball lenses mounted directly onto the 3J cells) concentrate direct sunlight (1000x) onto the 3J cells (InGaP/GaAs/InGaAsNSb, 1.9eV/1.4eV/1.0eV). Adjacent Si cells collect diffuse sunlight, which cannot be captured effectively by the concentrating optics. These Si cells are laser cut from larger, commercially available cells (interdigitated back contact (IBC); A3000, SunPower Corp) to sizes that fit the areas between the 3J cells, as illustrated in Figure 8.1*B*. Representative *I-V* characteristics from the unmodified HCPV module measured under flash test conditions (1000 W·m^{-2}, T_{cell} = 25 ºC) and from an interconnected array of laser-cut Si cells under sun exposure outdoors (950 W·m^{-2}, measured without the primary lens) appear in Figure 8.1*C*. The HCPV module shows an open-circuit voltage (V_{oc}) of 105.2 V, a short-circuit current (I_{sc}) of 1.09 A and an energy conversion efficiency (η) of 34.0%. The array of Si cells has a V_{oc} of 57.8 V, an I_{sc} of 0.816 A and a η of 18.5%. Photographs of the module backplane before and after integrating the Si cells are in Figure 8.1*D-E*: the complete HCPV$^+$-DS module consists of 660 3J cells (600 µm × 600 µm, inter cell spacing: 20 mm) and 93 Si cells (16.1 mm × 127 mm) with a full HCPV aperture area of 0.264 m^2 and total Si cell area of 0.190 m^2. These components mount in a white powder coated steel enclosure (636 mm × 476 mm × 68 mm) with a polymer encapsulated copper backplane. The Si cells, interconnected in series without bypass diodes, cover 72% of the available backplane area. These components bond onto a white plastic insulating substrate for mechanical support and for ease of integration into the overall housing.

The CPV$^+$-LP embodiment provides complementary capabilities and illustrates the versatility of the overall concepts. Here, an array of 3J cells mount on a transparent substrate with a form factor (~100 mm x 100 mm) designed to match that of commodity Si cells, without modification (Maxeon, SunPower Corp, η = 20% under one sun). Stacking these two sub-

systems and integrating a corresponding set of single-stage low concentration (LC) optics yields a complete module in which direct sunlight focuses onto the array of microcells while the diffuse light strikes the unmodified, underlying Si cell as illustrated in Figure 8.2*A*. In an example shown here, the optics consist of an array of glass LC outward-facing PCX aspheres (18x) with thickness of 2.5 mm and focal length of 1 mm, in a hexagonal array with 3 mm pitch. The entire stack, as shown in Figure 8.2*B*, provides for a low profile module with a thickness that is less than 5 mm and a Si cell coverage that approaches ~100% (96% after taking the shading by the 3J cells into account). Characteristic *I-V* performance curves for the array of 3J cells and the Si cell appear in Figure 8.2*C*. These data correspond to simultaneous measurements from a single module on a tracker during an outdoor field test in Washington DC under partly cloudy skies on March 3, 2016 (GNI = 1053.0 W m^{-2}, DNI = 682.2 W m^{-2}). The 3J cell array operates at high voltage (V_{oc} = 87.0 V) and low current (I_{sc} = 21.9 mA), due to an electrical configuration of 34 parallel-connected strings of 30 series connected cells, each of which generates over 3 V under CSTC. The Si cell yields correspondingly higher currents (I_{sc} = 740 mA) and lower voltages (V_{oc} = 0.631 V). Figures 8.2*D-E* present optical images of the assembled device before and after integrating with the underlying Si cell without a top LC outward-facing PCX lens array. Inset images show a cell arrangement and an interconnection scheme.

8.4 Diffuse Radiation Distribution on the Panel Backplane

Diffuse solar radiation has a wide angular spread and follows a broad range of beam trajectories through the concentrating optics. As the angular distribution of diffuse irradiance can vary with meteorological conditions, the calculations presented here assume a Lambertian distribution. For the front lens arrays in both module architectures, the transmittance of light incident at various incidence angles (θ) can be simulated by ray tracing (LightTools®). Results for the primary, inward-facing HC PCX lens array in the HCPV-DS module (f/# = focal length/ lens diameter = 3) appear in Figure 8.3*A*. At incidence angles greater than 30°, the transmittance suffers from total internal reflection (TIR) within the array, as highlighted by calculations that do not consider Fresnel reflection losses (black curves in Figure 8.3*A*; see Figure 8.9 for ray path illustrations). These losses (both TIR and Fresnel) continue to increase as the incidence angle increases. Similar trends appear in simulations for the outward-facing LC PCX lens array for the CPV-LP module (f/# = 2.3, see Figure 8.10).

The averaged transmittance of diffuse light through a PCX lens unit in either module design is also related to its focusing power. As shown by the simulated results in Figure 8.3*B* and Figure 8.10, larger values of f/# (i.e., a smaller focusing power) lead to higher transmittance due to reduced TIR losses within the PCX lens, while the Fresnel losses (difference between the red and black curves) remain nearly constant. The f/# also influences the irradiance distribution on the focal plane, as shown by the calculated results in Figure 8.3*C* and Figure 8.10. The spatial uniformity of these irradiance profiles can be defined by their root mean square deviation (RMSD), according to:

$$\mathrm{RMSD} = \sqrt{\frac{1}{n-1}\sum_{i=1}^{n}\left(\frac{I_i}{I_{avg}} - 1\right)^2} \qquad \textbf{[1]}$$

where I_i is the irradiance of a sampling pixel at some location and I_{avg} is the overall averaged irradiance on the panel backplane. As presented in Figure 8.3*B* and Figure 8.10, the RMSD reaches negligible values when the f/# is larger than 2. The PCX lens arrays in both module architectures fulfill this criterion.

Similar ray-tracing methods can simulate the distribution of diffuse irradiance that forms on the both types of module backplanes after passage through the PCX lens array. This quantity is important for efficient capture and conversion by the Si cells. Calculations, again assuming Lambertian angular distribution for the incoming diffuse light, for the HCPV$^+$-DS module reveal these distributions for three different sidewall reflectivity conditions (mirror, diffuse and absorbing), as shown in Figure 8.4. Reflecting sidewalls (i.e., 100% specular reflection) generate the most even backplane diffuse light distribution (RMSD =0.0059, Figure 8.4*A*), equivalent to the case of an infinite lens array where projections of diffuse light through multiple single lenses (see Figure 8.11) overlap to create uniform irradiance. The overall optical efficiency (η_{op}) for passage of diffuse light through the primary lens array and arrival at the backplane is 76%, restricted by losses from Fresnel reflections (11%) and limited acceptance angles for photons at large incidence angles due to TIR within the primary lens array (13%). For the case of a 10% diffuse light component in the incident solar illumination, the total normalized irradiance in the form of concentration level (relative to one-sun illumination) can be calculated along a dashed line (Figure 8.4*A*) that overlaps with the locations of the 3J cells, as plotted in Figure 8.4*B*. The

sharp peaks and flat regions represent the concentrated light and diffuse radiation, respectively. The module housings involve sidewalls covered by glossy white powder coat paint, with a scattering reflective condition closer to a Lambertian diffusive surface. The simulation results for this case are in Figure 8.4*C-D*. Although the diffuse irradiance distribution shows some variation near the edges of the module, leading to RMSD = 0.11 over the whole panel backplane, the uniformity remains excellent in the central region (16 × 24 lens units, RMSD = 0.016). The overall optical efficiency (η_{op}) for the diffuse irradiance in this case (diffuse sidewall) is 73%. The global efficiency gain (η_{gain}) of the HCPV^{+}-DS module can be estimated by multiplying η_{op} with the Si cell efficiency (η_{Si} = 18.5%), the fraction of the solar illumination that is diffuse (f_{diff}) and the Si cell areal coverage ratio on the panel backplane (f_A=0.72). When f_{diff} = 20% (e.g., a typical sunny day in New Mexico, California and Nevada), the expected η_{gain} from the array of the Si cells is f_{diff} x η_{op} x η_{Si} x f_A = 1.9%. In complete overcast conditions (f_{diff} = 100%), the estimated efficiency gain from the Si cells reaches 9.7% (assuming η_{Si} remains the same under the cloudy sky spectra). An unmodified HCPV system ceases to function under such circumstances. Further improvements are possible through the addition of Si cells on the sidewalls to reach η_{op} = 76%. Such schemes involve, however, additional costs and they significantly increase non-uniformities in the irradiance distribution on the sidewalls and backplane (The RMSD of irradiance profile on the backplane is 0.18, Figure 8.4*E*). Furthermore, the irradiance on the sidewall is only ~1/3 of that of the center of the backplane (Figure 8.4*F*), which would result in a voltage drop in the Si cells that may not be fully compensated by the gain in optical efficiency.

Corresponding results for the CPV^{+}-LP system appear in Figure 8.4*G-H*. Here, η_{op} is 75.6%, mainly limited by optical losses from the top lens array, following considerations that are similar to those associated with the primary optic in the HCPV^{+}-DS design. For this type of module (η_{op} =75.6%, η_{Si} = 20%, f_A =0.96), the expected η_{gain} is 2.9% and 14.5% on sunny (f_{diff} = 20%) and overcast (f_{diff} = 100%) days, respectively, both of which exceed values estimated for the HCPV^{+}-DS architecture due to the improved Si cell coverage.

8.5 Outdoor Testing Results

Outdoor testing of HCPV^{+}-DS modules on a two-axis solar tracker located at Durham, NC reveals their performance under realistic operational conditions. (Data measured in Bondville, IL

are in Figure 8.12). Separate measurements collected approximately once per minute yield values for the power output from the 3J and the Si cells. Representative *I-V* curves measured under sun are in Figure 8.13. A pyranometer (LiCor) and normal incidence pyrheliometer (NIP, Eppley Lab) located on a nearby tracker record the global normal irradiance (GNI) and DNI. Representative data (GNI, DNI along with the power density from the HCPV-DS module, the Si cells and the summed values, corresponding to the total output of the HCPV$^+$-DS system) under three typical weather conditions (i.e., sunny, partly sunny and cloudy) are in Figure 8.5*A*-*C*. Figure 8.5*D* and Table 8.1 summarize the diffuse component (i.e., (GNI-DNI)/GNI) and efficiency data against GNI (calculated over the entire module area) extracted from these measurements. For the case of the sunny day (Nov 20, 2015, Figure 8.5*A*), the DNI is over 90% and is stable (red shaded area, ~ 900 W/m^2) throughout the day. Here, the HCPV$^+$-DS power density (blue curve) peaks at 309.4 W/m^2 (12:19 pm) and reaches an average global efficiency ($\eta_{\text{HCPV-DS}}$) of 29.5% between 11 am to 4 pm (note that the efficiency against the DNI is 31.9% here). The Si cells provide an added power density of 9.57 W/m^2 at the same time (red curve), which translates to an averaged absolute global efficiency gain of 1.02% when the averaged diffuse component is 7.64%, to enable $\eta_{\text{HCPV}^+\text{-DS}}$ = 30.5% (global). On the partly sunny day (Nov 28, 2015, Figure 8.5*B*), the DNI remains relatively high (~ 450 W/m^2 on average) although with strong transient variations due to clouds. The result is a peak HCPV$^+$-DS power density of 280.7 W/m^2 at 12:36 pm (DNI = 884 W/m^2) and averaged $\eta_{\text{HCPV}^+\text{-DS}}$ = 16.9% (global; 29.8% against DNI). The Si cells (peak power density 43.6 W/m^2 at 1:13 pm) add 4.36% to the averaged global efficiency due to the increased diffuse illumination (f_{diffuse}= 43.5%), thereby yielding averaged $\eta_{\text{HCPV}^+\text{-DS}}$ = 21.2% (global). The total power density from the HCPV$^+$-DS here peaks at 12:36 pm with a value of 296.5 W/m^2. By contrast, under cloudy conditions (Oct 25, 2015, Figure 8.5*C*), $\eta_{\text{HCPV-DS}}$ (global) drops to 1.73%. Here, when the diffuse component is 84.4%, the Si cells produce a peak power density of 43.1 W/m^2 at 12:28 pm, and add 8.45% to the averaged global efficiency, to enable $\eta_{\text{HCPV}^+\text{-DS}}$ = 10.2% (global). As expected, the data in Figure 8.5*D* show that the absolute efficiency gain provided by the Si cells follows the trend of the diffuse component of incident radiation, with average cell efficiencies (calculated using only the area of the Si cells) of 18.4% (sunny, Nov 20) and 13.9% (partly sunny, Nov 28 and cloudy, Oct 25) against diffuse irradiance. The latter value matches predictions by optical simulation ($\eta_{\text{op}} \times \eta_{\text{Si}} = 0.73 \times 0.185 =$ 13.5%). The former exceeds simulation, likely because the Si cell can generate additional power

from DNI scattered from intersections between lens arrays and/or imperfections in the lens surfaces (see Figure 8.14).

Outdoor field test measurements with a CPV$^+$-LP module in Washington DC on a partly sunny day (March 3, 2016) provide operational insights similar to those described above. The measured DNI and GNI, together with the power density generated by the CPV$^+$-LP module appear in Figure 8.5*E*. As with the HCPV$^+$-DS system, the maximum power generated by the 3J cell array follows the DNI profile while the output power from the Si cell remains fairly constant, following the trend of the diffuse irradiance (i.e., GNI-DNI). The efficiency of the 3J cell array measured in the integrated module (i.e., with optical losses from the lens array) against DNI is ~30%; that of the Si cell relative to the diffuse irradiance is ~10% (dashed orange lines in Figure 8.5*F*). This Si efficiency includes effects of shading losses associated with the grid interconnects and the 3J cells as well as reflection losses associated with the concentration optics and the glass support for the 3J cell array. Compared to the previously described design, the glass support represents an additional source of loss, partly compensated by the improved coverage of the Si cell (nearly 100%), such that a similar level of averaged global efficiency gain (5.20%) relative to the averaged diffuse component (54.3%) results, as shown in Figure 8.5*F*. The averaged efficiency of a CPV-LP module against GNI is 13.8%, while the CPV$^+$-LP system reaches 19.0% on this particular day. The data, as provided in Figure 8.14, indicate a linear relationship between the output power from the Si cells and the diffuse irradiance (GNI-DNI). Interestingly, the data from the Si cell are more tightly correlated with diffuse power at low levels of DNI (<300 W/m^2, black points) than at high levels (red points). This observation again suggests that the DNI lost by scattering from the lens array intersections and imperfections on the lens surfaces is recycled by the Si cell, similar to the effects described previously for the HCPV$^+$-DS modules (Figure 8.14).

8.6 Discussion

For both types of CPV$^+$ modules, the low per-area cost of energy from Si cells make them attractive for use on the module backplane as diffuse light collectors. Emerging alternatives based on perovskites, organics, epitaxial lift-off III-Vs, each with the additional possibility of use in advanced luminescent concentration schemes [31,40-44], may also be considered. The bandgaps, in particular, are important. Figure 8.6*A* presents the detailed balance limit for the absolute

efficiency gain from diffuse light capture as a function of the cell bandgap and the air mass value, calculated based on the simulation package SMARTS [45,46]. At AM 1.5, with panel tilting angle tracking the sun, rather than a fixed 37° tilt angle used for the standard ASTM G173-03 reference spectrum (Figure 8.15 for comparison), the absolute efficiency gain from diffuse light capture (i.e., the difference between the tilted global and direct normal irradiance) peaks at a bandgap of 1.41 eV, which is different than the values (1.14 and 1.34 eV) optimized for the full spectrum conversion [3]. This difference follows from the increased weight of the diffuse solar spectrum in the visible band as compared with the full solar spectrum (see Figure 8.16). The maximal efficiency gain (4.6% at 1.41 eV, with a diffuse component of 13%) is ~0.5% higher than that predicted for Si (4.1% at 1.11 eV). As the atmosphere becomes thicker (i.e., higher AM value), the achievable efficiency gain tends to increase slightly due to the increased diffuse component, with the optimum bandgap shifting to a smaller values due to spectral variation. A ~5% gain in efficiency is theoretically possible under thick air mass numbers (e.g., AM = 4). Increases in atmospheric turbidity, either in the form of soil dust or air pollution, lead to further increases in the diffuse component. Figure 8.6*B* shows the detailed balance limit for the efficiency gain from diffuse light capture as a function of single junction bandgap and the aerosol optical depth (τ) under AM 1.5 condition. In "clean air" where $\tau = 0.1$, 5.0% absolute efficiency gain is expected; while in "smoky/foggy air" ($\tau = 0.8$) 17.1% absolute efficiency boost is possible. Such simulations suggest value in custom backplane cell designs that optimize the cell bandgap for different terrestrial and climate conditions.

In addition to the careful selection of cell bandgaps for diffuse light utilization, several other strategies can improve the efficiencies of the two CPV$^+$ modules introduced here. The performance of the CPV$^+$-LP system can be enhanced by: (1) mitigating reflection losses from lens surfaces by introducing full spectrum anti-reflection (AR) coatings with broad acceptance angles, with the potential for increasing the optical efficiency by 8% for direct light (i.e., 4% at each interface) and from 76% to 88% for diffuse light; (2) reducing the reflections losses from the transparent substrate that supports the arrays of 3J cells, by adding the AR layer on top and an index matching liquid underneath to fill the air gap between the substrate and the Si cell, with the potential to improve the optical efficiency by 8% for diffuse light; (3) increasing the concentration ratio to hundreds of suns, with the potential to increase the efficiency for direct sunlight by ~3%; (4) incorporating world-record MJ cells (~46% efficiency), with the potential

to increase the efficiency for direct light by 9%. Extrapolations based on implementing all of these enhancements combined with the use of cells with optimized bandgap for diffuse light (GaAs ~1.4 eV, optimized for AM=1.5, η = 28.8% [5]), suggest that the global efficiency for the CPV$^+$-LP module measured on a partly sunny day (54.3% diffuse) like the one in Table 8.1 can be improved from 19.0% to 28.8%; while on a sunny day (10% diffuse), projected global efficiency can be improved from 28.9% to 35.2%. These improved efficiency values for the CPV$^+$-LP systems are comparable to, and can even exceed, world-record flat plate modules formed by epitaxial growth (InGaP/GaAs dual junction from Alta Devices, η = 31.6% [5]).

For the HCPV$^+$-DS system, besides (1) employing the AR coatings on lens surfaces (8% enhancement for direct light, 19% for diffuse light) and (2) using the world-record MJ cells (9% enhancement for direct light) as mentioned earlier, the efficiency can also benefit from (3) increasing the Si cell coverage on the backplane from 72% to nearly 100%. The collective impact of changes (1-3), together with use of cells that have optimized bandgaps (GaAs ~1.4eV, η = 28.8%) could improve the module efficiencies reported in Table 8.1 from 30.5% to 36.6% (for sunny days) and from 21.2% to 30.8% (for partly sunny days).

For both CPV$^+$ module designs, these enhancements correspond to significant gains in annual average efficiency at various geographic locations in the US (see the Future Innovations chart in Figure 8.7). In high DNI regions such as Tucson (with an annual diffuse radiation component ($f_{diff,avg}$) of 17.0%) and Dagett ($f_{diff,avg}$ = 20.2%), the yearly average absolute increases in efficiency ($\Delta\eta_{diff,avg}$) by adding the diffuse collector are 3.8% and 4.6%, respectively; while in medium DNI regions with more frequent overcast conditions such as San Francisco ($f_{diff,avg}$ = 29.6%) and Portland ($f_{diff,avg}$ = 39.2%), $\Delta\eta_{diff,avg}$ reaches 6.7% and 8.8%, respectively. Data from installation in these and others regions of the world will yield data useful for detailed LCOE analyses, as future work.

8.7 Conclusions

In summary, this paper demonstrates schemes by which advanced CPV module technologies can be readily converted into systems capable of capturing and converting both direct and diffuse solar radiation, with potentially important consequences on the cost of energy for photovoltaics. Outdoor testing results in Durham, NC, in Bondville, IL and in Washington DC, indicate

absolute increases in daily averaged module efficiencies between 1.02 to 8.45%, measured against global normal incident solar radiation, depending on weather conditions. Exploiting improved AR coatings on the concentrating optics and glass surfaces and implementing optimized bandgaps for the flat plate PV materials offer near-term potential for further significant improvements in the performance characteristics. Furthermore, because these module architectures are independent of the MJ cell designs, immediate improvements in module efficiencies will be possible by leveraging future advances in MJ cell technology. The overall results suggest promising routes toward high efficiency PV platforms, suitable wide geographic deployment.

8.8 Figures

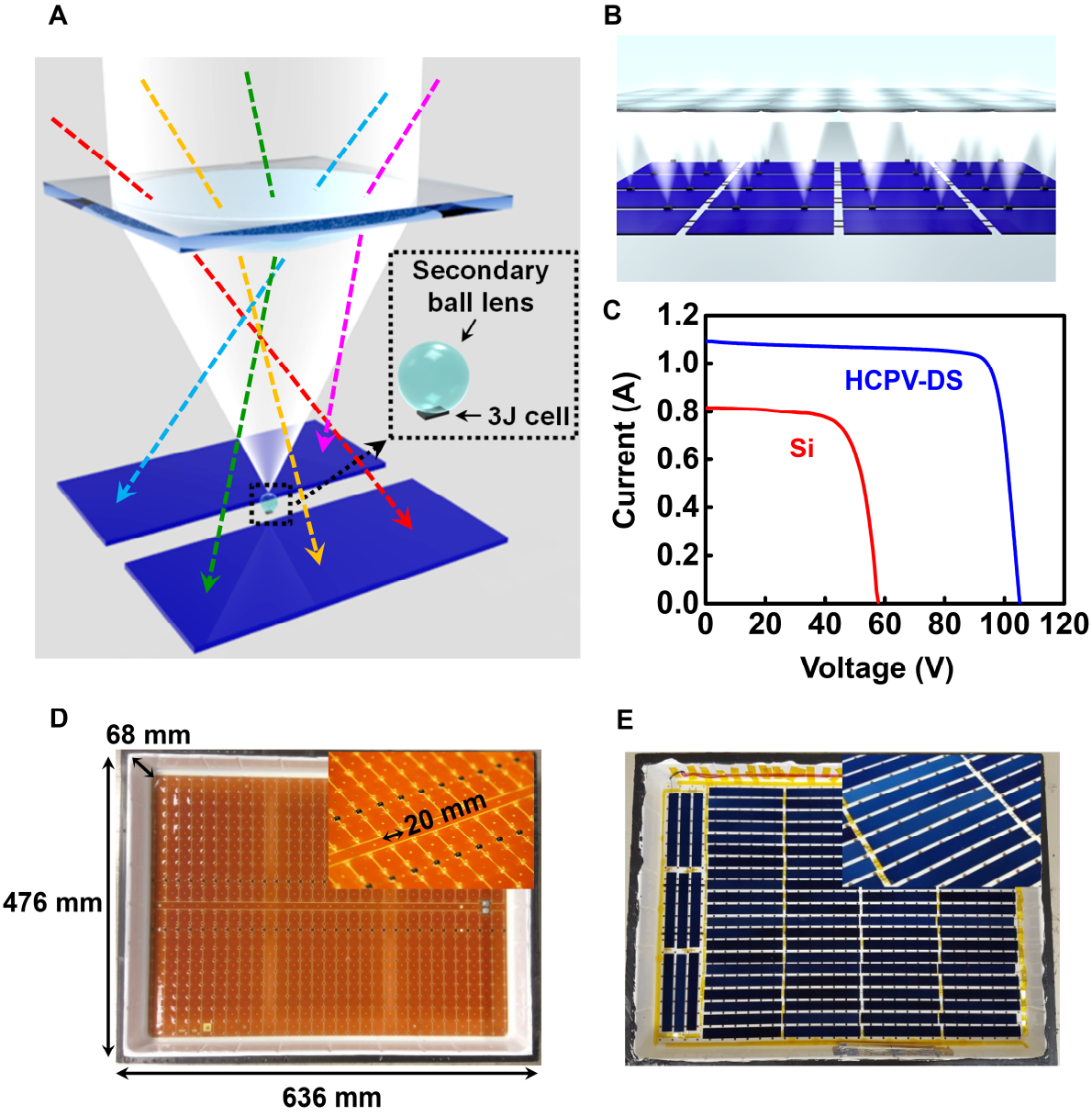

Figure 8.1 (*A*) Schematic illustration of a unit cell in the module that highlights the two-stage optics design and Si cells (blue) between the 3J cells. (*B*) Schematic view at the module level. (*C*) Current (*I*)-voltage (*V*) curves for the HCPV-DS module. Photographs and magnified views as insets showing (*D*) the standard HCPV-DS module panel backplane consisting of an array of the 3J cells coupled with ball lenses and (*E*) the hybrid HCPV^{+}-DS module which includes the Si cells.

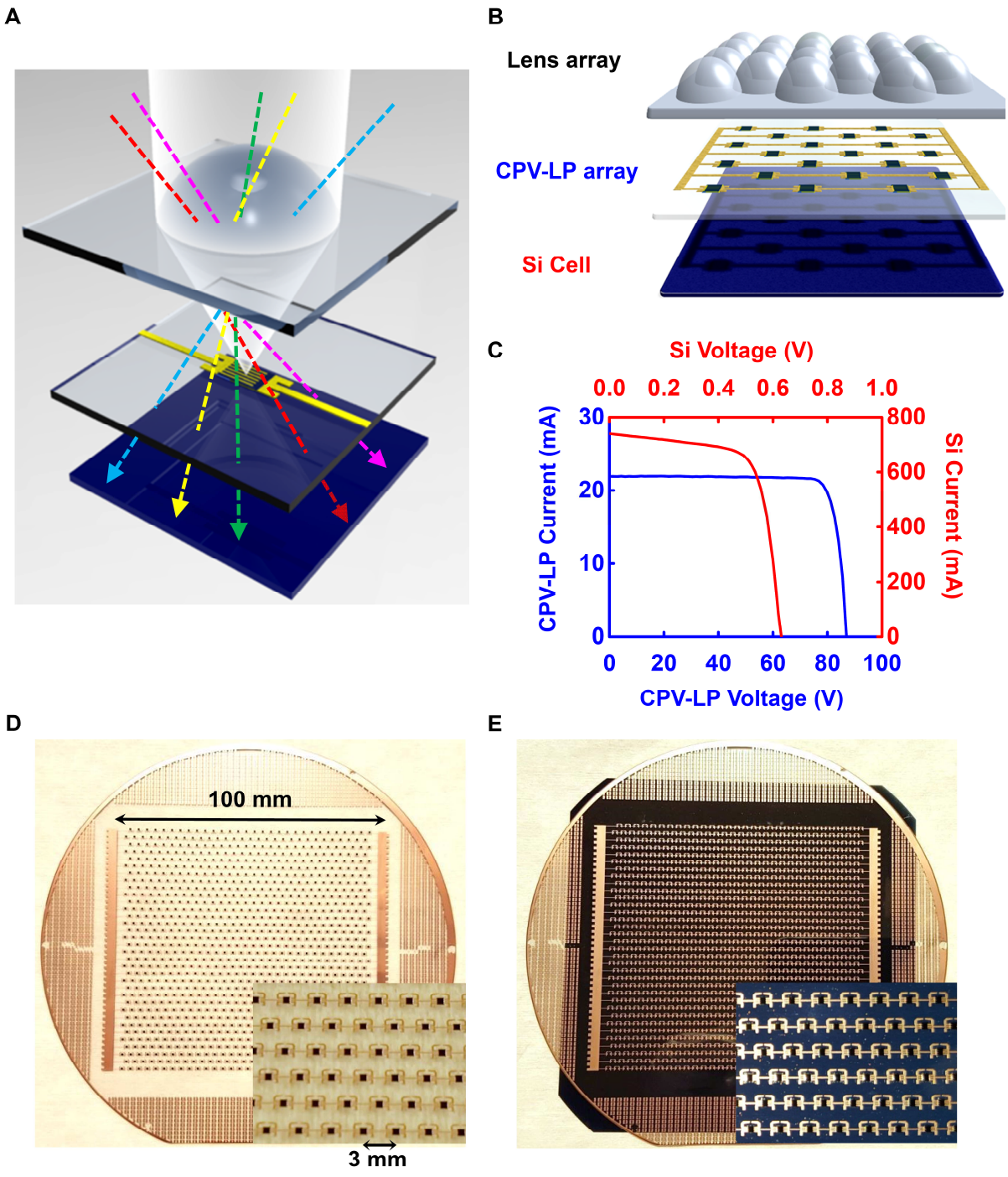

Figure 8.2 (*A*) Schematic illustration of a unit cell in the CPV-LP^{+} module that includes a 3J cell on a transparent substrate located between a focusing lens unit and a Si cell. (*B*) Exploded view of the CPV-LP^{+} module design. (*C*) *I-V* curves of the CPV-LP module and the Si cell. (*D* and *E*) Optics image of a CPV-LP module before and after Si cell integration.

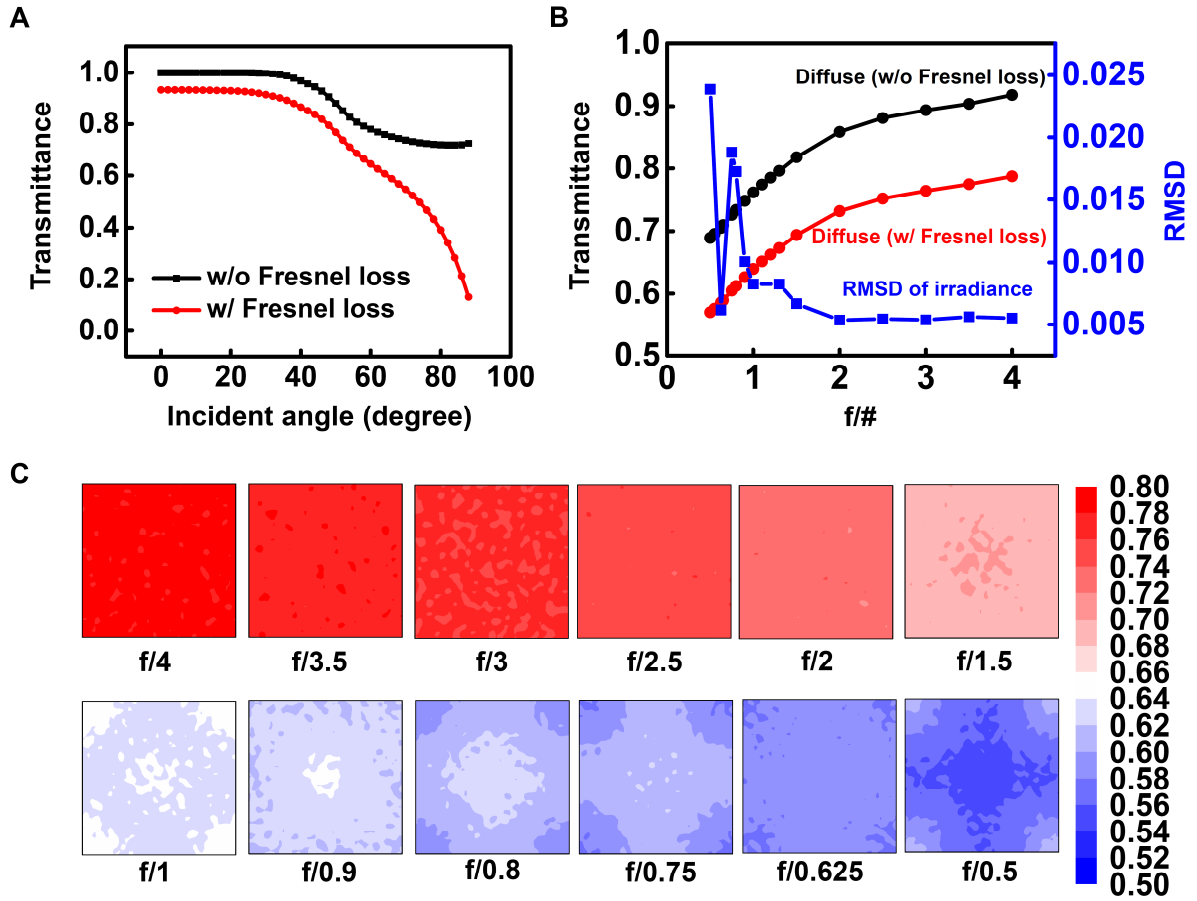

Figure 8.3 (*A*) Simulated averaged transmittance of the lens array as a function of the incident angle of light measured relative to the normal direction. (*B*) Dependence of the transmittance of diffuse/direct sunlight and diffuse irradiance uniformity on the f/#. The calculations involve ray tracing at a wavelength of 550 nm for the case of an infinite lens array, with the lens profile optimized as conic surfaces for convergent focal points. (*C*) Normalized irradiance distribution under an infinite lens array for different f/#, with a sampling area equivalent to that of a single lens unit: higher f/# leads to a higher irradiance uniformity.

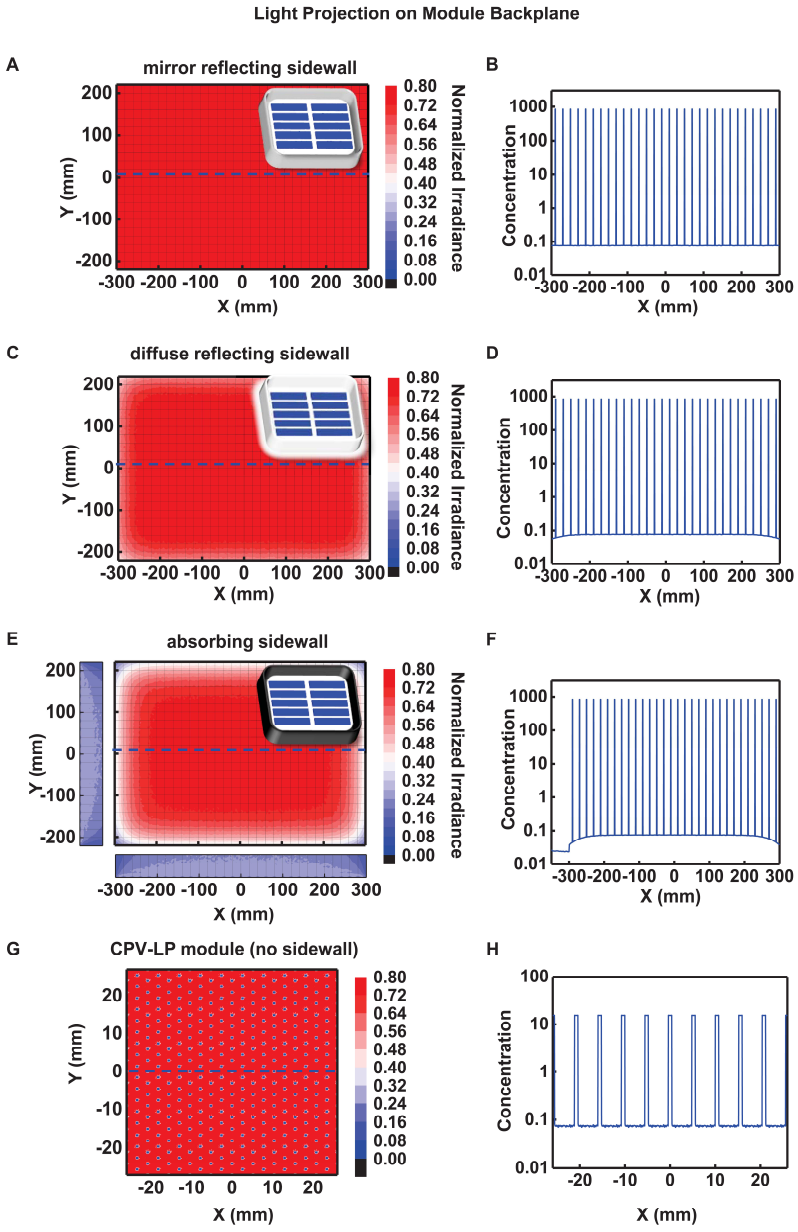

Figure 8.4 Simulated diffuse irradiance profiles and total concentration ratios for the HCPV^{+}-DS panel backplane with different sidewall conditions: (*A* and *B*) mirror reflecting sidewall, (*C* and *D*) diffuse reflecting sidewall, (*E* and *F*) absorbing sidewall. The concentration ratio is calculated along the blue dashed line across the panel backplane as shown on the diffuse irradiance profiles. (*G* and *H*) Simulated diffuse irradiance distribution and total concentration ratios of a part of the CPV^{+}-LP module.

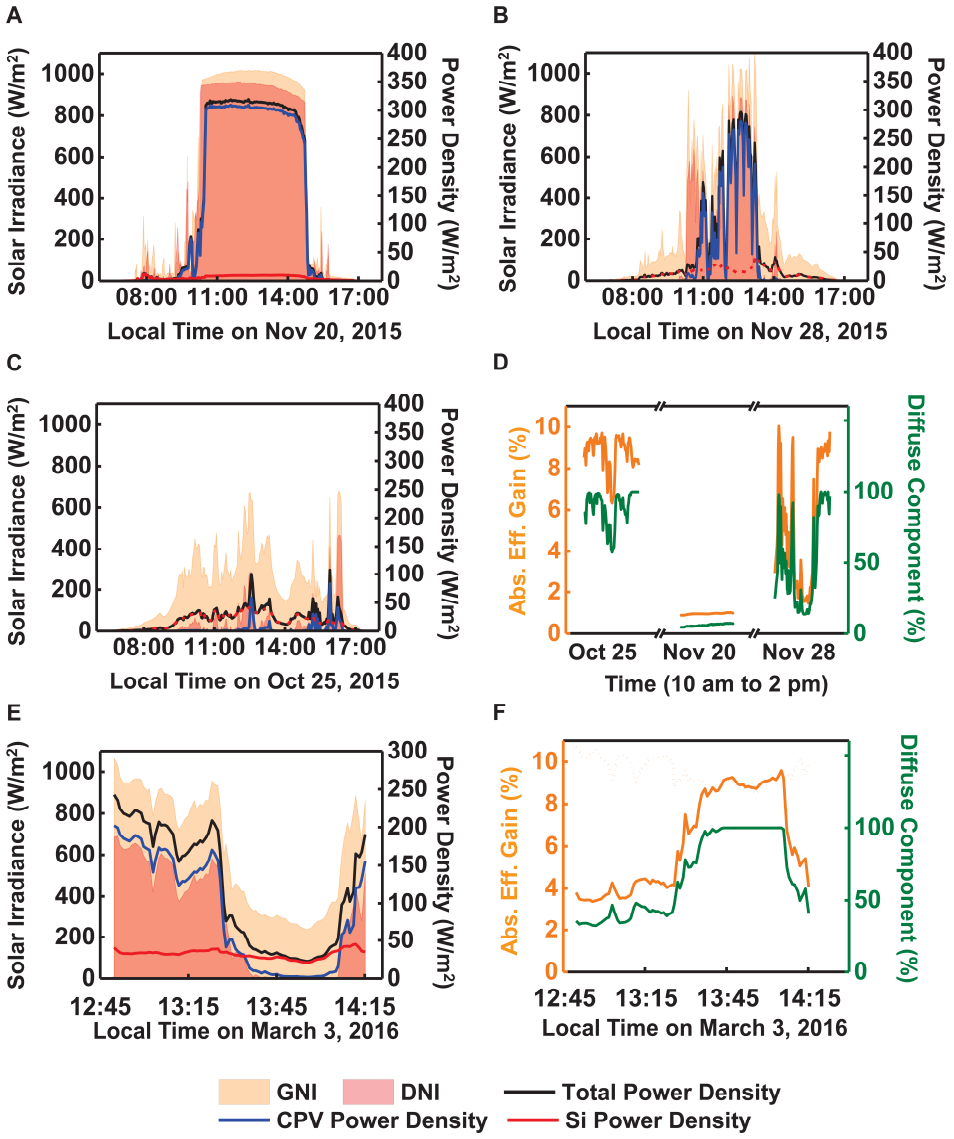

Figure 8.5 Real-time outdoor testing results of GNI, DNI and power density generated by Si (red line), CPV (blue line) and CPV$^+$ (black line): HCPV$^+$-DS module on a (*A*) sunny; (*B*) partly sunny and (C) cloudy day. (*D*) Measured real-time diffuse component of the solar spectra (green line) and absolute efficiency gain (orange line) contributed by the interconnected array of Si cells of the HCPV$^+$-DS module under different weather conditions. (*E*) CPV$^+$-LP module on a partly sunny day. (*F*) Measured real-time diffuse component of the solar spectra (green line) and absolute efficiency gain (orange line) contributed by the Si diffuse collector of the CPV$^+$-LP module under partly sunny condition.

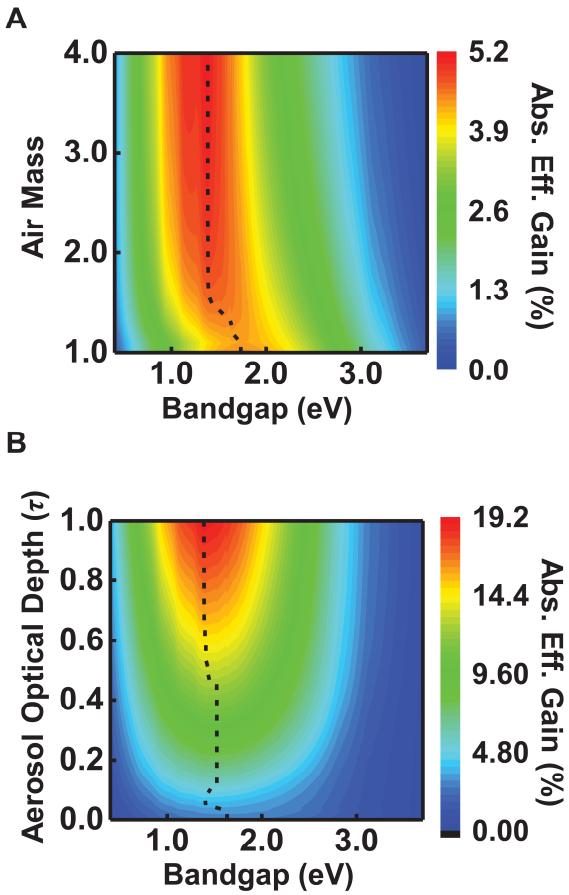

Figure 8.6 Detailed balance limit of the absolute efficiency gain from diffuse light capture as a function of (*A*) Air mass number and cell bandgap (τ=0.08). (*B*) Aerosol optical depth and cell bandgap (AM=1.5).

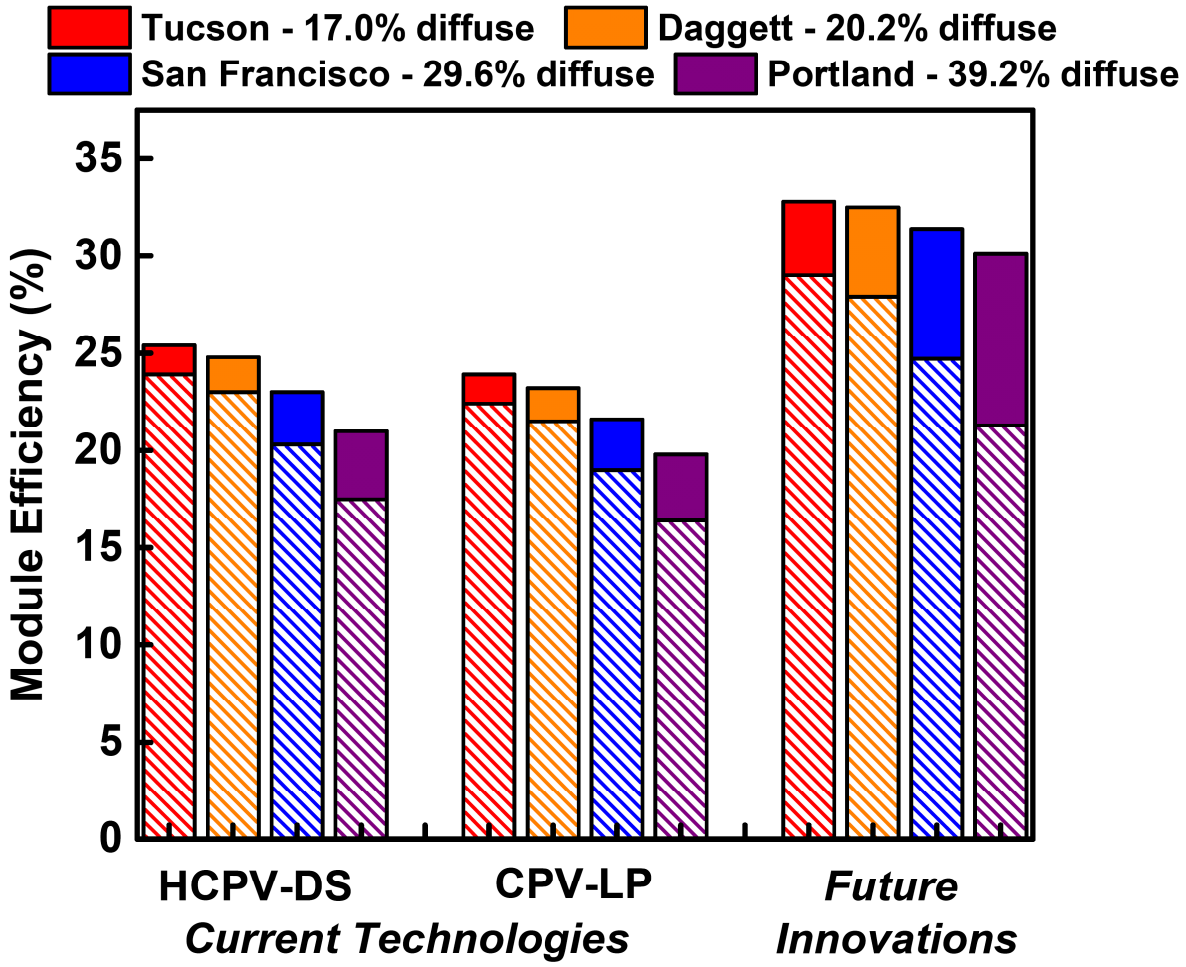

Figure 8.7 Estimated CPV and CPV^{+} module efficiency in different U.S. locations based on their yearly diffuse components. The current technologies tab assumes efficiencies achieved in this work (HCPV-DS module: 32.0%, CPV-LP module: 30.0%, Si cell: 18.5%), while future innovations tab uses improved PV efficiencies (CPV module: 38.9%, GaAs cell: 28.8%) along with reduced module optical losses due to implementations of AR coatings

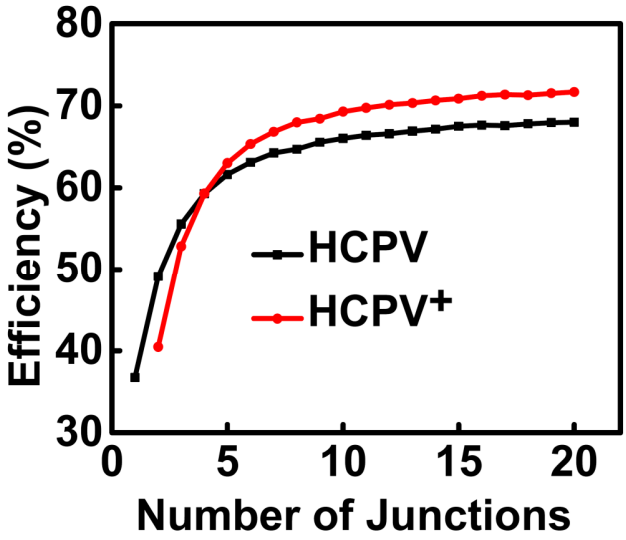

Figure 8.8 Detailed balance efficiency comparison between conventional HCPV MJ cells (n junctions for direct sunlight) and CPV^{+} configuration (n-1 junctions for direct sunlight and 1 junction for diffuse sunlight) at 1000 X concentration under ASTM G173-03 reference spectrum. When n=5, a combination of 4J CPV module and a diffuse collector would result in a higher efficiency than a 5J CPV system.

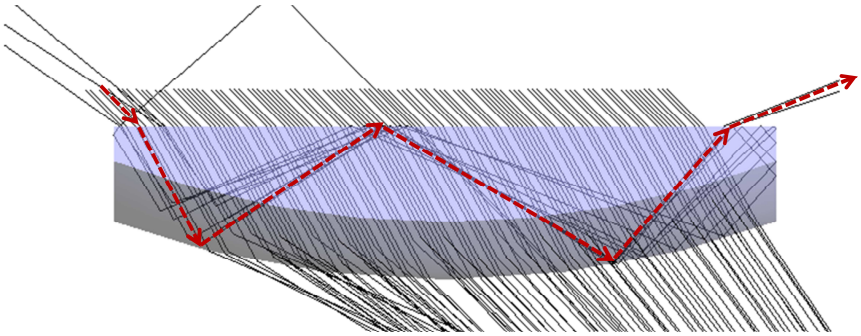

Figure 8.9 Simulated pathways of light rays at an incidence angle of 45°, one example pathway for the losses due to TIR in the primary lens is highlighted by dashed red lines.

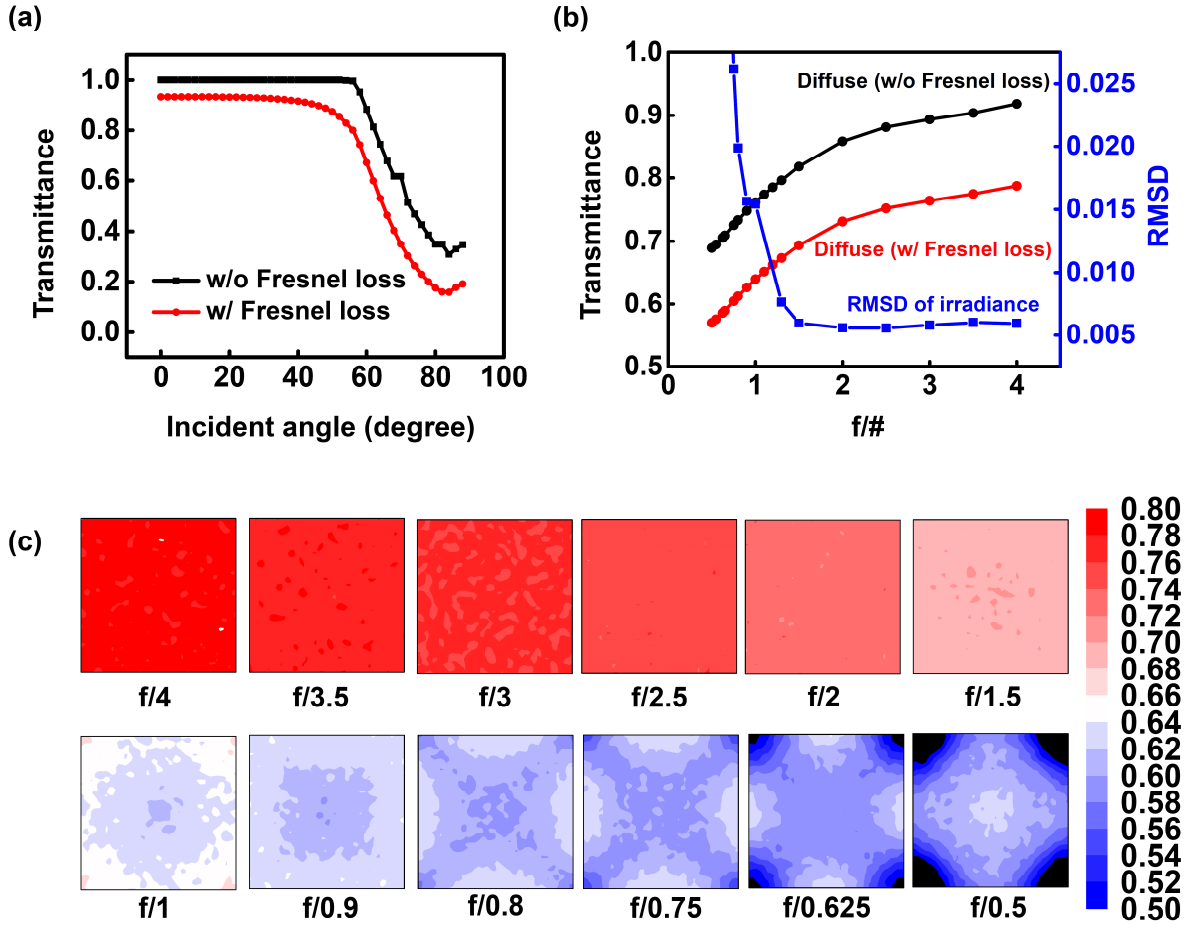

Figure 8.10 Simulation results for transmittance, irradiance uniformity and irradiance distribution associated with passage of diffuse light (Lambertian) through outward-facing plano-convex lens arrays, similar to the type used in CPV^{+}-LP systems. (A) Simulated averaged transmittance of the lens array as a function of the incident angle of light measured relative to the normal direction. (B) Dependence of the transmittance of diffuse/direct sunlight and diffuse irradiance uniformity on the f/# (focal length divided by lens diameter). The calculations involve ray tracing at a wavelength of 550 nm for the case of an infinite lens array, with the lens profile optimized as conic surfaces for convergent focal points. (C) Normalized irradiance distribution under an infinite lens array for different f/#, with a sampling area equivalent to that of a single lens unit: higher f/# leads to a higher irradiance uniformity.

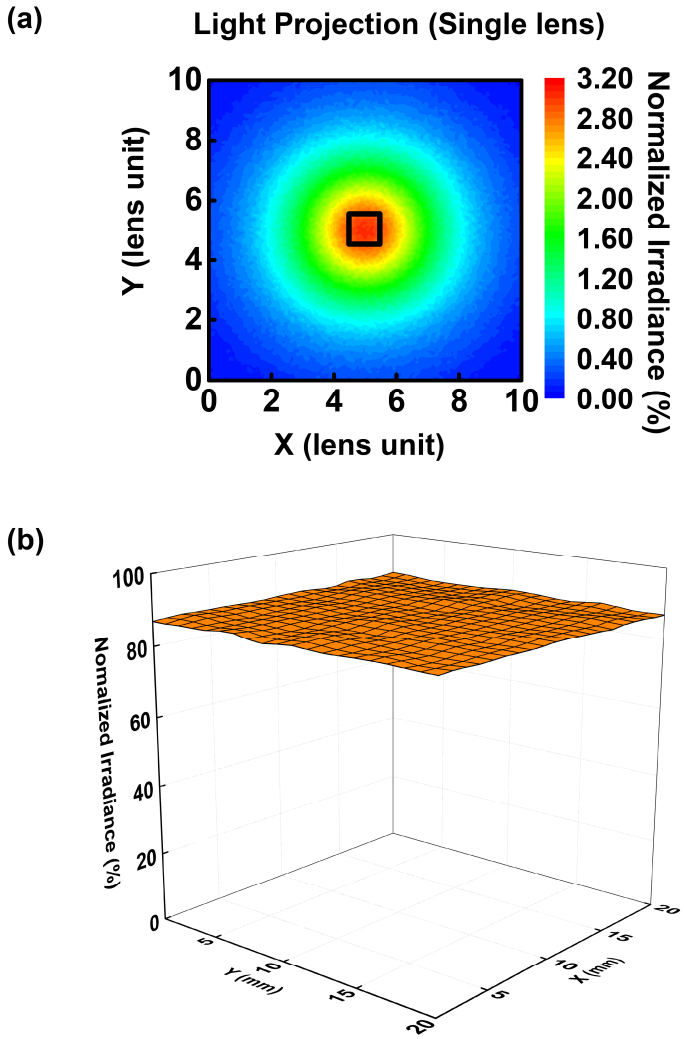

Figure 8.11 Simulated irradiance distribution of diffuse light projected by (a) a single primary lens unit and (b) an infinite primary lens array. The lens was configured based on the primary lens unit in the HCPV module, with a perfect AR coating (i.e. no Fresnel losses). The angle distribution of the incoming rays in the simulation was assumed to be Lambertian, while their spectral distribution matches the diffuse sunlight in the AM 1.5 diffuse spectrum. The square in the center of (a) illustrates the lens aperture, with a normalized peak irradiance of ~3%, as most rays are projected on areas outside the aperture; in contrast, the normalized irradiance in (b) is much higher (~87%) and more uniform, as a result of the superposition of the single-lens projected irradiance profile.

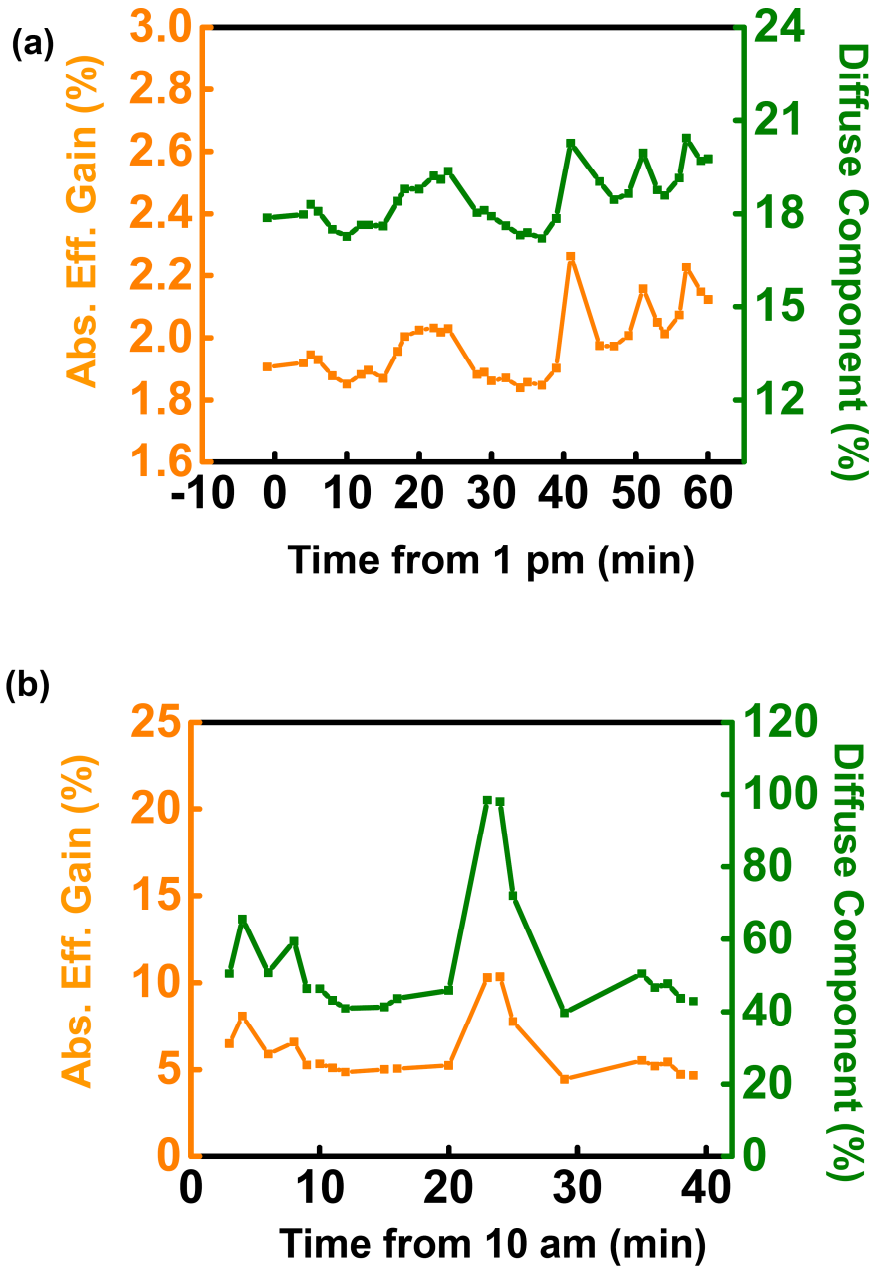

Figure 8.12 Real-time data of the efficiency gains from Si cells and diffuse components on a (a) sunny day (1.97% enhancement, peaked at 2.2%) and (b) cloudy day (6.06% enhancement, peaked at 10.3%) measured at Bondville, IL on Aug 16th and 31st, 2015

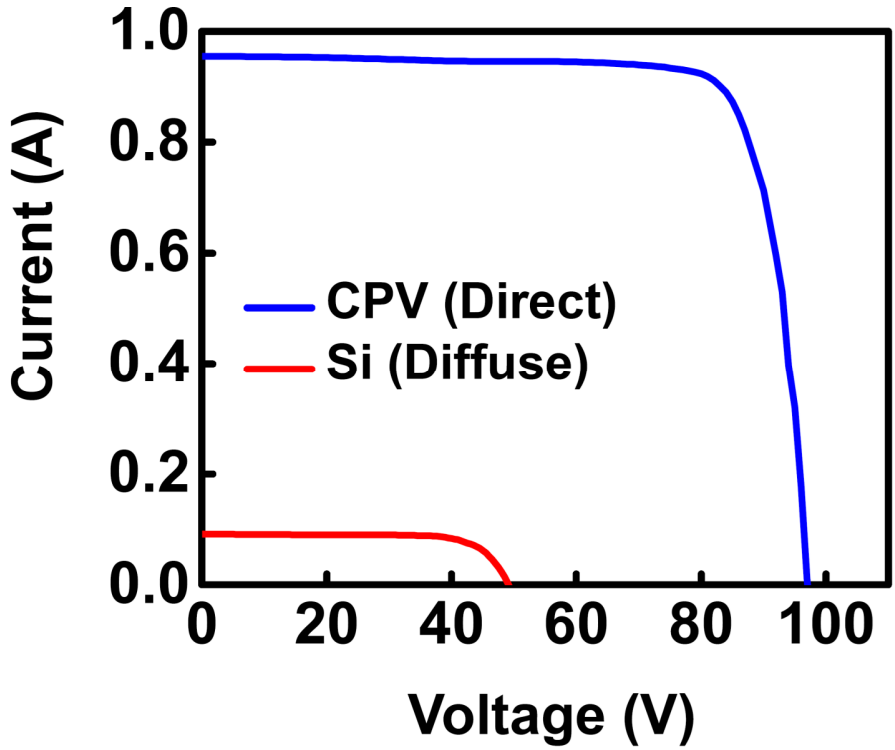

Figure 8.13 *I-V* curves from the HCPV and Si component of the HCPV+ module measured on sun Oct 20, 2015

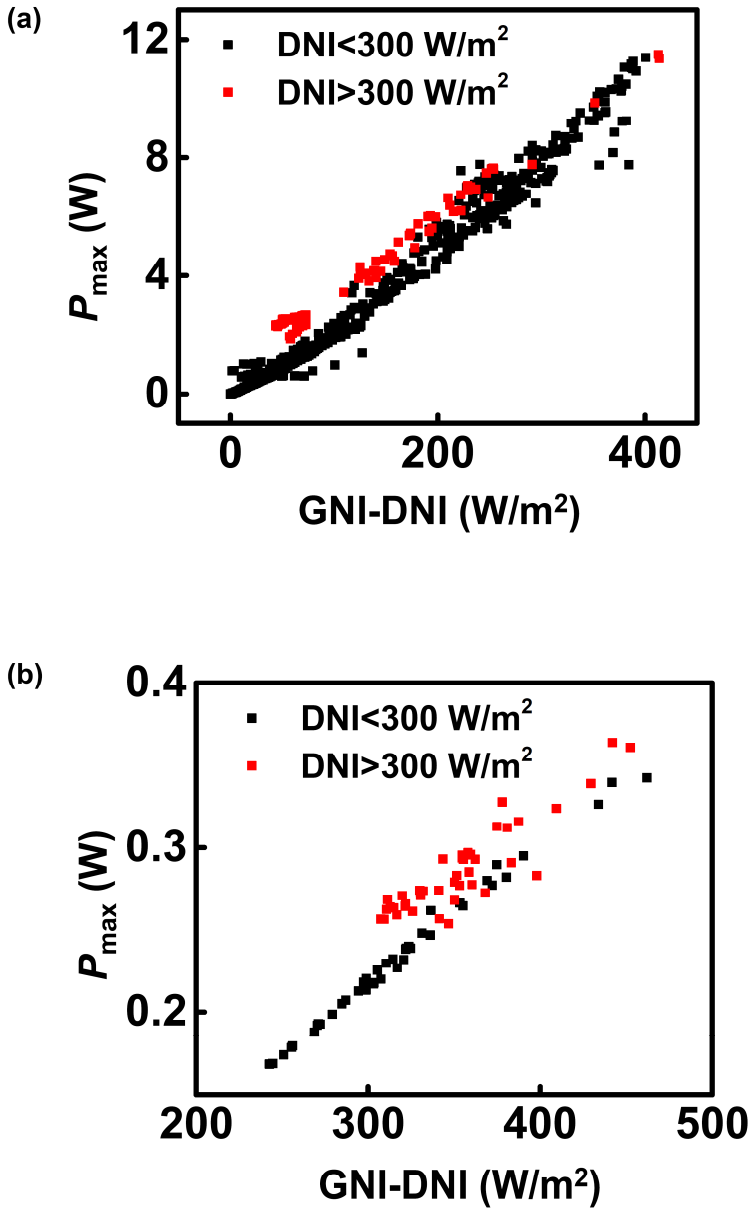

Figure 8.14 Maximum power generated by Si cells against diffuse solar irradiance (i.e., GNI-DNI) measured for (a) HCPV^{+}-DS module on three different days (Nov 20, Nov 28 and Oct 25, 2015) in Durham, NC; (b) CPV^{+}-LP module on March 3, 2016 in Washington, DC

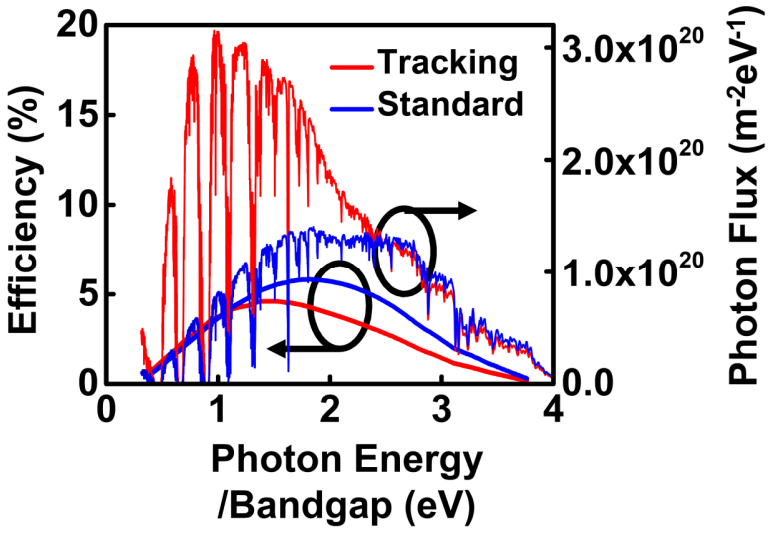

Figure 8.15 Comparison of diffuse component of standard ASTM G173-03 reference spectrum (AM = 1.5, tilted angle = 37^0, diffuse = tilted global –(tilted direct + circumsolar)) and the corresponding tracking diffuse spectrum (AM=1.5, tilted angle = 48.19^0, diffuse = titled global – titled direct) generated by SMARTS 2.9.5; detailed balance efficiency for both are plotted as well and the optimized bandgap blue-shifted under the standard spectrum. Due to the facts that circumsolar rays can not be fully used by the CPV and the standard spectrum is more suitable for flat plate PV, tracking spectra are used at all AM# for simulations in the main text.

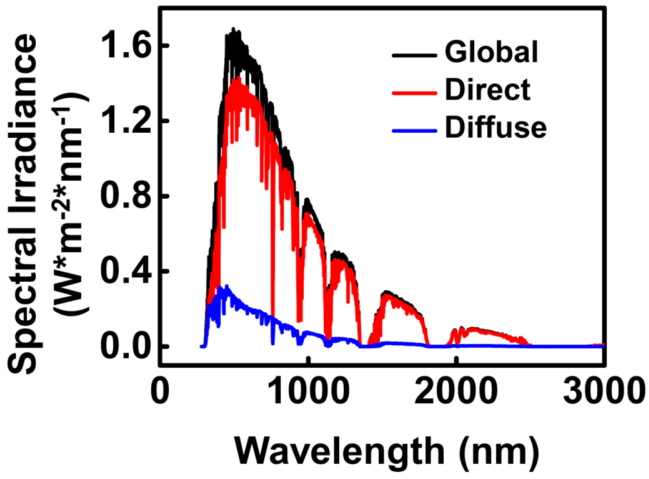

Figure 8.16 Comparison of the tilted direct, diffuse and global components of the solar spectra at AM=1.5 (tracking), as generated by SMARTS 2.9.5.

8.9 Table

Table 8.1 Summary of measured PV characteristics of Si, CPV and CPV^{+} modules on different weather conditions.

Condition	Date	Diffuse Component	CPV^{+} Efficiency	CPV Efficiency	Si Efficiency
Sunny	Nov-20	7.64%	30.5%	29.5%	1.02%
Partly Sunny	Nov-28	43.5%	21.2%	16.9%	4.36%
Cloudy	Oct-25	84.4%	10.2%	1.73%	8.45%
Partly Sunny	Mar-03	54.3%	19.0%	13.8%	5.20%

8.10 References

[1] Branker, K.; Pathak, M. J. M.; Pearce, J. M. A review of solar photovoltaic levelized cost of electricity. *Renewable Sustainable Energy Rev.* **2011**, *15*, 4470-4482.

[2] Luque, A.; Hegedus, S. *Handbook of Photovoltaic Science and Engineering*; Wiley, 2011.

[3] Shockley, W.; Queisser, H. J. Detailed Balance Limit of Efficiency of p-n Junction Solar Cells. *J. Appl. Phys.* **1961**, *32*, 510-519.

[4] Polman, A.; Atwater, H. A. Photonic design principles for ultrahigh-efficiency photovoltaics. *Nat. Mater.* **2012**, *11*, 174-177.

[5] Green, M. A.; Emery, K.; Hishikawa, Y.; Warta, W.; Dunlop, E. D. Solar cell efficiency tables (version 48). *Prog. Photovoltaics: Res. Appl.* **2016**, *24*, 905-913.

[6] Luque, A. Will we exceed 50% efficiency in photovoltaics? *J. Appl. Phys.* **2011**, *110*, 031301.

[7] Derkacs, D.; Jones-Albertus, R.; Suarez, F.; Fidaner, O. Lattice-matched multijunction solar cells employing a 1 eV GaInNAsSb bottom cell. *J. Photon. Energy* **2012**, *2*, 021805.

[8] King, R. R.; Law, D. C.; Edmondson, K. M.; Fetzer, C. M.; Kinsey, G. S.; Yoon, H.; Sherif, R. A.; Karam, N. H. 40% efficient metamorphic GaInP/GaInAs/Ge multijunction solar cells. *Appl. Phys. Lett.* **2007**, *90*, 183516.

[9] Geisz, J. F.; Kurtz, S.; Wanlass, M. W.; Ward, J. S.; Duda, A.; Friedman, D. J.; Olson, J. M.; McMahon, W. E.; Moriarty, T. E.; Kiehl, J. T. High-efficiency GaInP/GaAs/InGaAs triple-junction solar cells grown inverted with a metamorphic bottom junction. *Appl. Phys. Lett.* **2007**, *91*, 023502.

[10] King, R. R.; Boca, A.; Hong, W.; Liu, X.; Bhusari, D.; Larrabee, D.; Edmondson, K.; Law, D.; Fetzer, C.; Mesropian, S. Band-gap-engineered architectures for high-efficiency multijunction concentrator solar cells. *Proc. 24th Euro. Photovolt. Solar Energy Conf.* **2009**, 55-61.

[11] Wojtczuk, S.; Chiu, P.; Zhang, X.; Pulver, D.; Harris, C.; Siskavich, B. 42% 500X bi-facial growth concentrator cells. *AIP Conf. Proc.* **2011**, *1407*, 9-12.

[12] Sasaki, K.; Agui, T.; Nakaido, K.; Takahashi, N.; Onitsuka, R.; Takamoto, T. Development of InGaP/GaAs/InGaAs inverted triple junction concentrator solar cells. *AIP Conf. Proc.* **2013**, *1556*, 22-25.

[13] Sheng, X.; Bower, C. A.; Bonafede, S.; Wilson, J. W.; Fisher, B.; Meitl, M.; Yuen, H.; Wang, S.; Shen, L.; Banks, A. R.; Corcoran, C. J.; Nuzzo, R. G.; Burroughs, S.; Rogers, J. A. Printing-based assembly of quadruple-junction four-terminal microscale solar cells and their use in high-efficiency modules. *Nat. Mater.* **2014**, *13*, 593-598.

[14] Tanabe, K.; Watanabe, K.; Arakawa, Y. III-V/Si hybrid photonic devices by direct fusion bonding. *Sci. Rep.* **2012**, *2*, 349.

[15] Zhao, L.; Flamand, G.; Poortmans, J. Recent progress and spectral robustness study for mechanically stacked multi-junction solar cells. *AIP Conf. Proc.* **2010**, *1277*, 284-289.

[16] Dimroth, F.; Grave, M.; Beutel, P.; Fiedeler, U.; Karcher, C.; Tibbits, T. N. D.; Oliva, E.; Siefer, G.; Schachtner, M.; Wekkeli, A.; Bett, A. W.; Krause, R.; Piccin, M.; Blanc, N.; Drazek, C.; Guiot, E.; Ghyselen, B.; Salvetat, T.; Tauzin, A.; Signamarcheix, T.; Dobrich, A.; Hannappel, T.; Schwarzburg, K. Wafer bonded four-junction GaInP/GaAs/GaInAsP/GaInAs concentrator solar cells with 44.7% efficiency. *Prog. Photovoltaics: Res. Appl.* **2014**, *22*, 277-282.

[17] Derendorf, K.; Essig, S.; Oliva, E.; Klinger, V.; Roesener, T.; Philipps, S. P.; Benick, J.; Hermle, M.; Schachtner, M.; Siefer, G.; Jager, W.; Dimroth, F. Fabrication of GaInP/GaAs//Si Solar Cells by Surface Activated Direct Wafer Bonding. *IEEE J. Photovoltaics* **2013**, *3*, 1423-1428.

[18] Takamoto, T.; Ikeda, E.; Agui, T.; Kurita, H.; Tanabe, T.; Tanaka, S.; Matsubara, H.; Mine, Y.; Takagishi, S.; Yamaguchi, M. InGaP/GaAs and InGaAs mechanically-stacked triple-junction solar cells. *Proc. 26th IEEE Photovolt. Spec. Conf.* **1997**, 1031-1034.

[19] Gee, J. M.; Virshup, G. F. A 31% efficient GaAs/silicon mechanically stacked, multijunction concentrator solar cell. *Proc. 20th IEEE Photovolt. Spec. Conf.* **1988**, *1*, 754-758.

[20] Fraas, L. M.; Avery, J. E.; Sundaram, V. S.; Dinh, V. T.; Davenport, T. M.; Yerkes, J. W.; Gee, J. M.; Emery, K. A. Over 35% efficient GaAs/GaSb stacked concentrator cell assemblies for terrestrial applications. *Proc. 21st IEEE Photovolt. Spec. Conf.* **1990**, *1*, 190-195.

[21] Chong, K.-K.; Lau, S.-L.; Yew, T.-K.; Tan, P. C.-L. Design and development in optics of concentrator photovoltaic system. *Renewable Sustainable Energy Rev.* **2013**, *19*, 598-612.

[22] Menard, E. Optics development for micro-cell based CPV modules. *Proc. SPIE* **2011**, *8108*, 810805.

[23] Ghosal, K.; Burroughs, S.; Heuser, K.; Setz, D.; Garralaga-Rojas, E. Performance results from micro-cell based high concentration photovoltaic research development and demonstration systems. *Prog. Photovoltaics: Res. Appl.* **2013**, *21*, 1370-1376.

[24] Ghosal, K.; Lilly, D.; Gabriel, J.; Whitehead, M.; Seel, S.; Fisher, B.; Wilson, J.; Burroughs, S. Semprius Field Results and Progress in System Development. *IEEE J. Photovoltaics* **2014**, *4*, 703-708.

[25] Kurtz, S.; Muller, M.; Jordan, D.; Ghosal, K.; Fisher, B.; Verlinden, P.; Hashimoto, J.; Riley, D. Key parameters in determining energy generated by CPV modules. *Prog. Photovoltaics: Res. Appl.* **2015**, *23*, 1250-1259.

[26] Carlson, A.; Bowen, A. M.; Huang, Y.; Nuzzo, R. G.; Rogers, J. A. Transfer printing techniques for materials assembly and micro/nanodevice fabrication. *Adv. Mater.* **2012**, *24*, 5284-5318.

[27] Burroughs, S.; Conner, R.; Furman, B.; Menard, E.; Gray, A.; Meitl, M.; Bonafede, S.; Kneeburg, D.; Ghosal, K.; Bukovnik, R.; Wagner, W.; Seel, S.; Sullivan, M. A New Approach

For A Low Cost CPV Module Design Utilizing Micro-Transfer Printing Technology. *AIP Conf. Proc.* **2010**, *1277*, 163-166.

[28] Bower, C. A.; Menard, E.; Garrou, P. E. In *Electronic Components and Technology Conference, 2008. ECTC 2008. 58th* 2008, p 1105-1109.

[29] Furman, B.; Menard, E.; Gray, A.; Meitl, M.; Bonafede, S.; Kneeburg, D.; Ghosal, K.; Bukovnik, R.; Wagner, W.; Gabriel, J.; Seel, S.; Burroughs, S. In *Proc. 35th IEEE Photovolt. Spec. Conf.* 2010, p 000475-000480.

[30] Yoon, J.; Jo, S.; Chun, I. S.; Jung, I.; Kim, H.-S.; Meitl, M.; Menard, E.; Li, X.; Coleman, J. J.; Paik, U.; Rogers, J. A. GaAs photovoltaics and optoelectronics using releasable multilayer epitaxial assemblies. *Nature* **2010**, *465*, 329-333.

[31] Yoon, J.; Li, L.; Semichaevsky, A. V.; Ryu, J. H.; Johnson, H. T.; Nuzzo, R. G.; Rogers, J. A. Flexible concentrator photovoltaics based on microscale silicon solar cells embedded in luminescent waveguides. *Nat. Commun.* **2011**, *2*, 343.

[32] Yao, Y.; Brueckner, E.; Li, L.; Nuzzo, R. Fabrication and assembly of ultrathin high-efficiency silicon solar microcells integrating electrical passivation and anti-reflection coatings. *Energy Environ. Sci.* **2013**, *6*, 3071-3079.

[33] Denholm, P.; Hand, M.; Mai, T.; Margolis, R.; Brinkman, G.; Drury, E.; Mowers, M.; Turchi, C. *The potential role of concentrating solar power in enabling high renewables scenarios in the United States*, 2012.

[34] Hernández, M.; Benítez, P.; Miñano, J. C.; Cvetkovic, A.; Mohedano, R.; Dross, O.; Jones, R.; Whelan, D.; Kinsey, G. S.; Alvarez, R. 2007; Vol. 6670, p 667005-667005-10.

[35] Marion, W.; Wilcox, S. *Solar radiation data manual for flat-plate and concentrating collectors*; National Renewable Energy Laboratory, 1994.

[36] Yamada, N.; Okamoto, K. Experimental measurements of a prototype high concentration Fresnel lens CPV module for the harvesting of diffuse solar radiation. *Opt. Express* **2014**, *22*, A28-A34.

[37] Mailoa, J. P.; Bailie, C. D.; Johlin, E. C.; Hoke, E. T.; Akey, A. J.; Nguyen, W. H.; McGehee, M. D.; Buonassisi, T. A 2-terminal perovskite/silicon multijunction solar cell enabled by a silicon tunnel junction. *Appl. Phys. Lett.* **2015**, *106*, 121105.

[38] KOST, C.; MAYER, J. N.; THOMSEN, J.; HARTMANN, N.; SENKPIEL, C.; PHILIPPS, S.; NOLD, S.; LUDE, S.; SAAD, N.; SCHLEGL, T. *LEVELIZED COST OF ELECTRICITY RENEWABLE ENERGY TECHNOLOGIES study*; FRAUNHOFER ISE, 2013.

[39] Menard, E.; Wagner, W.; Furman, B.; Ghosal, K.; Gabriel, J.; Meitl, M.; Burroughs, S. In *Proc. 37th IEEE Photovolt. Spec. Conf.* 2011, p 002268-002272.

[40] Bronstein, N. D.; Li, L.; Xu, L.; Yao, Y.; Ferry, V. E.; Alivisatos, A. P.; Nuzzo, R. G. Luminescent Solar Concentration with Semiconductor Nanorods and Transfer-Printed Micro-Silicon Solar Cells. *ACS Nano* **2014**, *8*, 44-53.

[41] Sheng, X.; Shen, L.; Kim, T.; Li, L.; Wang, X.; Dowdy, R.; Froeter, P.; Shigeta, K.; Li, X.; Nuzzo, R. G.; Giebink, N. C.; Rogers, J. A. Doubling the Power Output of Bifacial Thin-Film GaAs Solar Cells by Embedding Them in Luminescent Waveguides. *Adv. Energy Mater.* **2013**, *3*, 991-996.

[42] Sheng, X.; Corcoran, C. J.; He, J.; Shen, L.; Kim, S.; Park, J.; Nuzzo, R. G.; Rogers, J. A. Enhanced ultraviolet responses in thin-film InGaP solar cells by down-shifting. *Phys. Chem. Chem. Phys.* **2013**, *15*, 20434-20437.

[43] Bronstein, N. D.; Yao, Y.; Xu, L.; O'Brien, E.; Powers, A. S.; Ferry, V. E.; Alivisatos, A. P.; Nuzzo, R. G. Quantum Dot Luminescent Concentrator Cavity Exhibiting 30-fold Concentration. *ACS Photonics* **2015**, *2*, 1576-1583.

[44] Xu, L.; Yao, Y.; Bronstein, N. D.; Li, L.; Alivisatos, A. P.; Nuzzo, R. G. Enhanced Photon Collection in Luminescent Solar Concentrators with Distributed Bragg Reflectors. *ACS Photonics* **2016**.

[45] Gueymard, C. *SMARTS2: a simple model of the atmospheric radiative transfer of sunshine: algorithms and performance assessment*; Florida Solar Energy Center Cocoa, FL, 1995.

[46] Gueymard, C. A. Parameterized transmittance model for direct beam and circumsolar spectral irradiance. *Sol. Energy* **2001**, *71*, 325-346.